

Optimisation and Characterisation of Alternative Hole Transporting Media of Dye-Sensitised Solar Cells and Stability Study of Perovskite Solar Cells

Chun Hung Law

Imperial College London

Department of Chemistry

This thesis is submitted for the degree of *Doctor of Philosophy*

2014

Abstract

Dye-sensitised solar cells (DSSCs) are regarded as a possible alternative to silicon-based photovoltaics because of their potential for low-cost production. The processing of two alternative hole transport media, one for liquid-state DSSCs and the other for solid-state DSSCs is studied in this thesis. Also, research interest in methyl ammonium lead iodide perovskite solar cells has been increasing quickly. This thesis also reports some preliminary studies on the stability of $\text{TiO}_2/\text{CH}_3\text{NH}_3\text{PbI}_3$ perovskite solar cells.

Water is not commonly used as a solvent in liquid electrolyte DSSCs, but there are many reasons to re-examine water, ranging from cost advantage to fundamental science. The first part of the thesis addresses the wetting and recombination issues of water-based DSSCs. DSSCs using only water as the solvent and guanidinium iodide/iodine as the redox couple have been fabricated and they operate at 4% energy efficiency under 1-sun illumination.

The second part of this thesis studies melt-processing of hole transport materials. This technique overcomes the problem of poor pore filling which is commonly observed in solid-state dye-sensitised solar cells. It is found that the low efficiency of melt-processed DSSCs is due to the heat applied during the melting process which causes a decrease in recombination lifetime. Solid-state DSSCs made with melt-processed spiro-OMeTAD are shown, with a maximum efficiency of 0.45 %.

Stability of $\text{TiO}_2/\text{CH}_3\text{NH}_3\text{PbI}_3$ perovskite solar cells is examined in the third part of the thesis. Most literature in the perovskite solar cells focuses on the efficiency of devices, with little attention being paid to stability. A $\text{TiO}_2/\text{CH}_3\text{NH}_3\text{PbI}_3$ solar cell has been exposed to 40 sun-equivalent constant illumination for 63 hours (which delivers over 2700 hours equivalent of 1 sun photo-excitations). The loss in the cell's J_{sc} was only 7 %, however the loss in V_{oc} was 190 mV (24 %) at 1 sun.

Declaration of Originality

The work presented in this thesis was performed under the supervision of Dr. Brian O'Regan in the Department of Chemistry at Imperial College London.

I declare that the work presented in the thesis is my own except where specific reference is made.

The copyright of this thesis rests with the author and is made available under a Creative Commons Attribution Non-Commercial No Derivatives licence. Researchers are free to copy, distribute or transmit the thesis on the condition that they attribute it, that they do not use it for commercial purposes and that they do not alter, transform or build upon it. For any reuse or redistribution, researchers must make clear to others the licence terms of this work.

Table of Contents

Abstract	2
Declaration of Originality	3
Table of Contents	4
Acknowledgements	8
List of Publications	9
List of Figures	10
List of Tables	19
Abbreviations	21
1 Introduction	24
1.1 Motivation	24
1.2 Composition of Dye-Sensitised Solar Cells (DSSCs)	26
1.3 Operating Principles of Dye-Sensitised Solar Cells	27
1.4 Liquid-State Dye-Sensitised Solar Cells	29
1.5 Water in Liquid-State Dye-Sensitised Solar Cells	31
1.6 Diffusion-Limited Current Density (J_{DL}) in Liquid-State DSSCs	36
1.7 Solid-State Dye-Sensitised Solar Cells	38
1.8 Pore Filling in Solid-State Dye-Sensitised Solar Cells	40
1.9 Deposition Methods of Hole Transporting Materials	42
1.10 Methylammonium Lead Halide Perovskite Solar Cells	45
1.11 Aims of the Thesis	49
2 Experimental Methods	50
2.1 Materials	50
2.2 Fabrication of Liquid-State Dye-Sensitised Solar Cells	51
2.2.1 Preparation of Working Electrodes	51
2.2.2 Preparation of Counter Electrodes	52
2.2.3 Cell Assembly	53
2.3 Fabrication of Solid-State Dye-Sensitised Solar Cells	54
2.3.1 Spray Pyrolysis	54
2.3.2 Melt-Processing of Hole Transporting Materials	55

2.3.3	Graphite Counter Electrodes	57
2.4	Fabrication of Mesoporous-TiO ₂ /CH ₃ NH ₃ PbI ₃ Perovskite Solar Cells	58
2.4.1	Preparation of Methylammonium Iodide	58
2.4.2	Cell Fabrication	58
2.5	Characterisation Techniques	61
2.5.1	Optical Measurements	61
2.5.2	Current Density-Voltage (<i>JV</i>) Measurements	61
2.5.3	Transient Photovoltage and Photocurrent, and Charge Extraction Measurements	61
3	Water-Based Dye-Sensitised Solar Cells	62
3.1	Improving Wetting and Diffusion-Limited Current Density in Water-Based Dye-Sensitised Solar Cells	63
3.1.1	Introduction	63
3.1.2	Experimental Methods	66
3.1.3	Results	67
3.1.3.1	Symmetrical Cells in Water vs. MPN. Systems	67
3.1.3.2	Effect of Chenodeoxycholic Acid in Wetting	69
3.1.4	Discussion	70
3.1.5	Conclusion	77
3.2	Optimisation of Water-Based Dye-Sensitised Solar Cells	78
3.2.1	Introduction	78
3.2.2	Experimental Methods	80
3.2.3	Results	82
3.2.3.1	Varying Iodine Concentrations	82
3.2.3.2	Varying Iodide Concentrations	87
3.2.3.3	Al ₂ O ₃ Overlayer	89
3.2.3.4	Injection	97
3.2.3.5	Optimising Efficiency	98
3.2.4	Discussion	102
3.2.5	Conclusion	106
4	Melt-Processed Solid-State Dye-Sensitised Solar Cells	107
4.1	Brief Air Heating of Dye-Sensitised TiO ₂ Films, to 120-255 °C; the Effect on Resulting Liquid-State DSSCs	108

4.1.1	Introduction	108
4.1.2	Experimental Methods	110
4.1.3	Results	110
4.1.4	Discussion	118
4.1.5	Conclusion	119
4.2	Melt-Processing Hole Transporting Materials in Solid-State Dye-Sensitised Solar Cells	120
4.2.1	Introduction	120
4.2.2	Experimental Methods	122
4.2.3	Results	123
4.2.3.1	Toluene Treatment	123
4.2.3.2	Effect of Heat and Toluene Treatment on TiO ₂ /Dye Films and the Resultant Cell Performance	125
4.2.3.3	Effect of Heat on Thinner TiO ₂ /Dye Films (1-2 μm) and the Resultant Cell Performance	133
4.2.3.4	Fabricating Solid-State DSSCs by Melt-Processing Hole Transporting Materials (HTMs)	137
4.2.4	Discussion	138
4.2.5	Conclusion	140
5	Preliminary Stability Study on Methylammonium Lead Halide Perovskite Solar Cells	141
5.1	Introduction	142
5.2	Experimental Methods	143
5.3	Results	146
5.3.1	Relative Stability of Perovskite Films against Oxygen and Moisture in Air and Light	146
5.3.2	Stability of mp-TiO ₂ /MAPI Solar Cells	152
5.3.2.1	Most Efficient mp-TiO ₂ /MAPI Solar Cells with P3HT, DPPTTT and Spiro-OMeTAD	152
5.3.2.2	Stability of Encapsulated mp-TiO ₂ /MAPI/P3HT Solar Cells under Constant Illumination with UV Cutoff Filter vs. without UV Cutoff Filter	154

5.3.2.3	Stability of Encapsulated vs. Non-Encapsulated mp-TiO ₂ /MAPI/P3HT Solar Cells	156
5.3.2.4	Stability of Encapsulated mp-TiO ₂ /MAPI/P3HT Solar Cells at 60 °C in the Dark	158
5.3.2.5	Most Photo-Stable mp-TiO ₂ /MAPI Solar Cells with P3HT, DPPTTT and Spiro-OMeTAD	159
5.3.2.6	Most Photo-Stable mp-TiO ₂ /MAPI/Spiro-OMeTAD Solar Cells (Illuminated at 40 SE over 63 Hours)	161
5.4	Results	166
5.5	Conclusion	170
6	Conclusion	171
	References	173
	Appendix	186
	Summary of Permission for Third Party Copyright Works	203

Acknowledgements

I would like to express my most heartfelt thanks and sincere appreciation to my supervisor, Dr. Brian O'Regan for giving me the chance to study a Ph.D degree and for his simulating advice and constructive criticism during the years of research. I would also like to extend my appreciation to Prof. James Durant for his support during my study.

I would like to gratefully acknowledge the funding contribution from the UK EPSRC project APEX and SPECIFIC, the UK TSB project "Water based electrolytes" and the EU FP7 project SMARTOP.

Many thanks to all those who has helped me in the laboratory: Dr. Xiaoe Li, Dr. Piers Barnes, Dr. Andrea Listorti, Dr. Assaf Anderson, Mindaugas Juozapavicius, Caryl Richards, Roger Jiang, Xavier Jeanbourquin, Niall Killilea, Cameron Jellett, Piers Barnes, Davide Moia, Yanling Fan, Aurelien Legeuy, Sheehan Pathirana, Ryan Spence, Kee Sheng Yeo, Eric Tan and Dr. Pabitra Shakya Tuladhar. I really enjoyed working with all of you.

My heartfelt thanks also go to my dear friends who have made my time at Imperial College so enjoyable and memorable: Steven, Yvonne, Yimeng, ChingHong, Zhe, Christina and Florent.

Finally, my deepest gratitude goes to my parents, brother (Jason), sister (Regina) and my girlfriend (Ruby) for all their selfless support and unconditional love. Without them, I would not have made it today.

List of Publications

1. Law, C.; Pathirana, S. C.; Li, X.; Anderson, A. Y.; Barnes, P. R. F.; Listorti, A.; Ghaddar, T. H.; O'Regan, B. C., Water-Based Electrolytes for Dye-Sensitized Solar Cells. *Advanced Materials* **2010**, 22 (40), 4505-4509.
2. Law, C.; Moudam, O.; Villarroja-Lidon, S.; O'Regan, B., Managing wetting behavior and collection efficiency in photoelectrochemical devices based on water electrolytes; improvement in efficiency of water/iodide dye sensitised cells to 4%. *Journal of Materials Chemistry* **2012**, 22 (44), 23387-23394.
3. Law, C.; Spence, R.; O'Regan, B., Brief air heating of TiO₂/dye films, to 120-250 °C; the effect on resulting liquid junction dye sensitised solar cells (DSSCs) and melt-processed solid-state DSSCs. *Journal of Materials Chemistry A* **2013**, 1 (45), 14154-14161.

List of Figures

Fig. 1.1 Highest recorded solar cell efficiencies and the institutions accredited for research into these devices over the last 39 years.

Fig. 1.2 Schematic diagram showing the composition of a typical liquid junction DSSC.

Fig. 1.3 Energy diagram showing the energy levels of different components and the possible routes an electron can take in a DSSC during its operation.

Fig. 1.4 A typical JV curve and the positions of the maximum power point, V_{OC} , J_{SC} , V_M , J_M .

Fig. 1.5 Chemical structures of the N3 and Z907 dyes.

Fig. 1.6 Chemical structures of the YD2-*o*-C8 and Y123 dyes.

Fig. 1.7 Chemical structures of the N719 and TPA2 dyes.

Fig. 1.8 Chemical structure of the TG6 dye.

Fig. 1.9 One-sun and dark JV of a typical DSSC which J_{SC} is limited by J_{DL} .

Fig. 1.10 Chemical structures of spiro-OMeTAD and FK102.

Fig. 1.11 Schematic diagram showing the pore filling issue in the porous TiO_2 layer in solid-state DSSCs.

Fig. 1.12 Schematic diagram showing the film forming and material infiltration process during spin-coating.

Fig. 1.13 Chemical structures of D149 and D205.

Fig. 1.14 Schematic diagram showing the structure of the methylammonium lead iodide (MAPI) perovskite.

Fig. 1.15 Chemical structure of poly[bis(4-phenyl)(2,4,6-trimethylphenyl)amine] or PTAA.

Fig. 2.1 Schematic diagram showing the procedures of the ‘doctor blade’ technique.

Fig. 2.2 Schematic diagram showing the positions of the holes, the Surlyn and the platinised area of a counter electrode.

Fig. 2.3 Schematic diagram showing the procedures of assembling DSSC.

Fig. 2.4 Schematic diagram showing the procedures of melt-processing HTM on a TiO_2 /dye film.

Fig. 2.5 Schematic diagram showing the construction of graphite counter electrode.

Fig. 2.6 Schematic diagram showing the procedures of fabricating mp-TiO₂/CH₃NH₃PbI₃ perovskite solar cells.

Fig. 3.1 a) One-sun JV curves vs. water content for cells with TG6 dye. Illuminated using simulated AM 1.5 (filtered xenon lamp) at 100 mW cm⁻². b) J_{sc} vs. bias light intensity for selected W00 and high-water-content cells. W00, W20, etc. refer to electrolytes with 0 %, 20 %, etc. water, relative to MPN. Percentages are J_{sc} relative to the W00 cell at the same light intensity. Illuminated using white light-emitting diodes. (The currents differ from panel (a) due to large spectral mismatch compared to AM1.5.)

Fig. 3.2 a) Dark and illuminated (≈ 0.8 suns) extended JV curves for TS4 cells with varying water content. The sign of voltage is that applied to the counter electrode. b) Excess electron density in the TiO₂ at short circuit (relative to dark) vs light level for different water content in TS4 cells. W00, W20, etc. refer to electrolytes with 0 %, 20 %, etc. water, relative to MPN.

Fig. 3.3 Chemical structure of guanidinium thiocyanate (GuSCN).

Fig. 3.4 Schematic diagram of the symmetric cells used to examine J_{DL} .

Fig. 3.5 Top: Current density–voltage (JV) curves of different symmetrical cells with electrolyte consisting of 0.1 M NaI and 0.01 M iodine in water. Bottom: Current density–normalised voltage curves of different symmetrical cells with electrolyte consisting of 0.1 M NaI and 0.01 M iodine in MPN. Label, e.g. Pt–TiO₂, refers to the symmetric structure Pt–TiO₂–gap–TiO₂–Pt. Total thickness: 75 μ m for all cells. TiO₂: DyeSol 7 μ m.

Fig. 3.6 Chemical structure of chenodeoxycholic acid (cheno)

Fig. 3.7 One-sun JV curves of water-based DSSCs with and without cheno in the cell. Without cheno cell: TiO₂ film: DyeSol 7 μ m; Dye: Z907; Electrolyte: water with 2 M NaI, 20 mM iodine and 1 M GuSCN. With cheno cell: identical except: dye solution had 1:50 Z907:cheno, electrolyte had 0.5 M GuSCN.

Fig. 3.8 Schematic diagram showing how applied voltage and additional layers of porous TiO₂ affect the concentration gradient of triiodide in symmetrical cells.

Fig. 3.9 Schematic diagram showing the wetting problem in the Z907-sensitised TiO₂ layer in water-based DSSCs.

Fig. 3.10 Chemical structures of polyethylene glycol (left) and the MK2 dye (right).

Fig. 3.11 Chemical structures of Tween®20 (left) and Triton X-100 (right).

Fig. 3.12 Chemical structures of the JK-259 and JK-262 dyes.

Fig. 3.13 Chemical structure of the TS4 dye.

Fig. 3.14 Chemical structure of 1,2-dihydroxybenzene (catechol)

Fig. 3.15 One-sun JV curves of water-based Z907 DSSCs with varying added iodine concentration.

Fig. 3.16 Recombination lifetime vs. charge density (bottom), of water-based Z907 DSSCs with varying added iodine concentration.

Fig. 3.17 J_{sc} vs. bias light intensity of water-based Z907 DSSCs with varying added iodine concentration.

Fig. 3.18 Charge density vs. J_{sc} of water-based Z907 DSSCs with varying added iodine concentration.

Fig. 3.19 One-sun JV curves of water-based D149 DSSCs with varying added iodine concentration.

Fig. 3.20 Recombination lifetime vs. charge density of water-based D149 DSSCs with varying added iodine concentration.

Fig. 3.21 J_{sc} vs. bias light intensity of water-based D149 DSSCs with varying added iodine concentration.

Fig. 3.22 One-sun JV curves of water-based Z907 DSSCs with varying sodium iodide concentration.

Fig. 3.23 One-sun JV curves of water-based D149 DSSCs with varying sodium iodide concentration.

Fig. 3.24 Absorption spectra showing the change in absorbance of a catechol-sensitised nanoporous (np) Al_2O_3 control film, and np- TiO_2 films treated in $Al(Bu^sO)_3$ solution for 0, 15, 30, 45 min and 3 hours and then sensitised in catechol solution.

Fig. 3.25 One-sun JV curves of water-based D149 DSSCs with TiO_2 film treated in different ways.

Fig. 3.26 Absorption spectra showing the change in absorbance of np- TiO_2 films, treated by $TiCl_4$, then treated in $Al(Bu^sO)_3$ solution for 0, 15, 30, 45 min and 3 hours and finally sensitised in catechol solution.

Fig. 3.27 Absorption spectra showing the change in absorbance of np- TiO_2 films, treated by $TiCl_4$, then treated in $Al(Bu^sO)_3$ solution for 15 min for 1, 2 and 3 times and finally sensitised in catechol solution.

Fig. 3.28 One-sun JV curves of water-based D149 DSSCs with TiO_2 films (all with $TiCl_4$) treated in $Al(Bu^sO)_3$ solution for 0, 1 and 3 times.

Fig. 3.29 Charge density vs. V_{oc} of water-based D149 DSSCs with TiO_2 films (all with $TiCl_4$) treated in $Al(Bu^sO)_3$ solution for 0, 1 and 3 times.

Fig. 3.30 Charge density vs. J_{sc} of D149-based DSSCs with TiO_2 films (all with $TiCl_4$) treated in $Al(Bu^sO)_3$ solution for 0, 1 and 3 times.

Fig. 3.31 Transport lifetime vs. charge density of D149-based DSSCs with TiO_2 films (all with $TiCl_4$) treated in $Al(Bu^sO)_3$ solution for 0, 1 and 3 times.

Fig. 3.32 Recombination lifetime vs. charge density of D149-based DSSCs with TiO₂ films (all with TiCl₄) treated in Al(Bu^sO)₃ solution for 0, 1 and 3 times.

Fig. 3.33 One-sun *JV* curves of water-based D149 DSSCs with varying HI concentration.

Fig. 3.34 One-sun *JV* curves of three efficient water-based DSSCs.

Fig. 3.35 One-sun *JV* curves of water-based D149 DSSCs with varying guanidinium iodide and iodine concentrations.

Fig. 3.36 *Jsc* vs. light intensity of water-based D149 DSSCs with varying guanidinium iodide and iodine concentrations.

Fig. 3.37 Recombination lifetime vs. charge density of water-based D149 DSSCs with varying guanidinium iodide and iodine concentrations.

Fig. 3.38 Chemical structures of 1-ethyl-3-methylimidazolium 4-methyl-1,2,4-triazole-3-thiolate (TTEMI⁺)/3,3'-dithiobis[4-methyl-(1,2,4)-triazole] (DTT), D45 and D51.

Fig. 4.1 Chemical structure of the D5 dye.

Fig. 4.2 Absorption spectra of Z907-sensitised TiO₂ film (DyeSol, 7 μm) after 1 minute heating at different temperatures.

Fig. 4.3 One-sun *JV* curves of liquid-state DSSCs fabricated with Z907-sensitised TiO₂ electrodes (DyeSol, 7 μm) heated at different temperatures for 1 minute.

Fig. 4.4 Charge density vs. *Voc* of liquid-state DSSCs fabricated with Z907-sensitised TiO₂ electrodes (DyeSol, 7 μm) heated at different temperatures for 1 minute.

Fig. 4.5 Charge density vs. *Jsc* of liquid-state DSSCs fabricated with Z907-sensitised TiO₂ electrodes (DyeSol, 7 μm) heated at different temperatures for 1 minute.

Fig. 4.6 Recombination lifetimes vs. charge density of liquid-state DSSCs fabricated with Z907-sensitised TiO₂ electrodes (DyeSol, 7 μm) heated at different temperatures for 1 minute.

Fig. 4.7 Electron lifetimes at *Jsc* vs. charge density of liquid-state DSSCs fabricated with Z907-sensitised TiO₂ electrodes (DyeSol, 7 μm) heated at different temperatures for 1 minute.

Fig. 4.8 Absorption spectra of D149-sensitised TiO₂ film (transparent, 4.2 μm) heated at different temperatures for 1 minute.

Fig. 4.9 One-sun *JV* curves of liquid-state DSSCs fabricated with D149-sensitised TiO₂ electrodes (transparent, 4.2 μm) heated at different temperatures for 1 minute.

Fig. 4.10 Charge density vs. *Voc* of liquid-state DSSCs fabricated with D149-sensitised TiO₂ electrodes (transparent, 4.2 μm) after 1 minute heating at different temperatures.

Fig. 4.11 Charge density vs. *Jsc* of liquid-state DSSCs fabricated with D149-sensitised TiO₂ electrodes (transparent, 4.2 μm) after 1 minute heating at different temperatures.

Fig. 4.12 Recombination lifetime vs. charge density of liquid-state DSSCs fabricated with D149-sensitised TiO₂ electrodes (transparent, 4.2 μm) after 1 minute heating at different temperatures.

Fig. 4.13 Transport lifetime vs. charge density of liquid-state DSSCs fabricated with D149-sensitised TiO₂ electrodes (transparent, 4.2 μm) after 1 minute heating at different temperatures.

Fig. 4.14 Chemical structure of 4,4',4''-tris(N,N-diphenyl-amino)-triphenylamine.

Fig. 4.15 Chemical structures of 4-(diethyl-amino)benzaldehyde-1,1)-diphenyl-hydrazone (left) and the D35 dye (right).

Fig. 4.16 Chemical structure of VM3.

Fig. 4.17 Absorption spectra of TiO₂ film, in air, with melt-processed TPD, and with TPD desorbed by toluene treatment.

Fig. 4.18 Absorption spectra of TiO₂ film, in air, with melt-processed spiro-OMeTAD (SOT), and with SOT desorbed by toluene treatment.

Fig. 4.19 Absorption spectra of Z907-sensitised TiO₂ film (DyeSol, 7 μm) before and after different treatments.

Fig. 4.20 One-sun *JV* curves of liquid-state DSSCs fabricated with Z907-sensitised TiO₂ electrodes (DyeSol, 7 μm) having undergone different treatments.

Fig. 4.21 Recombination lifetime vs. charge density of liquid-state DSSCs fabricated with Z907-sensitised TiO₂ electrodes (DyeSol, 7 μm) having undergone different treatments.

Fig. 4.22 Absorption spectra of Z907-sensitised TiO₂ film (DyeSol, 7 μm) before and after different treatments.

Fig. 4.23 One-sun *JV* curves of liquid-state DSSCs fabricated with Z907-sensitised TiO₂ electrodes (DyeSol, 7 μm) having undergone different treatments.

Fig. 4.24 Recombination lifetime vs. charge density of liquid-state DSSCs fabricated with Z907-sensitised TiO₂ electrodes (DyeSol, 7 μm) having undergone different treatments.

Fig. 4.25 Absorption spectra of D149-sensitised TiO₂ film (DyeSol, 7 μm) before and after different treatments.

Fig. 4.26 One-sun *JV* curves of liquid-state DSSCs fabricated with D149-sensitised TiO₂ electrodes (DyeSol, 7 μm) having undergone different treatments.

Fig. 4.27 Recombination lifetime vs. charge density of liquid-state DSSCs fabricated with Z907-sensitised TiO₂ electrodes (DyeSol, 7 μm) having undergone different treatments.

Fig. 4.28 Absorption spectra of Z907-sensitised TiO₂ film (transparent, 1.3 μm) after 1 minute heating at different temperatures.

Fig. 4.29 Absorption spectra of D149-sensitised TiO₂ film (transparent, 2 μm) after 1 minute heating at different temperatures.

Fig. 4.30 One-sun *JV* curves of liquid-state DSSCs fabricated with Z907-sensitised TiO₂ electrodes (transparent, 1.3 μm) heated at different temperatures for 1 minute.

Fig. 4.31 One-sun *JV* curves of liquid-state DSSCs fabricated with D149-sensitised TiO₂ electrodes (transparent, 2 μm) heated at different temperatures for 1 minute.

Fig. 4.32 Recombination lifetime vs. charge density of liquid-state DSSCs fabricated with Z907-sensitised TiO₂ electrodes (transparent, 2 μm) heated at different temperatures for 1 minute.

Fig. 4.33 Recombination lifetime vs. charge density of liquid-state DSSCs fabricated with D149-sensitised TiO₂ electrodes (transparent, 2 μm) heated at different temperatures for 1 minute.

Fig. 4.34 *JV* curves of the two best solid-state DSSCs fabricated by melt-processing HTMs and a reference cell fabricated by spin-coating solution of spiro-OMeTAD (SOT).

Fig. 5.1 Schematic diagram showing the conditions in which the perovskite films were stored in during the stability test.

Fig. 5.2 Output spectrum of the Luxim plasma lamp from Luxim Corp.

Fig. 5.3 Chemical structures of P3HT and DPPTTT.

Fig. 5.4 One-sun *JV* curves of three efficient mp-TiO₂/MAPI solar cells with different hole transporting materials (HTMs).

Fig. 5.5 One-sun *JV* curves of the encapsulated mp-TiO₂/MAPI/P3HT solar cells with and without a 420 nm long pass filter before and after continuous 1 SE illumination from the Luxim lamp for 1 hour.

Fig. 5.6 Normalised one-sun *Jsc* of encapsulated mp-TiO₂/MAPI/P3HT solar cells with and without a 420 nm long pass filter as a function of time. The cells were under continuous 1 sun-equivalent (SE) illumination from the Luxim lamp for 1 hour. *Jsc*'s were normalised according to the initial value.

Fig. 5.7 One-sun *JV* curves of the encapsulated and non-encapsulated mp-TiO₂/MAPI/P3HT solar cells before and after continuous 1 SE illumination from the Luxim lamp for 1-2 hours.

Fig. 5.8 Normalised one-sun *Jsc* of an encapsulated and a non-encapsulated mp-TiO₂/MAPI/P3HT solar cells as a function of time. The cells were under continuous 1 sun-equivalent (SE) illumination from the Luxim lamp with a 420 nm long pass filter for 1-2 hours. Relative humidity was ~40%. *Jsc*'s were normalised according to the initial value.

Fig. 5.9 One-sun and dark *JV* curves of an encapsulated mp-TiO₂/MAPI/P3HT solar cell before and after storage at 60 °C in the dark for 18 hours. *JV* measurements were taken at 20 °C.

Fig. 5.10 Normalised two-sun J_{sc} of encapsulated TiO₂/MAPI/ solar cells with different HTMs as a function of time. The cells were under continuous 2 sun-equivalent (SE) illumination from the Luxim lamp with a 420 nm long pass filter for 12-23 hours. Temperature ~25 °C. J_{sc} 's were normalised according to the initial value.

Fig. 5.11 Two-sun JV curves of encapsulated TiO₂/MAPI solar cells with HTMs before and after the stability test.

Fig. 5.12 Forty-sun J_{sc} of an encapsulated mp-TiO₂/MAPI/spiro-OMeTAD solar cell as a function of time. The cell was under continuous 40 sun-equivalent (SE) illumination from the Luxim lamp with a 420 nm long pass filter for 63 hours. Gaps correspond to short periods where the cell was at open circuit under illumination. Temperature ~50 °C.

Fig. 5.13 Forty-sun JV curves of the encapsulated mp-TiO₂/MAPI/spiro-OMeTAD solar cell before and after the stability test and when the J_{sc} was at its maximum.

Fig. 5.14 One-sun JV curves of the encapsulated mp-TiO₂/MAPI/spiro-OMeTAD solar cell before and after continuous 40 sun-equivalent (SE) illumination from the Luxim lamp with a 420 nm long pass filter for 63 hours, and the same cell after heating at 60 °C in the dark for 20 hours.

Fig. 5.15 Charge density vs. V_{oc} , of the encapsulated TiO₂/MAPI/spiro-OMeTAD solar cell before and after continuous 40 sun-equivalent (SE) illumination from the Luxim lamp with a 420 nm long pass filter for 63 hours, and the same cell after heating at 60 °C in the dark for 20 hours.

Fig. 5.16 Recombination lifetime vs. charge density, of the encapsulated TiO₂/MAPI/spiro-OMeTAD solar cell before and after the stability tests.

Fig. 5.17 Charge density vs. J_{sc} , of the encapsulated TiO₂/MAPI/spiro-OMeTAD solar cell before and after the stability tests.

Fig. 5.18 Transport lifetime vs. charge density, of the encapsulated TiO₂/MAPI/spiro-OMeTAD solar cell before and after the stability tests.

Fig. 5.19 shows the maximum value, 75th percentile, median, 25th percentile and minimum value of the J_{sc} (top left), V_{oc} (top right), fill factor (bottom left), overall conversion efficiency (bottom right) of mp-TiO₂/MAPI with HTMs as indicated in the bottom axes. Number of P3HT cells: 15; DPPTTT cells: 15; spiro-OMeTAD cells: 21.

Fig. 5.20 Chemical structures of PDPPDBTE and PCBTDP.

Fig. A.1 Recombination lifetime vs. charge density of D149 DSSCs with different solvent in electrolyte. (**Cell Type A:** TiO₂ film: G24i paste, 8.4 μm; Dye: D149 1:4 cheno; Electrolytes: 1 M GuI and 20 mM iodine in solvent as noted in legend. **Cell Type B:** TiO₂ film: G24i paste, 4.1 μm; Dye: D149 1:4 cheno; Electrolytes: 2 M NaI, 20 mM iodine and 0.5 M GuSCN in water or MPN)

Fig. A.2 Charge density vs. redox potential corrected V_{oc} of water-based Z907 DSSCs with varying added iodine concentration.

Fig. A.3 Transport lifetime vs. charge density of water-based Z907 DSSCs with varying added iodine concentration.

Fig. A.4 Charge density vs. redox potential corrected V_{oc} of water-based D149 DSSCs with varying added iodine concentration.

Fig. A.5 Charge density vs. J_{sc} of water-based D149 DSSCs with varying added iodine concentration.

Fig. A.6 Transport lifetime vs. charge density of water-based D149 DSSCs with varying added iodine concentration.

Fig. A.7 Recombination lifetime vs. charge density of water-based Z907 DSSCs with varying iodide concentration.

Fig. A.8 Charge density vs. redox potential corrected V_{oc} of water-based Z907 DSSCs with varying iodide concentration.

Fig. A.9 Charge density vs. J_{sc} of water-based Z907 DSSCs with varying iodide concentration.

Fig. A.10 Transport lifetime vs. charge density of water-based Z907 DSSCs with varying iodide concentration.

Fig. A.11 Recombination lifetime vs. charge density of water-based D149 DSSCs with varying iodide concentration.

Fig. A.12 Charge density vs. redox potential corrected V_{oc} of water-based D149 DSSCs with varying iodide concentration.

Fig. A.13 Charge density vs. J_{sc} of water-based D149 DSSCs with varying iodide concentration.

Fig. A.14 Transport lifetime vs. charge density of water-based D149 DSSCs with varying iodide concentration.

Fig. A.15 Charge density vs. redox potential corrected V_{oc} of water-based D149 DSSCs with varying guanidinium iodide and iodine concentrations.

Fig. A.16 Charge density vs. J_{sc} of water-based D149 DSSCs with varying guanidinium iodide and iodine concentrations.

Fig. A.17 Transport lifetime vs. charge density of water-based D149 DSSCs with varying guanidinium iodide and iodine concentrations.

Fig. A.18 Charge density vs. V_{oc} of liquid-state DSSCs fabricated with Z907-sensitised TiO_2 electrodes (DyeSol, 7 μm) having undergone different treatments.

Fig. A.19 Charge density vs. J_{sc} of liquid-state DSSCs fabricated with Z907-sensitised TiO_2 electrodes (DyeSol, 7 μm) having undergone different treatments.

Fig. A.20 Electron lifetime at J_{sc} vs. charge density of liquid-state DSSCs fabricated with Z907-sensitised TiO₂ electrodes (DyeSol, 7 μm) having undergone different treatments.

Fig. A.21 Charge density vs. V_{oc} of liquid-state DSSCs fabricated with D149-sensitised TiO₂ electrodes (DyeSol, 7 μm) having undergone different treatments.

Fig. A.22 Charge density vs. J_{sc} of liquid-state DSSCs fabricated with D149-sensitised TiO₂ electrodes (DyeSol, 7 μm) having undergone different treatments.

Fig. A.23 Electron lifetime at J_{sc} vs. charge density of liquid-state DSSCs fabricated with D149-sensitised TiO₂ electrodes (DyeSol, 7 μm) having undergone different treatments.

Fig. A.24 Charge density vs. V_{oc} of liquid-state DSSCs fabricated with Z907-sensitised TiO₂ electrodes (transparent, 1.3 μm) heated at different temperatures for 1 minute.

Fig. A.25 Charge density vs. J_{sc} of liquid-state DSSCs fabricated with Z907-sensitised TiO₂ electrodes (transparent, 1.3 μm) heated at different temperatures for 1 minute.

Fig. A.26 Electron lifetime at J_{sc} vs. charge density of liquid-state DSSCs fabricated with Z907-sensitised TiO₂ electrodes (transparent, 1.3 μm) heated at different temperatures for 1 minute.

Fig. A.27 Charge density vs. V_{oc} of liquid-state DSSCs fabricated with D149-sensitised TiO₂ electrodes (transparent, 2 μm) heated at different temperatures for 1 minute.

Fig. A.28 Charge density vs. J_{sc} of liquid-state DSSCs fabricated with D149-sensitised TiO₂ electrodes (transparent, 2 μm) heated at different temperatures for 1 minute.

Fig. A.29 Electron lifetime at J_{sc} vs. charge density of liquid-state DSSCs fabricated with Z907-sensitised TiO₂ electrodes (transparent, 1.3 μm) heated at different temperatures for 1 minute.

Fig. A.30 Two-sun and dark JV curves of encapsulated TiO₂/MAPI solar cells with HTMs after the stability test of continuous illumination (P3HT: @2 suns for 12 hours; DPPTTT: @2 suns for 21 hours).

List of Tables

Table 3.1 One-sun performance of water electrolyte water-based Z907 DSSCs with varying added iodine concentration.

Table 3.2 One-sun performance of water-based D149 DSSCs with varying added iodine concentration.

Table 3.3 One-sun JV performance of water-based Z907 DSSCs with varying sodium iodide concentration.

Table 3.4 One-sun JV performance of water-based D149 DSSCs with varying sodium iodide concentration.

Table 3.5 One-sun performance of water-based D149 DSSCs with TiO₂ film treated in different ways.

Table 3.6 One-sun performance of D149-based DSSCs with TiO₂ films (all with TiCl₄) treated in Al(Bu^sO)₃ solution for 0, 1 and 3 times.

Table 3.7 One-sun performance of water-based D149 DSSCs with varying HI concentration.

Table 3.8 Compositions and one-sun performance of three efficient pure water DSSCs.

Table 3.9 One-sun performance of water-based D149 DSSCs with varying guanidinium iodide and iodine concentrations, and active area.

Table 4.1 One-sun performance of liquid-state DSSCs fabricated with Z907-sensitised TiO₂ electrodes (DyeSol, 7 μm) heated at different temperatures for 1 minute.

Table 4.2 One-sun performance of liquid-state DSSCs fabricated with D149-sensitised TiO₂ electrodes (transparent, 4.2 μm) heated at different temperatures for 1 minute.

Table 4.3 One-sun performance of liquid-state DSSCs fabricated with Z907-sensitised TiO₂ electrodes (DyeSol, 7 μm) having undergone different treatments.

Table 4.4 One-sun performance of liquid-state DSSCs fabricated with Z907-sensitised TiO₂ electrodes (DyeSol, 7 μm) having undergone different treatments.

Table 4.5 One-sun performance of liquid-state DSSCs fabricated with Z907-sensitised TiO₂ electrodes (DyeSol, 7 μm) having undergone different treatments

Table 4.6 One-sun performance of liquid-state DSSCs fabricated with TiO₂/Z907 and TiO₂/D149 electrodes having undergone different treatments.

Table 4.7 One-sun performance of the best solid-state DSSCs fabricated by melt-processing HTMs and a reference cell fabricated by spin-coating solution of spiro-OMeTAD (SOT).

Table 5.1 Photos of a series of perovskite films before and after storage for 2 weeks. All film thicknesses (with or without mesoporous layer) are ~150 nm. All films were stored in the dark in a glovebox (humidity: <0.01 %, oxygen level: <0.01 %).

Table 5.2 Photos of a series of perovskite films before and after storage for 2 weeks. All films were stored under constant 0.1 sun-equivalent (SE) illumination from white LEDs in a glovebox (humidity: <0.01 %, relative oxygen concentration: <0.01 %).

Table 5.3 Photos of a series of perovskite films before and after storage for 2 weeks. All films were stored in the dark in a 'dry' box (humidity: ~25 %, relative oxygen concentration: 20-21 %, air).

Table 5.4 Photos of a series of perovskite films before and after storage for different periods of time. All films were stored under constant 0.1 sun-equivalent (SE) illumination from white LEDs in a 'dry' box (humidity: ~25 %, relative oxygen concentration: 20-21 %, air).

Table 5.5 Photos of a series of perovskite films before and after storage for different periods of time. All films were stored in the dark in a 'wet' box (humidity: >90 %, relative oxygen concentration: 20-21 %, air).

Table 5.6 Photos of a series of perovskite films before and after storage for different periods of time. All films were stored under constant 0.1 sun-equivalent (SE) illumination from white LEDs in a 'wet' box (humidity: >90 %, relative oxygen concentration: 20-21 %, air).

Table 5.7 One-sun performance of three efficient mp-TiO₂/MAPI solar cells with different hole transporting materials (HTMs).

Table 5.8 One-sun performance of the encapsulated mp-TiO₂/MAPI/P3HT solar cell with and without a 420 nm long pass filter before and after continuous 1 SE illumination from the Luxim for 1 hour.

Table 5.9 One-sun performance of the encapsulated and non-encapsulated mp-TiO₂/MAPI/P3HT solar cells before and after continuous 1 SE illumination from the Luxim with a 420 nm long pass filter for 1-2 hours.

Table 5.10 One-sun performance of the encapsulated mp-TiO₂/MAPI/P3HT solar cell before and after storage at 60 °C in the dark for 18 hours.

Table 5.11 Two-sun performance of encapsulated TiO₂/MAPI solar cells with different HTMs before and after stability test.

Table 5.12 Forty-sun performance of the encapsulated mp-TiO₂/MAPI/spiro-OMeTAD solar cell before and after stability test, and when the *J*_{sc} was at its maximum.

Table 5.13 One-sun JV curves of the encapsulated mp-TiO₂/MAPI/spiro-OMeTAD solar cell before and after stability tests.

Table A.1 shows the photos of lead iodide, lead chloride and methylammonium iodide (NH₃CH₃I or MAI) on a glass plate with or without mesoporous titania (mp-TiO₂) layer or mesoporous alumina (mp-Al₂O₃) layer.

Abbreviations

ACN	Acetonitrile
ALD	Atomic layer deposition
AM	Air mass
AOT	Aeraol OT
a_{ox}	Activity coefficient of the oxidised product
a_{red}	Activity coefficient of the reduced product
b.p.	Boiling point
Cheno	Chenodeoxycholic acid
CTAB	Hexadecyltrimethylammonium bromide
CuSCN	Copper thiocyanate
δ	Constrictivity
D	Diffusion coefficient
D_e	Effective diffusion coefficient
DI	Deionised
DMF	Dimethylformamide
DPPTTT	Poly-thieno[3,2 <i>b</i>]thiophene-diketopyrrolopyrroleco-thiophene
DSSC	Dye-sensitised solar cell
ε	Porosity
EDS	Energy dispersive x-ray spectrometry
E_F	Fermi level
η_{eff}	Power conversion efficiency
EIS	Electrochemical impedance spectroscopy
F	Faraday constant
FB	Forward bias
FF	Fill factor
FTO	Fluorine doped tin oxide
GB	Glovebox
GBL	γ -butyrolactone
Gu^+	Guanidinium ion
GuI	Guanidinium iodide
GuSCN	Guanidinium thiocyanate
HOMO	Highest occupied molecular orbital

HTM	Hole transporting material
IPA	Isopropanol
IPCE	Incident photon to electron conversion efficiency
ITO	Indium tin oxide
J_{DL}	Diffusion-limited current density
J_M	Current density at maximum power point
J_{sc}	Short circuit current density
JV	Current density-voltage
LED	Light-emitting diode
Li-TFSI	Lithium bis(trifluoromethylsulfonyl)imide
LUMO	Lowest unoccupied molecular orbital
MAPB	Methylammonium lead tribromide
MAPI	Methylammonium lead triiodide
MAPIC	Methylammonium lead iodide chloride
MEHPPV	Poly[2-methoxy-5-(2'-ethylhexyloxy)-p-phenylene vinylene]
MEISCN	1-methyl-3-ethylimidazolium thiocyanate
m.p.	Melting point
mp	Mesoporous
MPN	3-methoxypropionitrile
MPP	Maximum power point
ms	Meso-superstructured
NHE	Normal hydrogen electrode
NMBI	N-methylbenzimidazole
np	nanoporous
P3HT	Poly(3-hexylthiophene)
PC	Propylene carbonate
PCE	Power conversion efficiency
PEDOT	Poly(3,4-ethylenedioxythiophene)
PEO	Poly(ethylene oxide)
PES	Photoelectron spectroscopy
PET	Polyethylene terephthalate
PFF	Pore filling fraction
P_{in}	Power input
PMII	2-propyl-1-methylimidazolium iodide

P_{out}	Power output
PTAA	Polytriarylamine polymer
PVDF	Poly(vinylidene fluoride)
R	Universal gas constant
Rmv. Tol.	Hole transporting materials removed by toluene
rpm	Revolutions per minute
R_{ser}	Series resistance
SC	Short circuit
SE	Sun-equivalent
SEI	Solid electrolyte interphase
SEM	Scanning electron microscopy
SOT	2,2',7,7'-tetrakis-(N,N-di-p-methoxyphenylamine)9,9'-spirobifluorene
SPD	Spray pyrolysis deposition
Spiro-OMeTAD	2,2',7,7'-tetrakis-(N,N-di-p-methoxyphenylamine)9,9'-spirobifluorene
τ	Tortuosity
T	Temperature
TAS	Transient Absorption Spectroscopy
TBA ⁺	Tetrabutylammonium counterion
TBP	4- <i>tert</i> -butylpyridine
TCO	Transparent conducting oxide
THF	Tetrahydrofuran
TPD	N,N'-bis(3-methylphenyl)-N,N'-diphenylbenzidine
TRACER	Transient and charge extraction robot
UV	Ultra-violet
V_M	Voltage at maximum power point
V_{oc}	Open circuit voltage

Chapter 1

Introduction

1.1 Motivation

The world's population is projected to increase from 7 billion people in late 2011 to an unprecedented size between 8.3 billion to 10.9 billion people, according to a study published by United Nation in 2013.¹ Energy use is clearly expected to increase in order to accommodate the rapid expansion of population and strong economic growth of emerging economies around the world. The International Energy Outlook 2013 predicts that the global energy consumption will grow by 56 % between 2010 and 2040.² This obviously requires a larger energy generation capacity. While ~80 % of the world's energy currently consumed comes from the combustion of fossil fuels,² the concern of global warming caused by its enormous carbon emission has also been growing. Thus, generating energy in a carbon neutral way is desperately needed. One exciting prospect that has attracted wide-spread interest is photovoltaic solar energy conversion. Apart from being clean and renewable, photovoltaic also has an enormous energy source for conversion into electricity. It is estimated that the energy of sunlight reaching the surface of the Earth in an hour is already more than the total energy used by the global population in a year.³ Therefore, efficient harnessing of solar energy in an economic way will undoubtedly help to ease the energy problems that we are facing.

Best Research-Cell Efficiencies

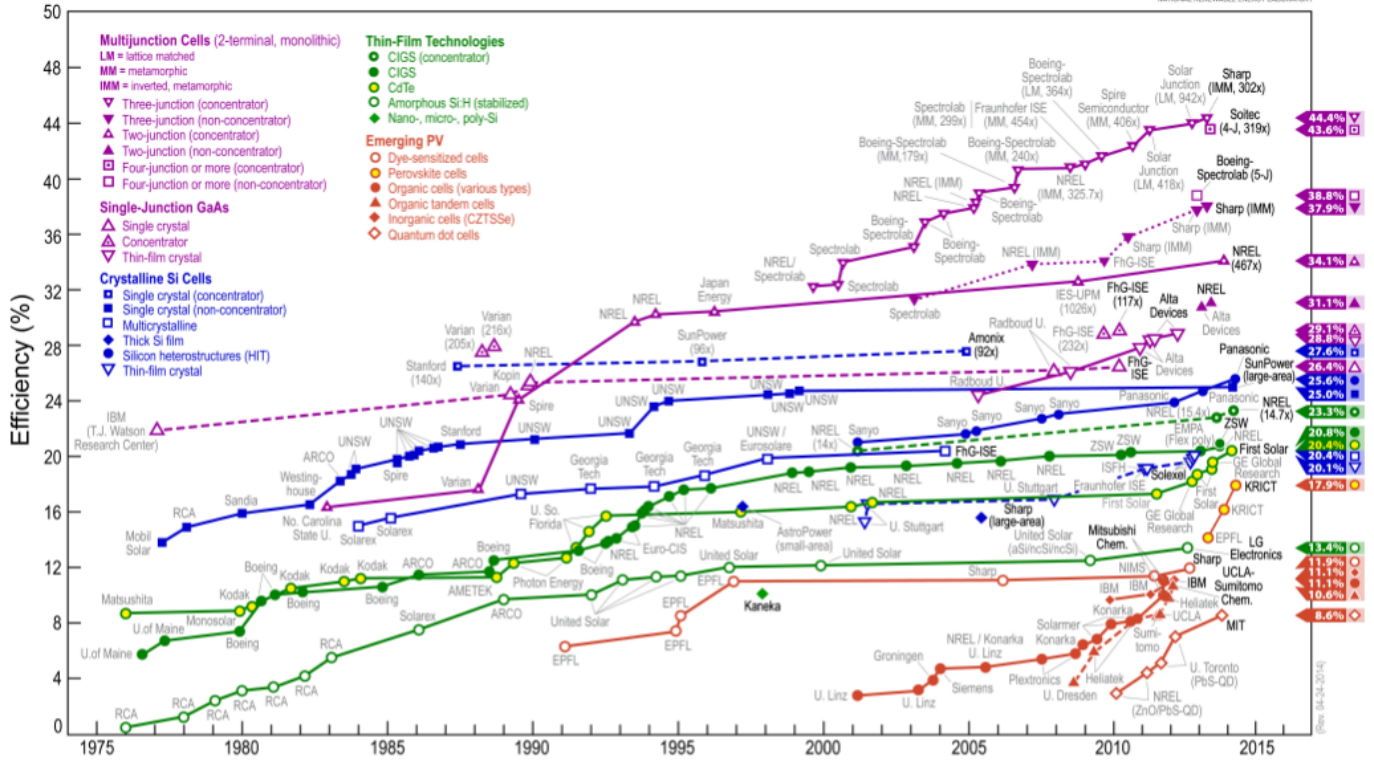


Fig. 1.1 Highest recorded solar cell efficiencies and the institutions accredited for research into these devices over the last 38 years. Dye-sensitized solar cell and perovskite solar cell are two of the emerging photovoltaic technologies shown in orange.⁴

The current market of photovoltaics is dominated by crystalline silicon solar cells, which has a market share of 80-90 %.⁵ However, its commercialisation is hindered by the high production cost. Without government subsidies, it is hard for crystalline silicon solar cells to compete with conventional grid electricity. A promising alternative is dye-sensitized solar cell (DSSC) pioneered by B. O'Regan and M. Grätzel.⁶ It has the advantages of compatibility with low-cost roll-to-roll processing and possible application on lightweight flexible substrates. The trend of highest efficiency achieved by DSSC comparing with other photovoltaic technologies over time is shown in Fig. 1.1. Although it seems the increase in DSSC efficiency has slowed down over the last 17 years, perovskite solar cell which employs a similar structure to DSSC has recently shown very encouraging efficiencies. Since perovskite solar cell shares the same advantages as DSSC, it has caught much attention in the field of photovoltaics. While DSSC and perovskite solar cell have the potential to compete with the conventional method of generating energy by combusting fossil fuels, much research is still needed to improve their efficiency and stability before putting into market.

1.2 Composition of Dye-Sensitised Solar Cells (DSSCs)

A typical liquid-state DSSC is composed of a porous nano-crystalline titanium dioxide film, commonly 5-20 μm in thickness and with 50-60 % porosity, on a transparent conducting oxide (TCO). The TCO is usually either fluorine doped tin oxide (FTO) coated glass substrate or indium tin oxide (ITO) coated on polyethylene terephthalate (PET) for flexible device. The surface of TiO_2 particles is adsorbed with a monolayer of sensitising dye. An electrolyte with a redox couple (usually triiodide-iodide) fills up the voids between the TiO_2 particles and separates the TiO_2 film from the counter electrode. The counter electrode is platinised to catalyse the reduction of triiodide to iodide.

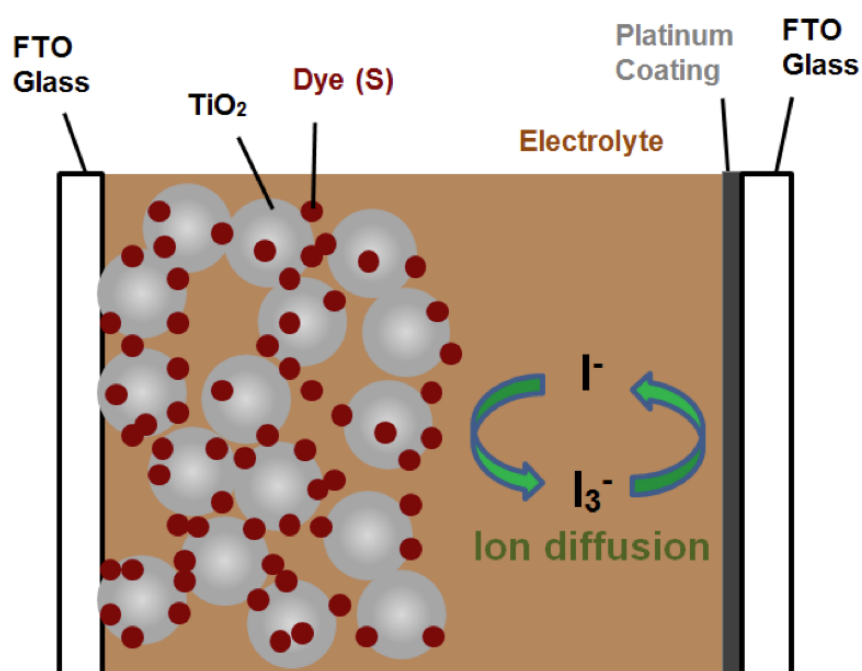


Fig. 1.2 Schematic diagram showing the composition of a typical liquid junction DSSC.

1.3 Operating Principles of Dye-Sensitised Solar Cells

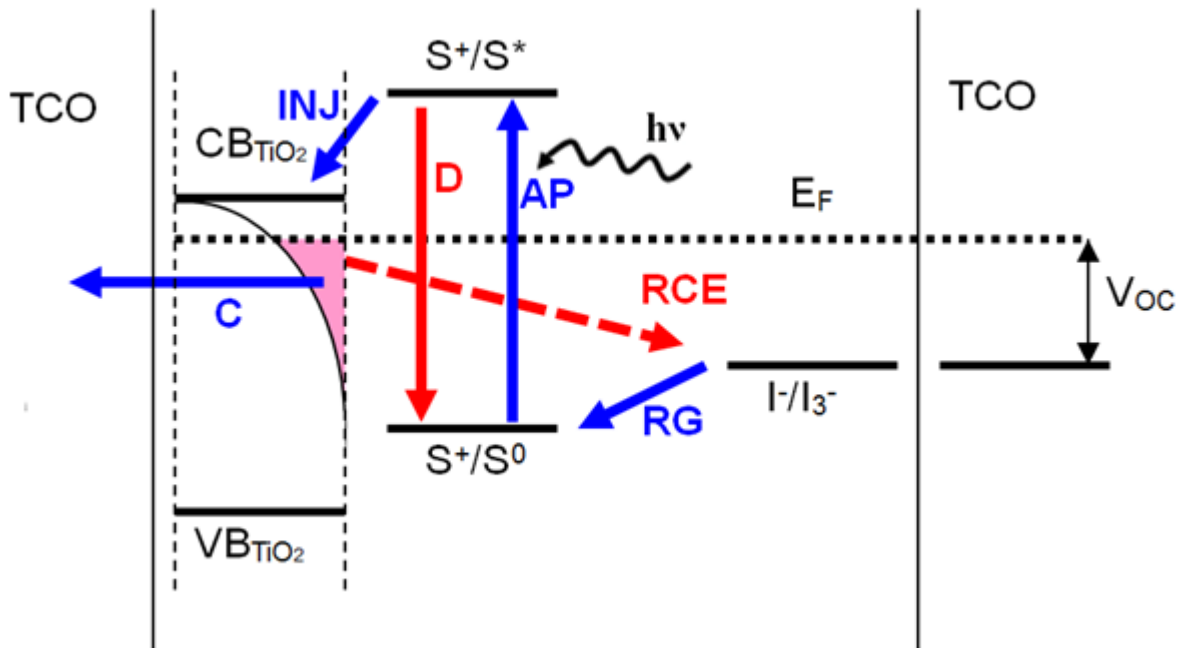


Fig. 1.3 Energy diagram showing the energy levels of different components and the possible routes an electron can take in a DSSC during its operation. The routes in blue are the favorable routes which help transfer of electrons to the external circuit for doing work. The routes in red are loss routes which lower the conversion efficiency of a DSSC.

An ideal cycle for the conversion of sunlight to electricity with no quantum efficiency loss is shown by the blue arrows on Fig. 1.3. When a DSSC is illuminated, not all the photons reaching the cell are absorbed by the dye. Only those photons with suitable energy which matches the spectral response of the sensitising dye are absorbed by a dye with sufficiently high extinction coefficient. Thus, the light harvested primarily depends on the absorption spectrum and the dye loading on TiO₂.⁷ Upon absorption of a photon, an electron in the dye is promoted to an excited state (AP). The photo-excited electron can then be injected to the conduction band of the TiO₂ (INJ). The efficiency of this process is dependent on the electronic coupling of the dye on TiO₂ and the energy of the lowest unoccupied molecular orbital (LUMO) of the dye relative to the band of electron-accepting orbital in TiO₂.⁷ It has been found that the dynamics of electron injection are affected by its surrounding environment and thus, the composition of electrolyte⁸ and injection can occur over a wide timescale from femtoseconds to nanoseconds.⁹

By a trap controlled diffusion process through the TiO₂, the injected electrons are transported to and collected by the FTO (C).¹⁰ The electrons flow through the external circuit and do work in the load before flowing to the counter electrode. This process leaves behind an oxidised dye (S⁺) which is reduced (or regenerated) back to its ground state (S⁰) by iodide in

the electrolyte (**RG**), leaving behind triiodide. The kinetics of the regeneration of ruthenium-based dyes and organic dyes by iodide has previously been studied in our research group.¹¹ The triiodide diffuses across the electrolyte and is reduced back to iodide by an electron at the counter electrode interface to complete the circuit. The potential difference between the Fermi level (E_F) of TiO_2 and the redox potential of the electrolyte corresponds to the open circuit voltage (V_{oc}) generated.

However, in reality, during the operation of DSSCs, there are also some processes which lead to losses in overall efficiency (shown as red arrows in Fig. 1.3). An excited dye (S^*) may decay (**D**) back to its ground state (S^0) before injecting an electron to the conduction band of TiO_2 (**INJ**). This process depends on photoluminescence lifetime of the dye. For N719, a benchmark dye employed in DSSCs, the average luminescence lifetime was found to be ~ 20 nanoseconds.¹² Also, the diffusion of electrons in TiO_2 to the collection electrode is in competition with recombination with oxidising species in the electrolyte (**RCE**). Our research group has demonstrated that when a triiodide/iodide-based electrolyte is used, the main recombination pathway is the reduction of uncomplexed iodine¹³ and recombination is increased by iodine binding molecules bound to the TiO_2 surface.¹⁴

The performance of DSSCs and other solar cells is rated by their power conversion efficiency (η_{eff} or PCE), which is typically found by measuring the current density of the device as a function of external applied voltage. Fig. 1.4 shows a typical current density-voltage (JV) curve and the position of four JV parameters of a device under illumination.

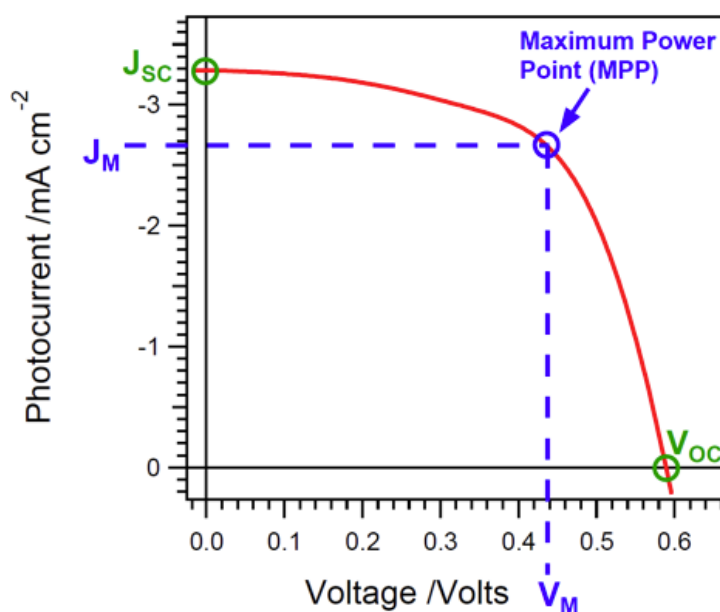


Fig. 1.4 A typical JV curve and the positions of the maximum power point, V_{oc} , J_{sc} , V_M , J_M .

J_{SC} is the current density measured under short circuit when no external voltage is applied. Current is extracted under the internal electric field of the device. V_{oc} is the voltage at open circuit when no current flows through the electrical circuit. η_{eff} can be calculated by the following equation:

$$\eta_{eff} = \frac{P_{out}}{P_{in}} = FF \times V_{OC} \times J_{SC} \quad (1),$$

P_{out} is the maximum power output (at MPP in Fig. 1.4) under illumination. P_{in} is the power of light incident onto the device for a given area. The standard P_{in} used when reporting efficiency of solar cells is 100 mW cm^{-2} . FF refers to the fill factor and is the ratio of maximum power output and the product of J_{sc} and V_{oc} .

$$FF = \frac{V_M \times J_M}{V_{OC} \times J_{SC}} \quad (2),$$

J_M and V_M are the current density and voltage at maximum power point. The product of J_M and V_M gives the maximum power output of the device as shown in Fig. 1.4.

1.4 Liquid-State Dye-Sensitised Solar Cells

In the early development of DSSCs, all studies were based on liquid electrolytes. Before the 1990s, the highest conversion efficiencies achieved were below 2 %. One of the reasons for the low efficiencies is the poor light harvesting. The use of a mesoporous film of TiO_2 was introduced by O'Regan *et al.* in 1990.¹⁵ This film of 15-nm-sized particles was estimated to produce a 2000-fold increase in surface area for dye adsorption as reported in the famous Nature paper written by B. O'Regan and M. Grätzel.⁶ The efficiency of DSSC made a giant leap up to 7-8 %. Further modifications of sensitising dyes and electrolyte systems increased the efficiency of triiodide/iodide-based DSSC to 11-12 % by 2010.¹⁶ Other than high performance, a high stability is also required before commercialisation of DSSCs. It has been reported that when using a butyronitrile-based¹⁷ and an MPN-based electrolyte¹⁸ with triiodide/iodide redox couple, the DSSCs successfully retained 95 % of their initial conversion efficiency of 10 % after 1000 hours of 0.6-sun illumination at 60 °C. In another report, a MPN-based DSSC with triiodide/iodide redox couple has also been shown to maintain its 4 % efficiency after continuous exposure to ≥ 0.8 -sun illumination at 55-60 °C for 25600 hours.¹⁹ However, recently, a thermally-activated depletion of triiodide in a MPN electrolyte was observed after ageing in the dark at 85 °C for 500 hours on the TiO_2 surface.²⁰ This results in

the nucleation and the growth of a solid electrolyte interphase (SEI) layer covering the TiO₂. The authors argued that the SEI layer is responsible for the downshift in intra-band trap states in TiO₂ and the change in electron lifetime and transport time typically observed in aged cells relative to newly fabricated cells.

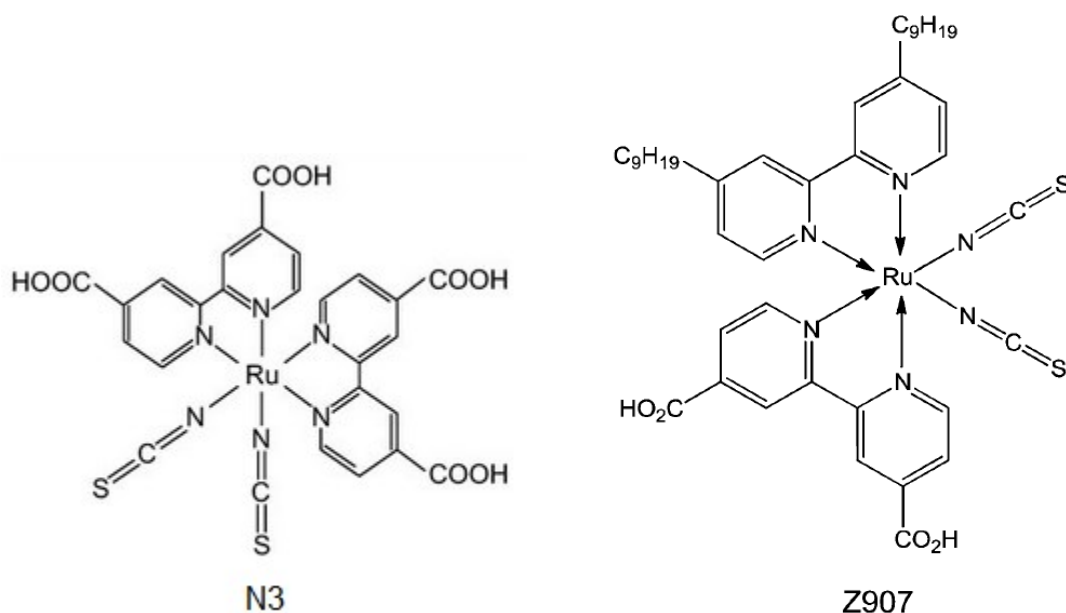


Fig. 1.5 Chemical structures of the N3 and Z907 dyes.

Other than triiodide/iodide redox couple, cobalt-based systems have also been utilised in DSSCs and achieved good results. In an early study, a number of Co(II) and Co(III) complexes with substituted polypyridine ligands were tested. When used in conjunction with the N3 dye, an overall efficiency of 1.6 % at 1 sun was obtained.²¹ By employing the Co^(III/II) bis[2,6-bis(1'-butylbenzimidazol-2'-yl)pyridine] redox couple, conversion efficiencies of 2.2 and 5.2 % were achieved under 1 and ~0.1 sun respectively.²² A non-linear dependence of photocurrent on light level was observed, which was attributed to a limitation in mass transport of the cobalt complexes due to their bulky sizes. After some modifications of the cobalt complexes and the dyes, an overall efficiency of 12.3 % under 1-sun illumination was yielded by a DSSC incorporating a Co^(III/II) tris(bipyridyl) tetracyanoborate electrolyte and a TiO₂ electrode co-sensitised with the YD2-*o*-C8 and Y123 dyes (see Fig. 1.6) by Yella *et al.*²³ While the highest certified power conversion efficiency of liquid junction DSSCs is 11.9 % achieved by Sharp,²⁴ the 12.3 % produced by this DSSC with Co(III/II) electrolyte is by far the highest reported (but not certified) efficiency. Although, no ageing tests were reported in this cell, promising stability data of cobalt-based electrolyte have been reported in our research group.²⁵ A DSSC with the Z907 dye (see Fig. 1.5) and the Co^(III/II) tris(bipyridine) redox couple in a MPN

electrolyte retained 91 % of its initial efficiency of 3.7 % after 2000 hours of 1-sun equivalent illumination. It was also found that, according to charge extraction, J_{sc} vs. light intensity and impedance data, it is likely that there was a decrease in the Co(III) concentration, or a restriction in Co(III) diffusion during light soaking.

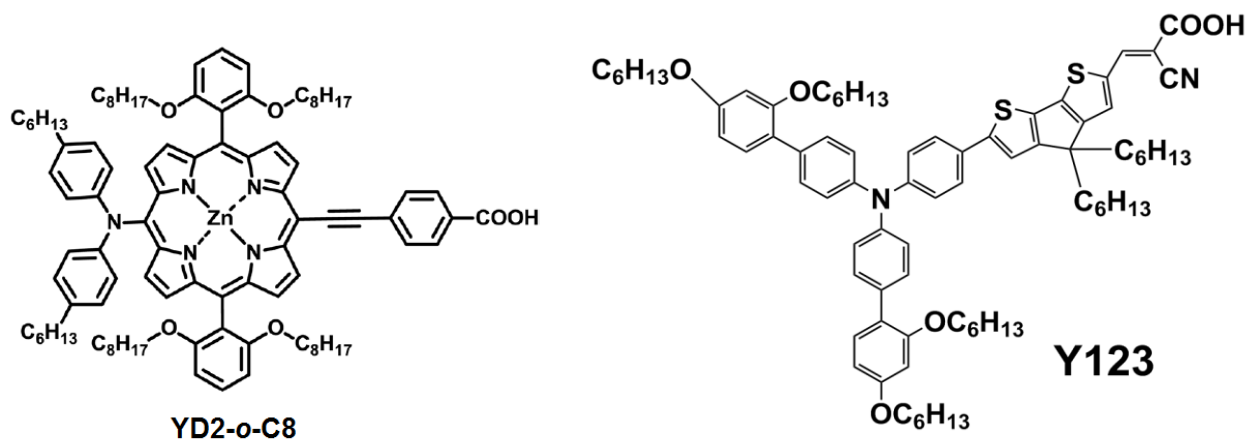


Fig. 1.6 Chemical structures of the YD2-*o*-C8 and Y123 dyes.

1.5 Water in Liquid-State Dye-Sensitised Solar Cells

One advantage of DSSC technology is the possible roll-to-roll production of flexible, lightweight devices using low-cost plastic foils such as poly(ethylene terephthalate), polystyrene, polypropylene and polycarbonate substrates. However, the permeation of water into this flexible plastic device is relatively fast. Barrier layers can be used to reduce permeation but it increases the cost. An economic permeation barrier can be achieved by coating the plastic films with thin layers of silicon oxide and aluminium oxide.²⁶ But such a barrier still allows water vapor to transmit at a rate of at least $5 \times 10^{-3} \text{ g m}^{-2} \text{ day}^{-1}$.²⁶ Assuming this rate to stay constant over time, after one year of outdoor use, the water content of the electrolyte may reach over 7 %. Therefore, it is imperative to understand the effect of water on the performance of dye-sensitised solar cells which are typically based on organic solvent. An alternative way to circumvent the water permeation issues completely is to fabricate DSSCs with water-based electrolyte. Such an electrolyte should also have the advantages of being lower cost and more environmentally friendly. Nevertheless, despite of these driving forces, there have been very few publications studying water-electrolyte DSSCs over the last 20 years.

In fact, water played a significant role in the early development of DSSCs. Before 1990s, water was used as the solvent in dye solution for sensitisation of semiconductor electrodes and also in electrolytes. A maximum overall efficiency of 2 % was achieved under 0.07-sun illumination when TiO₂ electrode was sensitised in an aqueous solution of the diaqua-*cis*-

bis(2,2'-bipyridyl-4,4'-dicarboxylato)ruthenium(II) dye and a water electrolyte with 0.1 M potassium iodide and 1 mM iodine was employed.²⁷ A maximum short circuit current density (J_{sc}) of $\sim 0.8 \text{ mA cm}^{-2}$ was reported under 0.5-sun illumination when TiO_2 electrode was sensitised by the tris(2,2'-bipyridyl-4,4'-dicarboxylate)ruthenium(II) dye in water and an aqueous electrolyte with 0.1 M lithium bromide, 1 mM bromine and 1 mM perchloric acid was used.²⁷ In this case, the overall efficiency of the cell was 1.2 %. Nevertheless, all the above measurements were made at relatively low light levels. The role of water in DSSCs rapidly declined after higher efficiency was reported by Nazeeruddin *et al.* using ethanol as the solvent in electrolytes.²⁸ Within one year, the record efficiency had already reached over 7 % under 0.75-sun illumination in a DSSC with a mesoporous TiO_2 film and an organic solvent-based electrolyte consisting of 0.5 M tetrapropylammonium iodide, 0.02 M potassium iodide and 0.04 M iodine in a solvent mixture of ethylene carbonate (80 % by volume) with acetonitrile (ACN).⁶ Since the publication of this paper in 1991, the electrolytes, sensitising dyes and the TiO_2 synthesis had all undergone significant evolution along with the development of DSSCs, leading to the replacement of water by organic solvents in electrolytes.

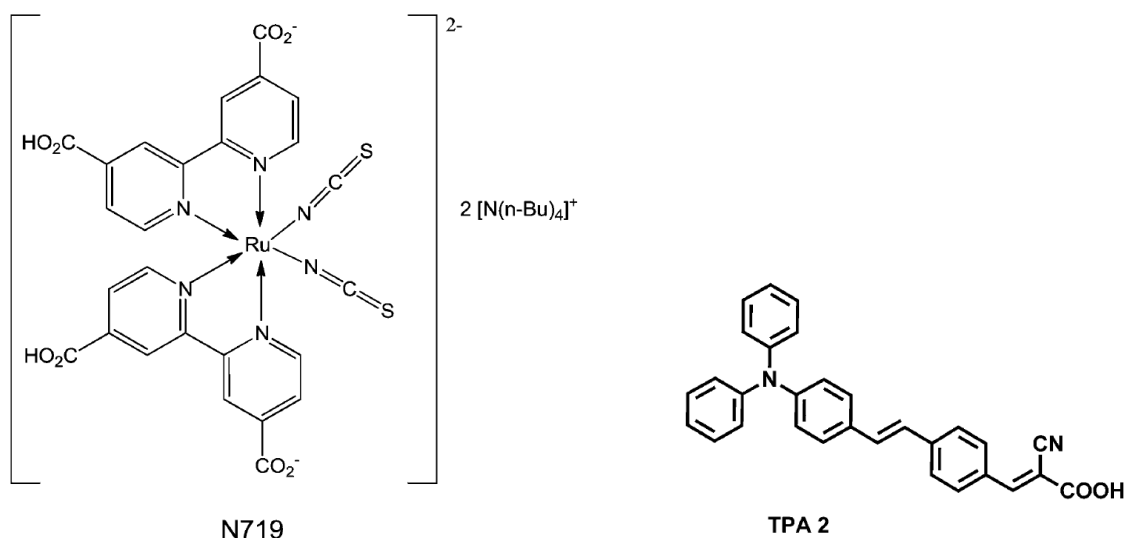


Fig. 1.7 Chemical structures of the N719 and TPA2 dyes.

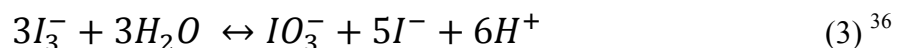
The presence of water has then been reported to degrade DSSCs with organic solvent-based electrolyte. In some studies, water was added to DSSCs in order to examine its effect on cell performance. A ~ 40 % decrease in J_{sc} was reported under 0.8-sun illumination when 2.2 M water was added to a lithium iodide-based 3-methoxypropionitrile (MPN) electrolyte.²⁹ The authors suggested that water hydrolyses or weakens the bonding between the N3 dye and TiO_2 , leading to desorption of N3. In another paper, a similar MPN electrolyte based on an ionic liquid, 1-hexyl-2,3-dimethylimidazolium iodide was used. The J_{sc} decreased by ~ 13 % upon

the addition of 2.2 M water and 0.02 M Triton X-100 (surfactant).³⁰ The authors also speculated that it is caused by the desorption of dye which is N719 in this case (see Fig. 1.7). In fact, desorption of another ruthenium-based dye, Z907 has been shown by two-dimension transmission mapping of DSSCs near the filling hole (where electrolyte was injected during cell assembly) when a water electrolyte based on another ionic liquid, 2-propyl-1-methylimidazolium iodide (PMII), was employed.³¹ This results in a >2 fold reduction in J_{sc} in the area near the filling hole, when compared to most of the other area of the cell. Apart from ruthenium-based dyes, organic dyes have also been reported to desorb from TiO_2 surface in the presence of water.³² When 10 vol% water as added to a LiI-based acetonitrile electrolyte, a complete loss in conversion efficiency in DSSCs with the TPA2 dye (see Fig. 1.7) was observed after continuous exposure to 1-sun illumination for 300 hours. According to mass spectrometry and ^1H NMR data, the cyanoacrylic acid unit of the dye was converted to the aldehyde group in the presence of water and upon exposure to UV light. The above speculation and observation of dye desorption are supported by data collected from density-functional molecular dynamics simulations of acetonitrile/ TiO_2 interfaces involving a water molecule by Sumita *et al.* It was found that water adsorbs on TiO_2 captures holes generated by irradiation to form a cation radical, which may then attack dye molecule toward desorption.³³

Apart from dye desorption, a change in dye orientation toward TiO_2 surface due to the presence of water has been suggested to cause the decrease in J_{sc} observed.³⁴ In this study, prior to assembly with a water-free acetonitrile electrolyte, N3- and N719-sensitised TiO_2 electrodes were immersed in a solution containing 30 vol% water and 70 vol% ethanol for 20 minutes. This resulted in a 20 % reduction in J_{sc} , when compared to electrodes without water treatment. According to data collected from photoelectron spectroscopic (PES) measurements, the presence of water causes a change in orientation of the dye and forces the NCS ligand toward the TiO_2 surface. In the case of N719, PES results also show that water induces desorption of tetrabutylammonium counterion (TBA^+). Nonetheless, DSSC with Z907 showed no decrease in J_{sc} upon treatment in water-containing solution prior to cell assembly. The authors attributed this to the presence of hydrophobic chains on Z907 which effectively inhibits the surface reorganisation by water.

In some long-term stability studies of DSSCs based completely on organic solvent, water was believed to be one of the culprits of their degrading performance over time. For example, the photocurrent of N3 DSSCs with LiI-based ACN electrolyte was found to become diffusion-limited after exposing to 1-sun illumination at 45 °C for over 40 days.³⁵ The authors proposed

that water may cause the formation of iodate in the expense of triiodide, leading to bleaching of electrolyte (see equation (3)).



Although no sign of iodate was observed in Fourier transform infrared analysis, the authors argued that the concentration of water was found to be higher in cells which showed diffusion-limited photocurrent. Bleaching of electrolyte has also been studied in another paper where Z907 DSSCs with a PMII-based MPN electrolyte also showed diffusion-limited photocurrent after experiencing an accelerated ageing test (1 sun visible light, 1.5 suns UV light, at 110 °C for 12 hours).³⁷ A reduction in triiodide concentration was also observed in these cells by a camera imaging technique where the cells were photographed under controlled illumination conditions.³⁸ However, the authors did not relate these results to the formation of iodate or the presence of water. Recently, Flasque *et al.* published a paper which focuses on electrolyte bleaching and they do not agree on the formation of iodate in aged cells.²⁰ Therefore, up to now, it is still not clear whether water causes bleaching of electrolyte in DSSCs. In any case, these studies have created a general impression that water is bad for DSSCs.

Despite the general view that water degrades DSSCs, there are a few studies where water was added to the electrolyte on purpose to improve cell performance. Zhu *et al.* claimed that recombination rate decreased by 4-fold upon the addition of 10 vol% water to both of the two tetrabutylammonium iodide-based electrolytes (one in MPN, the other in ACN/valeronitrile (85 : 15 by volume)) in Z907 DCCSs, according to electrochemical impedance spectroscopy (EIS) data.³⁹ The authors also reported that the addition of water does not reduce the cell stability during 1000-hour continuous (AM 1.5) illumination. In another study, a sodium bis(2-ethylhexyl) sulfosuccinate (aerosol OT or AOT)/water system was proposed to reduce recombination in DSSCs with triiodide/iodide-based electrolytes.⁴⁰ A ~50 % reduction in recombination rate measured by EIS was observed at 1 sun upon the addition of 1 mM sodium bis (2-ethylhexyl) sulfosuccinate (AOT) and 10 mM water in an ACN/valeronitrile electrolyte based on an ionic liquid, 1-butyl-3-methylimidazolium iodide.

Other than being used as an additive, water has also been employed as a major solvent in electrolytes in some studies. Su *et al.* fabricated DSSCs with a mercurochrome dye and electrolyte with a Fe^{(III)/(II)} redox couple in 35 vol% ethanol and 65 vol% water, which produced a J_{sc} of ~6 mA cm⁻² and an overall efficiency of 0.95 %.⁴¹ In second attempt, they used a range of natural dyes with an electrolyte based on a Ce^{(IV)/(III)} redox couple in 35 vol%

vol% Triton X-100 was fabricated and achieved 4.7 mA cm^{-2} , 0.74 V and 2.4% . Also, an electrolyte with 20% water fraction showed very good stability as tested by S. Pathirana, a MSci student in our research group. The efficiency of the cell with this electrolyte stayed the same after continuous exposure to 1-sun illumination (with a 430 nm longpass filter to eliminate the effects of UV light) at $35 \text{ }^\circ\text{C}$ at open circuit for 750 hours. These promising results have drawn attention to the use of water in the electrolytes of DSSCs again after 20 years.

As a continuation of my work in my MSci project, the wetting issue and J_{DL} were examined in the first year of my Ph.D. project. By managing the wetting behavior and also the collection efficiency, an overall efficiency of 4% was achieved in a DSSC with a water electrolyte. The results will be presented and discussed in Chapter 3 of this thesis. In the next part, the meaning of diffusion-limited current density (J_{DL}) in liquid junction DSSCs will first be explained.

1.6 Diffusion-Limited Current Density (J_{DL}) in Liquid-State DSSCs

Diffusion-limited current density (J_{DL}) is the maximum current density which can flow through a cell. It is limited by the diffusion coefficient of the limiting species, the concentration of that species, the morphology of the pore space and the wetting of the TiO_2 pores by the electrolyte. In the case of dye-sensitised solar cells with triiodide/iodide redox couple, since triiodide is usually present at >5 times lower concentration than iodide, triiodide is normally the limiting species. Possible causes for a low diffusion-limited current include low triiodide concentration, viscous electrolyte and poor wetting of TiO_2 pores by the electrolyte. In water-based dye-sensitised solar cells, the problem of poor wetting is more apparent. Since most of the dyes commonly employed in DSSCs are relatively hydrophobic, a poor wetting of TiO_2 surface which is covered by a monolayer of dye molecules is expected when using a water-based electrolyte.

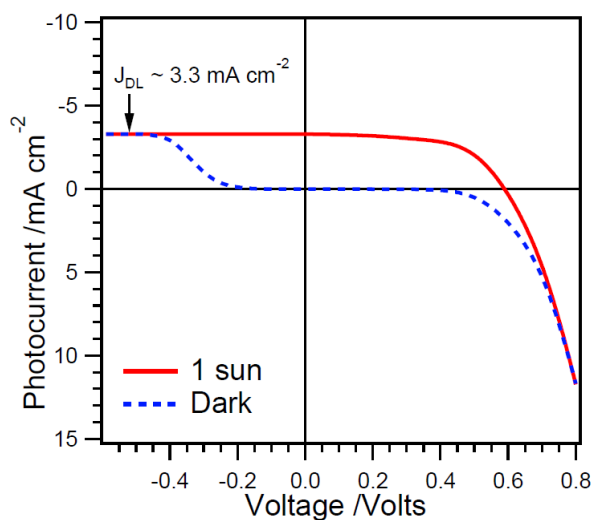


Fig. 1.9 One-sun and dark JV of a typical DSSC which J_{sc} is limited by J_{DL} . TiO₂ film: DyeSol, 7 μm ; dye: 1:4 D149:chenodeoxycholic acid (cheno); electrolyte: water with 0.2 M NaI, 20 mM iodine, 0.1 M GuSCN and \sim saturated cheno.

J_{DL} 's of DSSCs can be determined from saturation in photocurrent in the far reverse bias of the cell. Fig. 1.9 presents a dark and a 1-sun JV of a typical cell which J_{sc} is limited by J_{DL} . In the dark, at reverse bias (to the left), a positive potential is applied to the TiO₂. This leads to a depletion of electrons in TiO₂, making it insulating. Therefore, the current measured is caused by the diffusion of iodide through the pores of TiO₂ layer to the surface of bare SnO₂ and the diffusion of triiodide out of the porous TiO₂ layer to the counter electrode. This can be shown by depositing a blocking layer (a thin compact TiO₂ layer) to the SnO₂ surface, which reduces current at reverse to near zero. The saturated current is caused either by the limited diffusion of iodide through the TiO₂ pores to SnO₂, which would result in a depletion of iodide near the SnO₂ surface, or by the limited diffusion of triiodide out of the porous TiO₂ layer to the counter electrode, which would lead to a depletion of triiodide near the counter electrode. In either case, when complete depletion occurs near the electrode, the current is limited by the diffusion of iodide or triiodide to the electrode but not by the electrode potential. As a result, the measured current plateaus at far reverse bias as observed in Fig. 1.9, which corresponds the J_{DL} of the cell. If the wetting of TiO₂ pores is poor, there will certainly be higher constrictivity and tortuosity, which inhibits ion diffusion, resulting in a lower J_{DL} .

When the cell is illuminated at short circuit, the same explanation can be applied. If injection and collection are kept constant, the current is limited by either the diffusion of iodide through the pores to reach the dye adsorbed deep inside the TiO₂ film where the iodide regenerates the oxidised dye, or the diffusion of triiodide created deep inside the TiO₂ film out of porous layer to the counter electrode. Therefore, when the J_{DL} is so small that it falls below

the photocurrent that could be generated by the cell with the given injection and collection at short circuit, J_{sc} becomes limited by J_{DL} as shown in the 1-sun JV in Fig. 1.9.

On the other hand, TiO_2 is conductive at far forward bias where electrons can flow through the TiO_2 film. Triiodide is reduced and iodide is created only at the outer surface of the TiO_2 film. Iodide and triiodide only need to diffuse through the electrolyte gap but not through the porous structure. Without the effect of constrictivity and tortuosity of the porous layer, the current plateaus at a much higher level, which is not usually observed as in Fig. 1.9 where the forward bias only goes as far as 0.8 V.

1.7 Solid-State Dye-Sensitised Solar Cells

Although a record efficiency of 12 % has been reached by liquid junction DSSCs,²³⁻²⁴ their long-term stability is still questionable due to dye desorption, solvent evaporation and degradation and seal imperfections. This creates interest in the development of solid-state DSSCs where solid hole transporting material (HTM) is used instead of liquid electrolyte. These practical advantages over liquid-state DSSC, together with the high conversion efficiency of 7.2 % claimed by Burschka *et al.*,⁴⁶ have made solid-state DSSC a promising technology. Solid-state DSSC has a very similar basic structure to its liquid counterpart. The only difference is that the pores in the dye-sensitised TiO_2 layer, together with the gap between the working and counter electrodes, are, ideally, completely filled by solid HTM in solid-state DSSCs. Hole (or positive charge) created upon regeneration of dye by HTM is transported to the counter electrode by a hopping mechanism towards the counter electrode instead of by ion diffusion as in liquid cell.

In the early research of solid-state dye-sensitised solar cells, inorganic p-type semiconductors were often employed as the hole transporting material (HTM). Reasonably good conversion efficiencies were achieved when copper iodide was used.⁴⁷ By sensitising a nanoporous film of TiO_2 with the N3 dye and depositing copper iodide by drop casting, a J_{sc} of 0.8 mA cm^{-2} and an overall efficiency of 6 % were claimed under 0.05-sun illumination.^{47c} However, the cell was relatively unstable. The J_{sc} decreased by ~20 % after only 5 hours of 1-sun illumination. One of the suggested reasons responsible for the degradation is the loosening of the contact between the dye-sensitised TiO_2 and copper iodide as CuI crystals are formed. Kumara *et al.* found that an ionic liquid, 1-methy-3-ethylimidazolium thiocyanate (MEISCN), can inhibit the growth of CuI crystals. With the introduction of MEISCN in the drop casting solution, a similar N3 cell with copper iodide gave 6.8 mA cm^{-2} , 0.6 V and an overall efficiency of 3.8 % under 0.6-sun illumination.^{47d} The authors also suggested that MEISCN

improves the electrical contact between the dye-sensitised TiO₂ and copper iodide. Better stability results than the previous study were also reported. After 2 weeks of continuous 0.6-sun illumination, the J_{sc} decreased by 15 %. An alternative to CuI is copper thiocyanate (CuSCN), which has been reported to be more stable than CuI.⁴⁸ One of the difficulties of employing CuSCN is its low solubility in most solvents. By electrodeposition, CuSCN was incorporated into the porous dye-sensitised zinc oxide film.⁴⁹ The dye used here was Ru^{II}LL'NCS where L is 4'-(4-phenylphosphonate)-2,2':6',2''-terpyridine and L' is 4,4'-dimethylbipyridine. Under 1-sun illumination, the cell gave 4.5 mA cm⁻² and 0.55 V. It also showed good stability for several weeks when illuminated with sunlight filtered to remove the effect of UV light. By the application of a modified drop casting technique and n-propylsulphide ((C₂H₇)₂S) as the solvent, an improved pore filling by CuSCN was achieved in a TiO₂/N3 cell which gave 7.8 mA cm⁻², 0.6 V and an overall efficiency of 2 %.⁵⁰ In another study, with an aim to enhance the p-type conductivity of CuSCN, triethylamine was added to the CuSCN solution to form Cu₅[(C₂H₅)₃N]₃(SCN)₁₁.⁵¹ The introduction of triethylamine was reported to increase the conductivity of CuSCN by >10 fold and the resulting TiO₂/N719 cell with this copper complex produced 10.5 mA cm⁻², 0.56 V and 3.4 % efficiency. However, no stability data was reported in this paper, making the stability of this cell questionable.

As opposed to p-type inorganic materials, the properties of organic materials, such as solubility, band gap and hole mobility, are more easily tuneable by synthesis. Therefore, they are also often used as the HTM in solid-state DSSCs. Organic small molecules like pentacene,⁵² triarylamine-type oligomers⁵³ and polymers such as polyaniline,⁵⁴ polypyrrole,⁵⁵ poly[2-methoxy-5-(2'-ethylhexyloxy)-p-phenylene vinylene] (MEHPPV)⁵⁶ and poly(3,4-ethylenedioxythiophene) (PEDOT)⁵⁷ have been incorporated in solid-state DSSCs as HTMs. But none of them shows a conversion efficiency higher than 3 %. The best result among them was achieved by a TiO₂/Z907/PEDOT cell where PEDOT was deposited by photoelectropolymerisation.^{57b} This cell gave 5.3 mA cm⁻², 0.75 V and an overall efficiency of 2.85 %. Another promising polymer, poly(3-hexylthiophene) (P3HT) has also been studied for years⁵⁸ due to its high conductivity and good stability at room temperature. Using P3HT as HTM and Sb₂S₃ as sensitiser, an inorganic-organic heterojunction solar cell with nanostructured TiO₂ claimed 13 mA cm⁻², 0.65 V and 5.13 % efficiency.⁵⁹ The same JV characteristics were shown from this cell after one month of storage in ambient atmosphere but the cell stability under light was not reported.

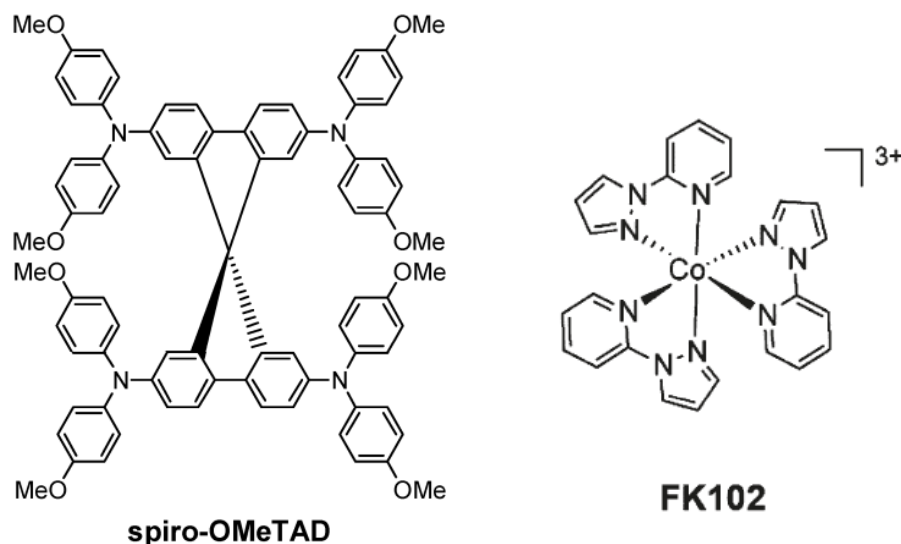


Fig. 1.10 Chemical structures of spiro-OMeTAD and FK102.

None of the HTMs mentioned above works better in solid-state DSSCs than 2,2',7,7'-tetrakis-(N,N-di-p-methoxyphenylamine)9,9'-spirobifluorene (spiro-OMeTAD). It is mainly due to its relatively high solubility and amorphous nature. A J_{sc} of 3.18 mA cm^{-2} under 1 sun was first reported by Bach *et al.* in a N719 cell with spiro-OMeTAD.⁶⁰ In this cell, the HTM layer was deposited by spin-coating a solution of 0.17 M spiro-OMeTAD in chlorobenzene containing $\text{N}(\text{PhBr})_3\text{SbCl}_6$ and $\text{Li}(\text{CF}_3\text{SO}_2)_2\text{N}$. With the addition of a base, 4-*tert*-butylpyridine (TBP), to a similar HTM solution as above for spin coating, the performance of the N719 DSSC based on spiro-OMeTAD was considerably improved by Kruger *et al.*⁶¹ The resulting cell showed a J_{sc} of 5.1 mA cm^{-2} and a V_{oc} of 0.9 V, yielding an overall efficiency of 2.56 % at 1 sun. Since then, spiro-OMeTAD has attracted much interest and become a benchmark HTM in solid-state DSSCs. Up to now, the record efficiency of solid-state DSSC was claimed to be 7.2 %. In this device, an organic dye, Y123 (see Fig. 1.5) was used and a cobalt complex, FK102, was added (1.6 wt%) as a p-dopant to the spin-coating solution of 0.15 M spiro-OMeTAD, 0.02 M lithium bis(trifluoromethylsulfonyl)imide (Li-TFSI) and 0.12 M TBP in chlorobenzene.⁴⁶ FK102 is shown to enhance the conductivity of spiro-OMeTAD in the HTM layer.

1.8 Pore Filling in Solid-State Dye-Sensitised Solar Cells

The best efficiency obtained in solid-state DSSCs is still much lower than the 12 % achieved by liquid-state cells.²³⁻²⁴ One of the major losses in efficiency comes from the poor filling of the TiO_2 pores by solid HTMs. The most studied reason comes from the spin-coating technique which we currently employ to deposit HTM. For this reason, the thickness the

porous TiO₂ film is often limited to 2-3 μm (e.g. the cell with record efficiency of 7.2 % has a TiO₂ film with a thickness of 2.5 μm), when compared to a TiO₂ thickness of >7 μm usually used in liquid junction DSSCs. Another reason which may also play a part in the pore filling is the compatibility of the dye with the HTM. It has been reported that substituting a fluorine atom by a methoxy group in an organic dye enhances pore filling and surface coating by HTM, according data collected from scanning electron microscopy (SEM) and transient absorption spectroscopy (TAS) respectively.⁶² This results in increase in *J*_{sc} from 7.6 to 9.3 mA cm⁻² and overall efficiency from 2.7 to 3.6 %.

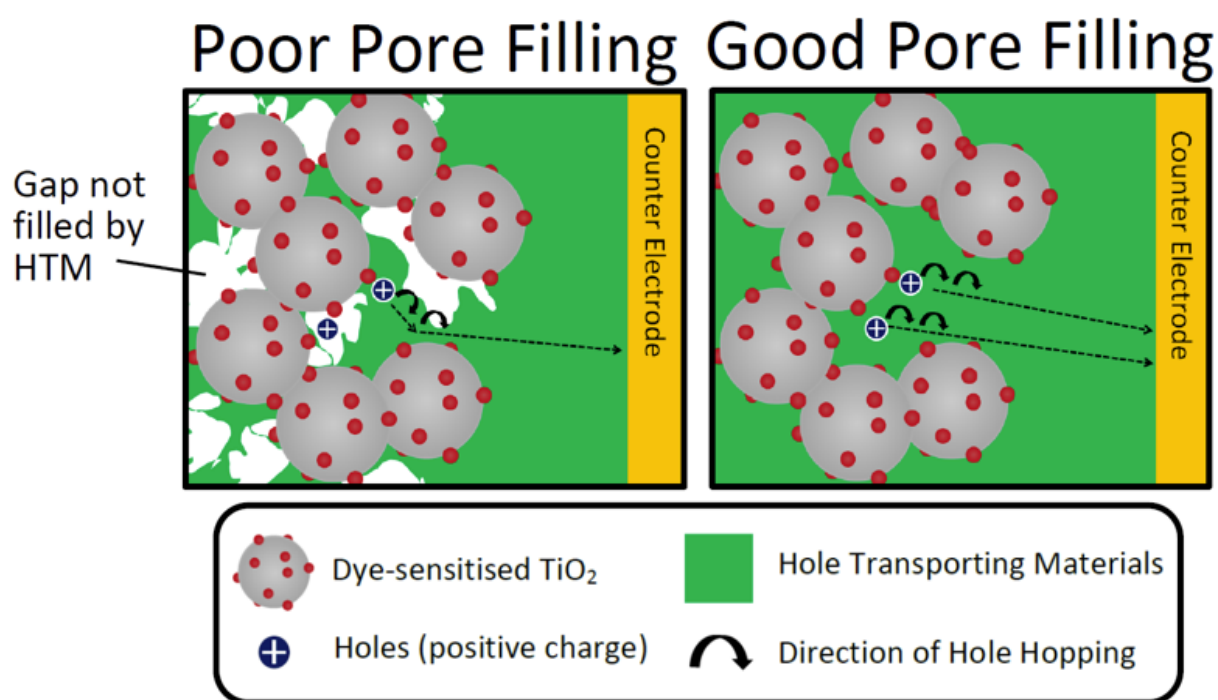


Fig. 1.11 Schematic diagram showing the pore filling issue in the porous TiO₂ layer in solid-state DSSCs.

The first issue with incomplete filling of TiO₂ pores by solid HTM is its effect on dye regeneration. As shown in the left diagram of Fig. 1.11, when the dye molecules which are not in direct contact with HTM are excited upon absorption of a photon and inject an electron to the conduction band of TiO₂, they cannot be regenerated by HTM. No charge collection can occur, resulting in a lower *J*_{sc} and thus efficiency. This is supported by the TAS results reported. When the pore filling fraction (i.e. the volume fraction of the pore filled by HTM) decreases from 65 to 26 %, the regeneration efficiency decreases from 94 to 57 % and the *J*_{sc} also decreases proportionally from ~5 to ~2.5 mA cm⁻².⁶³

Pore filling fraction (PFF) also affects recombination in solid-state DSSCs. The holes created in HTM layer after the regeneration of a dye molecule need to travel a longer and more tortuous path before reaching the counter electrode (left diagram in Fig. 1.11), when compared

to a cell with good pore filling (right diagram in Fig. 1.11). As a result, the chance of recombination between an electron in the conduction band of TiO₂ and a hole in the HTM layer increases. Therefore, J_{sc} and V_{oc} will decrease, lowering the conversion efficiency of the cell. This is supported by the published transient photovoltage data.⁶³ It was shown that the recombination lifetime decreases linearly with pore filling fraction. When PFF decreases from 65 to 26 %, the recombination lifetime is reduced from 10 to 1.5 ms under 1-sun illumination.

In order to obtain a reasonably good pore filling, either a thin film of porous TiO₂ or a film with larger pore size has to be used. Both of these reduce the total surface area of the TiO₂ where the dye molecules can adsorb, resulting in a smaller number of dye molecules in the cell. Fewer photons can then be absorbed and the J_{sc} and efficiency will again decrease. It has been estimated, in a TiO₂/Z907/spiro-OMeTAD cell, if the PFF could increase from 65 to 100 % regardless of the TiO₂ thickness, the TiO₂ thickness that gives the optimum overall efficiency would increase from 2 to 5 μm, leading to a higher light harvesting. This would result in a 25 % relative efficiency improvement when compared to the state-of-the-art solid-state DSSCs with 2 μm thick TiO₂ and a PFF of 65 %.⁶³ However, it is noted that this estimation does not take into account the extra light absorbed by oxidised form of spiro-OMeTAD upon the increase in TiO₂ thickness and the PFF. This may cause a small overestimation because it has been reported that the oxidised spiro-OMeTAD, which is required for appreciable conductivity of the HTM layer, also absorbs light in the visible region⁶⁴ and thus reduces the incident photon to electron conversion efficiency (IPCE).

1.9 Deposition Methods of Hole Transporting Materials

Due to its ease and reliability, spin coating has been the most popular technique for depositing hole transporting materials in solid-state DSSCs. The mechanism of this deposition technique has been described in literature by Snaith *et al.*⁶⁵ The HTM, spiro-OMeTAD, together with other additives, is first dissolved in a volatile solvent, chlorobenzene and then deposited onto the dye-sensitised TiO₂ film to form a reservoir overlayer. When the spin-coating starts, the solution at the surface flows off the substrate. As the spinning proceeds, the solvent (chlorobenzene) evaporates off, increasing the concentration of the solution. By diffusion and possibly convection, spiro-OMeTAD is driven down into the pores. As the solution concentration increases further to maximum, no more spiro-OMeTAD can be infiltrated deeper into the pores. In the end, all the solvent is evaporated, leaving behind only the solid HTM and additives with a thin overlayer of HTM and additives on top of the sensitised TiO₂.

Pore filling fraction is dependent on the concentration of HTM solution, spinning speed and thickness of the porous TiO₂ film.⁶⁵⁻⁶⁶ It was reported that for 2.8 μm thick TiO₂ films, the pore filling fraction increased proportionally up to at 225 mg mL⁻¹ of spiro-OMeTAD in chlorobenzene.^{66b} Any further increase in concentration did not increase pore filling fraction but instead increased the thickness of the overlayer of spiro-OMeTAD. This in turn resulted in an increase in the series resistance of the cell. On the other hand, when 3.0 μm films were used, slowing down the spinning speed from 2000 to 600 revolutions per minute (rpm) again increased pore filling fraction but slowing down further resulted in a thicker overlayer.^{66b} In the same paper, increasing the TiO₂ layer thickness was found to reduce the pore filling fraction. The highest pore filling fraction reported so far is 85 % when a 2 μm film was used, compared to only 60 % when a 7 μm film was used.

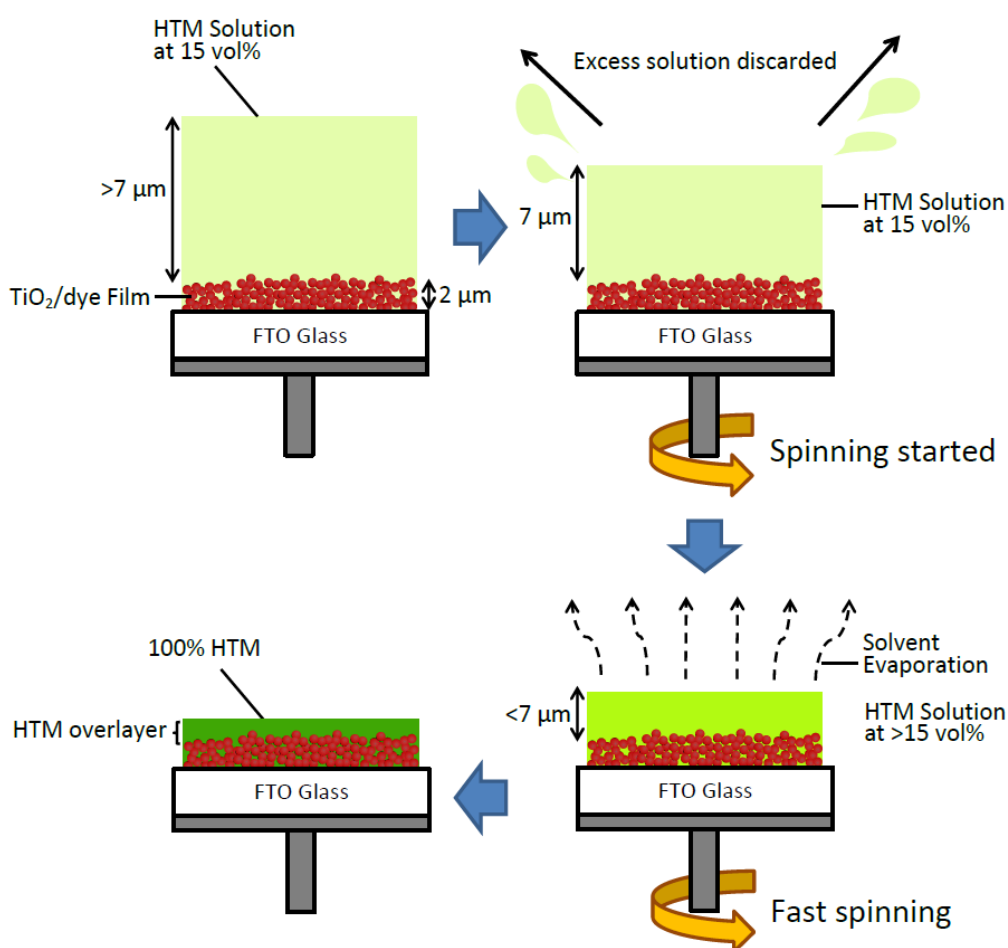


Fig. 1.12 Schematic diagram showing the film forming and material infiltration process during spin-coating.

Drop casting is another common method employed to deposit HTM in solid-state DSSCs. A small amount of concentrated HTM solution is dispensed onto the film and the solvent is allowed to evaporate off completely under ambient conditions. However, this technique is not

as reproducible and effective as spin coating because the thickness of overlayer is often found to be inhomogeneous over the film and TiO₂ pores are poorly filled. It has been reported that pore filling can be improved by drop casting the HTM solution on the porous TiO₂/dye film under vacuum due to a reduction in air cavities, changes in surface energy, and improved wetting of TiO₂ surface by the HTM solution.⁶⁷ Han *et al.* observed a better pore filling in a 7.2 μm TiO₂/N719 film by the HTM, poly(ethylene oxide) (PEO)/poly(vinylidene fluoride) (PVDF) when drop casting the HTM solution in vacuum according to data from energy dispersive x-ray spectrometry (EDS), relative to drop casting in ambient environment. This results in an increase in J_{sc} from 5.4 to 10.5 mA cm⁻² and conversion efficiency from 1.33 to 3.54 %.

Doctor-blading, which is a roll-to-roll compatible and large-area coating technique, has also been reported to show similar pore filling fraction (65 % when 2.5-μm films were used) to spin coating method.⁶⁸ In this study, a 2 μm TiO₂/Z907/spiro-OMeTAD fabricated by this method produced 6.9 mA cm⁻², 0.73 V and an overall efficiency of 3 %.

In order to obtain a pore filling fraction >65 % in a TiO₂ film of thickness >2 μm, a new technique of HTM deposition is apparently required. It could be argued that pore filling can be enhanced by enhancing the solubility of HTM. This involves a change in chemical structure of the HTM, which may also result in a change in other properties such as the hole mobility of HTM. It could also be argued that the loss in light harvesting due to a smaller number of dyes adsorbed can be compensated by using dyes with higher extinction coefficients. Organic dyes such as D149 and D205 (structures shown in Fig. 1.13) have been synthesised for this purpose. However, in any case, in principle, whenever HTM is deposited by solution, the pore filling fraction can never reach unity. As a result, the potential of these DSSCs can never be fully exploited. Therefore, the best way to circumvent the pore filling issues is to deposit HTMs on dye-sensitised TiO₂ film without the use of any solvent. One promising technique which fulfils this requirement is the melt-processing method. Although an efficient pore filling and a good TiO₂ surface coverage indicated by SEM images and TAS measurements respectively⁶⁹ have been reported, the high temperature applied during melt-processing may degrade the dye adsorbed on TiO₂. Also, the high melting temperature of Spiro-OMeTAD (~248 °C⁷⁰) may make this benchmark HTM employed in solid-state DSSCs not suitable for this method. Therefore, in the second and third year of my Ph.D project, the impact of heat on dye-sensitised TiO₂ film was first examined. Melt-processing of two different HTMs on dye-sensitised TiO₂ was also studied and applied in the fabrication of solid-state DSSCs. An overall

efficiency of 0.45 % was obtained by melt-processing spiro-OMeTAD on a TiO₂/D149 film. The experimental results will be presented and discussed in Chapter 4.

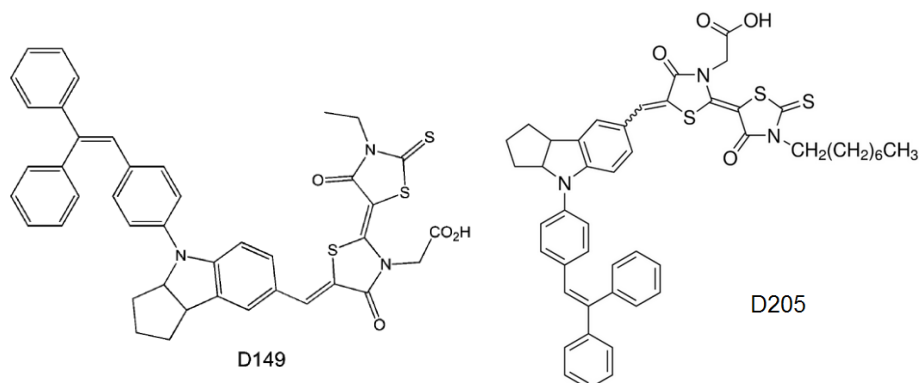


Fig. 1.13 Chemical structures of D149 and D205.

1.10 Methylammonium Lead Halide Perovskite Solar Cells

Perovskite originally referred to a mineral containing calcium titania (CaTiO₃), which was discovered and is named after a mineralogist, Lev Perovski. The term, perovskite, has now been extended to a whole class of compounds with the same ABX₃-type crystal structure as CaTiO₃. Recently, methylammonium lead halide perovskites (i.e. A = CH₃NH₃⁺; B = Pb²⁺; X = Cl⁻, Br⁻, I⁻) have attracted much attention in the field of photovoltaics due to some of its unique properties. The optical, excitonic and electrical properties of methylammonium lead halide perovskites have been investigated over the last two decades.⁷¹ But it was not until 2009, methylammonium lead halide was first employed in DSSCs.⁷² In this paper, CH₃NH₃PbI₃ (methylammonium lead triiodide or MAPI) and CH₃NH₃PbBr₃ (methylammonium lead tribromide or MAPB) were used as a dye to sensitise the TiO₂ electrodes. A MAPI DSSC with an I₂/LiI liquid electrolyte obtained 11 mA cm⁻², 0.6 V and 3.81 % efficiency under 1-sun illumination. A higher Voc of 0.96 V but a lower Jsc (5.6 mA cm⁻²) were produced by a MAPB cell with a Br₂/LiBr electrolyte, resulting in a conversion efficiency of 3.1 %, at the same light level. By modifying the surface of mesoporous TiO₂ layer (mp-TiO₂) by Pb(NO₃)₂ and optimising the MAPI concentration, Im *et al.* improved the Jsc and overall efficiency of the cell to 16 mA cm⁻² and 6.5 % respectively at 1 sun.⁷³ In the same paper, a remarkable absorption coefficient of 1.5 x 10⁴ cm⁻¹ at a wavelength of 550 nm of MAPI was also reported, when compared to 5 x 10³ cm⁻¹ at 540 nm for the N719 dye. However, the stability of these cells is poor due to the fast dissolution of perovskites in liquid electrolyte. Degradation in cell performance by as much as 80 % was observed after continuous illumination for only 10 minutes.

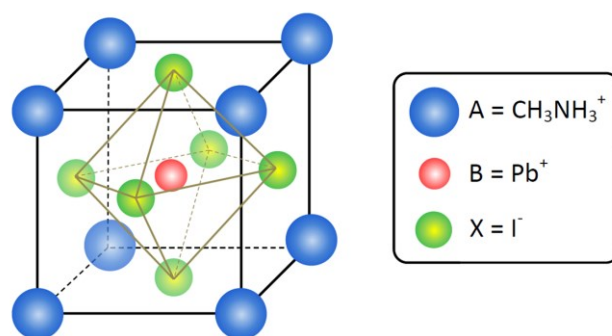


Fig. 1.14 Schematic diagram showing the structure of the methylammonium lead iodide (MAPI) perovskite.

A year later, the problem of perovskite dissolution was bypassed by replacing liquid electrolytes with a solid hole transporting material (HTM). Using 2,2',7,7'-tetrakis-(N,N-di-p-methoxyphenylamine)-9,9'-spiro-bifluorene (spiro-OMeTAD) as the HTM, Kim *et al.* increased the overall efficiency of mp-TiO₂/MAPI cell significantly to 9.7%.⁷⁴ Considering the thickness of the mp-TiO₂ layer is only 600 nm, it is very impressive that the cell manages to generate a photocurrent of 17.6 mA cm⁻² and an incident photon to electron conversion efficiency (IPCE) of >50% from light with a wavelength of 450 nm up to 750 nm. The authors also presented a mp-TiO₂/MAPI/spiro-OMeTAD cell with no degradation in cell performance (overall efficiency, in fact, increases from ~6.8 to ~8.2% when measured at 1 sun) after storage in air at room temperature in the dark for 500 hours. However, no data of cell stability under light were reported. At about the same time, another perovskite, CH₃NH₃PbI_{3-x}Cl_x, (methylammonium lead iodide chloride or MAPIC) was employed in solar cells with a mp-TiO₂ film and spiro-OMeTAD as HTM.⁷⁵ A *J*_{sc} of 18 mA cm⁻² and an overall efficiency of 7.6% were obtained by Lee *et al.* but no stability data were reported. There have also been attempts to employ HTMs other than spiro-OMeTAD. Among the four polymers investigated, a polytriarylamine polymer (PTAA) worked the best in a mp-TiO₂/MAPI system, producing 12.0% efficiency with a *V*_{oc} of 1 V.⁷⁶ The high *V*_{oc} in this cell relative to a mp-TiO₂/MAPI/spiro-OMeTAD was attributed to the more negative highest occupied molecular orbital (HOMO) energy level of PTAA (-5.2 eV)⁷⁷ than that of spiro-OMeTAD (-5.11 eV). Using a bromide-containing perovskite, CH₃NH₃Pb(I_{1-x}Br_x)₃ instead of MAPI, together with PTAA as the HTM, a similar efficiency of 12.3% was obtained by Noh *et al.*⁷⁸ The authors also reported that above certain bromide content (*x* > 0.2), the cells successfully maintained their overall efficiency (9-10%) after storage in air at room temperature without encapsulation for 4 days at a humidity of 35%, followed by 1 day at 55%, and finally at 35% again for 15 days. The power conversion efficiency (PCE) was further improved up to 15% by Burschka *et*

al. when a sequential deposition technique was used to fabricate a mp-TiO₂/MAPI/spiro-OMeTAD cell,⁷⁹ surpassing the highest reported efficiency of 12 % obtained in liquid electrolyte dye-sensitised solar cells. To test the device stability, a mp-TiO₂/MAPI/spiro-OMeTAD cell was encapsulated under argon and illuminated under 1-sun equivalent illumination from white light-emitting diodes at 45 °C for 500 hours. The cell was found to show no decrease in *J*_{sc} and retain >80 % of its initial PCE. It is noted that the initial PCE of the cell which underwent the ageing test was only 8 % initially. The loss in PCE was attributed to a reduced shunt resistance, leading to losses in *V*_{oc} and fill factor. The authors also reported a better control of perovskite morphology and better reproducibility of cell performance by the sequential deposition this technique.

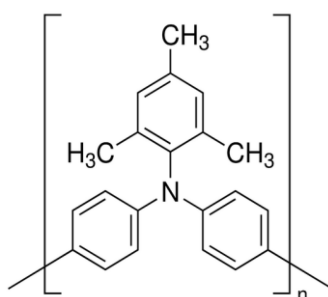


Fig. 1.15 Chemical structure of poly[bis(4-phenyl)(2,4,6-trimethylphenyl)amine] or PTAA.

While TiO₂ has been playing an unrivalled role in the DSSC technology for more than 20 years, there have been attempts to replace TiO₂ by Al₂O₃ in perovskite solar cells. By replacing TiO₂ by a 0.5 μm thick film of Al₂O₃ nanoparticles, the *V*_{oc} of MAPIC cell with spiro-OMeTAD increased by ~200 mV with no change in *J*_{sc}, improving the overall efficiency from 7.6 to 10.9 %.⁷⁵ Noting that alumina is an insulator with a wide band gap of 7 to 9 eV and a conduction band much higher than TiO₂, photo-excited electron in MAPIC cannot be injected to it. Therefore, alumina acts only as a meso-superstructured scaffold for MAPIC and electrons are transported through the MAPIC, without the involvement of Al₂O₃, to the FTO electrode. According to transient absorption and photoluminescence data, the effective diffusion length of electrons in MAPIC was later reported to be >1 μm,⁸⁰ making it possible to generate a photocurrent as high as 18 mA cm⁻² even when using the insulating Al₂O₃. The use of alumina also eliminates the loss in injection potential, leading to the observed increase in *V*_{oc} by ~200 mV. Although a stable optical density at 500 nm of an encapsulated meso-superstructured Al₂O₃/MAPIC/spiro-OMeTAD film after a 1000-hour 1-sun illumination was demonstrated, no stability data of complete devices were presented. With an aim to reduce the manufacturing

cost of perovskite solar cell, new processing methods of meso-superstructured Al_2O_3 (ms- Al_2O_3) film and compact TiO_2 blocking layer at a low temperature of $150\text{ }^\circ\text{C}$ were demonstrated.⁸¹ By optimising the thickness of Al_2O_3 film and TiO_2 blocking layer, a record efficiency of 15.9 % under 1-sun illumination was claimed by a ms- Al_2O_3 /MAPIC/spiro-OMeTAD perovskite solar cell.^{81b} It is noted that this power conversion efficiency is calculated from the maximum power output on the JV curve which was scanned from forward bias to short circuit. In a paper published a few months later, the same research group reported that the direction and rate of scanning in fact have a great effect on the JV curve measured and the corresponding maximum power point (MPP) of ms- Al_2O_3 /MAPIC/spiro-OMeTAD devices.⁸² For example, at a scan rate of 1 mV s^{-1} , scanning from forward bias to short circuit (FB-SC) gives a maximum power output of 13.7 mW cm^{-2} , relative to 8.9 mW cm^{-2} when scanned in the opposite direction. However, the authors have also shown that the MPP (15.5 mW cm^{-2}) of an Al_2O_3 /MAPIC/spiro-OMeTAD cell calculated from the JV scanned in the FB-SC direction matches the steady-state MPP measured within 0.74 and 0.75 V for 500 seconds. Therefore, they argued that the 15.9 % efficiency reported in the previous paper could still be a good estimate of the steady-state efficiency. Another point to note is that no stability results were reported in this paper. In fact, the general stability of ms- Al_2O_3 /MAPIC solar cell is questionable due to the limited ageing studies found in literature. In one such study, the PCE of an encapsulated ms- Al_2O_3 /MAPIC/spiro-OMeTAD device was actually shown to decrease from ~ 11 to ~ 6 % after continuous illumination at 0.8-sun (without UV cutoff filter) at $40\text{ }^\circ\text{C}$ for 200 hours.⁸³ But it is also worth noting that for the next 800 hours, the efficiency of the same cell had remained stable at ~ 6 % when ageing in the same environment.

Efficient planar heterojunction perovskite solar cells, with no mesostructure, have also been reported. By spin-coating MAPIC on a flat TiO_2 film, a MAPIC/spiro-OMeTAD solar cell was shown to give 8.6 % efficiency.⁸⁴ In the same paper, the efficiency was found to increase significantly to 15.4 % when depositing MAPIC by dual source vapour deposition of methylammonium iodide and lead chloride. However, it is noted that the efficiency reported here is calculated again from the JV scanned in the FB-SC direction. It has been demonstrated that the steady-state efficiency of a planar heterojunction MAPIC/spiro-OMeTAD cell is only ~ 8 %, relative to 14.4 % calculated from FB-SC scanned JV .⁸² Therefore, it is questionable if the vapour deposited device has the same steady-state efficiency as the one reported.

Although the efficiency of perovskite solar cells has been rising rapidly, little attention has been paid to the critical issue of device stability. In the fourth year of my Ph.D project, the stability of the mp- TiO_2 /MAPI perovskite cells was investigated. An encapsulated perovskite

solar cell with spiro-OMeTAD as the HTM has been fabricated and exposed to 40 sun-equivalent constant illumination for 63 hours (which delivers over 2700 hours equivalent of 1 sun photo-excitations). The loss in the cell's J_{sc} was only 7 %, however the loss in V_{oc} was 190 mV (24 %) at 1 sun. The experimental results will be presented and discussed in Chapter 5 of this thesis.

1.11 Aims of the Thesis

This thesis consists of three parts: water-based dye-sensitised solar cells, melt-processing of hole transporting materials in solid-state dye-sensitised solar cells and stability study of perovskite solar cells. The aims and objectives of each part are summarised as follows:

Water-Based Dye-Sensitised Solar Cells (Chapter 3)

Even with the application of permeation barrier and encapsulation, the slow transmission of water through the barrier will still result in considerable amount of water in dye-sensitised solar cells over time. The aims of Chapter 3 are to study the effect of water on liquid-state DSSCs, to find out the fundamental limitations in water-based DSSCs, and to optimise the overall efficiency of water-based DSSCs.

Melt-Processing of Hole Transporting Materials in Solid-State DSSCs (Chapter 4)

Spin-coating technique has been commonly employed to deposit hole transporting material in solid-state DSSCs. It has been found to give poor filling of TiO_2 pores, which will then result in a slower regeneration, degradation of dye molecules and thus, a lower overall efficiency of the solar cell. The aims of Chapter 4 are to investigate the effect of heating dye-sensitised TiO_2 films in air and melt-processing hole transporting materials onto dye-sensitised TiO_2 films on the resultant cell performance and to optimise the overall efficiency of solid-state dye-sensitised solar cells made by melt-processing technique.

Preliminary Stability Study of Perovskite Solar Cells (Chapter 5)

Recently, methylammonium halide perovskite solar cells have attracted much interest in the photovoltaic field as high overall efficiencies (>15 %) have been reported in literature. However, research on the stability of perovskite solar cells found in literature is very limited. This makes the stability of these solar cells questionable. The aims of Chapter 5 are to investigate the stability of methylammonium halide perovskite when stored under different conditions and to examine the photo-stability of complete methylammonium iodide (MAPI) solar cells. Although the tests performed in this study are rather preliminary, the experimental results provide insights on the further development of perovskite solar cells.

Chapter 2

Experimental Methods

2.1 Materials

All materials were used as received. Transparent conductive fluorine:SnO₂ (FTO) glasses, LOF Tec 15 were purchased from Hartford Glass (Indiana, USA). TiO₂ nanoparticle paste DSL18NRT (referred to as DyeSol pasted later in this thesis) was purchased from DyeSol (NSW, Australia). Another transparent TiO₂ nanoparticle paste used in Chapter 4 was made following published recipes⁸⁵ by Dr. X. Li in our research group. A more scattering TiO₂ paste (referred to as G24i paste later in this thesis) was formulated at G24i (Wales).

H₂PtCl₆, TiCl₄-tetrahydrofuran (THF), chenodeoxycholic acid (cheno), acetylacetone, titanium iso-propoxide, sodium iodide, lithium iodide, iodine, guanidinium thiocyanate, guanidinium carbonate, hydriodic acid, aluminium tri-sec-butoxide (Al(OBu^s)₃), 1,2-dihydroxybenzene (catechol), nitrosonium tetrafluoroborate (NOBF₄), 4-*tert*-butylpyridine (TBP) and bis(trifluoromethane)sulfonamide lithium salt (Li-TFSI), zinc powder, lead iodide, methylamine, N,N'-bis(3-methylphenyl)-N,N'-diphenylbenzidine (TPD), chlorobenzene, γ -butyrolactone (GBL), acetonitrile (ACN), 3-methoxypropionitrile (MPN) were purchased from Sigma-Aldrich. *Tert*-butanol (TBA) and propylmethylimidazolium iodide (PMII) were purchased from Alfa Aesar. Nitric acid, hydrochloric acid, absolute ethanol, diethyl ether, toluene and isopropanol (IPA) were purchased from VWR. 2,2',7,7'-tetrakis-(N,N-di-p-methoxyphenylamine)9,9'-spirobifluorene (spiro-OMeTAD) used in Chapter 4 and 5 was purchased from Merck kGaA. The hole transporting polymer poly(3-hexylthiophene-2,5-diyl) (P3HT) was purchased from Merck while poly-thieno[3,2*b*]thiophene-diketopyrrolopyrrole-co-thiophene (DPPTTT) was synthesised by the research group of Prof. Iain McCulloch in Imperial College, London.⁸⁶ Water used as solvent in electrolyte of DSSCs in Chapter 3 was deionised by ElgaPurelab Option-Q (resistivity: 18.2 Mohms cm @19 °C). Graphite powder used as the counter electrode of solid-state dye-sensitised solar cells in Chapter 4 was purchased from VWR. Gold pellets evaporated as the counter electrode of perovskite solar cells in Chapter 5 were purchased from Kurt J. Lesker.

Z907 used in Chapter 3 was kindly provided by Dr. M. K. Nazeeruddin (EPFL, Switzerland). Z907 used in Chapter 4 was purchased from Sigma-Aldrich. D149 was

purchased from Sigma-Aldrich. N719 purchased from DyeSol. TG6 was synthesised⁸⁷ and kindly provided by Professor Tarek H. Ghaddar (American University of Beirut, Lebanon).

2.2 Fabrication of Liquid-State Dye-Sensitised Solar Cells

2.2.1 Preparation of Working Electrodes

FTO substrates were first washed with a glass cleaner, followed by rinsing with deionised (DI) water and isopropanol (IPA). They were air-dried for 5 minutes and then heated on a hotplate (Detlef Gestigkeit Elektrotechnik) at 450 °C for 30 minutes.

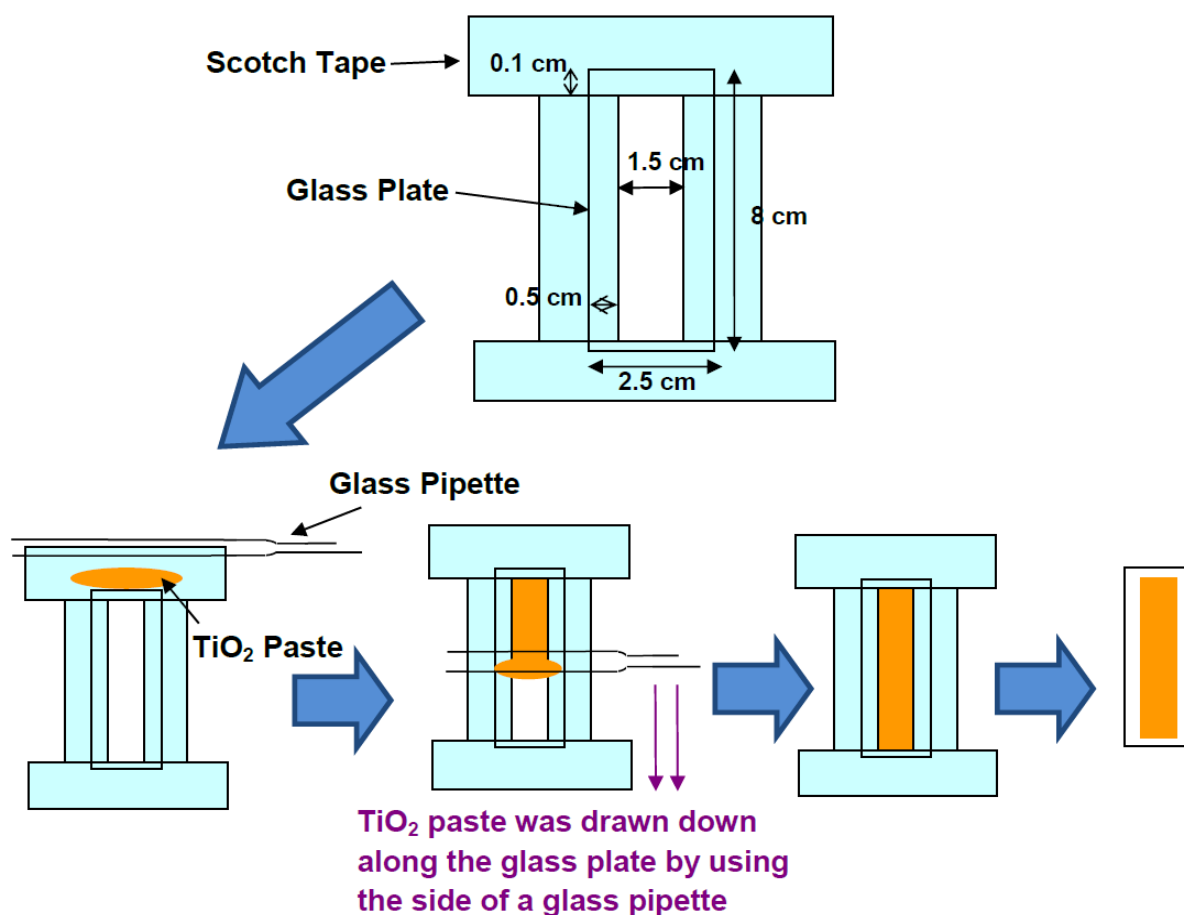


Fig. 2.1 Schematic diagram showing the procedures of the ‘doctor blade’ technique.

Doctor Blading

Film of TiO₂ nanoparticle was deposited onto the conductive side of the FTO substrate by the “doctor blade” technique as described in literature.⁸⁸ Depending on the thickness of the TiO₂ film required, one or two layers of Scotch Magic Tape was used to mask the four sides of substrate as shown in Fig. 2.1. TiO₂ paste was drawn down along the FTO substrates by using a glass pipette (VWR). The scotch tapes were carefully peeled off, leaving a thin layer of TiO₂ paste in the unmasked area. The paste was heated on the hot plate, (Detlef Gestigkeit

Elektrotechnik) with a ramping in temperature from 25 to 450 °C in 10 minutes and then at a constant temperature of 450 °C for 30 minutes. After cooling down to room temperature, the thickness of the TiO₂ film was measured by the Tencor Alphastep 200 Automatic Step Profiler.

Post-TiCl₄ Treatment

Post-TiCl₄ treatment was applied to TiO₂ films as described in papers.⁸⁹ TiCl₄-THF (0.8 g) was dissolved in DI water (80 mL) by stirring the solution for 30 minutes to give a 30 mM TiCl₄ solution. The FTO substrates with TiO₂ films were immersed in a glass Petri dish filled with the TiCl₄ solution. The Petri dish covered by a glass lid was then placed in an oven (Heraeus) preset at 70 °C for 30 minutes. The TiO₂ films were rinsed in DI water and heated on the hotplate at 450 °C for 30 minutes.

Dye Sensitisation

Each FTO substrate was cut into five 1.6 x 2.5 cm² pieces. The edges of TiO₂ film were scraped off to leave an area 1 x 1 cm² in the centre of the substrate. The substrates were heated on the hotplate at 450 °C for 30 minutes. The warm substrates were immersed in the vial containing the required dye solution and left in the dark at room temperature for 20 hours (ruthenium-based dyes) and 3 hours (D149).

2.2.2 Preparation of Counter Electrodes

FTO substrates were cut into 1.6 x 2.5 cm² pieces. Two holes were drilled at specific positions on each piece as shown in the Fig. 2.2 by using a mechanical drill (RS Components) with a 1 mm diamond drill head (Diama). The substrates with drilled holes were cleaned with a glass cleaner, followed by rinsing with DI water and isopropanol (IPA). They were air-dried for 5 minutes and then heated on a hotplate at 450 °C for 30 minutes. 4 µL of H₂PtCl₆ (5 nM) in IPA was spread evenly on the central 1 x 1 cm² area of the conductive side of the glass. They were then heated at 400 °C for 30 minutes.

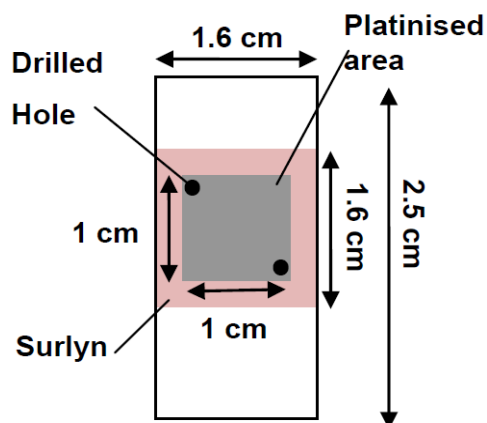


Fig. 2.2 Schematic diagram showing the positions of the drilled holes, the Surlyn and the platinised area of a counter electrode.

2.2.3 Cell Assembly

A $1 \times 1 \text{ cm}^2$ hole was cut out from a piece of $1.6 \times 1.6 \text{ cm}^2$, $25 \text{ }\mu\text{m}$ thick Surlyn gasket (Solaronix, SX1170-25PF) together with a piece of transparent polypropylene layer at the back by using a hole punch (Woodware Craft Collection). The Surlyn gasket was melted onto the conductive side of a platinised FTO substrate (i.e. the counter electrode) by using a heat press (Geo Knight, K8) preset at $120 \text{ }^\circ\text{C}$. A working electrode was removed from the dye solution and immersed in ACN for 15 minutes before use. After drying in air for 1 minute, the working electrode was placed on top of the counter electrode, with the conductive sides of the two electrodes facing each other. The stack was heated with pressure by the heat press at $120 \text{ }^\circ\text{C}$ for 1 minute to melt the Surlyn. An electrolyte ($2.5 \text{ }\mu\text{L}$) was injected into the space between the two electrodes via one of the drilled holes on the counter electrode by a pipette. The two drilled holes were then sealed by Surlyn and a glass cover slip (VWR) by using a hot iron to complete the cell assembly. Solder alloy (Cerazolzer, GS155) was deposited on the four sides of the cells by an ultrasonic soldering system (MBR Electronics GmbH).

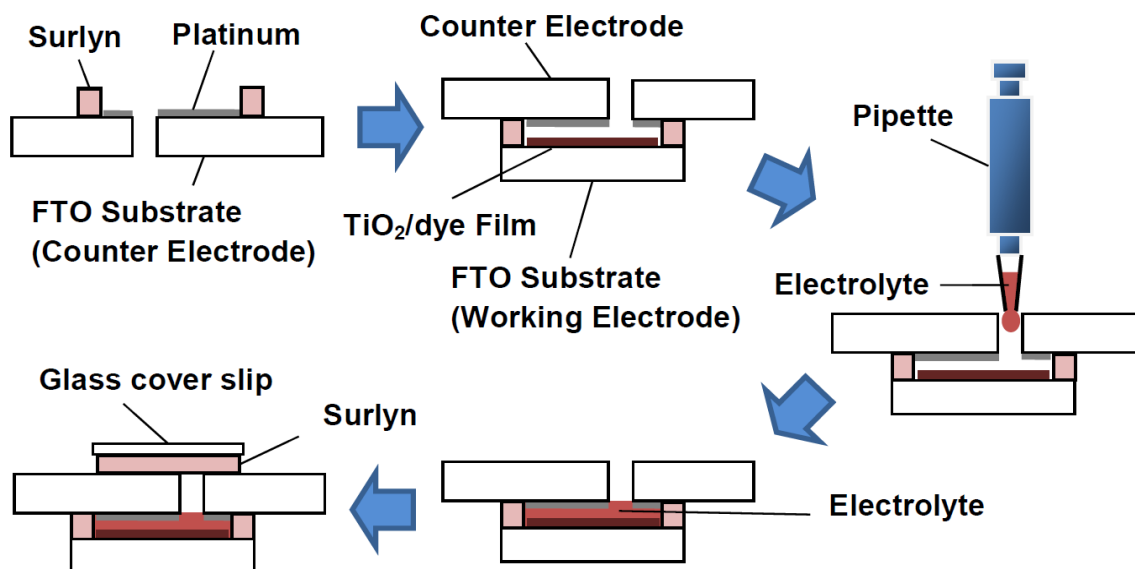


Fig. 2.3 Schematic diagram showing the procedures of assembling DSSC.

2.3 Fabrication of Solid-State Dye-Sensitised Solar Cells

2.3.1 Spray Pyrolysis

FTO substrates were first washed with a glass cleaner, and then rinsed with DI water and IPA. They were air-dried for 5 minutes. A compact TiO₂ layer (backing layer) was deposited on top of the conductive FTO layer by spray pyrolysis deposition (SPD).⁹⁰ With the conductive side facing up, the FTO substrates were placed on the hot plate (Detlef Gestigkeit Elektrotechnik). Microscope slides were used to cover about 0.5 cm of each side of the glasses to leave a conductive area for electrical contact for measurements. The temperature was then set to 450 °C for 30 minutes. A solution consisted of 0.4 mL acetylacetone, 0.6 mL titanium(IV) isopropoxide and 9 mL absolute ethanol was sprayed onto the glasses by means of a spray nozzle. Each next spray was applied after a 10 second pause to complete the pyrolysis of the previous layer and to restore the original substrate temperature. Sprays were applied across the whole area (20 x 28 cm²) of hotplate until 4 grams of solution was used (about 10 sprays). The pressure of the carrier gas (air) was always kept at 0.2 bar during the spraying process. Afterwards, the FTO glasses were heated at 450 °C for another 30 minutes to ensure a complete formation of TiO₂ on the uncovered area of the substrate.

Deposition of TiO₂ by the doctor blading technique, TiCl₄ treatment and dye sensitisation were then applied to these FTO substrates with compact TiO₂ layer in the same way as in the fabrication of liquid junction DSSCs.

2.3.2 Melt-Processing of Hole Transporting Materials

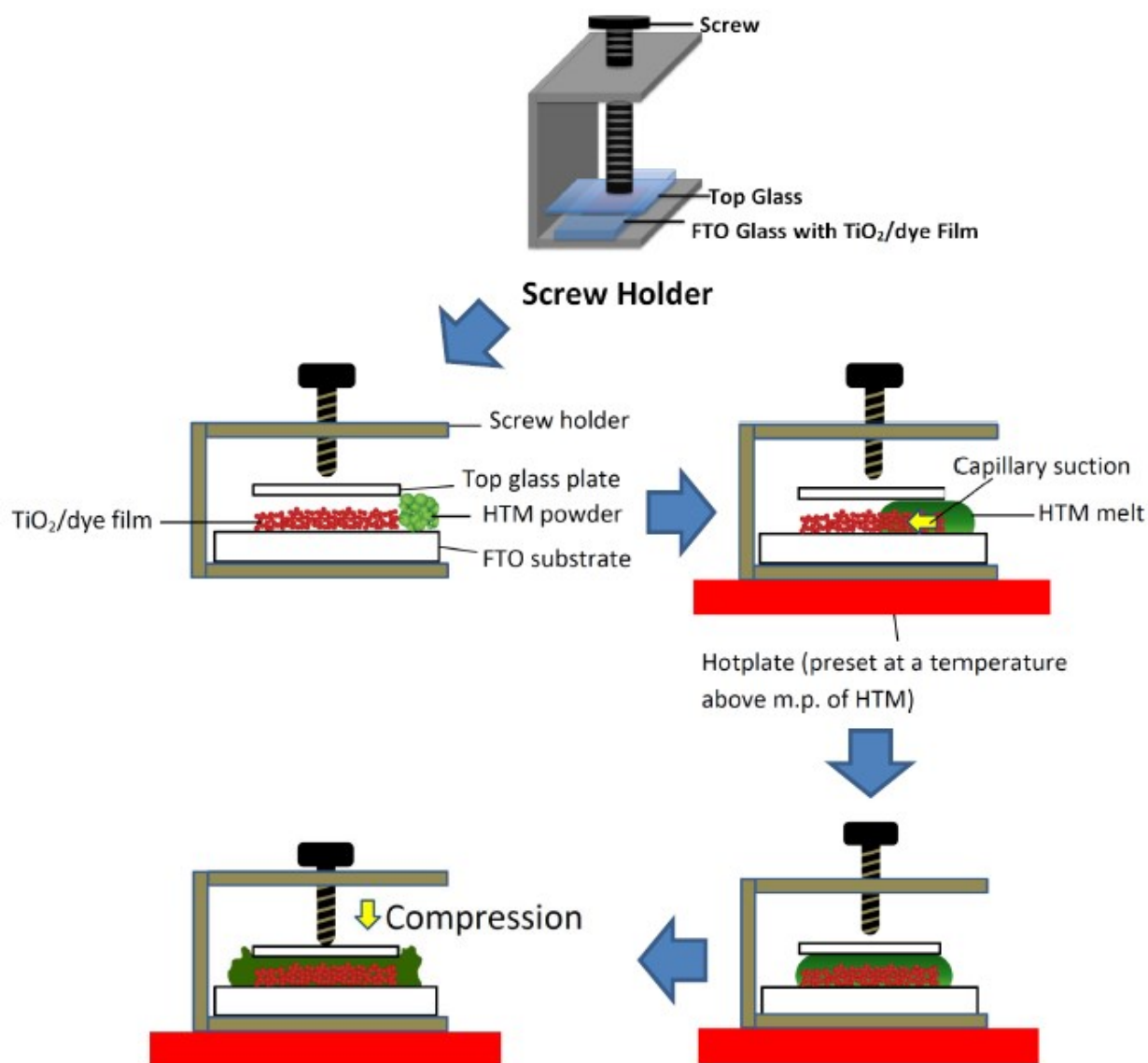


Fig. 2.4 Schematic diagram showing the procedures of melt-processing HTM on a TiO₂/dye film.

The dye-sensitised TiO₂ film, together with a clean glass plate on top, was placed in a screw holder (see top diagram of Fig. 2.4). About 8-10 mg of the solid HTM was placed on the interface where the two glasses meet (see Fig. 2.4). With the top glass plate only gently screwed, the whole screw holder was then placed on the hotplate pre-set at a temperature which is 7-10 °C higher than the melting point of the HTM. The slightly higher temperature used above the melting point reduces the melting time and thus, the time the dye was exposed to this high temperature. In the case where additives were employed, HTM and additives were heated on the hot plate (again at 7-10 °C above melting point of the HTM) before this melted mixture was transferred by using a hot glass pipette to the interface of the two glasses which were preheat at the same temperature on the hotplate. By capillary action, the HTM melt was

drawn through the porous TiO₂ (takes ~1 minute). Once the HTM melt covered all the dye-sensitised TiO₂ area, the screw was tightened with high pressure to reduce thickness of the overlayer of HTM on top of the dye-sensitised TiO₂ layer. The screw holder was then removed from the hotplate and cooled on a metal block. The top glass plate was pulled away after the TiO₂/dye/HTM film was cooled back to room temperature and the HTM completely solidified.

2.3.3 Graphite Counter Electrodes

Graphite powder was spread evenly in a 1 x 1 cm² basin at the bottom of a holder (see Fig. 2.5). The TiO₂/dye/HTM film (working electrode) was placed into the holder and faced down so that the active area was fully covered by the graphite basin. A 3 mm thick glass plate is placed on top of the working electrode in order to fix its position. The top glass plate was held in place by two screws on the two sides. The graphite basin was then raised towards the HTM layer of the working electrode by using a metal screw located on the bottom of the holder. Electrical contact was made at the conductive area (where there is no backing layer) on the working electrode and another at the metal bottom screw to complete the circuit.

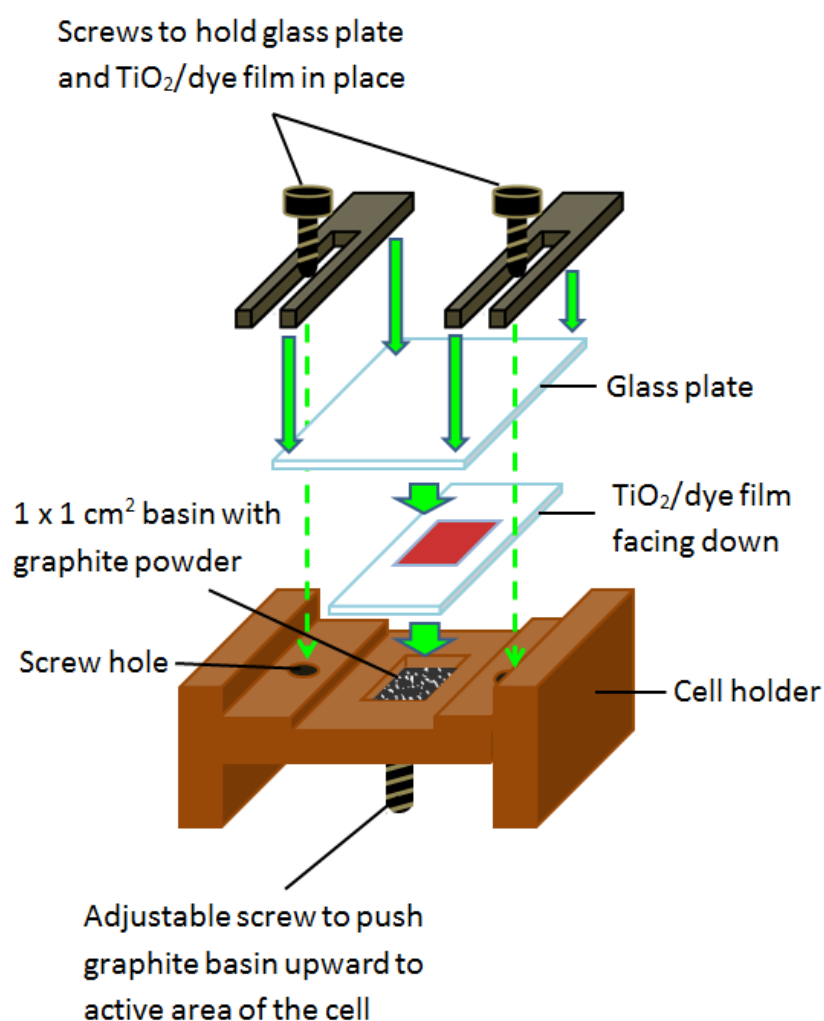


Fig. 2.5 Schematic diagram showing the construction of graphite counter electrode.

2.4 Fabrication of Mesoporous-TiO₂/CH₃NH₃PbI₃ Perovskite Solar Cells

2.4.1 Preparation of Methylammonium Iodide

Methylammonium iodide was prepared as published recipe.⁷⁴ Hydroiodic acid was slowly added to a solution of methylamine in absolute ethanol with stirring at 0 °C. This solution was allowed to stir for two hours for complete reaction. The solvent was removed via rotary evaporation. The off-white precipitate was washed with diethyl ether and recrystallised from absolute ethanol. The samples were stored in a desiccator until use.

2.4.2 Cell Fabrication

FTO substrates were cut into 2.5 x 2.5 cm² pieces. An area of 1.1 x 2.5 cm² of FTO was removed by etching by zinc powder and 2 M hydrochloric acid (see Fig. 2.6). The etched substrates were rinsed with DI water and ethanol to remove any remaining zinc or HCl. Then, the substrates were cleaned with a glass cleaner, followed by rinsing with deionised (DI) water and IPA. A compact TiO₂ blocking layer was deposited on FTO glass substrates spray pyrolysis as in the fabrication of solid-state DSSCs. Once cooled down, a diluted paste of TiO₂ nanoparticles from G24i (50 wt% in water) was spin-coated onto the glass substrates. Upon heating on the hotplate at 450 °C for 30 minutes, a mesoporous layer of TiO₂ was formed. The thickness of the TiO₂ film was ~0.5 μm as measured by the Tencor Alphastep 200 Automatic Step Profiler. A 1:1 molar solution of lead iodide and methylammonium iodide in gamma-butyrolactone (1.25 M) was heated and stirred at 60 °C for 1-2 hours until a clear yellow solution was formed. Before use, the mixture was allowed to cool to room temperature and any precipitate was separated from the solution via centrifuging at 8000 revolutions per minute (rpm) for 30 minutes. The supernatant was spread onto the mesoporous TiO₂ (mp-TiO₂), allowed to sit for 45 seconds and then spin-coated at 1200 rpm for 45 seconds in air (humidity: ~40 %). The substrates were then dried at 100 °C for 15 minutes to form the CH₃NH₃PbI₃ (MAPI) perovskite. Three hole transporting material (HTM) solutions, all in chlorobenzene, were prepared: (i) 68 mM spiro-OMeTAD, 9 mM Li-TFSI and 55 mM TBP (ii) 25 mg P3HT, 9 mM Li-TFSI and 55 mM TBP and (iii) 16 mg DPPTTT, 9 mM Li-TFSI and 55 mM TBP. The resulting solution was spread onto the perovskite film and spin-coated at 1200 rpm for 45 seconds. After that, the films were transferred to a nitrogen-filled MBRAUN glovebox (humidity: <0.01 %, relative oxygen concentration: <0.01 %). A gold counter electrode of ~100 nm was then evaporated onto the HTM layer by the Kurt J. Lesker evaporator. The devices were then encapsulated in a nitrogen atmosphere in the glovebox by a glass coverslip and a Surlyn gasket (see Fig. 2.6) which was then melted with a soldering iron to form a seal.

Solder alloy (Cerazolzer, GS155) was deposited on the bare FTO and on the gold electrodes (area which was not covered by cover slip) by an ultrasonic soldering system (MBR Electronics GmbH). During measurements under light, a black mask with an area of 0.08 cm^2 was placed on top of the cell to avoid additional contribution from light falling on the device outside the active area.

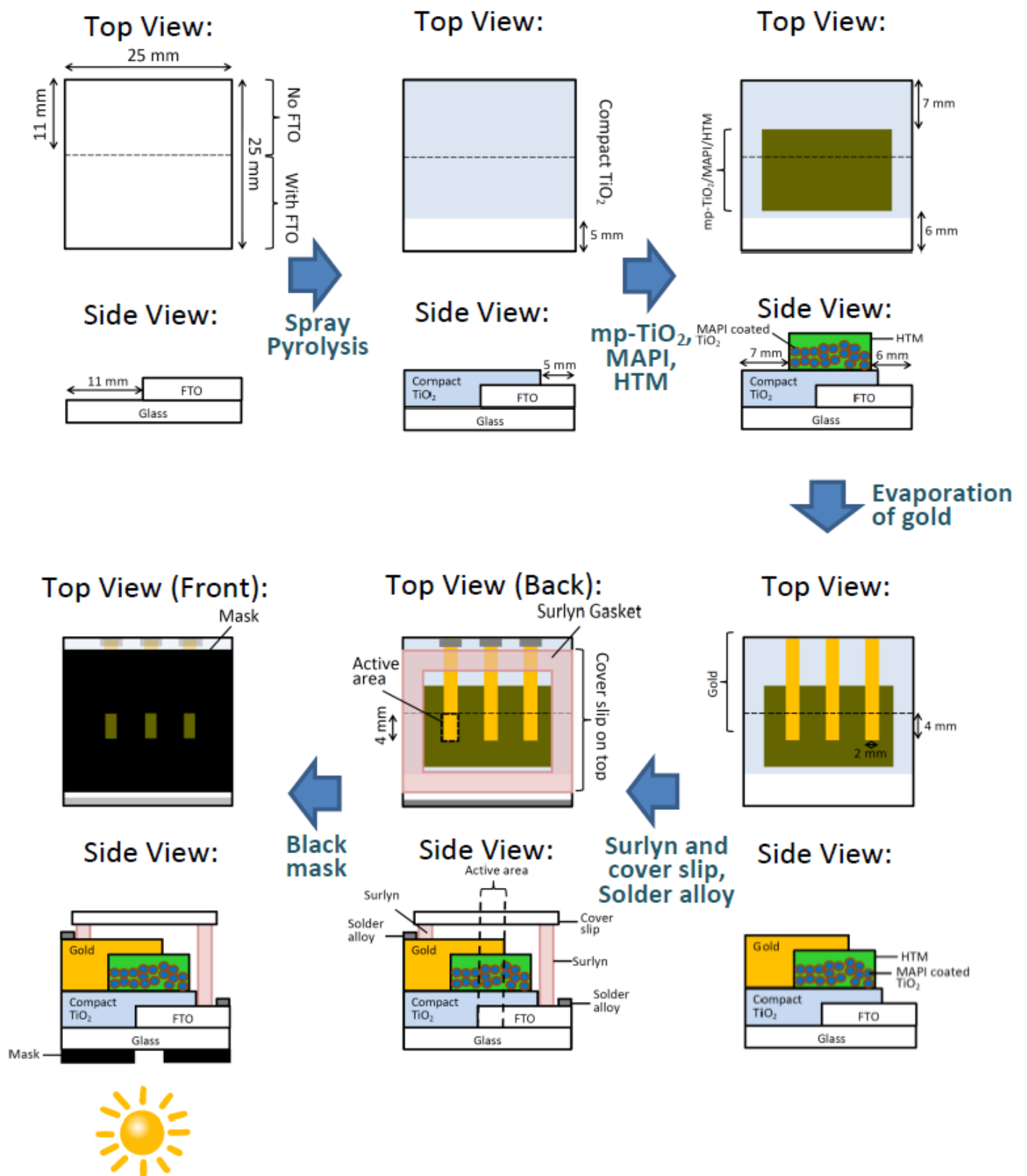


Fig. 2.6 Schematic diagram showing the procedures of fabricating mp-TiO₂/CH₃NH₃PbI₃ perovskite solar cells.

2.5 Characterisation Techniques

2.5.1 Optical Measurements

All the samples were immersed in acetonitrile for 15 minutes and then air-dried for 5 minutes before each measurement. UV-vis spectrophotometer (Thermo Electronic Corporation, Genesys 10UV) was used for optical measurements. Absorption of samples was measured over a spectral range from 300 nm to 800 nm, with 2 nm sampling intervals and using blank glass as reference.

2.5.2 Current Density-Voltage (*JV*) Measurements

DSSCs were illuminated at 1 sun by a 150 W Xenon lamp (Sciencetech, SS150W Solar Simulator) with an IR filter and an AM 1.5 spectral filter. During the measurements, the applied voltage was swept from 0 to 1 V and then back to -1 V before finishing at 0 V. Both the current and voltage were measured and controlled by a source meter (Keithley 2400). Before each set of measurements, the intensity of the light from the Xenon lamp was first calibrated with a silicon photodiode with a green filter, which has a spectral response similar to the absorption profile of the N719 dye. The light intensity was adjusted to within $\pm 0.5\%$ to that of AM 1.5.

2.5.3 Transient Photovoltage and Photocurrent, and Charge Extraction Measurements

Recombination, transport and trap density were characterised by transient measurements automated and analysed using the Transient and Charge Extraction Robot (TRACER) system designed and built by Dr. B. O'Regan.^{89b, 91} The system consists of five 1-W red light-emitting diodes (LEDs) controlled by a fast solid state switch to induce a pump pulse. An array of 10 white LEDs was used to provide bias light. Transient recombination lifetime was measured from the transient decay of photovoltage at open circuit after a $\leq 100\ \mu\text{s}$ flash from red LEDs. Transient transport lifetime was measured from the transient decay of the photocurrent at short circuit after the red pulse. Charge density at V_{oc} was determined by measuring the decay of current transient after switching off the white bias light and switching the cell to short circuit simultaneously. The current transient measured across a 2 ohm measuring resistor was then integrated over a period of 4 seconds to give the total charge extracted. Charge density at J_{sc} was measured by the decay of current transient after switching off the white bias light. Integration of the resulting current transient for a period of 1 second to give the charge extracted. All the above measurements were made under a series of 7-8 bias light levels between 0.02 and 1.3 suns.

Chapter 3

Water-Based Dye-Sensitised Solar Cells

Abstract

Dye-sensitised solar cells (DSSCs) employing iodine/guanidinium iodide redox couple in water as the only solvent have been fabricated. They show 4 % energy conversion efficiency under 1-sun illumination. This result is ~5 times higher than the best previously reported values. The wetting behavior of water electrolytes into the mesoporous dye-sensitised TiO₂ film is found to be critical, especially when using hydrophobic dyes. Chenodeoxycholic acid (cheno) was used as a surfactant which significantly improves the wetting of dye-sensitised TiO₂ surface by water electrolytes. By adjusting the concentrations of iodine and iodide, the above optimum efficiency has been achieved. It is also proposed that the water electrolyte may have intrinsically high recombination rate due to the significantly lower binding constant of iodine with iodide in water relative organic solvent.

Chapter 3.1

Improving Wetting and Diffusion-Limited Current Density in Water-Based Dye-Sensitised Solar Cells

3.1.1 Introduction

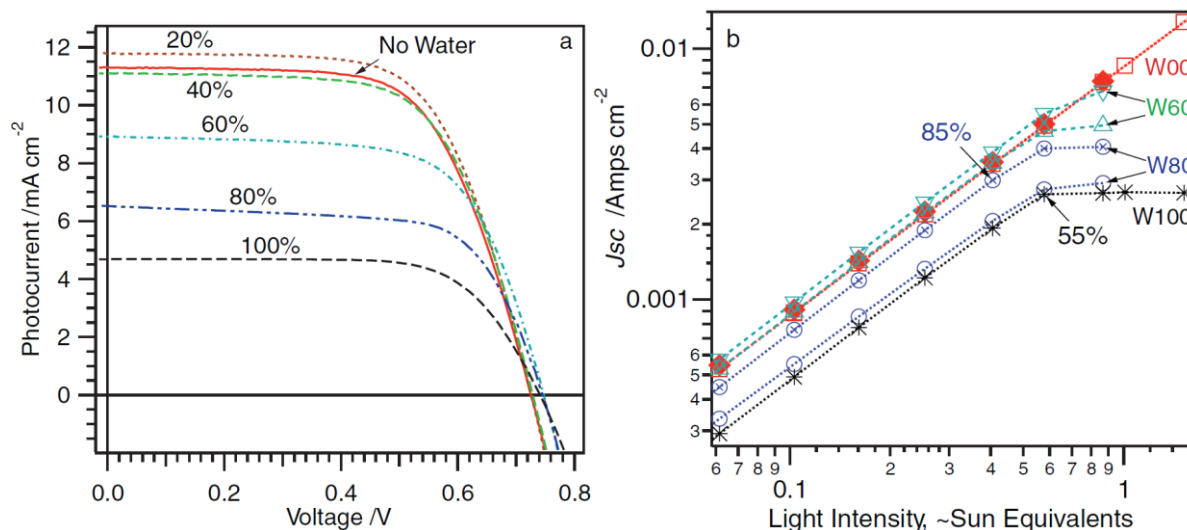


Fig. 3.1 a) One-sun JV curves vs. water content for cells with TG6 dye. Illuminated using simulated AM 1.5 (filtered xenon lamp) at 100 mW cm^{-2} . b) J_{sc} vs. bias light intensity for selected W00 and high-water-content cells. W00, W20, etc. refer to electrolytes with 0 %, 20 %, etc. water, relative to MPN. Percentages are J_{sc} relative to the W00 cell at the same light intensity. Illuminated using white light-emitting diodes. (The photocurrents differ from panel (a) due to large spectral mismatch compared to AM1.5.). [These figures are reproduced with the permission of the rights holder, WILEY-VCH Verlag GmbH & Co. KGaA, Weinheim.]⁴⁵

As described in Chapter 1, before 2010, water had generally been considered to be poisonous for dye-sensitised solar cells (DSSCs). However, research regarding water in DSSCs was limited. This drove me to examine the effect of water on the performance of DSSCs in my MSci project in 2009. In that project, a series of cells with 0, 20, 40, 60 80 and 100 % water fractions relative to 3-methoxypropionitrile (MPN) were fabricated and tested.⁴⁵

As shown in Fig. 3.1 the electrolyte functioned with no decrease in cell performance with up to 40 % water fraction. At 60 % water fraction, there is no decrease in J_{sc} at 0.4-sun illumination and below. Even at 80 % water fraction, the loss in efficiency is only 15 % at up to 0.4-sun illumination. These results show that the basic functions such as injection, regeneration and transport can perform well in electrolyte with high water content. As the light intensity increases above 0.5 suns, the J_{sc} 's of DSSCs with 60 % or higher water fraction do not increase any further with light intensity (i.e. plateaued or saturated). These saturated photocurrents are virtually identical to the plateaus reached in their corresponding dark current in reverse bias as shown in Fig. 3.2a. It was concluded in my MSci report that this indicated

the saturation of J_{sc} 's of these DSSCs with high water content is caused by a diffusion limitation of current through the electrolyte system. Also, a buildup of electrons in TiO_2 in DSSCs with 80 % and 100 % water fraction was observed as the light intensity increases past the level where the current saturates as shown in Fig. 3.2b. This indicates that the photo-injected electron cannot flow out of the TiO_2 , which is likely to be caused by a limitation in triiodide diffusion out of the porous TiO_2 and thus, a depletion of triiodide at the counter electrode. Phase segregation inside the pores of TiO_2 and/or incomplete wetting by the high-water-content electrolytes, were proposed to explain such a phenomenon in the J_{sc} 's of these cells. These interesting findings led me to carry on my research on water in DSSCs and extend my studies to electrolytes with only water as solvent in this Ph.D. project.

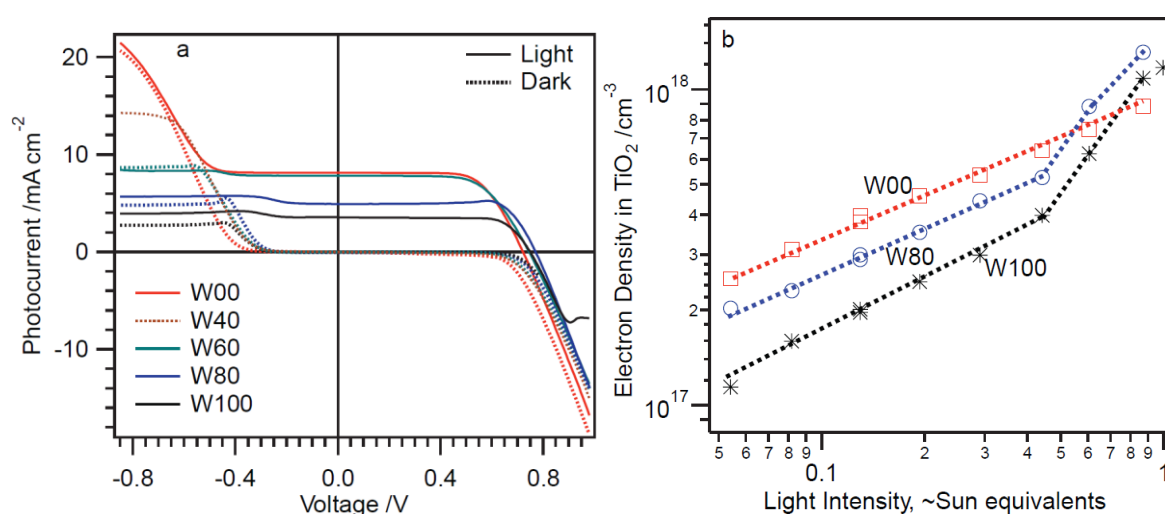


Fig. 3.2 a) Dark and illuminated (≈ 0.8 suns) extended J - V curves for TS4 cells with varying water content. The sign of voltage is that applied to the counter electrode. b) Excess electron density in the TiO_2 at short circuit (relative to dark) vs light level for different water content in TS4 cells. W00, W20, etc. refer to electrolytes with 0 %, 20 %, etc. water, relative to MPN. [These figures are reproduced with the permission of the rights holder, WILEY-VCH Verlag GmbH & Co. KGaA, Weinheim.]⁴⁵

It is worth to note that in my MSci project, in order to avoid phase segregation in electrolytes, a relatively high volume fraction of the ionic liquid 1-propyl-3-methylimidazolium iodide (PMII) was employed such that the actual water content was never above 60 %. In the case of 100 % water fraction, 1 % by volume of Triton X-100 (surfactant) was added to the electrolyte for the same reason. In the following work, instead of adding any extra surfactant which complicates the electrolyte system further, a simple system with sodium iodide, iodine and guanidinium thiocyanate (GuSCN) in water was first employed to solve the problem of phase segregation. GuSCN is commonly added in DSSCs and guanidinium ion (Gu^+) was later found by our research group to reduce electron/iodine recombination rate

constant and thus, improve efficiency in DSSCs by binding strongly to the N719 and D131 dyes and probably to dyes with a similar structure.⁹²

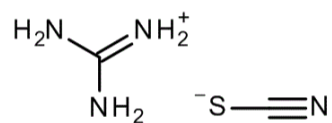


Fig. 3.3 Chemical structure of guanidinium thiocyanate (GuSCN).

Due to the hydrophobic nature of dyes commonly used in DSSCs such as Z907, another probable limiting factor of water electrolyte is its poor wetting ability on the dye-sensitised TiO₂ surface. This reduces the cross-sectional area through which the ion can diffuse and results in lower diffusion-limited current density (J_{DL}). In this section, the effect of TiO₂ and dye on J_{DL} of water electrolyte will be examined by using symmetrical cells and an enhancement in wetting and J_{DL} by the use of a wetting agent will be presented.

3.1.2 Experimental Methods

Preparation of Symmetrical Cells:

Both fluorine-doped tin oxide (FTO) plates were platinised. A series of symmetrical cells with progressively more layers were fabricated. They are platinised FTO plates only, with TiO₂ films, TiO₂ films with TiCl₄ treatment and TiO₂ films with TiCl₄ treatment and Z907 dye, all on both sides. These cells were assembled with 3 layers of 25 mm thick Surlyn sealant as opposed to only one layer in ordinary DSSCs. The extra thickness from the 3 layers of Surlyn allows the J_{DL} to be measured with less interference from the cell series resistance. 3-methoxypropionitrile (MPN) or water electrolyte with 0.1 M sodium iodide and 0.01 M iodine was introduced through holes on one side which were sealed with Surlyn and coverslip.

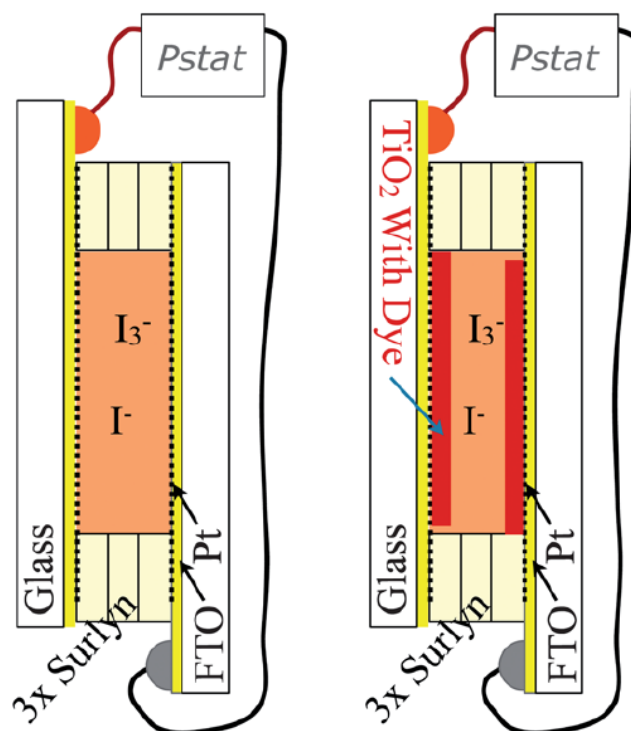


Fig. 3.4 Schematic diagram of the symmetric cells used to examine J_{DL} . [This figure is reproduced with the permission of the rights holder, The Royal Society of Chemistry.]⁹³

Standard DSSCs were fabricated as described in Chapter 2. TiO₂ nanoparticle paste DSL18NRT used in both symmetrical and standard cells was purchased from DyeSol (NSW, Australia). TiO₂ electrodes were sensitised either in a 0.3 mM Z907 in tertbutanol (TBA)/ acetonitrile (ACN) (1:1 by volume) or 0.3 mM Z907 and 15 mM chenodeoxycholic acid (cheno) in TBA/ACN (1:1 by volume) for 20 hours. Current density vs. voltage (JV) characteristics were measured as described in Chapter 2.

3.1.3 Results

3.1.3.1 Symmetrical Cells in Water vs. MPN Systems

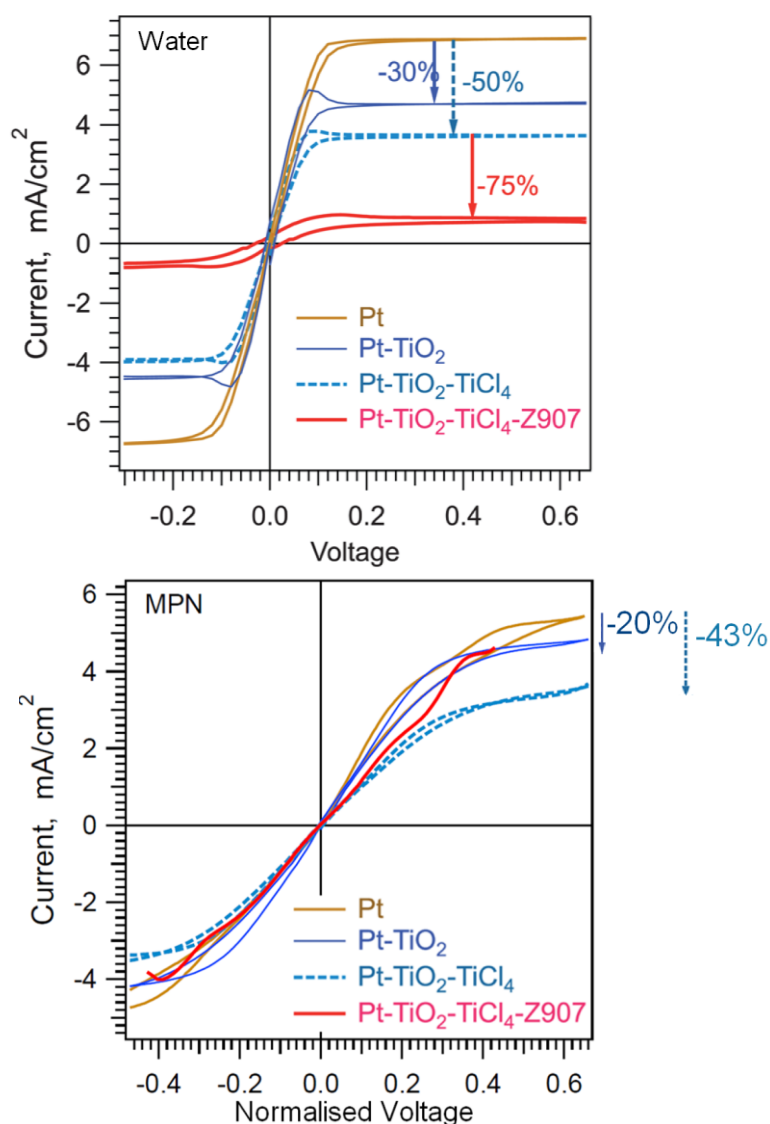


Fig. 3.5 Top: Current density–voltage (JV) curves of different symmetrical cells with electrolyte consisting of 0.1 M NaI and 0.01 M iodine in water. Bottom: Current density–normalised voltage curves of different symmetrical cells with electrolyte consisting of 0.1 M NaI and 0.01 M iodine in MPN. Label, e.g. Pt–TiO₂, refers to the symmetric structure Pt–TiO₂–gap–TiO₂–Pt (see Experimental Methods). Total thickness: 75 μm for all cells. TiO₂: DyeSol, 7 μm . [These figures are reproduced with the permission of the rights holder, The Royal Society of Chemistry.]⁹³

The JV 's of a series of four different symmetrical cells with water and MPN electrolyte are shown in Fig. 3.5. In the JV 's without any normalisation such as the top diagram of Fig. 3.5, the gradient across the origin indicates the resistance to charge transfer across the electrolyte/electrodes interface or the transfer resistance. Since the transfer resistance in the cells with water electrolyte is very consistent, no normalisation is needed in their JV 's. However, the cells with MPN electrolyte show quite a big variation in transfer resistance. For a

better comparison of the J_{DL} , the data in the bottom ‘MPN’ graph are normalised along the x-axis so that the plateau currents are all shown in a similar voltage range. Note that this normalisation does not result in any change in J_{DL} of any of the systems shown.

The saturation current density at both forward and reverse bias indicates the diffusion-limited current density (J_{DL}). In these symmetrical cells, the addition of 7 μm porous TiO_2 layer reduces the J_{DL} by 30 % and 20 % in water and MPN electrolytes respectively. TiCl_4 treatment on TiO_2 surface reduces the J_{DL} in both electrolytes by another ~ 20 %. However, when the TiO_2 surface is sensitised with Z907, a drastic difference in the resulting J_{DL} of water and MPN electrolyte is observed. The J_{DL} of water electrolyte drops by 75 % when compared to the same system without Z907, while the J_{DL} of MPN electrolyte remains the same.

3.1.3.2 Effect of Chenodeoxycholic Acid in Wetting

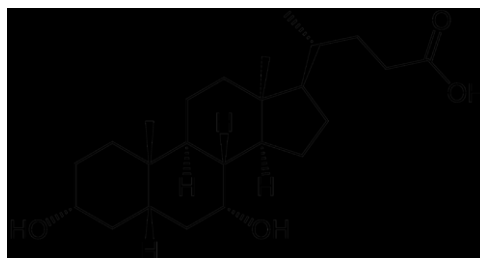


Fig. 3.6 Chemical structure of chenodeoxycholic acid (cheno)

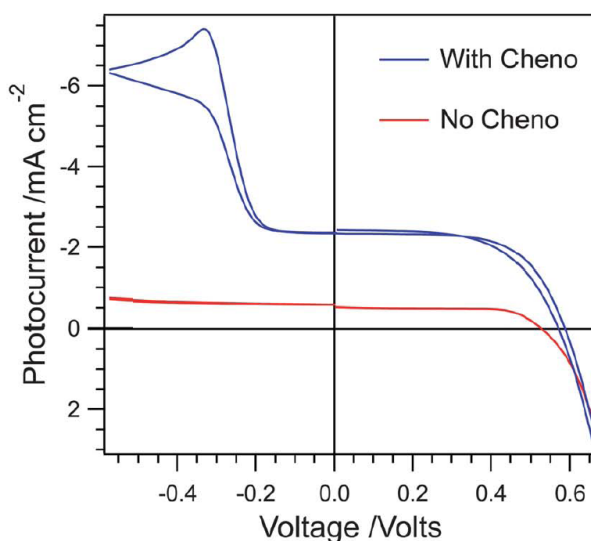


Fig. 3.7 One-sun J - V curves of water-based DSSCs with and without cheno in the cell. Without cheno cell: TiO₂ film: DyeSol, 7 μ m; Dye: Z907; Electrolyte: water with 2 M NaI, 20 mM iodine and 1 M GuSCN. With cheno cell: identical except: dye solution had 1:50 Z907:cheno, electrolyte had 0.5 M GuSCN. [This figure is reproduced with the permission of the rights holder, The Royal Society of Chemistry.]⁹³

Fig. 3.7 shows the JV of a standard Z907 DSSC with water electrolyte (red curve) and that of an identical system with chenodeoxycholic acid co-adsorbed with Z907 on the TiO₂ surface (blue curve) under one-sun condition. The standard cell without cheno shows a J_{sc} of ~ 0.5 mA cm⁻² which is limited by J_{DL} as indicated by the plateau in photocurrent at reverse bias of its JV curve. The addition of cheno to the TiO₂ surface clearly improves the J_{DL} by ~ 10 fold, resulting in an increase in J_{sc} to about 2 mA cm⁻², which is no longer diffusion-limited.

3.1.4 Discussion

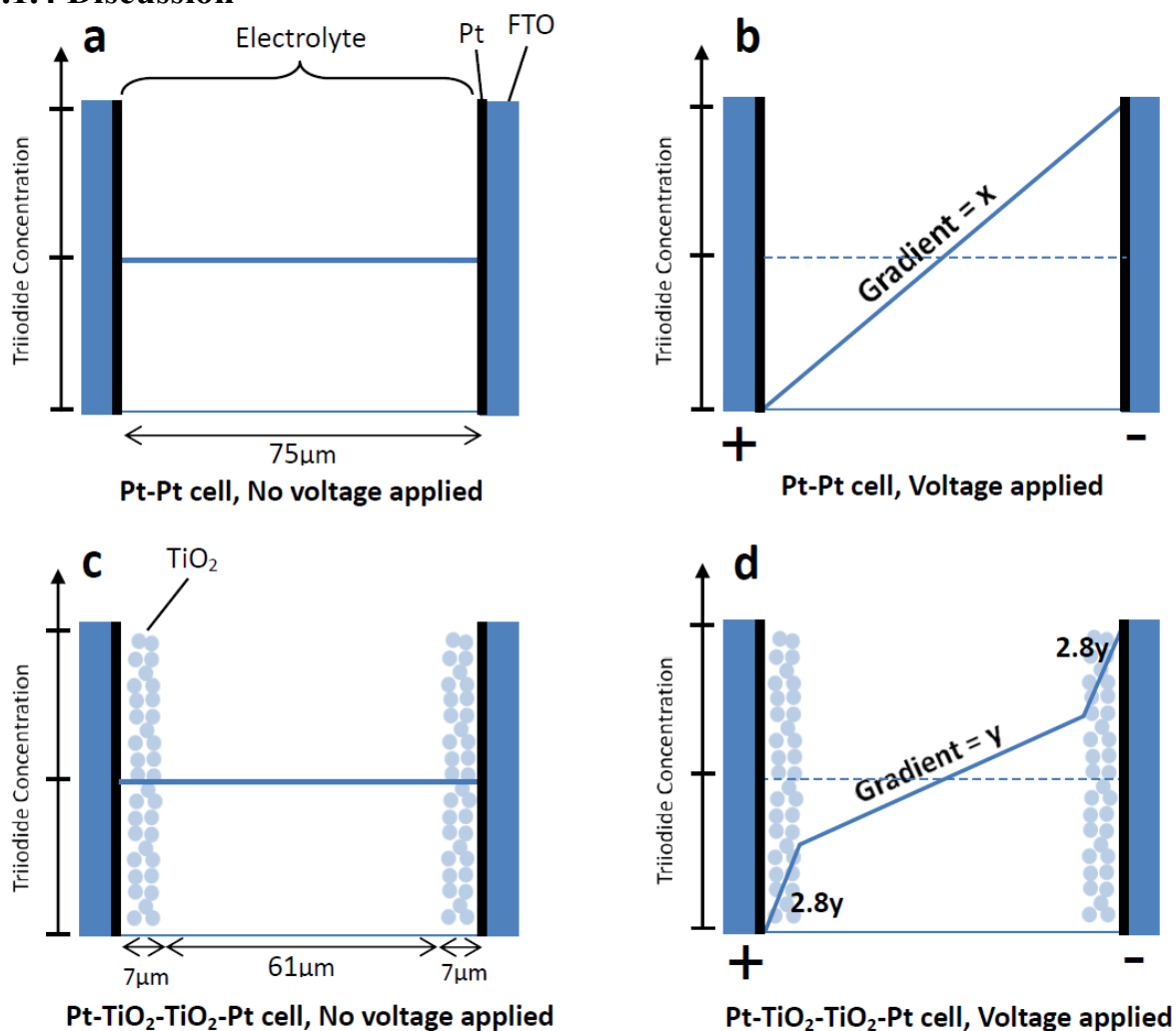
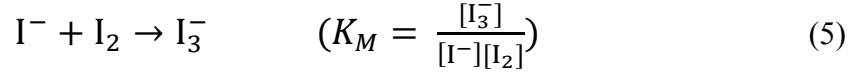


Fig. 3.8 Schematic diagram showing how applied voltage and additional layers of porous TiO₂ affect the concentration gradient of triiodide in symmetrical cells.

According to equation (4), diffusion-limited current density is directly proportional to the diffusion coefficient and the concentration gradient of the limiting ion. In this symmetrical cell experiment, due to the high binding constant of iodide and iodine (in water, $K_M = \sim 1000$ and in organic solvent e.g. ACN $K_M = 4 \times 10^6$; in MPN, $K_M > 10^5$)⁹⁴ and the relatively high iodide concentration (0.1 M), we can assume most of the iodine binds to iodide to form triiodide and the resulting concentration of triiodide in electrolyte is essentially the same as that of iodine added (0.01 M). Since triiodide concentration is 10 times lower than iodide concentration, triiodide is the limiting ion in this system.

$$J_{DL} = -FD \left(\frac{dC}{dx} \right) \quad (4),$$

where F , D and dC/dx are Faraday constant, diffusion coefficient, concentration gradient of the limiting ions respectively.



As shown in Fig. 3.8a, the concentration of triiodide is the same everywhere in the symmetrical cell when no voltage is applied across the cell. But when a voltage is applied, triiodide is reduced to iodide at the negative electrode whereas iodide is oxidised to triiodide at the positive end. Triiodide and iodide ions flow through the gap by diffusion between the electrodes to complete the circuit. The maximum current flowing through this symmetrical cell is limited by the triiodide concentration and its maximum concentration gradient that can be reached. J_{DL} can then be estimated by using equation (4). In the case of Pt-TiO₂-TiO₂-Pt cell shown in Fig. 3.8d where a layer of 7 μm porous TiO₂ is deposited on each Pt electrode, additional factors (porosity, constrictivity and tortuosity) which affect the effective diffusion coefficient in porous media have to be taken into account when estimating J_{DL} according in equation (6). Higher tortuosity means a longer path length that the triiodide ions must travel through the porous layer while high constrictivity can be viewed as a high resistance to transport in the porous media due to narrowed pores.

$$D_e = \frac{D\varepsilon\delta}{\tau^2} \quad (6),^{95}$$

where D_e , ε , δ and τ are effective diffusion coefficient in porous media, porosity, constrictivity and tortuosity of the porous media respectively.

Taking the values of porosity and matrix factor (i.e. τ^2/δ) in TiO₂ from literature (50 % and 1.37 respectively),⁹⁶ the triiodide concentration gradient in the porous layer must be higher than that in the bulk of electrolyte by a factor of 2.8 in order maintain a constant current density across the whole cell. A simple calculation based on equation (4) predicts ~25 % decrease in J_{DL} when compared to Pt-Pt cell. This prediction is in good agreement with the JV results shown in Fig. 3.5. Further reduction in J_{DL} after TiCl₄ treatment in both water and MPN electrolytes is also expected due to a reduction in porosity as reported previously^{89a} and presumably an increase in constrictivity. However, in the case where the TiO₂ surface is sensitised with Z907, the dramatic reduction in J_{DL} of water electrolyte is not expected when considering there is only a monolayer of dye of size ~1 nm only. Herein, an incomplete wetting of Z907-sensitised TiO₂ surface due to the hydrophobicity of Z907 (especially with its long hydrocarbon chains) is proposed. This is supported by the observed poor wetting of

TiO₂ surface when injecting the water electrolyte into the cell and also the high contact angle (110.8°) on Z907-sensitised TiO₂ reported by Wang *et al.*⁹⁷

In order to solve this wetting problem of water electrolytes, chenodeoxycholic acid (cheno) was added to the Z907 dye solution because of its hydrophilicity. Upon dyeing, cheno co-adsorbs, together with dye molecules, onto the TiO₂ surface. With cheno, the cell shows much higher J_{sc} (4 fold) and J_{DL} (~10 fold). The enhancement in wetting by water electrolyte is believed to be caused by the hydrophilic -OH groups at one end of the cheno molecule, together with its hydrophobic body in the centre portion (see Fig. 3.6). The hydrophobic body makes it compatible with the hydrophobic Z907 dye. Also, instead of lying flat, cheno presumably has long enough hydrophobic body to stand upright so that the hydrophilic -OH groups can reach out away from TiO₂ surface. This makes the surface of dye-sensitised TiO₂ more hydrophilic, enhancing wetting of TiO₂ pores by water electrolytes. However, the wetting effect of cheno does not seem to be permanent as it was observed that J_{DL} tends to decrease over time. After storage in the dark for a week, the J_{DL} decreased to a point where it started to limit the J_{sc} again. This is presumably caused by the desorption of cheno from TiO₂ surface over time. In order to improve the stability of J_{DL} and overall efficiency of the cheno cells, cheno was also added to the water electrolyte until it was saturated. Even though the addition of cheno to the water electrolyte helps to slow down the loss in J_{DL} , this loss is still fairly quick when a low concentration of iodine (<20 mM) is used. For example, a water-based D149 DSSC with 10 mM iodine gave a J_{sc} and J_{DL} of 3.94 and 5.27 mA cm⁻² respectively when measured within one hour of fabrication. But after 24 hours, the J_{sc} had already become limited by J_{DL} to <1 mA cm⁻². Moreover, a J_{DL} of just over 6 mA cm⁻² shown by the water-based cell in Fig. 3.7 is relatively low, when compared to similar non-aqueous electrolyte with the same iodine concentration (20 mM). This suggests that even with the use of cheno, the wetting of TiO₂ pores by water electrolyte is still not perfect.

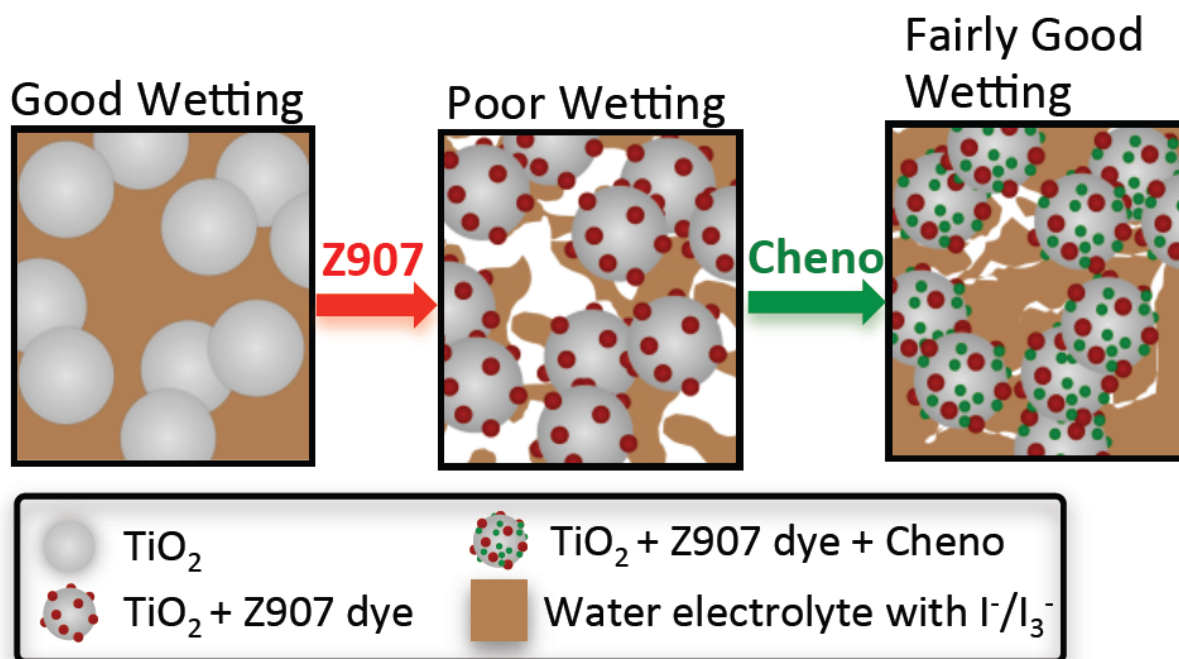


Fig. 3.9 Schematic diagram showing the wetting problem in the Z907-sensitised TiO_2 layer in water-based DSSCs.

The effect of guanidinium thiocyanate (GuSCN) on wetting has also been studied in this project. Apart from its tendency to bind to dye and reduce recombination rate,⁹² guanidinium thiocyanate has also been reported to be a chaotropic ion, which reduces the strength of hydrophobic interaction.⁹⁸ The latter property could possibly improve wetting and J_{DL} . It was found that in some cases, GuSCN can increase J_{DL} but its effectiveness is not as consistent as that of cheno. It was also observed that GuSCN does not always provide an additive increase on top of the effect of cheno. Therefore, further study will be needed to account for the beneficial effect caused by GuSCN on wetting of dye-sensitised TiO_2 pores by water electrolyte.

During the course of this study, surfactants other than cheno and GuSCN have also been reported in literature to improve wetting of TiO_2 pores by water-based electrolyte. For example, Zhang *et al.* found that the addition of 0.2 wt% of N,N,N-trimethyl-3-(perfluorooctylsulfonamido)propan-1-aminium iodide (FC-134), a cationic surfactant, increases the J_{sc} from 7.5 mA cm^{-2} to 10 mA cm^{-2} under 1-sun illumination.⁹⁹ In this paper, DSSCs with a very similar composition to the ones used in this thesis were tested. The authors sensitised the TiO_2 films with N719 and cheno with a molar ratio of 1:100 and employed an electrolyte with 2 M NaI, 0.02 M iodine and 0.1 M GuSCN in water. Since the photocurrent at far reverse bias and charge density vs. J_{sc} curve were not shown, J_{DL} of the cells had not been clearly determined in this paper. However, it was observed the J_{sc} 's of both the cells with and

without surfactant under 0.5-sun illumination were more than half (~60 %) of their respective J_{sc} 's under 1 sun. This indicates the J_{sc} 's of both cells were already diffusion-limited at 1 sun (if assuming J_{sc} of these cells increases linearly with light level as observed in my study) and the increase in J_{sc} after the addition of FC-134 can be viewed as an improvement in wetting. This interpretation was supported by a reduction in contact angle the water electrolyte on TiO₂ films sensitised with N179 and cheno (1:100, molar ratio) from 33.5° to 26.0° upon addition of FC-134. However, the stability of the cells was poor as the J_{sc} and overall efficiency dropped by ~50 % after just 1 day under 1-sun illumination. The authors attributed this to the desorption of the N719 dye from TiO₂ surface, which was also observed in my study when water electrolyte without carefully controlled pH was added to N719 DSSCs. In the same paper, three other surfactants: hexadecyltrimethylammonium bromide (CTAB), sodium anionic 1,4-bis(2-ethylhexyl)sulfosuccinate (AOT), perfluorooctane sulfonate triethylammonium (FK-1) were also tested and showed similar enhancement in wetting and overall cell performance to FC-134.

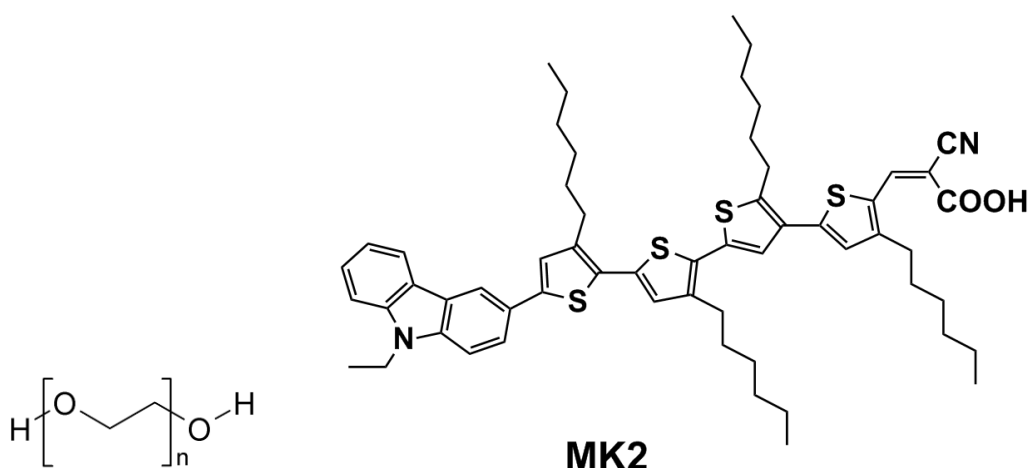


Fig. 3.10 Chemical structures of polyethylene glycol (left) and the MK2 dye (right)

In another example, polyethylene glycol (PEG 300) was added to a water electrolyte with cobalt^{(III)/(II)} tris(2,2'-bipyridine) used as the redox couple instead of the triiodide/iodide.¹⁰⁰ Upon addition of 1 wt% PEG 300, the J_{sc} of DSSCs with a relatively hydrophobic dye, MK2 (see Fig. 3.10), increased from 7.4 to 8.3 mA cm⁻². The authors attributed this to an improved wetting which is supported by the observed decrease in contact angle of the water electrolyte on MK2-sensitised film from 60° to 40° upon addition of PEG300. However, further addition of PEG300 led to mass transport problems for these aqueous electrolytes based on incident photon-to-current efficiency (IPCE), transient photocurrent and impedance spectroscopy measurements. In two other papers, Tween®20 and Triton X-100 (structures shown in Fig.

3.11) were added in water electrolyte and the authors suggested that both of these surfactants could improve wetting of dye-sensitised TiO₂ films.¹⁰¹ However, the J_{DL} or wetting had not been studied and discussed in detail in these two papers.

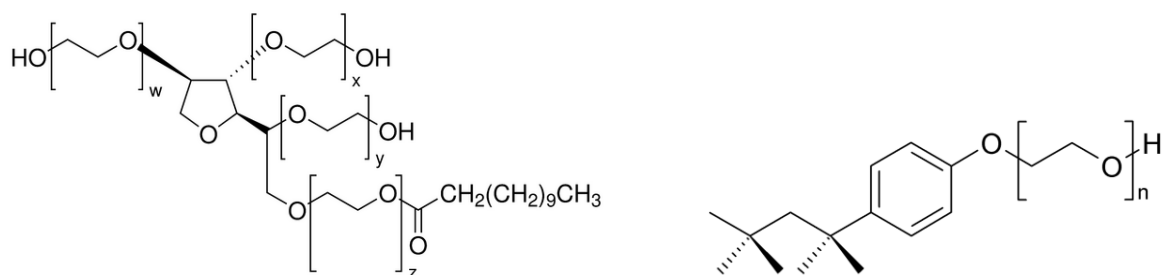


Fig. 3.11 Chemical structures of Tween®20 (left) and Triton X-100 (right).

Deposition of a thin layer of TiO₂ on dye-sensitised TiO₂ film by atomic layer deposition (ALD) has also been claimed to improve wetting by a water electrolytes and thus, cell performance.¹⁰² Nonetheless, the reported improvement in J_{DL} from ~ 4.9 to ~ 5.2 mA cm⁻² was only 6% which was relatively small and could just arise from variations in cell fabrication and measurements.

In the long run, the best solution to the wetting issue of water electrolyte is to use a dye which consists of many hydrophilic groups (e.g. -OH and ether groups) on the surface of the molecule and a strong anchor to TiO₂ (e.g. phosphonic acid). Two examples of this are the JK-259 and JK-262 dyes which structures are shown in Fig. 3.12.¹⁰³ Though the J_{DL} of the resulting DSSCs made with these two dyes were not reported or studied in this paper, the multiples side-chains with two to three units of ether group in these dyes should, in principle, enhance hydrophilicity and thus, the wetting of dye-sensitised TiO₂ pores by water electrolytes. However, due to the lack of such a dye available in our laboratory, a combination of dyes and cheno was used to sensitise the TiO₂ film in the project.

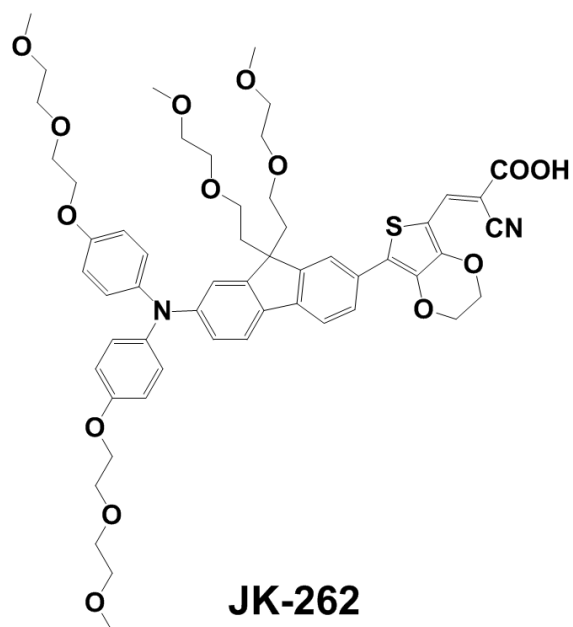
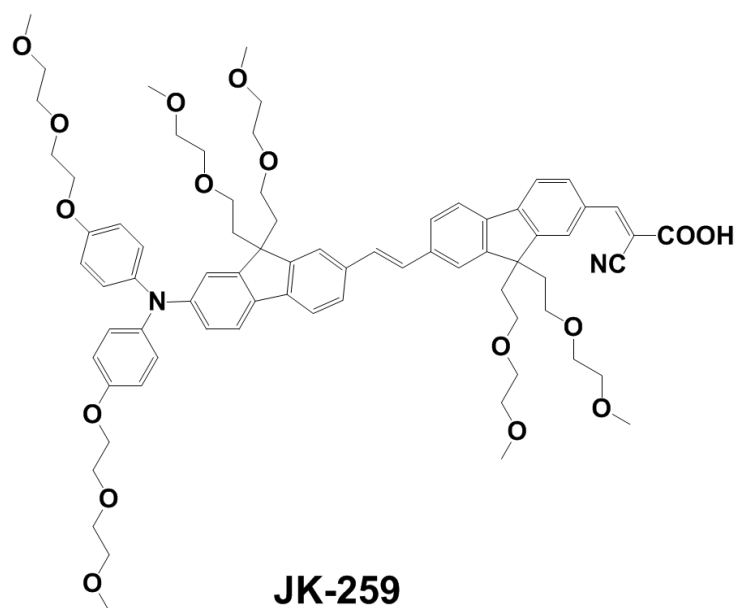


Fig. 3.12 Chemical structures of the JK-259 and JK-262 dyes.

3.1.5 Conclusion

Upon sensitisation of TiO_2 with Z907, the J_{DL} in symmetrical cells with water electrolyte has been found to decrease dramatically, presumably due to an incomplete wetting of TiO_2 pores. Co-adsorbing chenodeoxycholic acid with Z907 on TiO_2 improves the wetting and thus J_{DL} . However, even with the use of cheno, the J_{sc} of the water-based cell shown in Fig. 3.7 is still only $\sim 2.2 \text{ mA cm}^{-2}$ while an identical cell with an electrolyte in organic solvent can achieve $>10 \text{ mA cm}^{-2}$. Since the photocurrent of the cell is clearly no longer limited by diffusion of ions, it must then be limited by collection or injection. In order to improve the overall efficiency of DSSCs with water electrolyte, collection and injection will be examined and discussed in the next section.

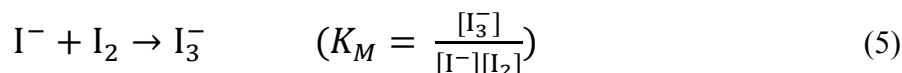
Chapter 3.2

Optimisation of Water-Based Dye-Sensitised Solar Cells

3.2.1 Introduction

In this section, recombination of photo-injected electrons in TiO₂ with the triiodide/iodide electrolytes in water-based DSSCs will first be examined. Recombination in DSSCs using 3-methoxypropionitrile (MPN) and propylene carbonate (PC) solvents has been recently studied in our research group.¹³ By independently changing uncomplexed iodine (free iodine) and triiodide concentration, the recombination lifetime of electrons was found to decrease with increasing free iodine concentration but independent of triiodide concentration. This shows that the main pathway for recombination is the reduction of free iodine rather than the reduction of triiodide.¹³

The concentration of the remaining uncomplexed iodine in the electrolyte at equilibrium (free iodine) can be described by equation (5) and (7);



$$I_2 = \frac{I_3^-}{K_M I^-} = \frac{(I_2^0 - I_2)}{K_M \{I^- - (I_2^0 - I_2)\}} \approx \frac{I_2^0}{K_M (I^- - I_2^0)} \quad (7),$$

where I_2^0 is the concentration of iodine added and the “[]” symbols of concentration in equation (7) have been dropped for readability so that for example I_2 and I_3^- are referred to concentration of iodine and triiodide respectively.

It is noted that the binding coefficient of I^- and I_2 is much lower in water ($K_M = \sim 1000$) compared to in organic solution (e.g. in acetonitrile, $K_M = 4 \times 10^6$; in MPN, $K_M > 10^5$).⁹⁴ According to equation (7), if the concentrations of iodide and iodine added are kept the same, the concentration of free iodine present in a water electrolyte is >100 and ~ 4000 times higher than that in MPN and ACN respectively. This suggests that the recombination rate in water-based DSSCs will be much faster than in organic solvent-based DSSCs. As a result, the collection efficiency in water-based systems could be significantly less than unity. To explore this possibility, several series of water-based DSSCs with varying iodine and iodide concentrations were fabricated and tested.

Apart from altering the composition of electrolyte, deposition of insulating metal oxide overlayers such as SiO₂, Al₂O₃ and ZrO₂ on TiO₂ surface, has also been shown to slow down recombination.¹⁰⁴ Ideally, all the surface of TiO₂ would be covered by the insulating overlayer

so that the photoinjected electron in TiO_2 can only recombine with free iodine by tunneling through it. This layer acts as a tunnel barrier which reduces the ‘per electron’ recombination rate. Given the same the same flux of electron injected under the same light intensity, the concentration of electron in the TiO_2 at V_{oc} will be higher in the cell with the overlayer. This results in a more negative Fermi level and a larger V_{oc} .^{104b} The overlayer needs to be thick enough to cause a significant decrease in recombination rate. However, too thick a layer would also reduce the injection of excited electron from dye molecule to TiO_2 . In a solid-state cell with copper thiocyanate as the hole transporting material, the application of one and two layers of Al_2O_3 was reported by O’Regan *et al.* to reduce the recombination rate by a factor of about 2 and 5 respectively, resulting in an increase in V_{oc} and fill factor.^{104b} This was attributed to a tunnel barrier effect caused by Al_2O_3 . In the case of liquid-state cells, a similar Al_2O_3 layer was reported to cause an in V_{oc} of up to 50 mV and a 35 % improvement in overall efficiency.^{104a, 104c} However, in both cases above, the photocurrent was reduced upon the application of Al_2O_3 layer. This is in agreement with another paper in which ultrafast infrared absorption measurements showed that one and two Al_2O_3 layers deposited on TiO_2 films decrease the rate of injection from dye to TiO_2 by a factor of 3.3 and 20 respectively.¹⁰⁵ It is noted that all the TiO_2 films in the ‘overlayer’ experiments mentioned above were not treated with TiCl_4 . Therefore, the additional beneficial effect of Al_2O_3 overlayers, if any, on top of TiCl_4 treatment on TiO_2 surface is still uncertain. Herein, the effect of Al_2O_3 overlayers on recombination and also the overall efficiency of water-based DSSCs (both with and without TiCl_4 treatment on TiO_2 films) will be presented.

Injection of excited electron from dye molecule to the conduction band of TiO_2 has also been investigated in this study. The excited-state lifetimes of ruthenium-based dyes have been reported to be lower in water than in MPN due to the higher dielectric constant of water.¹⁰⁶ Also, in my MSci project, it was found that the luminescence lifetime of TS4, a ruthenium-based dye with chemical structure shown in Fig. 3.13, on zirconia in 80 % water electrolyte shorter than that in MPN electrolyte by a factor of 2. This will in principle cause a reduction in injection efficiency. In fact, in the same project, the injection efficiency was found to decrease by 8 % going from MPN electrolyte to 80 % water electrolyte. In this work, hydriodic acid was added to the pure water electrolyte in order to lower the conduction band of TiO_2 and study the effect on injection.

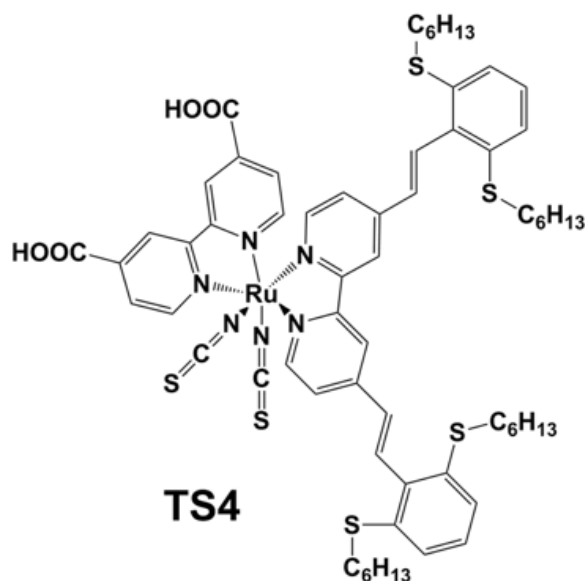


Fig. 3.13 Chemical structure of the TS4 dye.

3.2.2 Experimental Methods

In this chapter, in order to test generality of the results, one ruthenium-based dye, Z907 and an organic dye, D149, were used when studying the recombination in water electrolyte. Two other ruthenium-based dyes TG6 and N719 were used when optimising the overall efficiency of water-based DSSCs. Standard DSSCs were fabricated as described in Chapter 2. The transparent TiO₂ paste from DyeSol and the scattering TiO₂ paste from G24i were used in this chapter. The TiO₂ electrodes were sensitised either in a 0.3 mM Z907 and 15 mM cheno in TBA/ACN (1:1 by volume) for 20 hours, in 0.06 mM D149 and 0.24 M cheno in TBA/ACN (1:1) for 3 hours, 0.3 mM N719 and 30mM cheno in TBA/ACN (1:1 by volume) for 20 hours, or 0.3 mM TG6 and 30 mM cheno in chloroform/ethanol (1:1 by volume) for 20 hours. Current density vs. voltage (*JV*), transient photovoltage and photocurrent, and charge extraction at open and short circuit measurements were conducted as described in Chapter 2.

Preparation of Al₂O₃ Overlayer on TiO₂ Film:

A layer of nanoporous titania film was first deposited onto an FTO substrate in the same way as when fabricating DSSCs as described in Chapter 2. An Al₂O₃ overlayer was then deposited on titania film as reported.¹⁰⁴⁻¹⁰⁵ A coating solution of 0.15 M aluminium tri-*sec*-butoxide (Al(Bu^{sec}O)₃) in isopropanol was first prepared in the glovebox. All the following steps were performed in air. The TiO₂ films were first rinsed in distilled water and dried at 60 °C for 30 minutes. Before dipping the TiO₂ film the coating solution was heated to 60 °C. The films were then dipped in the coating solution in a closed vial and kept at 60 °C for a specific time period (15 min, 30 min, 45 min or 3 hours). Once taken out of the coating solution, the films

were rinsed by isopropanol before being hydrolysed in water. The films were heated at 400 °C for 30 minutes before uniformity test or cell fabrication.

Uniformity Test of Al₂O₃ Overlayer on TiO₂ by Catechol:

TiO₂ films with and without Al₂O₃ coatings were immersed in a saturated (~11 M) solution of 1,2-dihydroxybenzene (catechol) in ethanol for 2 hours.¹⁰⁵ It was observed that an equilibrium coverage of catechol on TiO₂ surface was reached after 2 hours. UV-vis spectra of these sensitised films were then taken as described in Chapter 2.

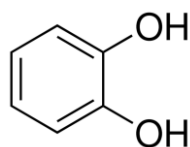


Fig. 3.14 Chemical structure of 1,2-dihydroxybenzene (catechol)

Synthesis of Guanidinium Iodide:

Guanidinium iodide (GuI) was prepared by adding the hydroiodic acid to guanidinium carbonate in a 1:1 mole ratio of iodide to guanidinium ions. The resulting solution was evaporated to dryness in air. The final product was recrystallised from a minimal volume of absolute ethanol.

3.2.3 Results

3.2.3.1 Varying Iodine Concentrations

Z907 DSSCs

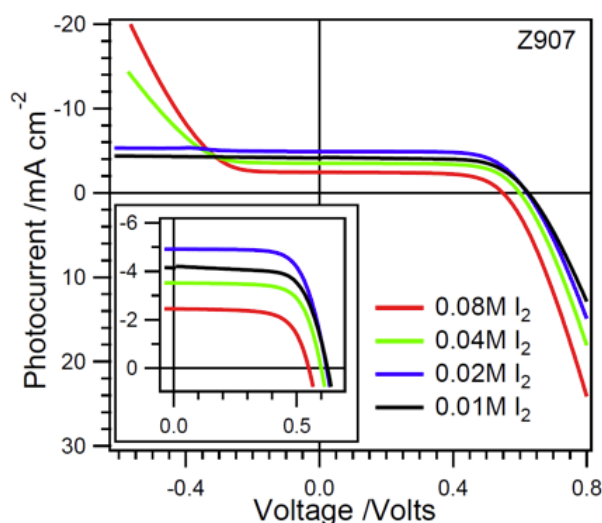


Fig. 3.15 One-sun JV curves of water-based Z907 DSSCs with varying added iodine concentration. (TiO₂ film: G24i paste, 8.9 μm ; Dye: Z907 1:100 cheno; Electrolytes: Water with 2 M NaI, 0.5 M GuSCN, \sim saturated cheno, and iodine as noted in legend.) [This figure is reproduced with the permission of the rights holder, The Royal Society of Chemistry.]⁹³

Table 3.1 One-sun performance of water electrolyte water-based Z907 DSSCs with varying added iodine concentration. Conditions as in Fig. 3.15. [This table is reproduced with the permission of the rights holder, The Royal Society of Chemistry.]⁹³

Iodine Concentration	$J_{sc}/\text{mA cm}^{-2}$	V_{oc}/V	Fill Factor	Efficiency/%	$J_{DL}/\text{mA cm}^{-2}$
80 mM	2.45	0.55	0.60	0.78	>20
40 mM	3.52	0.60	0.64	1.30	>15
20 mM	4.91	0.62	0.64	1.88	5.53
10 mM	4.09	0.62	0.70	1.78	4.44

Fig. 3.15 and Table 3.1 show the trend in J_{sc} 's and J_{DL} 's for a series of water-based Z907 cells consisting of different concentration of iodine added. It is worth to note that a relatively high iodide concentration of 2 M was used in all these cells in order to force the equilibrium of equation (5) to the right, resulting in a lower free iodine concentration. As expected, when the added iodine concentration decreases from 80 mM to 20 mM, the cell's J_{sc} increases by a factor of ~ 2 . This is correlated to an increased recombination lifetime in cells with lower added iodine concentration as shown in Fig. 3.16. The recombination lifetime of 40 and 20 mM iodine cells increases by a factor of ~ 2.5 and ~ 4 respectively, when compared to 80 mM iodine cells. The photocurrent and overall efficiency in this series of cells are optimum when the added iodine concentration is 20 mM as further reduction in concentration does not result in

the expected enhancement in J_{sc} . In fact, when the iodine concentration decreases further to 10 mM, J_{sc} actually decreases, even though the recombination lifetime is further lengthened. This is because the photocurrent in the cell with 10 mM added iodine is clearly limited by J_{DL} as shown in the reverse bias in its JV curve in Fig. 3.15. This observation is supported by the J_{sc} vs. bias light intensity graph in Fig. 3.17 where the J_{sc} of 10 mM iodine cells no longer increases linearly with light intensity above ~ 0.5 -sun illumination. The photocurrent of 20 mM iodine cells also becomes diffusion-limited above 1-sun illumination.

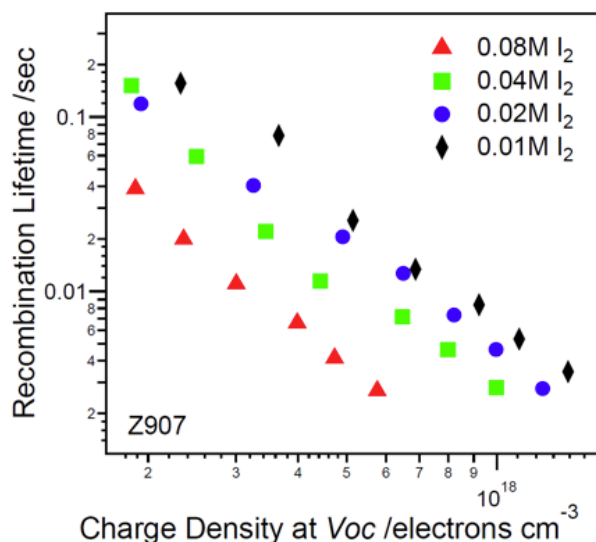


Fig. 3.16 Recombination lifetime vs. charge density of water-based Z907 DSSCs with varying added iodine concentration. Conditions as in Fig. 3.15. [This figure is reproduced with the permission of the rights holder, The Royal Society of Chemistry.]⁹³

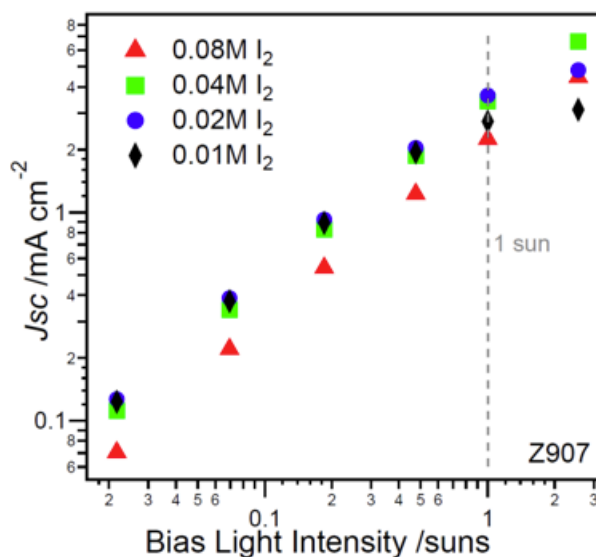


Fig. 3.17 J_{sc} vs. bias light intensity of water-based Z907 DSSCs with varying added iodine concentration. Conditions as in Fig. 3.15.

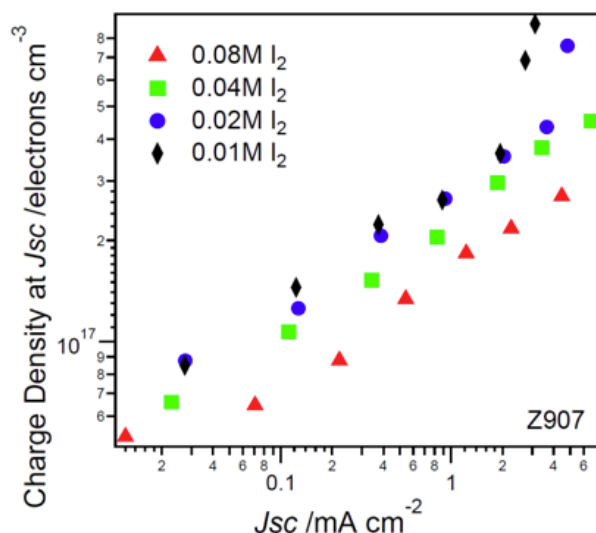


Fig. 3.18 Charge density vs. J_{sc} of water-based Z907 DSSCs with varying added iodine concentration. Conditions as in Fig. 3.15. [This figure is reproduced with the permission of the rights holder, The Royal Society of Chemistry.]⁹³

Fig. 3.18 shows the electron density in TiO_2 at short circuit as a function of J_{sc} . The higher than expected electron density at high light levels in 10 and 20 mM iodine cells, relative to 40 and 80 mM iodine cells, is another indication of limitation of triiodide diffusion. When the concentration gradient of triiodide across the cell reaches its maximum, the current density running through the cells will become diffusion-limited. At this point, the triiodide concentration reaches zero at the platinum counter electrode. If the light intensity is increased further, more electrons will be injected to the TiO_2 , reaching the external circuit. But these excess electrons cannot escape through the platinum counter electrode due to the depletion of triiodide there. This increases the resistance across the platinum/electrolyte interface. As a result, the electrons build up in the TiO_2 film, increasing the electron density as shown in Fig. 3.18. The electron density in the TiO_2 increases until the increase in recombination rate from TiO_2 to electrolyte plus the external current equals injection flux. The observed increase in electron density at short circuit under high light illumination provides a proof that the limiting species which causes J_{DL} is triiodide but not iodide. If the limiting species was iodide, its concentration near the TiO_2 film would become depleted and thus regeneration would decrease. As a result, recombination rate would increase and a decrease in the electron density in TiO_2 would be expected instead of an increase as observed in this experiment.

D149 DSSCs

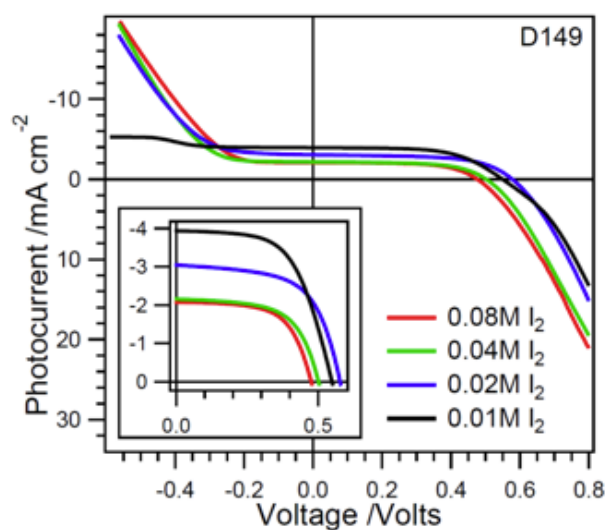


Fig. 3.19 One-sun JV curves of water-based D149 DSSCs with varying added iodine concentration. (TiO₂ film: DyeSol, 6.7 μm ; dye: D149 1:4 cheno; Electrolytes: Water with 2 M NaI, 0.1 M GuSCN, ~saturated cheno, and iodine as noted in the legend.) [This figure is reproduced with the permission of the rights holder, The Royal Society of Chemistry.]⁹³

Table 3.2 One-sun performance of water-based D149 DSSCs with varying added iodine concentration. Conditions as in Fig. 3.19. [This table is reproduced with the permission of the rights holder, The Royal Society of Chemistry.]⁹³

Iodine Concentration	$J_{sc}/\text{mA cm}^{-2}$	V_{oc}/V	Fill Factor	Efficiency/%	$J_{DL}/\text{mA cm}^{-2}$
80 mM	2.03	0.48	0.65	0.63	>20
40 mM	2.16	0.50	0.68	0.74	>20
20 mM	3.05	0.58	0.63	1.10	>20
10 mM	3.94	0.55	0.60	1.27	5.27

To test the generality of the results in Z907 cells series, a similar set of experiments were conducted on cells with a high performance organic dye, D149. Fig. 3.19 and Table 3.2 show the variation in photocurrent and J_{DL} for a series of D149 cells containing different added iodine concentration. Again, the J_{sc} increases with decreasing added iodine concentration. However, in this series, the trend in recombination lifetime shown in Fig. 3.20 is not as clear such that the 20 mM iodine cells unexpectedly show a faster recombination than 40 mM ones. Also, the photocurrents of both cells are clearly not diffusion-limited. Therefore, the invariance shown in Fig. 3.20 might suggest that recombination and J_{DL} are not the only factors influencing the photocurrent in this series of cells if it is not due to noise. However, further experiments are needed to confirm this. In any case, the general trend that an improvement in J_{sc} by reducing added concentration of iodine is still observed.

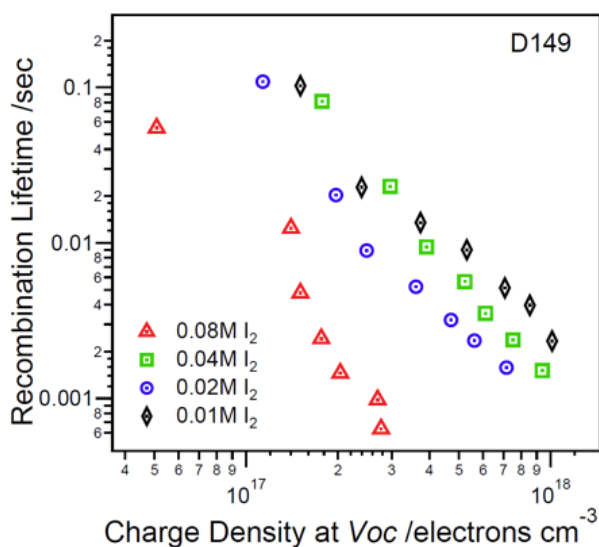


Fig. 3.20 Recombination lifetime vs. charge density of water-based D149 DSSCs with varying added iodine concentration. Conditions as in Fig. 3.19.

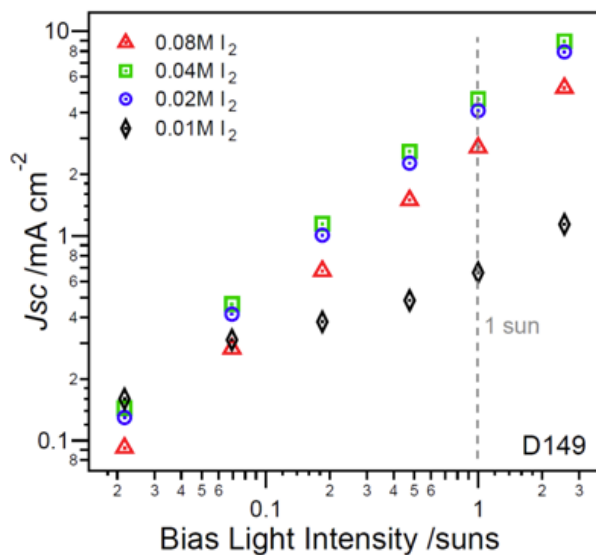


Fig. 3.21 J_{sc} vs. bias light intensity of water-based D149 DSSCs with varying added iodine concentration. Conditions as in Fig. 3.19. Measurements were taken 1 day after fabrication.

The optimum added iodine concentration in this series seems to be 10 mM as it is clear that further reduction in concentration would cause the J_{sc} to be limited by J_{DL} . But it was observed that the D149 cells with only 10 mM iodine tend to be unstable as the J_{DL} may decrease and limit J_{sc} over time as shown in Fig. 3.21. Therefore, an iodine concentration of 20 mM was used in most of the following experiments.

3.2.3.2 Varying Iodide Concentrations

Z907 DSSCs

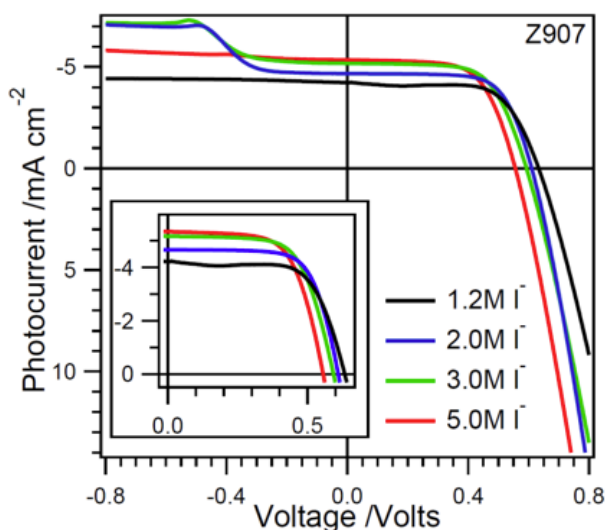


Fig. 3.22 One-sun JV curves of water-based Z907 DSSCs with varying sodium iodide concentration. (TiO₂ film: G24i paste, 8.1 μm ; Dye: Z907 1:100 cheno; Electrolytes: Water with 20 mM iodine, 0.5 M GuSCN, ~saturated cheno, and sodium iodide as noted in legend.)

Table 3.3 One-sun performance of water-based Z907 DSSCs with varying sodium iodide concentration. Conditions as in Fig. 3.22.

Iodide Concentration	$J_{sc}/\text{mA cm}^{-2}$	V_{oc}/V	Fill Factor	Efficiency/%	$J_{DL}/\text{mA cm}^{-2}$
1.2 M	4.22	0.63	0.62	1.64	4.22
2.0 M	4.67	0.61	0.64	1.82	7.03
3.0 M	5.17	0.59	0.62	1.89	7.16
5.0 M	5.34	0.56	0.61	1.82	5.76

If free iodine is responsible for the loss in collection efficiency in water electrolytes, increasing iodide concentration should also increase the photocurrent according to equation (7). Fig. 3.22 and Table 3.3 show the trend in photocurrent and J_{DL} for a series of Z907 cells containing different sodium iodide concentration. As iodide concentration decreases from 5.0 M to 2.0 M, the J_{sc} generally decreases. Even though the J_{sc} of 1.2 M iodide cell follows this trend and shows a further reduction in J_{sc} , the photocurrent is clearly limited by J_{DL} as shown in the reverse bias of its JV . In fact, the 1.2 M iodide cell does show the lowest J_{sc} in this series of cells at lower light levels where photocurrent is not limited. It is also noted that the J_{DL} does not increase as the iodide concentration increases from 1.2 M to 5.0 M, which gives an implication that photocurrent is not limited by diffusion of iodide. It is noted that the J_{DL} 's of these electrolytes are similar because the concentration of triiodide is essentially constant.

D149 DSSCs

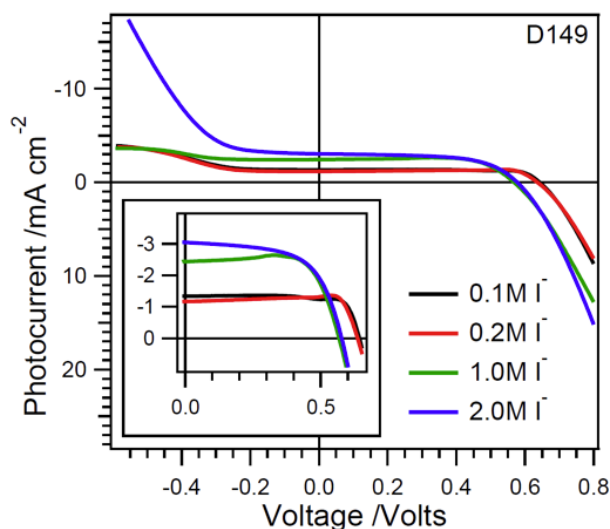


Fig. 3.23 One-sun JV curves of water-based D149 DSSCs with varying sodium iodide concentration. (TiO₂ film: DyeSol, 6.8 μm ; Dye: D149 1:4 cheno; Electrolytes: Water with 0.02 M iodine, 0.1 M GuSCN, \sim saturated cheno, with iodide as noted in the legend.) [This figure is reproduced with the permission of the rights holder, The Royal Society of Chemistry.]⁹³

Table 3.4 One-sun JV performance of water-based D149 DSSCs with varying sodium iodide concentration. Conditions as in Fig. 3.23. [This table is reproduced with the permission of the rights holder, The Royal Society of Chemistry.]⁹³

Iodide Concentration	$J_{sc}/$ mA cm^{-2}	$V_{oc}/$ V	Fill Factor	Efficiency/ %	$J_{DL}/$ mA cm^{-2}
0.1 M	1.34	0.63	0.70	0.59	3.90
0.2 M	1.17	0.62	0.70	0.58	3.75
1.0 M	2.44	0.55	0.66	0.89	3.63
2.0 M	3.05	0.58	0.63	1.10	>20

A similar series of cells with D149, this time with lower iodide concentrations, were tested for generality of the results above. Fig. 3.23 and Table 3.4 show the variation in photocurrent and J_{DL} for D149 cells with different sodium iodide concentration. Again, the photocurrent generally increases with increasing iodide concentration. While the J_{DL} remains constant when iodide concentration increases from 0.1 M to 1.0 M, the J_{DL} of 2 M iodide cell increases by at least a factor of 5 to $>20 \text{ mA cm}^{-2}$. The reason behind this is not clear. We propose that even in the presence of cheno, the wetting of TiO₂ pores is still not good enough and high concentration of sodium iodide also improves wetting. The reason that the J_{DL} in the D149 cells with 20 mM iodine and 2.0 M iodide is significantly higher than similar Z907 cells may be due to a lower cheno surface concentration on Z907-sensitised films. Since each Z907 dye molecule has two carboxylate groups while D149 only has one (see Fig. 1.5 and 1.13), the adsorption of Z907 on TiO₂ is stronger, limiting the surface for the adsorption of cheno.

It is noted that the low photocurrent observed in the D149 cells with low iodide concentrations (0.1 and 0.2 M) might partly be caused by a low regeneration efficiency. Though it has been reported that DSSCs with the D149 dye show essentially no loss in J_{sc} in 0.2 M iodide solution in MPN,^{11a} the regeneration of D149 in water electrolyte has not been measured in this study.

3.2.3.3 Al₂O₃ Overlayer

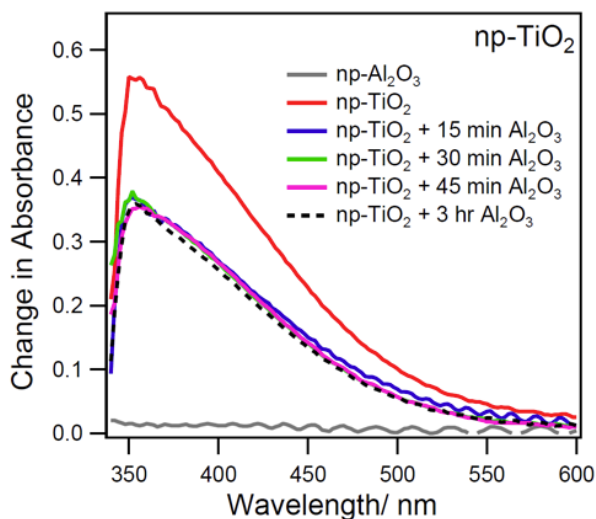


Fig. 3.24 Absorption spectra showing the change in absorbance of a catechol-sensitised nanoporous (np) Al₂O₃ control film, and np-TiO₂ films treated in Al(Bu^sO)₃ solution for 0, 15, 30, 45 min and 3 hours and then sensitised in catechol solution. All data have been subtracted by the absorbance before sensitisation. (np-Al₂O₃ film: 4 μm; np-TiO₂ film: DyeSol, 7 μm)

Another possible way to reduce recombination is to coat a thin insulating layer of Al₂O₃ on the surface of TiO₂ before sensitisation. This can be achieved by dipping the TiO₂ films in a precursor solution of Al(Bu^sO)₃, following by hydrolysis in water. Before examining the effect of such a coating on cell performance, the coverage of TiO₂ by Al₂O₃ was first tested by using catechol. Fig. 3.24 shows the change in absorption spectra of TiO₂ films which were not treated by TiCl₄. These films were instead treated in the Al₂O₃ precursor solution for different periods of time after sensitisation in catechol solution. A similar Al₂O₃ film without undergoing any Al₂O₃ treatment was also tested as a control. It has been reported that catechol adsorbed on TiO₂ nanoparticle forms an interfacial charge transfer complex and shows a charge transfer band around 370–390 nm.^{105, 107} On the other hand, catechol on Al₂O₃ shows no peaks within the visible range.¹⁰⁵ Therefore, the absorbance of the peak corresponding to catechol on TiO₂ (370–390 nm) can be used to determine the fraction of exposed TiO₂ surface and thus the coverage Al₂O₃ on TiO₂ surface.

Fig. 3.24 shows that treating TiO₂ film in alumina precursor solution for 15 min results in a ~20 % reduction in the peak at around 365 nm, which is in good agreement with the 25 % reduction reported by Guo *et al.*¹⁰⁵ This indicates an incomplete coverage of Al₂O₃ on TiO₂ surface. It was also observed that treating TiO₂ film in the precursor solution for a longer period of time (up to 3 hours) does not enhance the alumina coverage, when compared to the 15 min treatment. Therefore, in our first test on cell performance below, the 15 min treatment was employed.

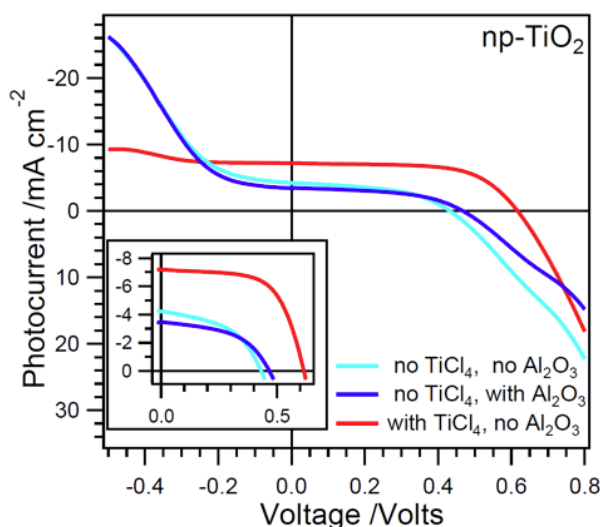


Fig. 3.25 One-sun *JV* curves of water-based D149 DSSCs with TiO₂ film treated in different ways as noted in the legend. (TiO₂ film: G24i Paste, 8.5 μm; Dye: D149 1:4 cheno; Al₂O₃ treatment: 15 min; Electrolytes: Water with 2 M NaI, 0.02M iodine, 0.5 M GuSCN, ~saturated cheno)

Table 3.5 One-sun performance of water-based D149 DSSCs with TiO₂ film treated in different ways. Conditions as in Fig. 3.25.

Treatments	<i>Jsc</i> / mA cm ⁻²	<i>Voc</i> / V	Fill Factor	Efficiency/ %
no TiCl ₄ , no Al ₂ O ₃	4.17	0.43	0.49	0.88
no TiCl ₄ , with Al ₂ O ₃	3.39	0.47	0.54	0.86
with TiCl ₄ , no Al ₂ O ₃	7.16	0.61	0.62	2.71

Fig. 3.25 shows the *JV*'s of water-based DSSCs with TiO₂ treated either by Al₂O₃ or TiCl₄. A cell which TiO₂ was not treated by Al₂O₃ nor TiCl₄ was also fabricated as a control. It is shown that a 15 min Al₂O₃ treatment on TiO₂ film increases the *Voc* and fill factor of the cells by 40 mV and ~10 % respectively but it also reduces the *Jsc* by ~20 %. The beneficial effect of increased *Voc* and fill factor is completely cancelled out by the drop in *Jsc*, resulting in no improvement in overall efficiency. The enhanced *Voc* and fill factor can be explained by a reduction in recombination rate¹⁰⁴ while the decrease in *Jsc* is probably caused by a decrease in injection rate¹⁰⁵ as reported in literature. When compared to Al₂O₃ treatment, TiCl₄

treatment shows much more obvious improvement to the cell performance. It increases the V_{oc} and fill factor by 180 mV and $\sim 25\%$ respectively while the J_{sc} is increased by $\sim 72\%$, resulting in ~ 2.5 fold increase in overall efficiency. The beneficial effect of $TiCl_4$ treatment on cell performance can be attributed to an increase in injection caused by a downward shift in TiO_2 conduction band and a decrease in recombination rate as previously reported by O'Regan *et al.*^{104b} The results here clearly show that the direct replacement of $TiCl_4$ by Al_2O_3 treatment does not bring any improvement to cell performance. Therefore, Al_2O_3 treatment was then conducted on TiO_2 films which had already been treated by $TiCl_4$ beforehand.

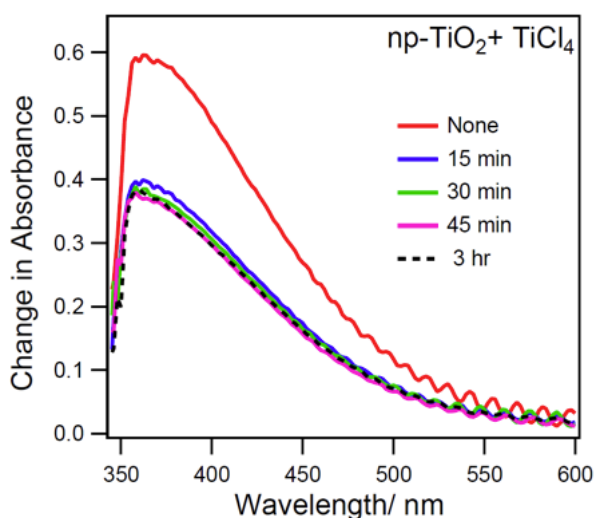


Fig. 3.26 Absorption spectra showing the change in absorbance of np- TiO_2 films, treated by $TiCl_4$, then treated in $Al(Bu^sO)_3$ solution for 0, 15, 30, 45 min and 3 hours and finally sensitised in catechol solution. All data have been subtracted by the absorbance before sensitisation. (TiO_2 film: DyeSol, 7 μm)

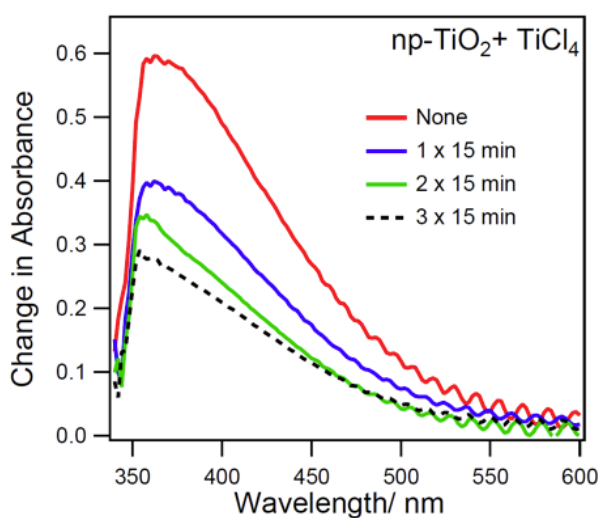


Fig. 3.27 Absorption spectra showing the change in absorbance of np- TiO_2 films, treated by $TiCl_4$, then treated in $Al(Bu^sO)_3$ solution for 15 min for 1, 2 and 3 times and finally sensitised in catechol solution. All data have been subtracted by the absorbance before sensitisation. (TiO_2 film: DyeSol, 7 μm)

Fig. 3.26 shows the change in absorption spectra of TiO₂ films, which had been treated by TiCl₄, treated in the Al₂O₃ precursor solution for different periods of time before sensitisation in catechol solution. As expected, these results are similar to those shown in Fig. 3.24 where the TiO₂ films were not treated by TiCl₄. A 15 min treatment on TiO₂ reduces the peak absorbance of the charge transfer band at around 365 nm by ~33 %. Treating the TiO₂ films in the precursor solution for longer time does not change in the peak absorbance. Therefore, the coverage of Al₂O₃ is still incomplete. In order to enhance the coverage, other than lengthening the time of Al₂O₃ treatment, the TiO₂ films were also treated in the Al₂O₃ precursor solution for different number of times. Fig. 3.27 shows that treating the TiO₂ films in the Al(Bu^sO)₃ solution for 2 and 3 times decreases the peak absorbance by 43 % and 52 % respectively. The results are in good agreement with those reported by Guo *et al.*¹⁰⁵ It means that even after 3 cycles of 15 min Al₂O₃ treatment, the coverage of Al₂O₃ on TiO₂ is still limited to 50 %. In other words, the fraction of exposed TiO₂ surface is still as high as ~50 %. Nevertheless, noticing the encouraging improvement in overall efficiency of DSSCs brought by Al₂O₃ treatment reported previously,^{104a, b} water-based DSSCs with Al₂O₃-treated TiO₂ films were fabricated and tested.

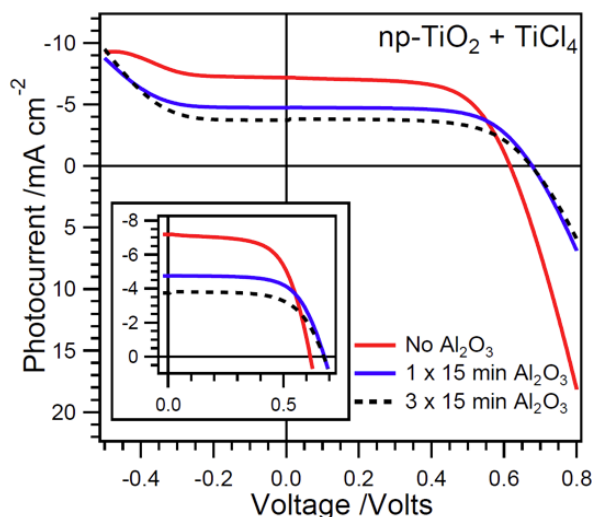


Fig. 3.28 One-sun JV curves of water-based D149 DSSCs with TiO_2 films (all with TiCl_4) treated in $\text{Al}(\text{Bu}^s\text{O})_3$ solution for 0, 1 and 3 times. (TiO_2 film: G24i Paste, $8.5 \mu\text{m}$; Dye: D149 1:4 cheno; Each Al_2O_3 treatment: 15 min; Electrolytes: Water with 2 M NaI, 0.02 M iodine, 0.5 M GuSCN and ~saturated cheno)

Table 3.6 One-sun performance of D149-based DSSCs with TiO_2 films (all with TiCl_4) treated in $\text{Al}(\text{Bu}^s\text{O})_3$ precursor solution for 0, 1 and 3 times. Conditions as in Fig. 3.28.

No. of Cycles of Al_2O_3 Treatments	$J_{sc}/$ mA cm^{-2}	$V_{oc}/$ V	Fill Factor	Efficiency/ %
None	7.16	0.61	0.62	2.71
1 x 15 min	4.72	0.67	0.66	2.09
3 x 15 min	3.74	0.67	0.69	1.73

Fig. 3.28 and Table 3.6 show the JV data of water-based DSSCs with TiCl_4 -treated TiO_2 film dipped in Al_2O_3 precursor solution for different number of times. Similar to the results shown in Fig. 3.25 and Table 3.5 where TiO_2 film were not TiCl_4 -treated, one layer of Al_2O_3 increases the V_{oc} and fill factor by 60 mV and 6 % respectively but decreases the J_{sc} by 34 %. Even though treating the TiO_2 film in Al_2O_3 precursor solution for 3 times increases the coverage of Al_2O_3 on TiO_2 surface as mentioned before, the V_{oc} of the cells remains constant while the J_{sc} is reduced further by another 20 %, when compared to cells with one Al_2O_3 layer.

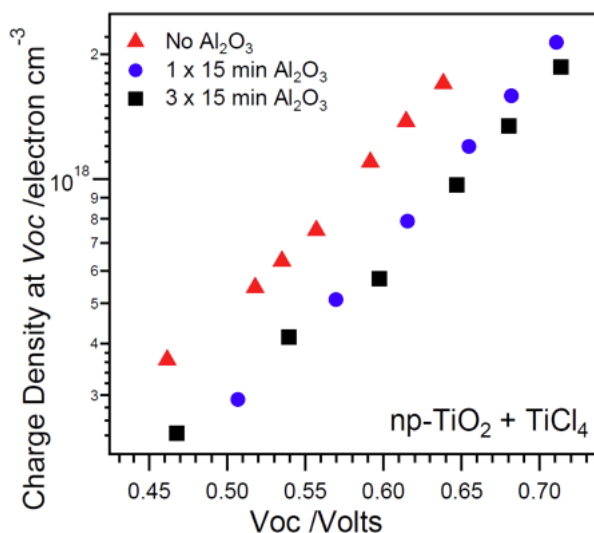


Fig. 3.29 Charge density vs. V_{oc} of water-based D149 DSSCs with TiO_2 films (all with $TiCl_4$) treated in $Al(Bu^sO)_3$ solution for 0, 1 and 3 times. Conditions as in Fig. 3.28.

In order to study the change in cell performance caused by the deposition of Al_2O_3 , the charge density versus V_{oc} has been measured for these cells. Fig. 3.29 shows that one layer of Al_2O_3 coating causes a strong shift in the charge density versus V_{oc} curve. Three cycles of Al_2O_3 treatment does not cause any further change to the curve relative to one cycle. The shift of the curve can first be interpreted as a rightward shift along the V_{oc} by 60 mV, which is most likely the result of a shift of the TiO_2 conduction band edge upward away from the iodine/iodide potential. This is termed the ‘surface dipole’ effect.^{104b} The deposition of Al_2O_3 coating changes the charge distribution across the TiO_2 /electrolyte interface when compared to the TiO_2 films without coating. If this treatment results in more negative charge closer to TiO_2 surface, with the surface dipole pointing more in the direction of the electrolyte, the resulting electric field will shift the conduction of TiO_2 away from the iodine/iodide potential. This results in an increase in band offset between TiO_2 and the electrolyte and thus, an increase in V_{oc} . Alternatively, the shift in charge density versus V_{oc} curve could also be viewed as a 2-fold decrease in charge density at each V_{oc} as described in literature.⁸⁹ Such a large decrease should decrease the charge density at short circuit and increase the transport rate. Nevertheless, Fig. 3.30 and 3.31 show that there is, in fact, no change in charge density at short circuit and transport lifetime in the cells with and without Al_2O_3 treatment. Therefore, an upward shift of the conduction band of TiO_2 caused by Al_2O_3 treatment on TiO_2 films is the more likely explanation for the shift of the charge density versus V_{oc} curve. In fact, this 60 mV shift observed in Fig. 3.29 is in very good agreement with the 60 mV increase in V_{oc} of the cells with one and three cycles of Al_2O_3 treatment shown in their JV 's.

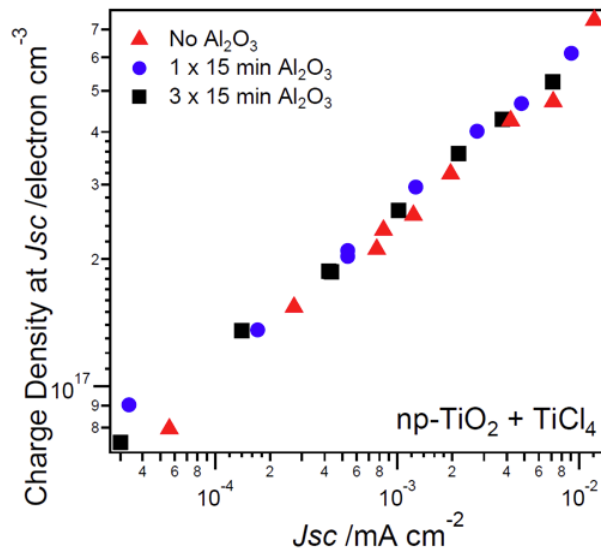


Fig. 3.30 Charge density vs. J_{sc} of D149-based DSSCs with TiO₂ films (all with TiCl₄) treated in Al(Bu^sO)₃ solution for 0, 1 and 3 times. Conditions as in Fig. 3.28.

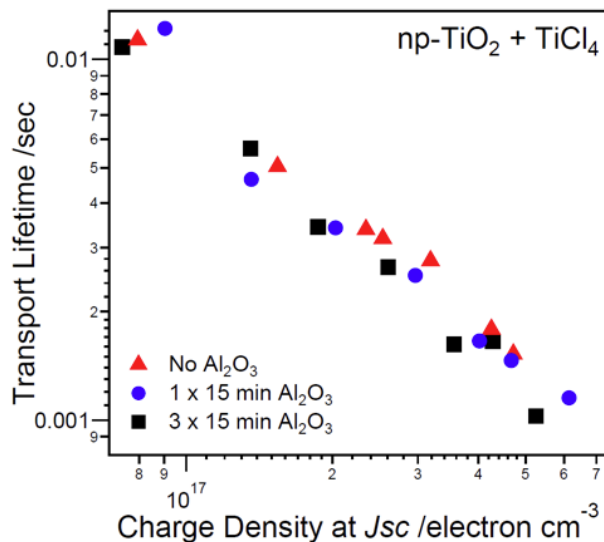
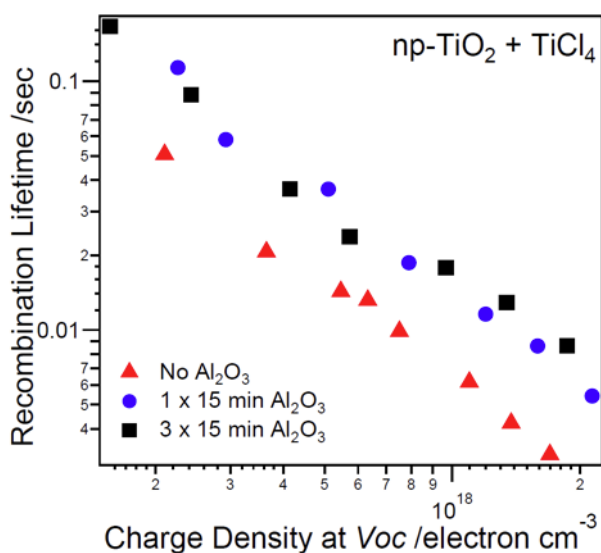


Fig. 3.31 Transport lifetime vs. charge density of D149-based DSSCs with TiO₂ films (all with TiCl₄) treated in Al(Bu^sO)₃ solution for 0, 1 and 3 times. Conditions as in Fig. 3.28.

From the results above, it seems that the increase in V_{oc} is mainly contributed by the upward shift in the conduction band of TiO₂. However, part of the 60 mV shift shown in Fig. 3.29 could also be attributed to random variations. Therefore, recombination lifetimes of the cells, which can also cause a change in V_{oc} , were measured. Fig. 3.32 shows the recombination lifetimes versus charge density at V_{oc} of these cells. It is clear that the Al₂O₃ coating does not change the slope of the curve. This suggests that the underlying mechanism of recombination does not change in the presence of Al₂O₃ coating. One layer of Al₂O₃ coating increases the recombination lifetime by a factor of 2 when compared to cells without coating. This indicates that Al₂O₃ provides the expected tunnel barrier effect to reduce recombination rate. Similar

increase in recombination lifetime caused by one layer of Al_2O_3 has also been observed by O'Regan *et al.* in solid-state dye cells where the TiO_2 used were P25 and colloidal TiO_2 .^{104b} In the same paper, it was reported that the application of 2 layers of Al_2O_3 coating increases recombination lifetime further by a factor of 2.7, when compared to cells with only one layer of coating. Nevertheless, in this experiment, the application of three layers of Al_2O_3 coating does not change the recombination relative to one coating. In literature, the increase in V_{oc} caused by the application of Al_2O_3 has been attributed mainly or solely to reduction in rate of recombination.^{104a, b, 108} However, the dependence of the magnitude of the V_{oc} change on the change in recombination rate varies in different systems. For example, it has been reported that a 2-fold reduction in recombination rate caused by a layer of Al_2O_3 increases the V_{oc} by 130 mV when P25 TiO_2 was used. But an increase in V_{oc} of only 50 mV was observed in a series of identical cells made with colloidal TiO_2 where the reduction in recombination rate was also 2 fold.^{104b} Therefore, it seems hard to quantify by what fraction of the 60 mV increase in V_{oc} is caused by the 2-fold decrease in recombination rate in this experiment. More experiments are needed to find out the correlation between the decrease in recombination rate caused by Al_2O_3 coating and the resulting increase in V_{oc} . In any case, even though the expected tunnel barrier effect of Al_2O_3 coating was observed, it does not result in an improvement in overall efficiency and in fact, the efficiency is decreased.



3.2.3.4 Injection

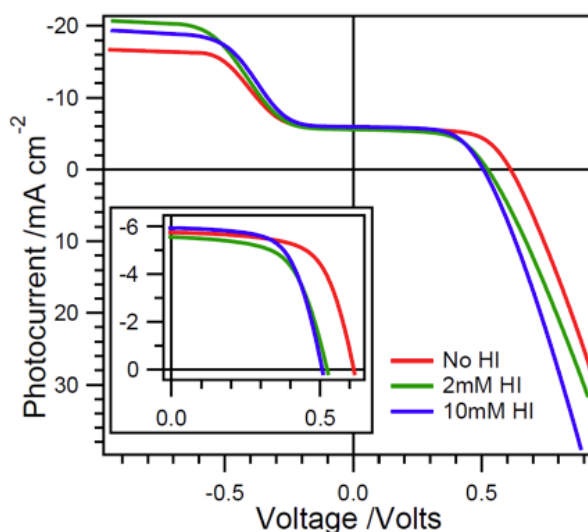


Fig. 3.33 One-sun JV curves of water-based D149 DSSCs with varying HI concentration. (TiO₂ film: G24i Paste, 8.9 μm ; Dye: D149 1:4 cheno; Electrolytes: Water with 2 M NaI, 0.02 M iodine, 0.5 M GuSCN, ~saturated cheno, with HI as noted in the legend)

Table 3.7 One-sun JV performance of water-based D149 DSSCs with varying HI concentration. Conditions as in Fig. 3.33.

HI Concentration	$J_{sc}/$ mA cm^{-2}	$V_{oc}/$ V	Fill Factor	Efficiency/ %
None	5.75	0.61	0.63	2.21
2 mM	5.56	0.52	0.57	1.65
10 mM	5.93	0.51	0.61	1.84

Injection of electrons from dye to TiO₂ conduction band has also been examined. Fig. 3.33 and Table 3.7 show the variation in J_{sc} 's and V_{oc} 's of a series of D149 cells with different hydriodic acid concentration. When 2 and 10 mM HI was added, the V_{oc} drops from 0.61 V to 0.52 and 0.51 V respectively. This clearly indicates the lowering of the conduction band edge of TiO₂. In other words, the difference in energy of the dye excited states relative to the conduction band of TiO₂ is increased. As a result, the driving force and the rate constant of injection of excited electron from dye to TiO₂ is increased. If photocurrent of water-based DSSCs was limited by injection, such a change in energetics of TiO₂ conduction band would result in an increase in J_{sc} . However, in this experiment, the cells essentially show no change in J_{sc} . This suggests the loss in injection does not contribute significantly to the loss in photocurrent in DSSCs with water-based electrolytes.

3.2.3.5 Optimising Efficiency

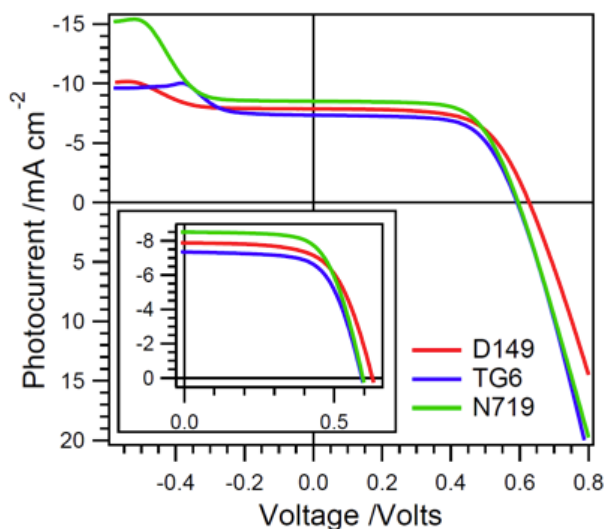


Fig. 3.34 One-sun JV curves of three efficient water-based DSSCs. Compositions of these cells are shown in Table 3.8. [This figure is reproduced with the permission of the rights holder, The Royal Society of Chemistry.]⁹³

Table 3.8 Compositions and one-sun performance of three efficient pure water DSSCs. [This table is reproduced with the permission of the rights holder, The Royal Society of Chemistry.]⁹³

TiO ₂ (Thickness)	Dye Solution	Electrolyte Composition	$J_{sc}/$ mA cm ⁻²	$V_{oc}/$ V	Fill Factor	Efficiency/ %
G24i (8.3 μm)	D149 1:4 Cheno	2 M NaI, 20 mM I ₂ , 0.5 M GuSCN, Cheno	7.87	0.62	0.62	3.00
G24i (8.9 μm)	TG6 1:100 Cheno	2 M NaI, 20 mM I ₂ , 0.5 M GuSCN, Cheno	7.34	0.59	0.63	2.64
G24i (4.4 μm)	N719 1:100 Cheno	2 M NaI, 20 mM I ₂ , 1 M GuSCN, Cheno, HNO ₃ (pH3)	8.50	0.59	0.63	3.08

In order to increase the photocurrent generated from DSSCs with pure water electrolytes, the type of TiO₂ paste and the thickness of the TiO₂ film have been optimised. Fig. 3.34 and Table 3.8 show the results for three efficient cells, each with a different dye. At the beginning of this study on water-based DSSCs, hydrophobic dyes such as Z907 and D149 were employed in order to avoid the dissolution of dye in water electrolyte. It is later found that water electrolyte can also work with the more hydrophilic N719 dye to give a high efficiency of 3 % with the addition of correct concentration of acid. The need to incorporate cheno in water electrolyte even for cell with the N719 dye suggests wetting of TiO₂ pores is still not perfect. The plateaus of current density in far reverse bias of the JV 's of D149 and TG6 cells show that their photocurrents are already in approximate balance with the J_{DL} . This indicates that further improvement in wetting is required to increase the J_{sc} 's of these cells.

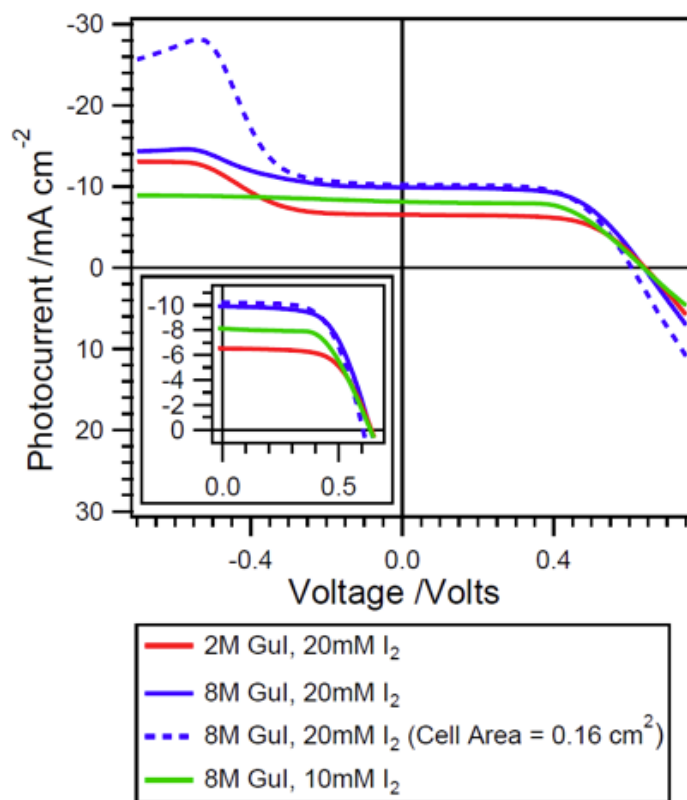


Fig. 3.35 One-sun JV curves of water-based D149 DSSCs with varying guanidinium iodide and iodine concentrations. (TiO₂ film: G24i Paste, 4.6 μm ; Dye: D149 1:4 cheno; Electrolytes: Water with 0.5 M GuSCN, ~saturated cheno, with guanidinium iodide and iodine as noted in the legend; Active area: 1 cm^2 unless otherwise specified)

Table 3.9 One-sun JV performance of water-based D149 DSSCs with varying guanidinium iodide and iodine concentrations, and active area. Conditions as in Fig. 3.35.

GuI Concentration	Iodine Concentration	Cell Area/ cm^2	$J_{sc}/$ mA cm^{-2}	$V_{oc}/$ V	Fill Factor	Efficiency/ %
2 M	20 mM	1.0	6.25	0.64	0.63	2.64
8 M	20 mM	1.0	9.92	0.63	0.62	3.85
8 M	20 mM	0.16	10.02	0.61	0.67	4.06
8 M	10 mM	1.0	7.82	0.63	0.61	3.00

Noticing the positive effect of guanidinium ion on wetting as mentioned in Chapter 3.1 and iodide on collection efficiency, guanidinium iodide (GuI), which is more water soluble than sodium iodide, was used to replace sodium iodide in electrolyte. Fig. 3.35 and Table 3.9 show the results of water-based DSSCs with varying guanidinium iodide and iodine concentrations. A guanidinium iodide concentration as high as 8 M and an iodine concentration as low as 10 mM were tested in order to force the equilibrium of equation (5) to the right, reducing the free iodine concentration as much as possible. It is interesting to find that the V_{oc} 's of all these cells are still about 100 mV smaller than the standard DSSCs with MPN

electrolyte. Also, in the cell with 8 M guanidinium iodide and 10 mM iodine, the photocurrent at 1-sun illumination is clearly limited by J_{DL} as shown in the reverse bias of its JV in Fig. 3.35 and 3.36.

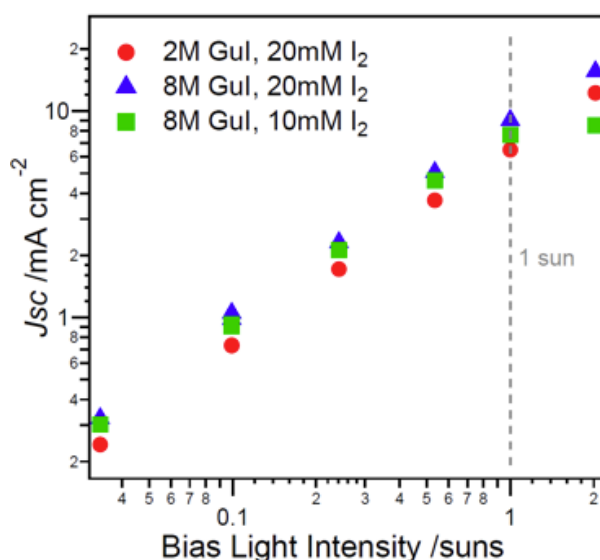


Fig. 3.36 J_{sc} vs. light intensity of water-based D149 DSSCs with varying guanidinium iodide and iodine concentrations. (TiO₂ film: G24i Paste, 4.6 μm ; Dye: D149 1:4 cheno; Electrolytes: Water with 0.5 M GuSCN, ~saturated cheno, with guanidinium iodide and iodine as noted in the legend)

When comparing the two 1 cm² cells with 20 mM iodine, the one with 8 M guanidinium iodide gives ~50 % higher J_{sc} , which is caused by a ~2-fold reduction in recombination rate as shown in Fig. 3.37. The photocurrent achieved in this optimum cell with 8 M guanidinium iodide is even higher than that of the D149 cells in Table 3.8. This enhancement in J_{sc} is caused by a combination of improved wetting of TiO₂ pores and increased collection efficiency due to the slower recombination.

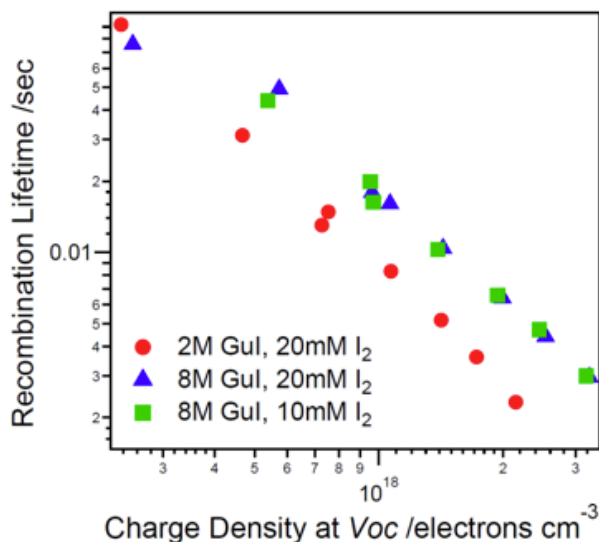


Fig. 3.37 Recombination lifetime vs. charge density of water-based D149 DSSCs with varying guanidinium iodide and iodine concentrations. (TiO₂ film: G24i Paste, 4.6 μm ; Dye: D149 1:4 cheno; Electrolytes: Water with 0.5 M GuSCN, ~saturated cheno, with guanidinium iodide and iodine as noted in the legend).

One would expect the V_{oc} to increase when recombination rate is reduced. However, in this case, the V_{oc} of the 8 M guanidinium iodide, 20 mM iodine cell shows no change in V_{oc} when compared to the D149 cell in Table 3.8. This is because the positive effect of reduced recombination on V_{oc} is cancelled out by the negative shift of redox potential of the electrolyte versus normal hydrogen electrode (NHE). According to the Nernst equation (9), the addition of more iodide makes the redox potential of the electrolyte more negative. Since V_{oc} is the potential difference between the Fermi level of the TiO₂ and the redox potential of the electrolyte, a negative shift in iodine/iodide potential results in a reduction in V_{oc} .



$$E = E^\ominus - \frac{RT}{nF} \ln\left(\frac{[\text{I}^-]^3}{[\text{I}_3^-]}\right) \quad (9),$$

where E and E^\ominus are potential and standard potential of the redox couple respectively; $E^\ominus = -\Delta G^\ominus/nF$; R , T , n and F are universal gas constant (8.31 J K⁻¹ mol⁻¹), temperature, number of moles of electrons transferred (in the case of iodine/iodide, $n = 2$) and Faraday constant (96485 C mol⁻¹) respectively.

Finally in order to optimised the overall efficiency further by improving fill factor, a cell with smaller area (0.16 cm²) was fabricated in order to reduce series resistance. Note that the saturation current shown in the reverse bias cannot be viewed as an improvement in wetting in this case. It is probably caused the larger fraction of exposed FTO without TiO₂ around the

edge of this smaller cell. An overall efficiency of 4 % is achieved which is 5 times higher than the best cells reported previously using an electrolyte where water is the only liquid component.⁴³

3.2.4 Discussion

In the experiment comparing water-based DSSCs with different iodine concentration, it is clear that the iodine concentration is critical in the two important factors affecting the cell performance. They are the diffusion-limited current density (J_{DL}) and rate of recombination. Too low an iodine concentration will reduce the J_{DL} and thus, the J_{sc} of the cell while too high a concentration will increase the rate of recombination, decreasing cell performance. Therefore, a balance between these two factors has to be found in order to optimise the overall cell efficiency. The optimum iodine concentration in water-based DSSCs found in this study is 20 mM. Nevertheless, even at such a low concentration, due to the relatively low binding constant of iodine with iodide in water (when compared to organic solvents such as ACN and MPN), there is still a high concentration of free iodine at equilibrium. This results in a high rate of recombination as shown in Fig. A.1 in Appendix.

In principle, increasing the iodide concentration pushes the equilibrium of the equation (5) to the right, resulting in a lower concentration of free iodine. In fact, the recombination rate was successfully reduced by employing guanidinium iodide and increasing its concentration from 2 M to 8 M. This 4-fold increase in the concentration of guanidinium iodide increases the photocurrent by ~50 % to ~10 mA cm⁻². However, the negative shift of redox potential of the electrolyte versus NHE caused by the higher iodide concentration cancels out the beneficial effect of reduced recombination on V_{oc} , resulting in no increase in V_{oc} . Even if we managed to increase the iodide concentration to such a high level that the J_{sc} reached 20 mA cm⁻², the low V_{oc} of 0.6 V would still limit the overall efficiency of the cell to ~8 % only. Therefore, it does not seem to worth trying to look for an iodide compound with unrealistically high solubility in water.

An insulating Al₂O₃ layer has also been deposited on the TiO₂ surface in an attempt to reduce rate of recombination by the tunnel barrier effect. A reduction in recombination was observed. But the resulting increase in V_{oc} and fill factor is too small to compensate the loss in photocurrent which is presumably caused by the loss in injection efficiency. This result is not too surprising given the limited success in improvement in overall efficiency by using the same coating method reported in literature.^{104a, b, 108} Also, the coating method used in this study results in a relatively low coverage of Al₂O₃. Therefore, for future study, a coating method

such as atomic layer deposition (ALD) which gives a high coverage of insulating oxide as reported can be employed.¹⁰⁹ Coating of SiO₂ by ALD on a dye-sensitised TiO₂ film in cells with ACN-based electrolyte has been reported.¹¹⁰ Son *et al.* claimed that tris(*tert*-butoxy)silanol, the SiO₂ precursor employed, would cover only the exposed TiO₂ selectively but not the surface with dye adsorbed because of its catalytic decomposition on TiO₂. A 4-fold increase in recombination lifetime was reported according to data measured from electrochemical impedance spectroscopy, leading to an increase in *J*_{sc} and *V*_{oc} by ~25 % and 70 mV respectively, relative to cells with no ALD treatment. This increases the overall efficiency from 4.36 to 5.94 %. Due to the finite solubility of SiO₂ in water, the same research group deposited thin layers of TiO₂ instead of SiO₂ by ALD on dye-sensitised TiO₂ film for fabricating cells with water electrolyte.¹⁰² However, in this case, no suppression of recombination was observed.

The low photocurrent and high recombination rate observed in DSSCs with water electrolytes might also be caused by a slow regeneration relative to electrolytes based on organic electrolytes. In fact, a slowing of regeneration of dye cation has been observed upon addition of water in electrolyte according to transient absorption data collected at short circuit under ~40 % sun illumination in my previous study.⁴⁵ In this paper, the regeneration lifetimes of the oxidised TS4 and TG6 dyes were found to increase by a factor 2 and 4.5 respectively in 80 % water electrolyte, relative to no-water electrolyte. Moreover, after the publication of the papers on water-based DSSCs,^{45, 93} it was reported that the redox potential of the I₂⁻/I⁻ couple in water and ACN were found to be 1.04 and 0.79 V versus NHE respectively, according to data measured by photomodulated voltammetry.^{94c} Since I⁻ regenerates the oxidised dye and that produces I₂⁻, it is the difference between the reduction potential of I₂⁻/I⁻ and D⁺/D (D refers to dye) which determines the driving force for dye regeneration.^{94c, 111} Therefore, the positive shift of this potential in water relative to organic solvent by 0.25 V significantly reduces the driving force. This will result in a slower rate of regeneration of the oxidised dyes. However, that alone may or may not change the *J*_{sc} of DSSCs, which also depends on the recombination rate constant. For future research, more transient absorption measurements will be needed to study the regeneration in water-based DSSCs.

From the results above, it seems that the limitation in the overall efficiency of water-based DSSCs studied in this project stems from the intrinsic properties of the iodine/iodide redox couple: the low binding constant of iodine with iodide in water, the high rate constant of recombination of electrons with free iodine and/or slow regeneration of oxidised dye by iodide due to a more positive redox potential of I₂⁻/I⁻ couple in water relative to organic solvents. If

we want to further improve the overall efficiency of water-based DSSCs, it makes more sense to look for alternative redox couples in the electrolyte. Ferrocyanide-ferricyanide couple was the first alternative to iodine/iodide redox couple employed in water-based DSSCs.^{101b} Daeneke *et al.* used an electrolyte consisting of 400 mM $K_4Fe(CN)_6$, 40 mM $K_3Fe(CN)_6$, 100 mM KCl and 50 mM Trizma-HCl buffer (pH 8) in water with 0.1 wt% Tween®20. The buffer was used to control the band potential of TiO_2 while Tween®20 was responsible for improving wetting of TiO_2 pores. The J_{sc} and V_{oc} achieved were 5.46 mA cm^{-2} and 0.73 V respectively, leading to an overall efficiency of nearly 3 %. However, the stability of the cells under unfiltered continuous white light illumination was poor. This was attributed to the photolysis and photocatalytic decomposition of the ferrocyanide-ferricyanide redox couple on TiO_2 under ultra-violet (UV) and near UV illumination. The authors suggested that the use of a UV cut-off filter could solve this problem but stability of cells under UV-filtered illumination was not reported.

The next redox couple used in water-based DSSCs is an organic thiolate/disulfide redox couple (TT⁻/DTT).^{101a} Their structures are shown in Fig. 3.38. The authors used a water electrolyte containing 0.2 M TT⁻EMI⁺, 0.2 M DTT and 0.5 M TBP in a 1 % Triton X-100, and two organic dyes, D45 and D51. The highest efficiency of 3.5 % was achieved with DSSCs with the D51 dye with a J_{sc} of 9.5 mA cm^{-2} , a V_{oc} of 0.61 V and a fill factor of 0.59. Again, the stability of these cells were not very promising as their efficiency dropped by ~100 % and 25 % after only 4 hours of unfiltered and UV-filtered 1-sun illumination respectively.

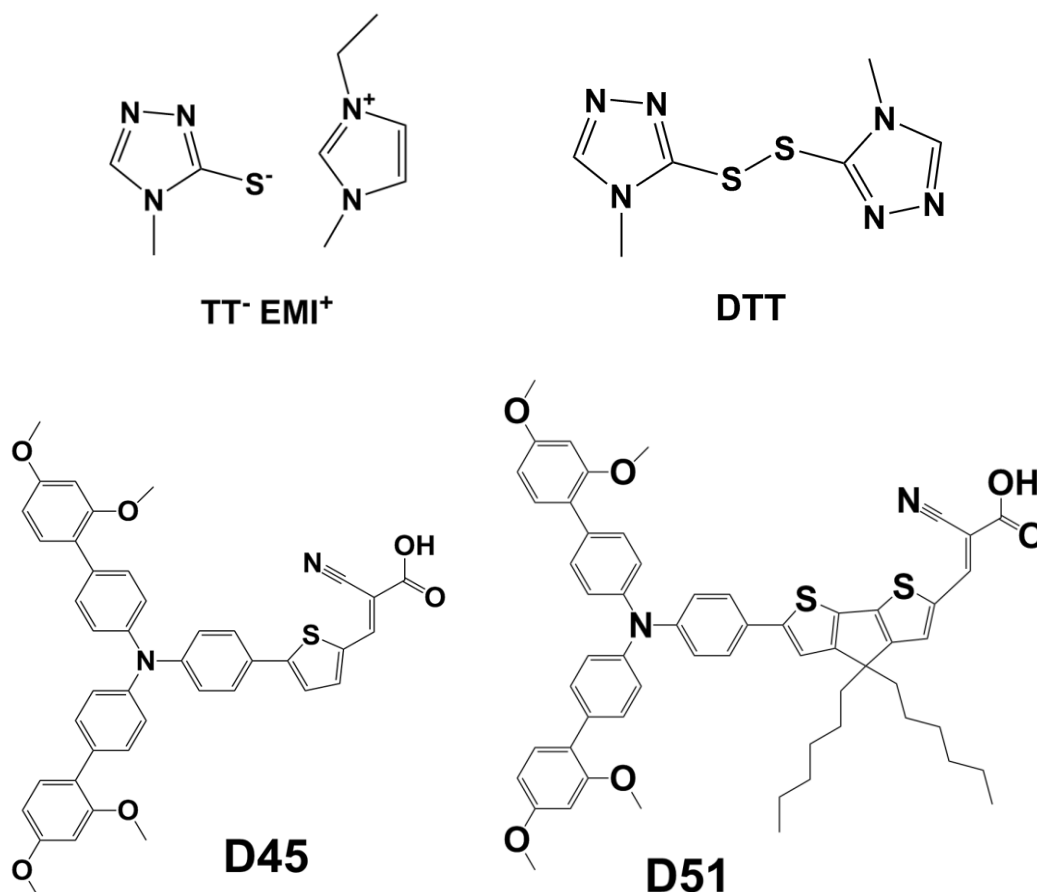


Fig. 3.38 Chemical structures of 1-ethyl-3-methylimidazolium 4-methyl-1,2,4-triazole-3-thiolate (TT·EMI⁺)/3,3'-dithiobis[4-methyl-(1,2,4)-triazole] (DTT), D45 and D51.

The latest redox couple used in water-based electrolyte is cobalt^{(III)/(II)} tris(bipyridine).¹⁰⁰ The electrolyte was composed of 0.20 M [Co(bpy)₃](NO₃)₂, 0.040 M [Co(bpy)₃](NO₃)₃, 0.70 M N-methylbenzimidazole (NMBI) with 1 wt% PEG 300 in water and the dye used was MK2. As mentioned in Chapter 3.1, PEG 300 was used here to improve wetting of TiO₂ pores. The authors replaced the platinum with a composite indium-doped tin oxide (ITO)/platinum counter electrode to address the mass transport limitations in their water-based DSSCs. A record efficiency of 5.1 % with a *J*_{sc} of 9.8 mA cm⁻², a *V*_{oc} of 0.88 V and a fill factor of 0.74 was yielded. These cells showed a better stability than the two previous cases but still the efficiency decreased by ~30 % after 60 hours of 1-sun white LED illumination.

3.2.5 Conclusion

DSSCs with 100 % water electrolyte that operate at a record efficiency of 4 % under 1-sun illumination have been fabricated by managing the wetting behavior and concentration of free iodine in cells. This result is ~5 times higher than the best previously reported values. Higher efficiency can certainly be achieved by further enhancement in wetting, dye and TiO₂ paste. It is noted that water electrolyte with triiodide/iodide may always suffer from the problem of high recombination rate due to the low binding constant of iodine with iodide together with the significant role that free iodine plays in recombination. This is indicated by the relatively low V_{oc} 's of all the water-based DSSCs studied in this thesis. Alumina coating has been deposited on TiO₂ surface prior to dye sensitisation as a tunnel barrier. However, the beneficial effect on performance gained from reduced recombination does not compensate the loss from reduced injection, resulting in an overall loss in conversion efficiency. Therefore, it is likely that an alternative redox couple to iodine/iodide is needed for further development of water-based DSSCs. In any case, the results in this chapter indicate that water-based DSSCs might not be the impossibility it was thought to be for the last 20 years.

Chapter 4

Melt-Processed Solid-State Dye-Sensitised Solar Cells

Abstract

Z907-sensitised and D149-sensitised films have been subjected to heating to 120 °C, 190 °C, and 255 °C for 1 minute in room air. Liquid junction dye-sensitised solar cells (DSSCs), assembled with these heat-treated films, were used to assess the degradation to the TiO₂/dye film by the heat. N,N'-bis(3-methylphenyl)-N,N'-diphenylbenzidine (TPD) and spiro-OMeTAD (SOT) hole transporting materials were also melt-processed onto the TiO₂/dye films, at a temperature of 190 °C and 255 °C respectively. The hole transporting materials (HTMs) have been removed by dissolution and liquid electrolyte DSSCs have been fabricated from the resulting TiO₂/dye films. The effect of the 120 °C heating step on cell performance was found to be minimal. After 190 °C heating, the efficiency loss is 10-20 % depending on dye and film thickness. In the case of 255 °C heating, the efficiency loss is 27-65 %. The efficiency loss occurs almost entirely due to a decrease in recombination lifetime, up to 100 fold in the worst case. This causes a decrease in V_{oc} , and also in collection efficiency for thicker films. Solid-state DSSCs made with melt-processed spiro-OMeTAD on 2 μm thick TiO₂/Z907 films are shown, with efficiency of 0.45 %. The relatively low efficiency is due to the presence of a thick capping layer of HTM and the loss by evaporation of base (4-*tert*-butylpyridine, TBP) during the melt-processing.

Chapter 4.1

Brief Air Heating of Dye-Sensitised TiO₂ Films, to 120-255 °C; the Effect on Resulting Liquid-State DSSCs

4.1.1 Introduction

During the fabrication of liquid-state dye cells, the dye-sensitised mesoporous TiO₂ films are normally exposed to elevated temperatures of 120 to 190 °C for short periods of time. For example, a temperature of 120 °C is applied to the dye-sensitised TiO₂ working electrode during the sealing process for melting the Surlyn sealant. For better durability, Bynel is often used instead of Surlyn as the sealant and the temperature for the sealing process needs to go up to as high as 190 °C. There is also a growing interest in drying the dye-sensitised TiO₂ films before cell assembly, which will only lengthen the time when dye adsorbed on TiO₂ is exposed to elevated temperature. Hence, it is important to examine the influence of heat treatment applied to dye-sensitised TiO₂ electrodes on the resultant photovoltaic performances of the cells fabricated with these electrodes.

Apart from liquid-state dye cells, heat is also applied during the fabrication of solid-state dye cells during the melt-processing of hole transport materials (HTMs). HTMs such as 2,2',7,7'-tetrakis-(N,N-di-p-methoxyphenylamine)9,9'-spirobifluorene (spiro-OMeTAD), have commonly been deposited from solution. However, as mentioned in Chapter 1, the resulting poor pore-filling fraction in the mesoporous TiO₂ layer has become a major limiting factor in cell performance, especially when the TiO₂ thickness is increased above 2 μm. In order to enhance pore filling, and to side step the necessity for hole conductor solubility, solvent-free methods of melt-processing HMTs have been attempted previously. A good pore filling and surface coverage of TiO₂ pores has been shown by scanning electron microscopy^{69a} and transient absorption spectroscopy (TAS) measurements^{69b} respectively. Nevertheless, the highest efficiency reported at 1-sun illumination is limited to only 0.12 %.¹¹² Therefore, an in-depth investigation in the thermal degradation to the dye adsorbed on TiO₂ during the melt-processing of HTMs will also be useful for understanding any limitations arising from the heating process and for the further development of this technique in the future.

The thermal stability of Ru-based dyes in free form and adsorbed on nanostructured TiO₂ films has been studied previously.¹¹³ The authors agreed on the occurrences of dehydration at about 40-100 °C, deamination of tetrabutylammonium counterion (in the case of N719) as well as decarboxylation and decomposition between 200 and 400 °C in dry air or under nitrogen.

There are also many studies regarding the thermal stability of complete DSSCs but the temperatures applied are always below 100 °C.¹¹⁴ To our knowledge, there is only limited investigation in the effect of thermal treatment with a temperature >100 °C applied to TiO₂/dye electrodes on the resulting performance of cell made with these electrodes. It has been reported that the efficiency of both N719 and Ruthenium 505 dye-sensitised solar cells decreases by >90 % when their TiO₂/dye electrodes were heated above 200 °C for 10 minutes before cell assembly.^{46, 115} The authors correlated these efficiency losses to the thermal degradation of the -SCN and -CN groups in the N719 and Ruthenium 505 dyes respectively. Similar experiments have been conducted where TiO₂ films sensitised by N719 and D5, a less well-known organic molecular dye (see Fig. 4.1), were heated for 5 minutes at different temperatures.¹¹⁶ The results are slightly better than the previous report. It was found that exposing the D5-sensitised and N719-sensitised TiO₂ films to temperature above 200 °C for 5 min caused >40 % reduction in their peak absorbance. When the TiO₂/dye electrodes were treated at 200 °C, the resulting overall efficiency of the N719 and D5 cells decreased by 80 % and 32 % respectively. The authors attributed these losses to a decrease in electron lifetime, according to data obtained by intensity modulated photovoltage spectroscopy.

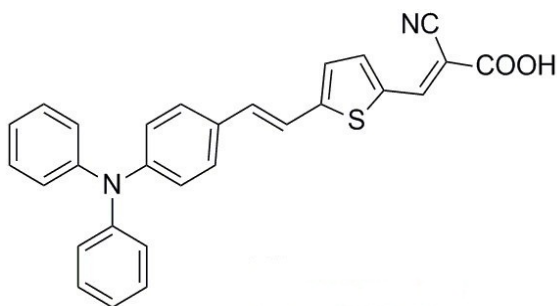


Fig. 4.1 Chemical structure of the D5 dye.

In the first part of this chapter, the effect of heating at 120, 190, and 255 °C on TiO₂/dye films for one minute will be examined. After the heating process, the film was incorporated into a standard TiO₂/dye/electrolyte DSSC using normal procedures. For the purpose of comparison, two sensitising dyes were used: Z907, a benchmark ruthenium-based dye and D149, an organic dye commonly employed in solid-state dye-sensitised solar cells. Absorption spectra of heat-treated TiO₂/dye films and *JV*'s, transient photovoltage and photocurrent data of the resultant liquid junction cells assembled with these films will be presented.

4.1.2 Experimental Methods

Heat Treatment on TiO₂/dye Films

A layer of nanoporous TiO₂ (DSL18NRT purchased from DyeSol) film was deposited on FTO glass by the same doctor-blading method used in the fabrication of standard DSSCs as described in Chapter 2. TiCl₄ post-treatment was applied as described in Chapter 2. The TiO₂ electrodes were sensitised either in a 0.3 mM Z907 in *tert*-butanol (TBA)/ acetonitrile (ACN) (1:1 by volume) for 20 hours or in 0.06 mM D149 and 0.24 mM cheno in TBA/ACN (1:1 by volume) for 3 hours. For the TiO₂/dye films that required heat treatment, the as-made films were placed on a hotplate (Heidolph MR Hei-Tec) preset to 120 °C, 190 °C or 255 °C for 1 minute in room air. The films, including the control film which was not heat-treated, were then rinsed in acetonitrile for 15 minutes before their UV-vis spectra were recorded. UV-vis spectra were taken as described in Chapter 2 before and after the heating procedure. Standard liquid junction DSSCs were assembled as described in Chapter 2 using the above films. Current density vs. voltage (*JV*), transient photovoltage and photocurrent, and charge extraction at open and short circuit were measured as described in Chapter 2.

4.1.3 Results

Effect of Heat on TiO₂/Dye Films and the Resultant Cell Performance

TiO₂/Z907 Films

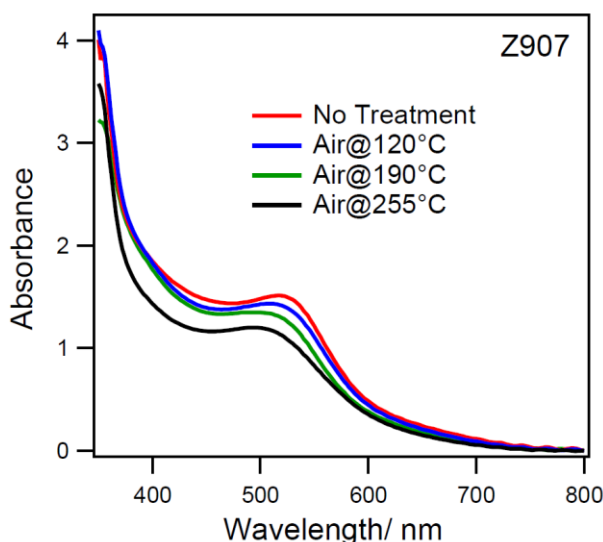


Fig. 4.2 Absorption spectra of Z907-sensitised TiO₂ film (DyeSol, 7 μm) after 1 minute heating at different temperatures.

Fig. 4.2 shows the changes in absorption spectra of the Z907-sensitised TiO₂ films heated at three different temperatures: 120, 190 and 255 °C. The absorption spectrum of a control TiO₂/Z907 film which was not heated was also shown for comparison. The data show that

heating a TiO₂/Z907 film at 120 °C causes a relatively small change in its absorption spectrum. The resulting peak of the absorption is blue-shifted by ~4 nm and the absorbance decreases by about ~5 %, when compared to the control film. Integration between 400 and 800 nm of the film absorption with the 1-sun AM 1.5 spectra shows that the light absorption fluxes of the control and 120 °C-treated films are both 14 mA cm⁻². Thus, despite the change in spectrum, the same number of photons are absorbed by the control and 120 °C-treated film. Above 120 °C, a general trend that high temperature results in a greater blue-shift and a larger decrease in absorbance of the absorption peak is observed.

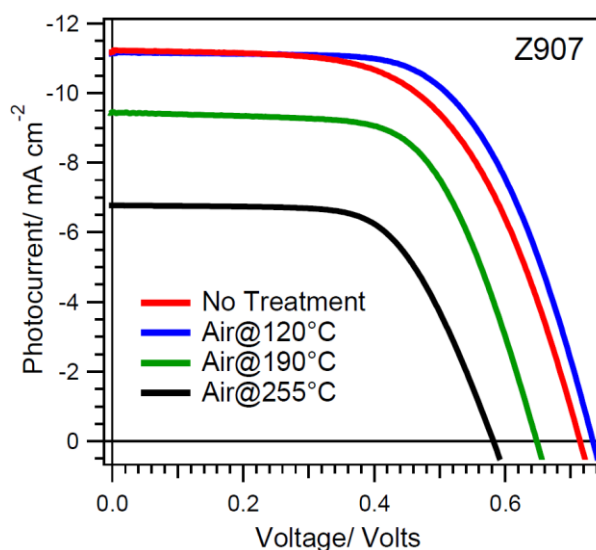


Fig. 4.3 One-sun *JV* curves of liquid-state DSSCs fabricated with Z907-sensitised TiO₂ electrodes (DyeSol, 7 μm) heated at different temperatures for 1 minute. (Electrolyte was 0.8 M PMII, 50 mM iodine, 50 mM GuSCN, 0.28 M TBP and 25 mM LiI in MPN, where PMII is propylmethylimidazolium iodide).

Table 4.1 One-sun performance of liquid-state DSSCs fabricated with Z907-sensitised TiO₂ electrodes (DyeSol, 7 μm) heated at different temperatures for 1 minute. Conditions as in Fig. 4.3.

Treatment	<i>J</i> _{sc} / mA cm ⁻²	<i>V</i> _{oc} / V	Fill Factor	Efficiency/ %
No Treatment	11.2	0.71	0.58	4.61
Air@120°C	11.2	0.73	0.62	5.06
Air@190°C	9.44	0.65	0.63	3.87
Air@255°C	6.77	0.58	0.62	2.43

Fig. 4.3 and Table 4.1 show the trend in cell performance of liquid-state DSSCs fabricated with the heated-treated TiO₂/Z907 electrodes. It is found that heating TiO₂/Z907 electrode at 120 °C for 1 minute does not cause any detrimental effect on the performance of DSSC. When a temperature of 190 °C is applied, short-circuit current density (*J*_{sc}) and open-circuit voltage (*V*_{oc}) decrease by 15 % and 30-70 mV respectively, relative to the control cells which electrodes were not heat-treated. It is noted that the drop in *J*_{sc} and *V*_{oc} in these cells are much

smaller than those reported previously when TiO₂/N719 films were heated at a similar temperature before cell assembly.¹¹⁵⁻¹¹⁶ This is likely due to the longer heating time (5-10 min) these authors have employed and/or the use of the N719 dye which has *tert*-butylammonium counter ions (TBA⁺). For our cells, when the temperature is increased to 255 °C, cell's *J*_{sc} reduces by almost 60 % and *V*_{oc} drops by 160 mV. Given that the photon absorption calculated by the same integration method mentioned above is only 19 % lower, there must be a large contribution from the decrease in charge separation and/or collection to cause the ~60 % reduction in *J*_{sc}.

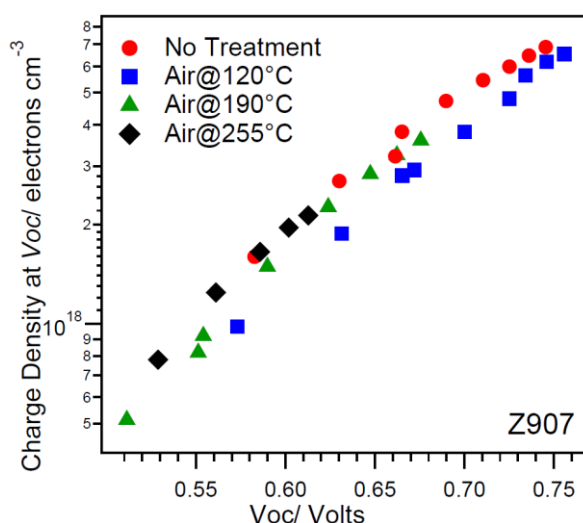


Fig. 4.4 Charge density vs. *V*_{oc} of liquid-state DSSCs fabricated with Z907-sensitized TiO₂ electrodes (DyeSol, 7 μm) heated at different temperatures for 1 minute. Conditions as in Fig. 4.3

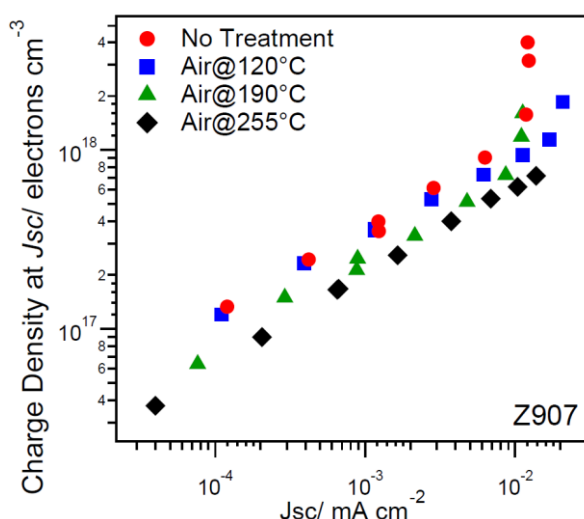


Fig. 4.5 Charge density vs. *J*_{sc} of liquid-state DSSCs fabricated with Z907-sensitized TiO₂ electrodes (DyeSol, 7 μm) heated at different temperatures for 1 minute. Conditions as in Fig. 4.3

Fig. 4.4 shows the charge density versus *V*_{oc} of the same series of cells. No apparent shift is observed even when the TiO₂/Z907 electrodes had been heated up to 255 °C for 1 minute

before cell fabrication. This indicates the conduction band edge of TiO₂ does not shift and the density of trap states does not change significantly upon the application of heat to the electrodes. This is supported by the data in Fig. 4.5 which shows that the occupied trap states at short circuit of the cells with heat-treated electrode decreases by less than a factor of 2, relative to the control cells. The change is relatively small and could be attributed to random variations.

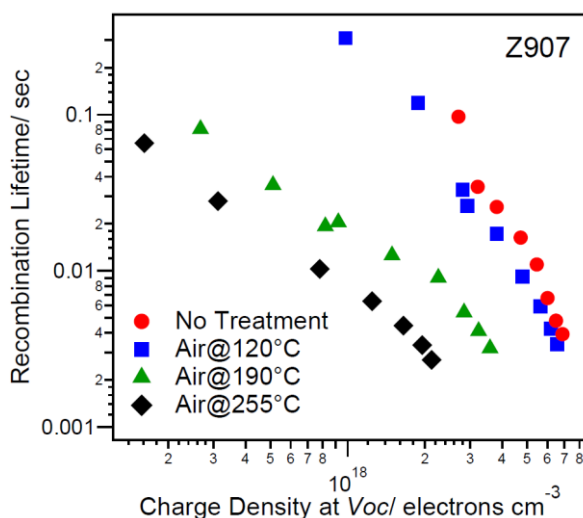


Fig. 4.6 Recombination lifetimes vs. charge density of liquid-state DSSCs fabricated with Z907-sensitized TiO₂ electrodes (DyeSol, 7 μm) heated at different temperatures for 1 minute. Conditions as in Fig. 4.3.

The recombination lifetimes of the cells above were measured by transient photovoltage technique and the results are shown in Fig. 4.6. It is found that after heating the TiO₂/Z907 electrodes at 255 °C for 1 minute, recombination lifetime decreases by about 2 orders of magnitude. With a V_{oc} ideality of ~ 80 mV per decade shown in the same cell, this change is sufficient to explain most or all of the reduction in V_{oc} . A decrease in recombination lifetime by 100 fold will also decrease the diffusion length by a factor of ~ 10 .¹¹⁷ As a result, the collection efficiency will decrease significantly, causing a much larger loss in photocurrent, relative to the loss predicted from decreased absorption, as observed in these cells. Fig. 4.7 shows the electron lifetime at short circuit versus charge density measured by the transient photocurrent technique. At short circuit, both transport and recombination are taking place at the same time. When recombination is much slower (>10 times) than transport, the electron lifetime essentially represents the transport lifetime. However, in the case of electrode treated at 255 °C (black diamond markers in Fig. 4.7), the recombination lifetime is so short that it becomes comparable with the transport lifetime. This results in a low collection efficiency and shifts its graph to the left, exaggerating the change in its electron lifetimes. Therefore, the

decrease in electron lifetime at J_{sc} in cells with heat-treated electrode, relative to control cells observed in Fig. 4.7, is mainly caused by the large reduction in recombination lifetime.

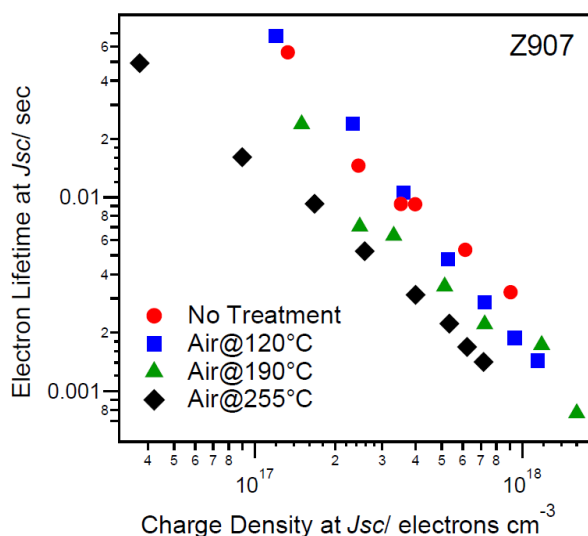


Fig. 4.7 Electron lifetimes at J_{sc} vs. charge density of liquid-state DSSCs fabricated with Z907-sensitised TiO_2 electrodes (DyeSol, 7 μm) heated at different temperatures for 1 minute. Conditions as in Fig. 4.3.

$\text{TiO}_2/\text{D149}$ Films

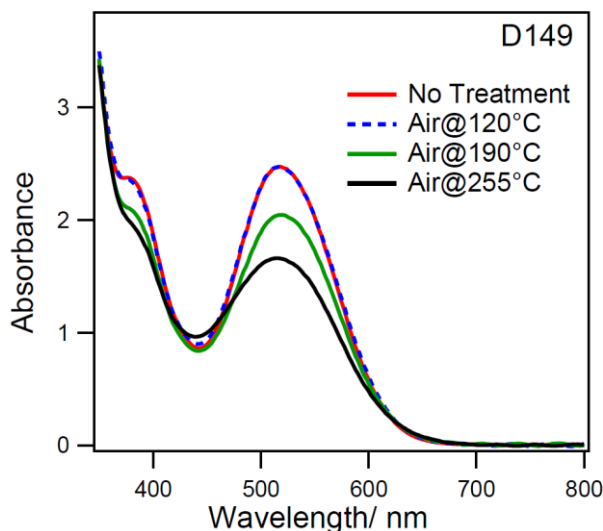


Fig. 4.8 Absorption spectra of D149-sensitised TiO_2 film (transparent, 4.2 μm) heated at different temperatures for 1 minute.

To test the generality of the results shown by $\text{TiO}_2/\text{Z907}$ electrodes, similar experiments were conducted on a high performance organic dye, D149 (structure shown in Fig. 1.13). Fig. 4.8 shows absorption spectra of the $\text{TiO}_2/\text{D149}$ electrodes treated at different temperatures. Heating $\text{TiO}_2/\text{D149}$ electrode at 120 $^\circ\text{C}$ for 1 minute does not cause any shift or decrease in absorbance of the absorption peak. Treatment on $\text{TiO}_2/\text{D149}$ electrodes above 120 $^\circ\text{C}$ results in a reduction in peak absorbance, which is larger at a higher temperature. In the case of D149, the

electrodes do not show any blue-shift in the peak absorption upon heating for 1 minute as opposed to the TiO₂/Z907 series.

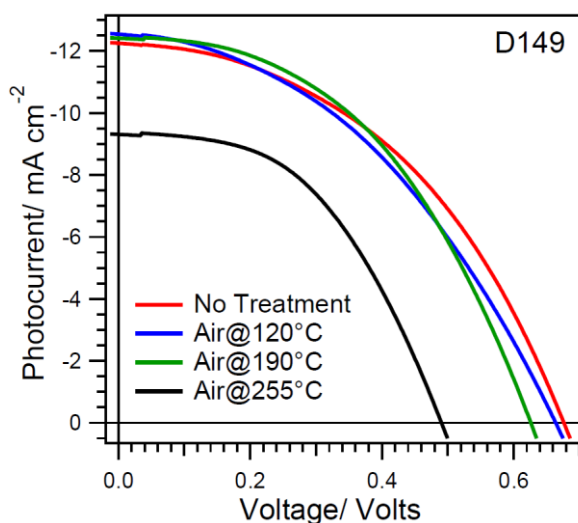


Fig. 4.9 One-sun JV curves of liquid-state DSSCs fabricated with D149-sensitised TiO₂ electrodes (transparent, 4.2 μm) heated at different temperatures for 1 minute. (Electrolyte: 0.8 M NaI, 40 mM iodine and 0.2 M GuSCN in MPN)

Table 4.2 One-sun performance of liquid-state DSSCs fabricated with D149-sensitised TiO₂ electrodes (transparent, 4.2 μm) heated at different temperatures for 1 minute. Conditions as in Fig. 4.9.

Treatment	$J_{sc}/\text{mA cm}^{-2}$	V_{oc}/V	Fill Factor	Efficiency/%
No Treatment	12.3	0.67	0.44	3.65
Air@120°C	12.6	0.66	0.41	3.41
Air@190°C	12.5	0.62	0.46	3.59
Air@255°C	9.33	0.48	0.49	2.20

Fig. 4.9 and Table 4.2 show the changes in cell performance of liquid-state DSSCs fabricated with the heated-treated TiO₂/D149 electrodes. Similar to the results shown in the TiO₂/Z907 cells, heating the TiO₂/D149 electrodes at 120 °C at 1 minute does not cause any detrimental effect on cell's J_{sc} , V_{oc} or overall efficiency, relative to the control cells. Apart from the 50 mV drop in V_{oc} , a higher temperature of 190 °C also results in no significant decrease in cell performance, when compared to the control cells. However, when the temperature applied is increased to 255 °C, the J_{sc} and V_{oc} of the resulting cells decrease by ~24 % and 190 mV respectively relative to control cells. It is worth noting that sodium iodide was used instead of the standard PMII in this series of D149 cells, which probably results in the relatively low fill factor as observed in Fig. 4.9 and Table 4.2. The reason for using sodium iodide is that desorption of the D149 dye was observed during cell fabrication when PMII-based electrolytes were used.

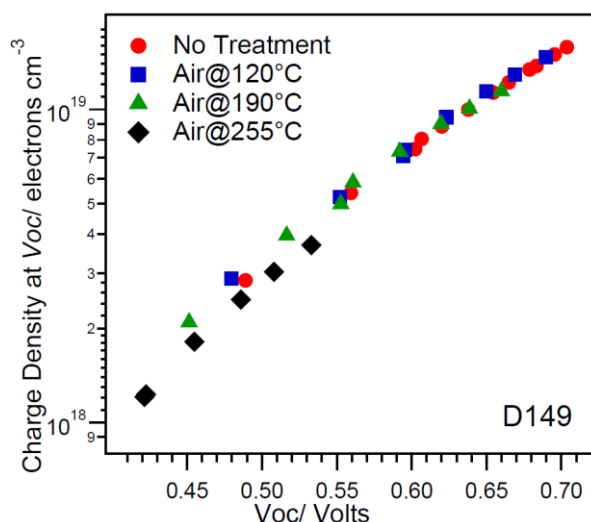


Fig. 4.10 Charge density vs. V_{oc} of liquid-state DSSCs fabricated with D149-sensitized TiO_2 electrodes (transparent, $4.2 \mu\text{m}$) after 1 minute heating at different temperatures. Conditions as in Fig. 4.9.

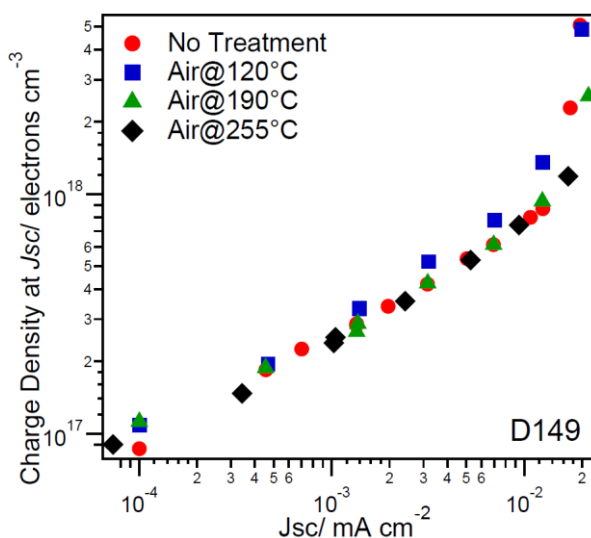


Fig. 4.11 Charge density vs. J_{sc} of liquid-state DSSCs fabricated with D149-sensitized TiO_2 electrodes (transparent, $4.2 \mu\text{m}$) after 1 minute heating at different temperatures. Conditions as in Fig. 4.9.

Fig. 4.10 and 4.11 show the charge density versus V_{oc} and the charge density versus J_{sc} of the same cells above respectively. The data show that there is essentially no shift in the TiO_2 conduction band edge and no change in the density of states in TiO_2 upon heat treatment on the $\text{TiO}_2/\text{D149}$ electrodes. Fig. 4.12 shows the recombination lifetime vs. charge density. Heating the $\text{TiO}_2/\text{D149}$ electrodes at 120°C and 190°C does not cause any significant change in recombination lifetime. However when a temperature of 255°C is applied, the recombination lifetime of the resulting cells decreases by ~ 60 fold, which is again sufficient to explain the large reduction in J_{sc} and V_{oc} , relative to the control cells. Electron lifetime at short circuit was also measured by transient photocurrent technique and the data are shown in Fig. 4.13. Since the recombination lifetime is ~ 30 times slower than the electron lifetime at short circuit,

the data displayed in Fig. 4.13 essentially show the transport lifetime versus charge density. This also explains the smaller decrease in J_{sc} (~25 %) observed in cells with TiO₂/D149 electrode treated at 255 °C for 1 minute, when compared to the cells with TiO₂/Z907 electrode treated in the same way (~60 % decrease in J_{sc}). Similar to Z907, no significant change in transport lifetime is observed in cells with heat-treated TiO₂/D149 electrodes, when compared with the control cells in the same series.

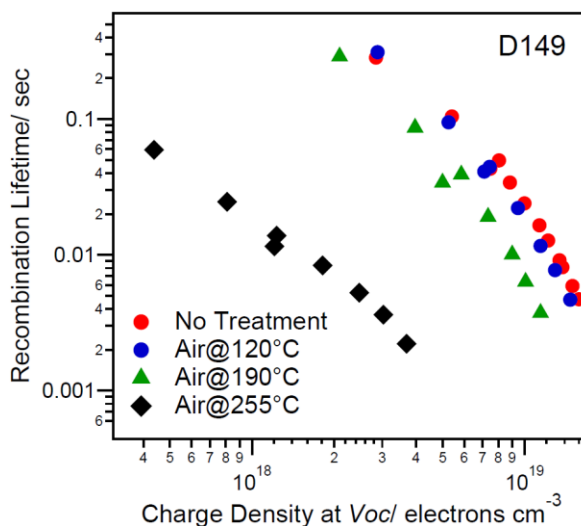


Fig. 4.12 Recombination lifetime vs. charge density of liquid-state DSSCs fabricated with D149-sensitised TiO₂ electrodes (transparent, 4.2 μm) after 1 minute heating at different temperatures. Conditions as in Fig. 4.9.

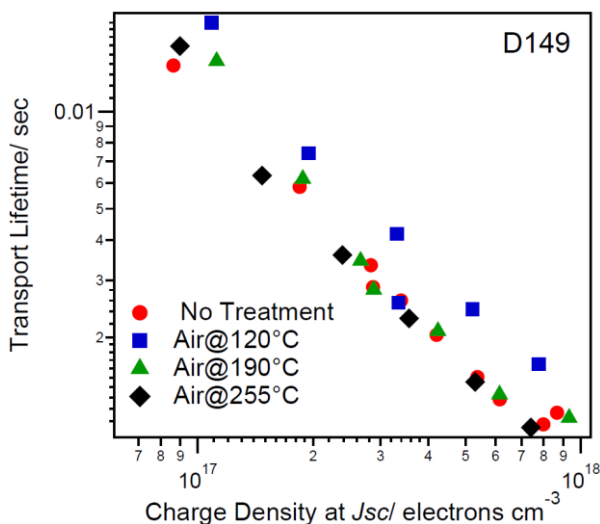


Fig. 4.13 Transport lifetime vs. charge density of liquid-state DSSCs fabricated with D149-sensitised TiO₂ electrodes (transparent, 4.2 μm) after 1 minute heating at different temperatures. Conditions as in Fig. 4.9.

4.1.4 Discussion

It is found that the heating TiO₂/Z907 and TiO₂/D149 films at a temperature higher than 120 °C prior to cell assembly reduces the recombination lifetime of the resulting cell. According to the results published in our group, a reduction in dye coverage on TiO₂ surface cannot result in an increase in recombination rate constant as large as 100 fold.^{91b} Herein, it is proposed that a breakdown product of the dye which strongly short-circuits the TiO₂/electrolyte interface, is formed during the heating process. It has also been reported in our group that the main pathway for recombination is the reduction of free iodine present in the electrolyte¹³ and that iodine binding molecules which are bound to the TiO₂ surface can increase recombination.¹⁴ Thus, it is considered that the breakdown products of Z907 and D149 can bind iodine at the surface. However, since the structures of the two dyes used in this work are so different, it is hard to identify what compounds the breakdown products would be. So far, only ruthenium phthalocyanine dyes have been shown to cause an increase in recombination of this large a magnitude.¹¹⁸ It may be that Z907 and D149 have two different breakdown products which by chance cause about similar effect on recombination. Identification of these breakdown products might make it possible to eliminate the specific reactive group and increase the thermal stability of the TiO₂/dye films. In literature, it has been reported that N3, a ruthenium-based dye (structure shown in Fig. 1.5), is stable up to 250 °C in powder form and 320 °C when adsorbed on TiO₂, both measured in a dry air environment. Given a breakdown of Z907, which has a similar structure to N3, was observed at much lower temperatures. It is assumed that the breakdown is caused by atmospheric water. Nevertheless, iodine does not usually bind to oxidised and hydroxylated hydrocarbons strongly. For future research, similar experiments of heating TiO₂/dye electrode in dry air or under nitrogen may help to find out the reasons for the increase in recombination rate constant observed in this work. It will also be interesting to fabricate similar cells in this work using cobalt electrolytes to see if the same reduction in recombination lifetime will be observed upon the same heat treatment.

4.1.5 Conclusion

Z907- and D149- sensitised nanoporous TiO₂ electrodes were heated at 120-255 °C for 1 minute. The thermal degradation to the dye and the reduction in light absorbed by the dye are small even when the electrodes are heated up to 255 °C. It has been demonstrated that a high conversion efficiency can be achieved in the resulting liquid-state cells even when the dye-sensitised TiO₂ electrodes are treated up to 190 °C for 1 minute before cell assembly. But the cell performance declines significantly when a temperature of 255 °C is used instead. When comparing the TiO₂ films sensitised with Z907 and D149, TiO₂/D149 film is found to be less prone to thermal degradation (especially at 255 °C) and decline in cell performance in the DSSCs assembled with it. From transient photovoltage measurements, a faster recombination is found to be the major cause of the reduced efficiency in both liquid-state Z907 and D149 cells. Considering the completely different chemical structures of the two dyes, it is interesting that their cells show a similar trend of dye degradation and decline in cell performance with increasing temperature applied to TiO₂ electrodes and even share the same reason for the reduction in their cell efficiencies.

Typically DSSCs intended for stability tests or commercial purposes are sealed with high melting sealant such as Bynel (m.p. ~190 °C). The degradation in performance of cells assembled with 190 °C-treated electrode observed in this work may partially explain the lower efficiency typical shown by cells designed specifically for stability tests. With a growing interest in drying the TiO₂/dye electrode before cell assembly and sealing DSSCs with Bynel for better durability, these results are certainly useful for the fabrication of DSSCs in industry. The results in this chapter also suggest that efficient solid-state DSSCs can possibly be fabricated by melt-processing hole transport materials with melting points ≤ 190 °C, especially when the D149 dye is used. The effect of melting hole transporting materials through TiO₂/dye film at elevated temperatures on the resultant cell performance will be studied in Chapter 4.2.

Chapter 4.2

Melt-Processing Hole Transporting Materials in Solid-State Dye-Sensitised Solar Cells

4.2.1 Introduction

Deposition of hole transporting materials (HTMs) from solution always results in low a pore-filling fraction as mentioned in Chapter 4.1. One promising technique to deposit HTM onto porous TiO₂ film without using any solvent is the melt-processing method, which was first reported by Fredin *et al.* in 2009.^{69a} The HTM, 4,4',4''-tris(N,N-diphenyl-amino)-triphenylamine (see Fig. 4.14), was spread on top on a D5-sensitised TiO₂ film which was placed on a hot plate. The HTM started to melt when the temperature of the hot plate reached its melting point. The HTM melt was then doctor-bladed on the TiO₂ film. During the process, the melted HTM was drawn deeper down while filling up the pores of TiO₂. SEM images show an efficient pore filling even when a 10 μm thick TiO₂ film was used. However, the photocurrent and efficiency of the cell are quite low (0.02 mA cm⁻² and 0.0037 % respectively). This is probably due to the high melting temperature of the HTM used (255 °C).

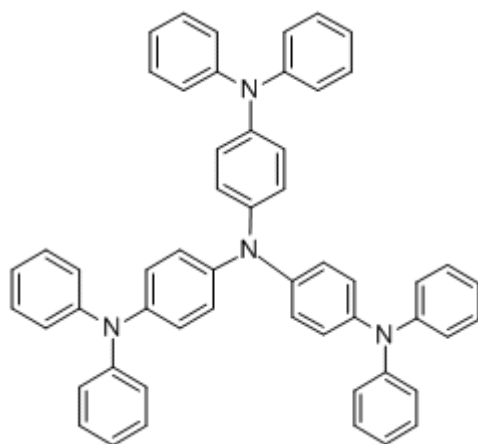


Fig. 4.14 Chemical structure of 4,4',4''-tris(N,N-diphenyl-amino)-triphenylamine.

A slightly different method and another HTM were attempted in another paper.¹¹² A solution of lithium salt and a separate solution of the HTM, 4-(diethyl-amino)benzaldehyde-1,1-diphenyl-hydrazone (m.p. = 92-95 °C) were dropped onto a D35-sensitised TiO₂ film successively. After evaporation of solvent, the hot plate was heated to 150 °C for 30 seconds to allow the HTM melt to infiltrate into TiO₂ pores. A higher conversion efficiency of 0.12 % under 1-sun illumination was achieved. But this is still >15 times smaller when compared to liquid-state DSSCs fabricated using the conventional method with the same TiO₂ film and dye.

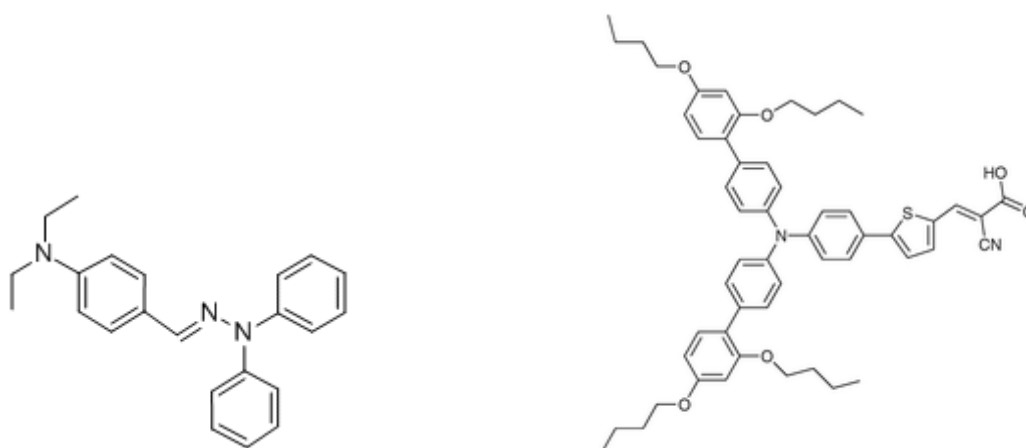


Fig. 4.15 Chemical structures of 4-(diethyl-amino)benzaldehyde-1,1-diphenyl-hydrazone (left) and the D35 dye (right).

A modified technique where the HTM was melted from one side of the dye-sensitised TiO₂ film (procedures have been described in Chapter 2) has been reported in our research group.^{69b} VM3, with a melting point of 134 °C, as HTM and the N719 dye were used. Iodine doping was applied to HTM after melt-processing to enhance the efficiency of the cell. An efficient pore coating was indicated by transient absorption spectroscopy (TAS) measurements where the regeneration lifetimes and the regeneration efficiency were found to be <1 μs and >90 % respectively. However, the 0.075 % conversion efficiency achieved is still relatively low.

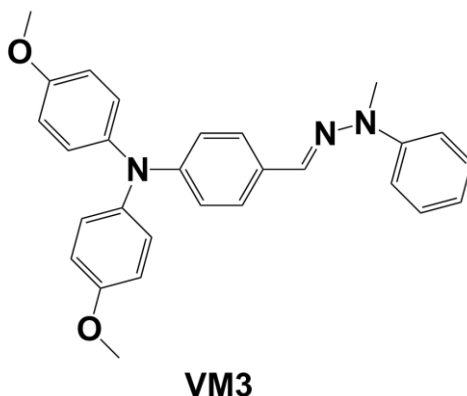


Fig. 4.16 Chemical structure of VM3.

Melt-processing of HTM has been shown to be a promising technique for the fabrication of solid-state DSSCs due to the higher pore-filling fraction achieved. But so far, all the DSSCs made by this method show low overall efficiencies. In the second part of this chapter, the effect of melt-processing two different HTMs, N,N'-bis(3-methylphenyl)-N,N'-diphenylbenzidine (TPD) and 2,2',7,7'-tetrakis-(N,N-di-p-methoxyphenylamine)9,9'-spirobifluorene (spiro-

OMeTAD) or SOT), at 190 and 255 °C respectively will be presented. The melt-processing approach previously published was employed.^{69b} It was followed by 20-hour soak in toluene to completely remove the HTMs. After removal of the HTM, the film is incorporated into a standard TiO₂/dye/electrolyte DSSC using normal procedures. For comparison, air-heated TiO₂/dye films were also immersed in toluene before assembling into a DSSC. Absorption spectra of these films and *JV*'s and transient photovoltage and photocurrent data of the resultant liquid junction DSSCs assembled with these films will be presented. Solid-state DSSCs have been fabricated by melt-processing TPD and spiro-OMeTAD and their *JV* characteristics will be also presented in this chapter.

4.2.2 Experimental Methods

Heat Treatment, Toluene Treatment and Melt-Processing of Hole Transporting Materials on TiO₂/dye Films

A layer of nanoporous TiO₂ film was deposited on FTO glass by the same doctor-blading method used in fabrication of standard DSSCs as described in Chapter 2. Two transparent TiO₂ pastes, one from DyeSol, the other prepared in our laboratory by Dr. X. Li, and the scattering TiO₂ paste from G24i were used in this chapter. TiCl₄ post-treatment was applied as described in Chapter 2. For the films that required dye sensitisation, the films were immersed either in a 0.3 mM Z907 in *tert*-butanol (TBA)/ acetonitrile (ACN) (1:1 by volume) for 20 hours or in 0.06 mM D149 and 0.24 mM cheno in TBA/ACN (1:1 by volume) for 3 hours. For the TiO₂/dye films that required heat treatment, the as-made films were placed on a hotplate (Heidolph MR Hei-Tec) preset to 190 °C or 255 °C for 1 minute in room air. Melt-processing of hole transporting materials (HTMs) was conducted as described in Chapter 2. For the TiO₂/dye and TiO₂/dye/HTM films that required toluene treatment, they were immersed in toluene for 20 hours. After each heat or toluene treatment, the films were then immersed in ACN for 15 minutes before their UV-vis spectra were recorded. UV-vis spectra were taken as described in Chapter 2. Standard liquid junction DSSCs were assembled as described in Chapter 2 using the above films.

Fabrication of Solid-State Dye-Sensitised Solar Cells

Preparation of dye-sensitised TiO₂ electrodes and melt-processing of HTM were performed as described in Chapter 2. In the case of solid-state DSSCs with TPD, the TPD was doped using vapour of NOBF₄. A small amount of NOBF₄ was placed in a 20 mL vial, and heated to 150 °C. The TiO₂/dye/TPD film was then placed in the vial, with TPD facing down,

about 1 cm above the NOBF_4 for 2 minutes. JV was measured after each 2 minute exposure. This doping procedure was repeated until optimum cell efficiency was achieved. For the melt-processed spiro-OMeTAD cell, spiro-OMeTAD was melt-processed together with 3 wt% bis(trifluoromethane)sulfonamide lithium salt (Li-TFSI) and 8 wt% 4-*tert*-butylpyridine (TBP). No intentional doping was conducted. For the reference solid-state DSSC, a solution of 68 mM spiro-OMeTAD, 9 mM Li-TFSI and 55 mM TBP in chlorobenzene was spin-coated onto a 2 μm $\text{TiO}_2/\text{Z907}$ film using a Laurell WS-400A-6NPP/LITE spin coater. No heat treatment was applied. The solution was rested on the $\text{TiO}_2/\text{Z907}$ film in the spin-coater for 45 seconds before applying a spin-coating rate of 2000 revolutions per minute (rpm) for 45 seconds. Pressed graphite was used as a cathode as described in Chapter 2. Current density vs. voltage (JV), transient photovoltage and photocurrent, and charge extraction at open and short circuit were measured as described in Chapter 2.

4.2.3 Results

4.2.3.1 Toluene Treatment

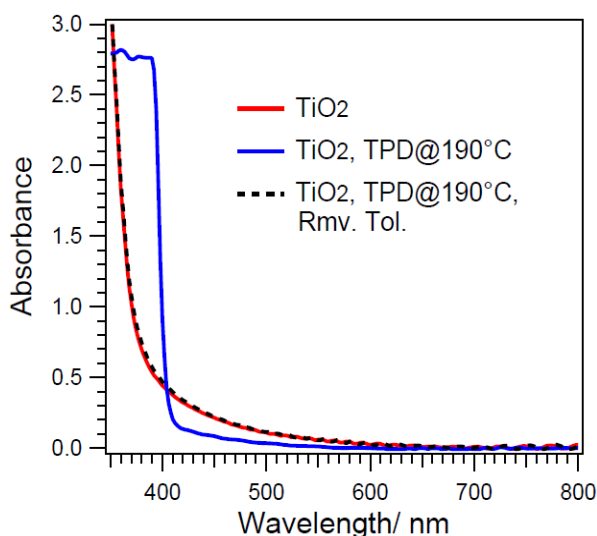


Fig. 4.17 Absorption spectra of TiO_2 film, in air, with melt-processed TPD, and with TPD desorbed by toluene treatment. The TiO_2 film was 7 μm thick, transparent, and on FTO glass. (Rmv. Tol. indicates HTM Removed by Toluene) [This figure is reproduced with the permission of the rights holder, The Royal Society of Chemistry.]¹¹⁹

Fig. 4.17 shows the absorption spectra of a blank TiO_2 film (red curve) and the same film after melt-processing of TPD (blue curve). Then the same film was immersed in toluene for 20 hours so as to desorb TPD and the resulting absorption spectrum (black dotted curve) is also shown in the Fig. 4.17. These spectra show that TPD melted on a nanoporous TiO_2 film has been removed by toluene completely. It is noted that due to the light scattering effect in air, the nanoporous TiO_2 film when it is on its own (red) shows an absorption with a broad tailing off

region from 400 nm up to 600 nm. This scattering effect is removed after the pores are filled up by TPD (blue) by melt-processing, resulting in a decrease in absorbance in the 400-600 nm region. The increase in absorbance below 400 nm is due to the presence of TPD, which was reported to show an absorption onset at about 400 nm and a peak at 375 nm when its solution is spin-coated onto a quartz glass substrate.¹²⁰ In the same figure, we can also see that the absorption spectrum of TiO₂ film with TPD after toluene treatment (dotted black curve) is almost identical to that before melting TPD through (red). This suggests that the toluene treatment successfully desorbs all the TPD from the TiO₂ film. A similar experiment was conducted using spiro-OMeTAD (abbreviated as SOT in figures). As shown in Fig. 4.18 the same toluene treatment completely removes spiro-OMeTAD melted on the nanoporous TiO₂ layer. This toluene treatment was then employed to remove TPD and spiro-OMeTAD in the next series of experiments.

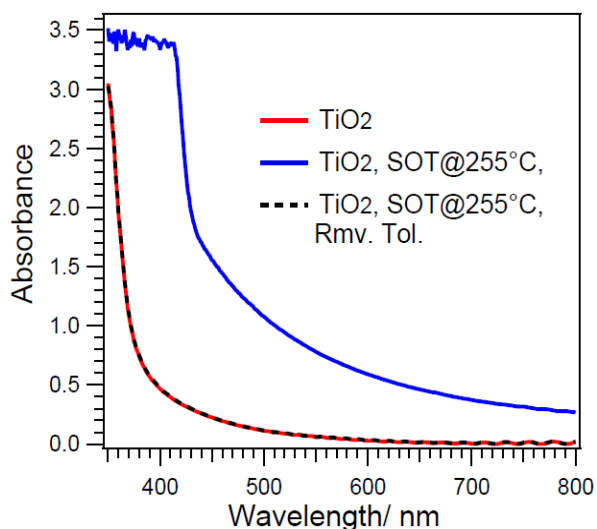


Fig. 4.18 Absorption spectra of TiO₂ film, in air, with melt-processed spiro-OMeTAD (SOT), and with SOT desorbed by toluene treatment. The TiO₂ film was 7 μm thick, transparent, and on FTO glass. (Rmv. Tol. indicates HTM Removed by Toluene)

4.2.3.2 Effect of Heat and Toluene Treatment on TiO₂/Dye Films and the Resultant Cell Performance

TiO₂/Z907 Films

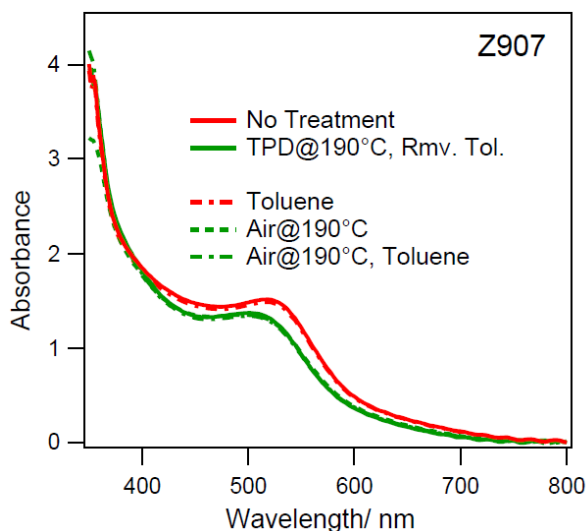


Fig. 4.19 Absorption spectra of Z907-sensitised TiO₂ film (DyeSol, 7 μ m) before and after different treatments as noted in legend. (Rmv. Tol. indicates HTM Removed by Toluene)

Fig. 4.19 shows the absorption spectra of five TiO₂/Z907 films, each of which has undergone different treatment(s). When comparing the two red curves, it can be seen that the toluene treatment does not cause any observable change in the absorption spectrum. After melt-processing TPD on the TiO₂/Z907 (which takes 1 minute) film and removal of TPD by toluene, the peak of the absorption (solid green curve) is blue-shifted by 8 nm and its absorbance decreases by ~10 %, when compared to the TiO₂/Z907 film without undergoing any treatment (solid red curve). A TiO₂/Z907 film which was heated at 190 °C in air without TPD shows the same absorption spectra as the one melt-processed with TPD, followed by TPD removal in toluene. This result shows that any change in the absorption spectrum during melt-process of TPD is entirely caused by the heat applied only but not by TPD. Furthermore, a TiO₂/Z907 film which was heated at 190 °C for 1 minute was immersed in toluene for 20 hours. Its absorption spectrum is also the same the one with TPD melt-processed and then removed. It indicates that the toluene treatment for removing TPD does not contribute to the change in absorption observed.

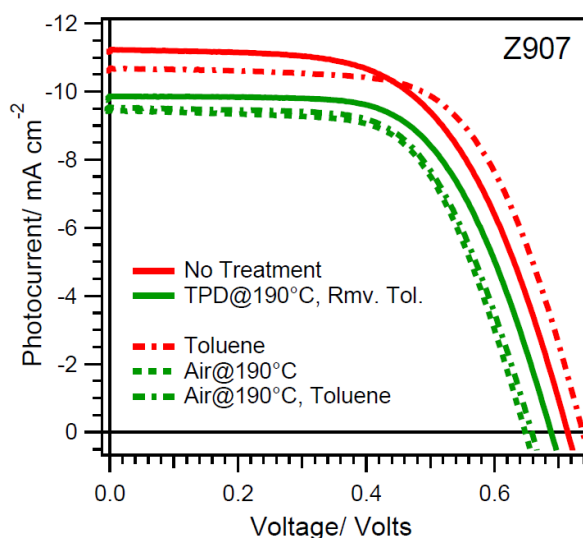


Fig. 4.20 One-sun JV curves of liquid-state DSSCs fabricated with Z907-sensitised TiO_2 electrodes (DyeSol, $7 \mu\text{m}$) having undergone different treatments as noted in legend. Electrolyte was 0.8 M PMII, 50 mM iodine, 50 mM GuSCN, 0.28 M TBP and 25 mM LiI in MPN. (Rmv. Tol. indicates HTM Removed by Toluene)

Table 4.3 One-sun performance of liquid-state DSSCs fabricated with Z907-sensitised TiO_2 electrodes (DyeSol, $7 \mu\text{m}$) having undergone different treatments as noted in legend. Conditions as in Fig. 4.20. (Rmv. Tol. indicates HTM Removed by Toluene)

Treatment	$J_{sc}/$ mA cm^{-2}	$V_{oc}/$ V	Fill Factor	Efficiency/ %
No Treatment	11.2	0.71	0.58	4.61
TPD@190°C, Rmv. Tol.	9.85	0.68	0.62	4.15
Toluene	10.7	0.74	0.63	4.95
Air@190	9.44	0.65	0.63	3.87
Air@190°C, Toluene	9.57	0.65	0.62	3.89

Fig. 4.20 and Table 4.3 show the change in JV 's of the liquid-state DSSCs assembled with the TiO_2 electrodes mentioned above. DSSCs made with the three 190 °C-treated films show similar decrease in JV characteristics (the three green curves), no matter treated with TPD and/or toluene or not. They show a ~15 % decrease in short-circuit current density (J_{sc}) and a 30-60 mV reduction in open-circuit voltage (V_{oc}). These data show that during melt-processing of TPD, the detrimental effect on $\text{TiO}_2/\text{Z907}$ film and the performance of the resultant liquid-state DSSCs is relatively small and caused by the heat applied. A cell with $\text{TiO}_2/\text{Z907}$ electrodes not heated nor treated in toluene only shows small change in JV characteristics, relative to the control cell which electrode has undergone no treatment. The observed change may be partly contributed by the removal of proton from the TiO_2 surface during the toluene treatment. This will result in a higher conduction band level and reduce

injection. If it is the case, the effect is relatively small as shown in Fig. 4.20. Another possible explanation for the observed change is simply random variation.

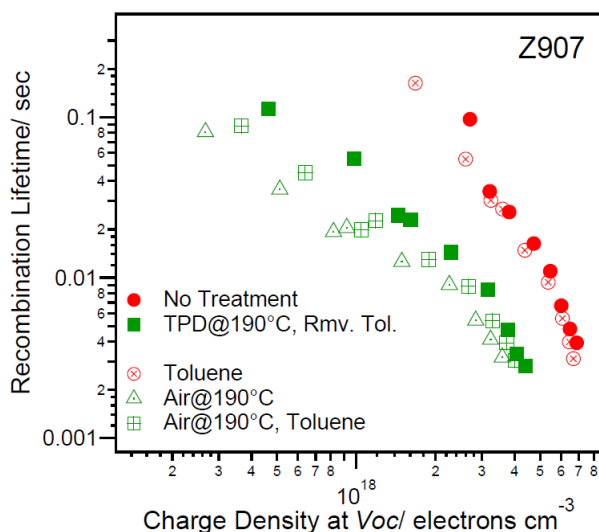


Fig. 4.21 Recombination lifetime vs. charge density of liquid-state DSSCs fabricated with Z907-sensitised TiO₂ electrodes (DyeSol, 7 μm) having undergone different treatments as noted in legend. Conditions as in Fig. 4.20. (Rmv. Tol. indicates HTM Removed by Toluene)

With an aim to confirm whether the heat applied during melt-processing is the main contributor of the detrimental effect on the resultant cell performance, transient photovoltage and photocurrent and charge extraction measurements were conducted on the same cells above. Fig. 4.21 shows the change in recombination lifetime of these cells. All the three cells with films treated at 190 °C show a similar reduction in recombination lifetime by a factor of ~6, relative to the control cell with non-treated film. This is sufficient to explain the drop in *J_{sc}*'s and *V_{oc}*'s of these cells.

Moreover, no significant change was observed in charge density versus *V_{oc}*, charge density versus *J_{sc}* and transport lifetime upon any of the above treatments (as shown in Fig. A.18, A.19 and A.20 in Appendix respectively). This supports the conclusion that it is the heat applied during melt-processing of TPD which reduces the recombination lifetime and it is the reduced recombination lifetime that causes a decline in the resultant cell performance when compared to the control cell.

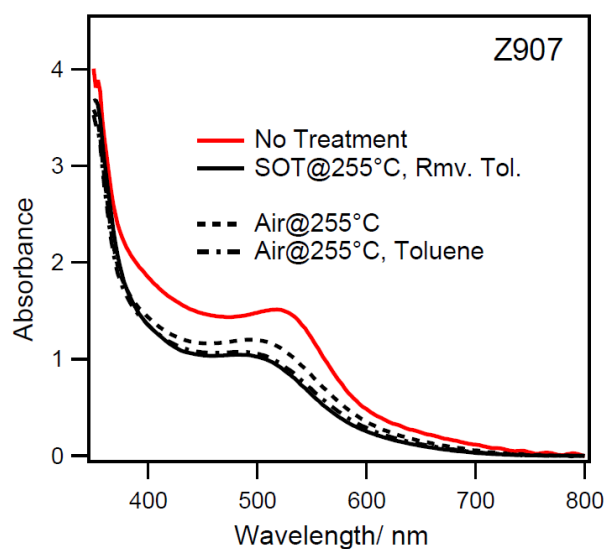


Fig. 4.22 Absorption spectra of Z907-sensitised TiO₂ film (DyeSol, 7 μm) before and after different treatments as noted in legend. (Rmv. Tol. indicates HTM Removed by Toluene)

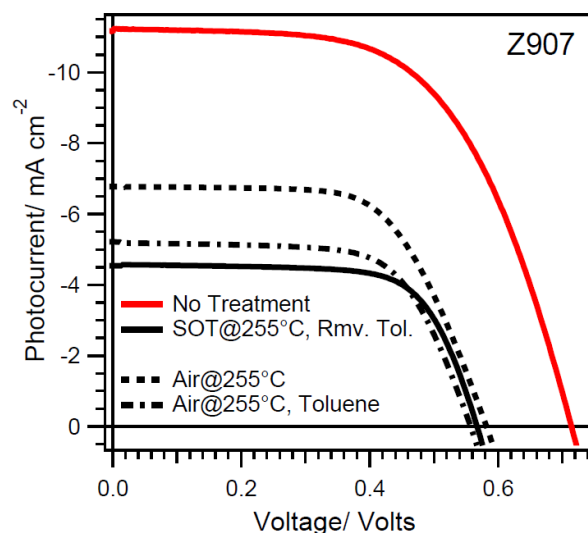


Fig. 4.23 One-sun *JV* curves of liquid-state DSSCs fabricated with Z907-sensitised TiO₂ electrodes (DyeSol, 7 μm) having undergone different treatments as noted in legend. Electrolyte was 0.8 M PMII, 50 mM iodine, 50 mM GuSCN, 0.28 M TBP and 25 mM LiI in MPN. (Rmv. Tol. indicates HTM Removed by Toluene)

Table 4.4 One-sun performance of liquid-state DSSCs fabricated with Z907-sensitised TiO₂ electrodes (DyeSol, 7 μm) having undergone different treatments as noted in legend. Conditions as in Fig. 4.23.

Treatment	<i>J</i> _{sc} / mA cm ⁻²	<i>V</i> _{oc} / V	Fill Factor	Efficiency/ %
No Treatment	11.2	0.71	0.58	4.61
SOT@255°C, Rmv. Tol.	5.21	0.56	0.65	1.88
Air@255°C	6.77	0.58	0.62	2.43
Air@255°C, Toluene	4.60	0.55	0.68	1.68

A similar series of experiments were performed on TiO₂/Z907 films with spiro-OMeTAD. Again, the absorption spectra of the three 255 °C-treated TiO₂/Z907 films are almost the same. It could be said the film which was heated at 255 °C but not treated in toluene shows a slightly higher absorption than the other two toluene-treated film. This would suggest some of the Z907 dye was desorbed in toluene. However the difference may also be within random variations. Fig. 4.23 and Table 4.4 show the *JV* characteristics of the cells assembled with the above films. As expected, the three cells with 255 °C-treated TiO₂/Z907 electrodes show a decrease in both *J*_{sc}'s (40-60 %) and *V*_{oc}'s (130-160 mV), relative to the control cells with non-treated electrodes. It is also noted that among the three cells with 255 °C-treated TiO₂/Z907 electrodes, the one not treated in toluene shows a higher *J*_{sc} by 30-40 % than the other 2 toluene-treated ones. Integration of their absorption spectra with AM 1.5 spectrum shows that the absorbed photon flux is only ~10 % higher in the cells with film not treated in toluene. This cannot fully explain the difference in photocurrent in these cells. Transient photovoltage measurements were then taken on these cells.

The recombination lifetimes of all the three cells with 255 °C-treated TiO₂/Z907 electrodes are two orders of magnitude shorter than the control cells with non-treated electrodes as shown in Fig. 4.24. Among these three cells with 255 °C-treated TiO₂/Z907 electrodes, the longer recombination lifetime (by a factor of 3) in the cell with electrode not treated in toluene than the other two can explain the high *J*_{sc} in this cell. The reason for the difference in recombination lifetime in these cells is not clear. More experiments will be needed to find out why. But in any case, this difference is still a lot smaller than that between the 255 °C-treated and non-treated ones. It can still be concluded that the heat applied to the TiO₂/Z907 film during melt-processing of spiro-OMeTAD is the main contributor to the decrease in resultant cell performance, relative to the control cells assembled with non-treated film.

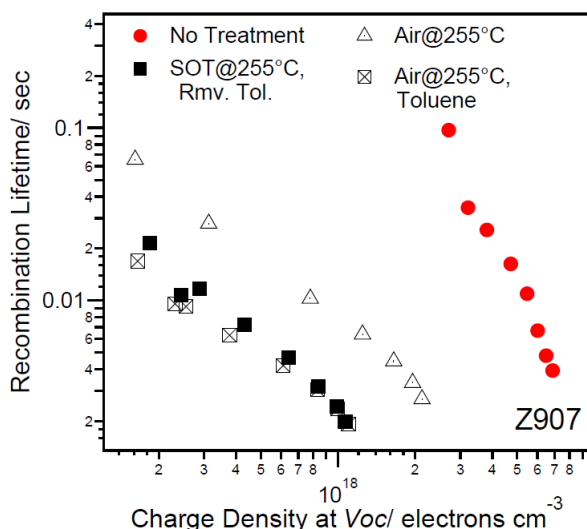


Fig. 4.24 Recombination lifetime vs. charge density of liquid-state DSSCs fabricated with Z907-sensitised TiO₂ electrodes (DyeSol, 7 μm) having undergone different treatments as noted in legend. Conditions as in Fig. 4.23. (Rmv. Tol. indicates HTM Removed by Toluene)

TiO₂/D149 Films

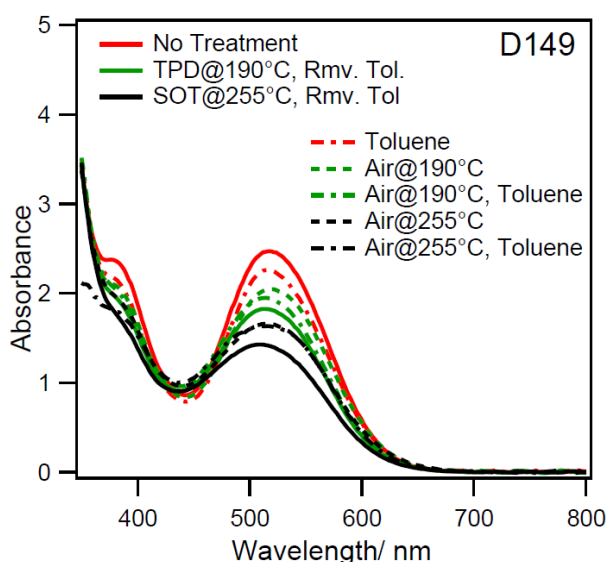


Fig. 4.25 Absorption spectra of D149-sensitized TiO₂ film (DyeSol, 7 μm) before and after different treatments as noted in legend. (Rmv. Tol. indicates HTM Removed by Toluene)

To test generality of the results shown in the TiO₂/Z907 series, similar experiments were conducted on the D149 dye. The data in Fig. 4.25 follow the general trend that the peak absorption decreases with temperature. More importantly, the presence of hole transporting materials (HTMs) during the heating process does not cause any significant additional change in absorption of the TiO₂/D149 films, relative to the film which was heated at the same temperature without HTMs. Fig. 4.26 and Table 4.5 show the variation in *JV* characteristics of cells assemble with TiO₂/D149 treated in different ways. The cells with the TPD-treated and the other two 190 °C-treated films show a decrease of only 50-70 mV in *Voc* and essentially no

change in J_{sc} relative to the control cells with non-treated films. Among the three cells with 190 °C-treated films, no significant difference is observed in their JV characteristics. A more significant decrease in cell performance (20-30 % drop in J_{sc} and 140-190 mV decrease in V_{oc}) is observed in the three cells with 255 °C-treated films, which can be explained by the 30-fold reduction in recombination lifetime, when compared to the control cells as shown in Fig. 4.27. But more importantly, the variation shown in the JV characteristics and recombination lifetime among the three cells with 255 °C-treated films is relatively small, when compared to the difference between them and the control cell. This again leads to the conclusion that it is the heat applied to the TiO_2 /D149 electrodes during melting process of TPD or spiro-OMeTAD which causes the detrimental effect on the resultant cell performance, when compared to the control cells.

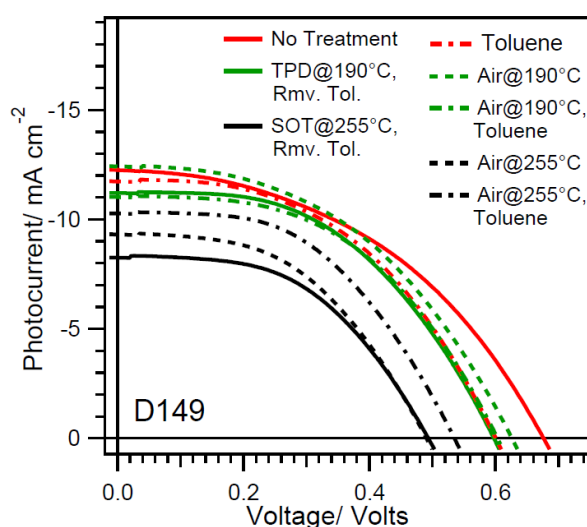


Fig. 4.26 One-sun JV curves of liquid-state DSSCs fabricated with D149-sensitized TiO_2 electrodes (DyeSol, 7 μm) having undergone different treatments as noted in legend. Electrolyte: 0.8 M NaI, 40 mM iodine and 0.2 M GuSCN in MPN. (Rmv. Tol. indicates HTM Removed by Toluene)

Table 4.5 One-sun performance of liquid-state DSSCs fabricated with Z907-sensitised TiO₂ electrodes (DyeSol, 7 μm) having undergone different treatments as noted in legend. Conditions as in Fig. 4.26. (Rmv. Tol. indicates HTM Removed by Toluene)

Treatment	$J_{sc}/$ mA cm^{-2}	$V_{oc}/$ V	Fill Factor	Efficiency/ %
No Treatment	12.3	0.67	0.44	3.65
TPD@190°C, Rmv. Tol.	11.2	0.59	0.49	3.27
SOT@255°C, Rmv. Tol.	8.39	0.49	0.49	2.01
Toluene	11.81	0.59	0.48	3.37
Air@190°C	12.5	0.62	0.46	3.59
Air@190°C, Toluene	11.1	0.60	0.49	3.26
Air@255°C	9.33	0.48	0.49	2.20
Air@255°C, Toluene	10.3	0.53	0.50	2.72

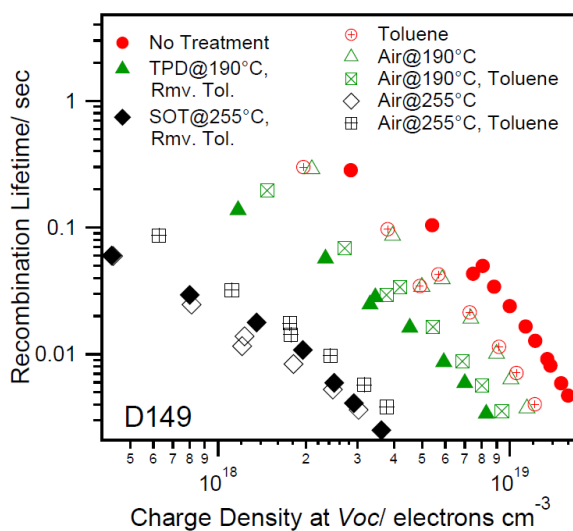


Fig. 4.27 Recombination lifetime vs. charge density of liquid-state DSSCs fabricated with Z907-sensitised TiO₂ electrodes (DyeSol, 7 μm) having undergone different DSSC treatments as noted in legend. Conditions as in Fig. 4.26. (Rmv. Tol. indicates HTM Removed by Toluene)

4.2.3.3 Effect of Heat on Thinner TiO₂/Dye Films (1-2 μm) and the Resultant Cell Performance

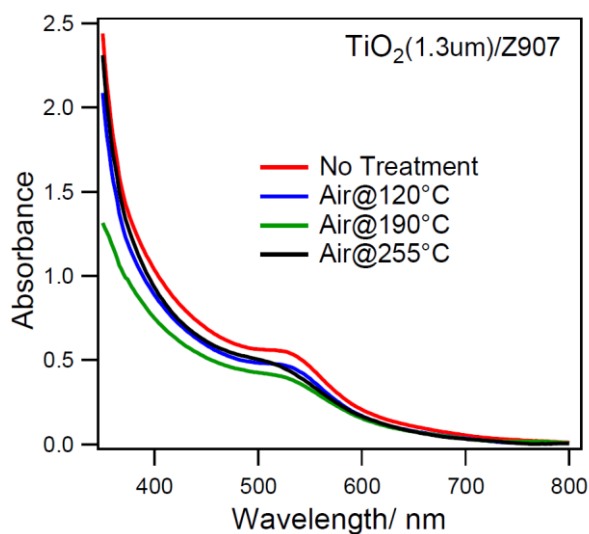


Fig. 4.28 Absorption spectra of Z907-sensitised TiO₂ film (transparent, 1.3 μm) after 1 minute heating at different temperatures. [This figure is reproduced with the permission of the rights holder, The Royal Society of Chemistry.]¹¹⁹

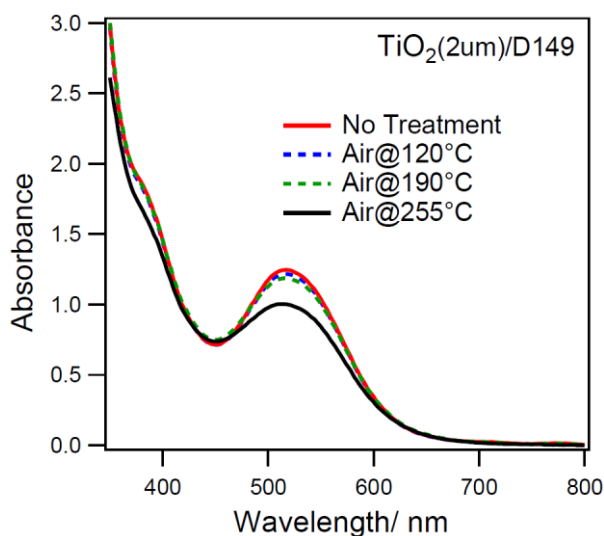


Fig. 4.29 Absorption spectra of D149-sensitised TiO₂ film (transparent, 2 μm) after 1 minute heating at different temperatures. [This figure is reproduced with the permission of the rights holder, The Royal Society of Chemistry.]¹¹⁹

The thickness of the TiO₂ films employed in most solid-state DSSCs is limited to 2 μm due to the pore-filling issues described in Chapter 1. In order to mimic the effect of heating on this kind of cell, TiO₂ films with a thickness of 1-2 μm were prepared and sensitised by either Z907 or D149. Again, a general trend that higher temperature causes a blue-shift and a decrease in peak absorbance in Z907 cells is found. In the case of D149, heating the electrode at 120 °C and 190 °C does not change the absorption spectrum while the same treatment at 255 °C reduces the peak absorbance but does not cause any blue-shift, relative to the control cells.

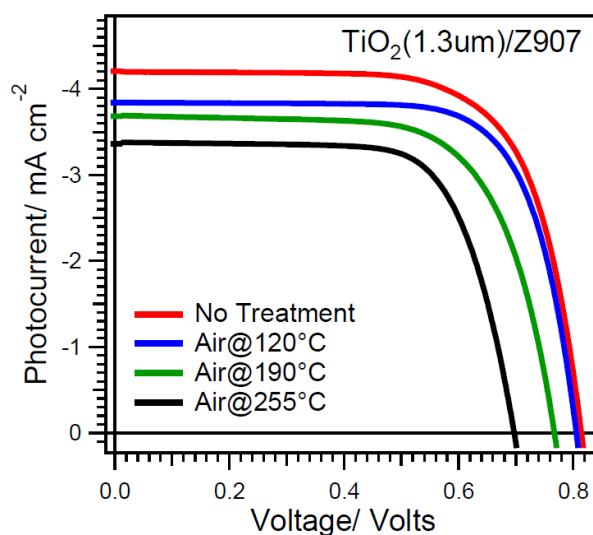


Fig. 4.30 One-sun JV curves of liquid-state DSSCs fabricated with Z907-sensitised TiO_2 electrodes (transparent, $1.3 \mu\text{m}$) heated at different temperatures for 1 minute. Electrolyte: 0.8 M PMII, 50 mM iodine, 50 mM GuSCN, 0.3 M benzimidazole in MPN. [This figure is reproduced with the permission of the rights holder, The Royal Society of Chemistry.]¹¹⁹

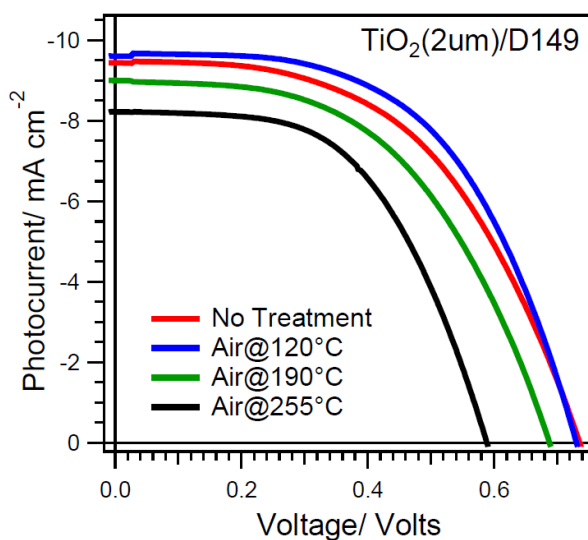


Fig. 4.31 One-sun JV curves of liquid-state DSSCs fabricated with D149-sensitised TiO_2 electrodes (transparent, $2 \mu\text{m}$) heated at different temperatures for 1 minute. Electrolyte: 0.8 M NaI, 40 mM iodine and 0.2 M GuSCN in MPN. [This figure is reproduced with the permission of the rights holder, The Royal Society of Chemistry.]¹¹⁹

Table 4.6 One-sun performance of liquid-state DSSCs fabricated with TiO₂/Z907 and TiO₂/D149 electrodes having undergone different treatments. Conditions as in Fig. 4.30 and 4.31. [This table is reproduced with the permission of the rights holder, The Royal Society of Chemistry.]¹¹⁹

Dye and Treatment	<i>J</i>_{sc}/ mA cm⁻²	<i>V</i>_{oc}/ V	Fill Factor	Efficiency/ %
Z907, No Treatment	4.20	0.81	0.70	2.39
Z907, Air@120°C	3.84	0.80	0.73	2.25
Z907, Air@190°C	3.69	0.77	0.68	1.92
Z907, Air@255°C	3.36	0.69	0.72	1.67
D149, No Treatment	9.49	0.73	0.52	3.58
D149, Air@120°C	9.63	0.73	0.56	3.90
D149, Air@190°C	8.98	0.68	0.52	3.16
D149, Air@255°C	8.22	0.58	0.55	2.61

Fig. 4.30 and 4.31, and Table 4.6 show the variation in *JV*'s of the liquid-state DSSCs made with 1-2 μm thick TiO₂ film sensitised by Z907 and D149 upon heating at different temperatures. The decrease in *J*_{sc}'s for cells with TiO₂/Z907 electrodes of 1.3 μm thickness is generally smaller than that of 7 μm thickness shown in Fig. 4.3. Heating the 1.3 μm thick TiO₂/Z907 electrode at 255 °C for 1 minute prior to cell fabrication decreases the *J*_{sc} by only 20 %, which is about the same as the decrease in the absorbed photon flux. However, the decrease in *V*_{oc} is 120 mV while the reduction in recombination lifetime is still ~30 fold as shown in Fig. 4.32. This will in principle result in a 5-fold decrease in diffusion length. Since the same decrease in diffusion length will have a smaller effect in thinner films, this data supports the conclusion that the loss in photocurrent in 7 μm films is mainly caused by the decrease in collection efficiency. For the D149 series, the trend with thinner TiO₂ electrodes (2 μm) is similar. Treatment on TiO₂/D149 films at 255 °C prior to cell fabrication decreases the *J*_{sc} and *V*_{oc} by ~13 % and 150 mV respectively. This change is mainly caused by the ~6-fold reduction in recombination lifetime as shown in Fig. 4.33. It is noted that the increase in *J*_{sc} and fill factor in the cell with electrode treated at 120 °C is probably due to random variations.

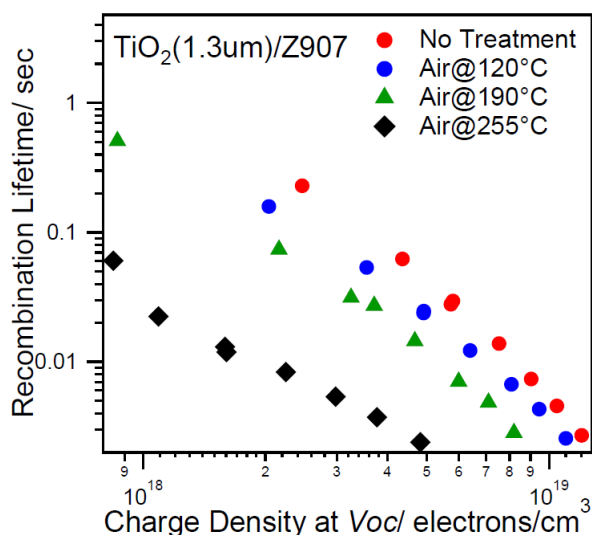


Fig. 4.32 Recombination lifetime vs. charge density of liquid-state DSSCs fabricated with Z907-sensitised TiO₂ electrodes (transparent, 2 μm) heated at different temperatures for 1 minute. Conditions as in Fig. 4.30. [This figure is reproduced with the permission of the rights holder, The Royal Society of Chemistry.]¹¹⁹

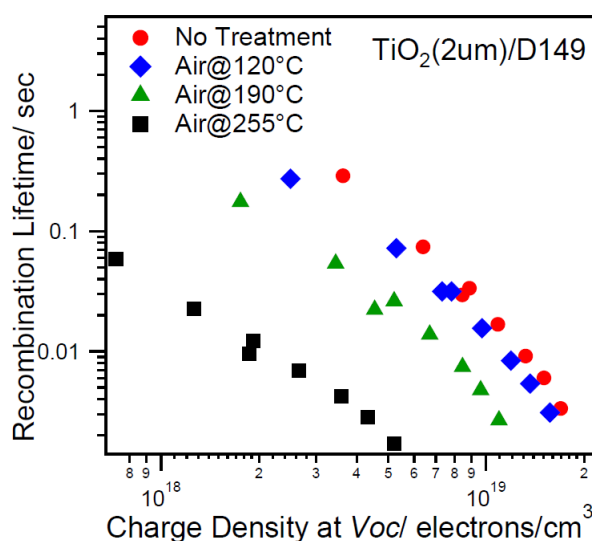


Fig. 4.33 Recombination lifetime vs. charge density of liquid-state DSSCs fabricated with D149-sensitised TiO₂ electrodes (transparent, 2 μm) heated at different temperatures for 1 minute. Conditions as in Fig. 4.31. [This figure is reproduced with the permission of the rights holder, The Royal Society of Chemistry.]¹¹⁹

4.2.3.4 Fabricating Solid-State DSSCs by Melt-Processing Hole Transporting Materials (HTMs)

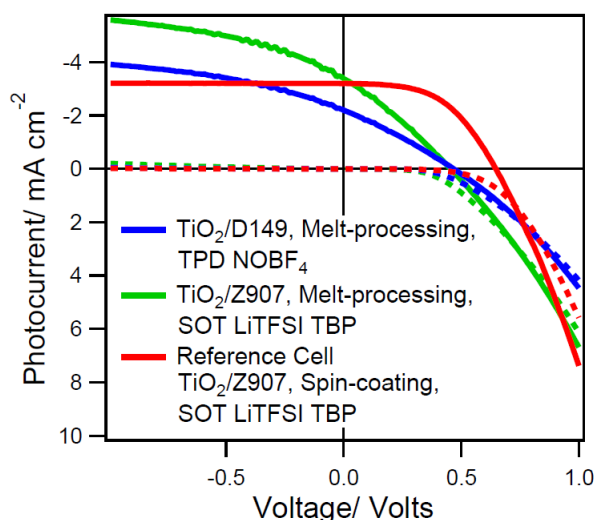


Fig. 4.34 *JV* curves of the two best solid-state DSSCs fabricated by melt-processing HTMs and a reference cell fabricated by spin-coating solution of spiro-OMeTAD (SOT). Compositions are shown in Table 4.7. (one-sun *JV*: solid line; dark *JV*: dotted line). [This figure is reproduced with the permission of the rights holder, The Royal Society of Chemistry.]¹¹⁹

Table 4.7 One-sun performance of the best solid-state DSSCs fabricated by melt-processing HTMs and a reference cell fabricated by spin-coating solution of spiro-OMeTAD (SOT). [This table is reproduced with the permission of the rights holder, The Royal Society of Chemistry.]¹¹⁹

Dye	TiO ₂ film (thickness)	HTMs	<i>Jsc</i> / mA cm ⁻²	<i>Voc</i> / V	Fill Factor	Efficiency/ %
D149	Scattering (2 μm)	Melt-processing TPD, doped by NOBF ₄	2.16	0.46	0.35	0.35
Z907	Scattering (2 μm)	Melt-processing SOT, Li-TFSI and TBP	3.30	0.46	0.30	0.45
Z907	Scattering (2 μm)	Spin-coating SOT, Li-TFSI and TBP in chlorobenzene	3.20	0.64	0.54	1.11

Noticing the relatively small detrimental effect of heat on performance of cells with 1-2 μm TiO₂/dye films, solid-state DSSCs were then fabricated by melt-processing TPD (m.p. ~180 °C) and spiro-OMeTAD (m.p. ~248 °C).⁷⁰ Fig. 4.34 and Table 4.7 show the *JV* results of these cells. The D149 cell melt-processed with TPD was fabricated by R. Spence, a MSci student in our research group. This result is included here because it is one of the most efficient solid-state DSSCs fabricated by melt-processing HTMs. For purpose of comparison, a reference cell was fabricated by spin-coating solution of spiro-OMeTAD and the results are also presented in Fig. 4.34 and Table 4.7. From the results of liquid-state DSSCs, a significant impact on the *Jsc* from melt-processing procedure would not be expected. Nevertheless, the *Jsc*'s of these melt-processed cells are in fact lower than expected from a 2 μm thick film with either D149 or Z907. This is in part due to the high series resistance (*R*_{ser}) of the HTM layer.

The series resistance of each cell can be calculated from the slope of the far forward bias portion of its JV . The R_{ser} of the melt-process TPD and spiro-OMeTAD are 85 and 60 ohms respectively, compared to 26 ohms in the spin-coated cell. In literature, it was demonstrated that the R_{ser} an efficient cell can be below 20 ohms.⁴⁶ Since the dark JV curves of both TPD and spiro-OMeTAD do not show any signs of current leakage at reverse bias, the photocurrent measured at reverse bias can be used to compare the photocurrent generation in the TiO_2 /dye electrodes. As shown in Fig. 4.34, the photocurrent generation of the melt-processed TiO_2 /Z907/spiro-OMeTAD cell is at least 5.5 mA cm^{-2} , which is close to the photocurrent expected from a $2 \mu\text{m}$ thick TiO_2 /Z907 film. The same cell fabricated by spin-coating solution of spiro-OMeTAD only gave 3.2 mA cm^{-2} . This suggests that the melt-processing cell shows a better charge generation and collection, which is possibly caused by a higher pore filling by spiro-OMeTAD than spin-coated cell. On the other hand, the photocurrent of the TiO_2 /D149/TPD measured at reverse bias is only half that of a $2 \mu\text{m}$ liquid-state cell assembled with $190 \text{ }^\circ\text{C}$ -treated film. The reason for the relatively low photocurrent is still unclear. The V_{oc} 's in both of the melt-processed cells are only 0.46 V, which is relatively low when compared with 0.64 V achieved in the spin-coated spiro-OMeTAD cells. In literature, efficient cells with spin-coated spiro-OMeTAD has even reached 0.98 V.⁴⁶

4.2.4 Discussion

It is found that treating TiO_2 /dye electrodes with or without hole transport materials at the same temperature result in similar absorption spectra and JV characteristics. Therefore, it is the heat applied to the TiO_2 /dye film during melt-processing of HTMs that causes the detrimental effect on the performance of liquid junction cells assembled with it. However, the heat applied is not the only contributor the relatively low efficiency of melt-processed cells reported in this thesis. It has been discussed in the Results section that the lower than expected J_{sc} 's are partly due to the high R_{ser} . In fact, the high R_{ser} in the melt-processed cells is mainly caused by overlayer of HTM sitting on top of the TiO_2 /dye electrode. The thickness of the overlayer of the melt-processed TPD and spiro-OMeTAD is found to be 2 and $5 \mu\text{m}$ respectively, compared to $\sim 200 \text{ nm}$ in the spin-coated one. Moreover, in the case of TPD cell where the TPD was doped by gaseous $NOBF_4$ after melt-processing. It is likely that the $NOBF_4$ was not able to reach the TPD which was deep inside the TiO_2 film, leaving the TPD there undoped. This would then increase the overall series resistance of the cell. On the other hand, the relatively high series resistance in spiro-OMeTAD cells might also be due to an uneven distribution of bis(trifluoromethane)sulfonamide lithium salt (Li-TFSI) in the spiro-OMeTAD melt during the

melt-processing process. The addition of Li-TFSI has been reported to give similar effects to spiro-OMeTAD as a p-dopant¹²¹ and a complex doping mechanism involving oxygen has been suggested by Abate *et al.*¹²² In this reaction mechanism, the oxidation of spiro-OMeTAD is catalysed by Li⁺ ions while TFSI stabilises the oxidised form of spiro-OMeTAD. Thus, an inhomogeneous distribution of oxidised spiro-OMeTAD will then result in a high resistance across the spiro-OMeTAD layer. The V_{oc} 's of the two melt-processed cells are both 0.46 V, which is relatively low. In the case of spiro-OMeTAD cell where Li-TFSI and the base 4-*tert*-butylpyridine (TBP) were melt-processed together with spiro-OMeTAD, much of the TBP (b.p. ~ 197 °C) presumably evaporated during the melt-processing which took place at 255 °C. Therefore, the low V_{oc} may also be partly due to the loss of TBP since base is added to DSSCs to increase the V_{oc} and spiro-OMeTAD without TBP have been reported to give significantly lower V_{oc} .^{61, 123} On the other hand, it is not clear yet if increased recombination is a contributor to this.

A melt-infiltration technique which is similar to the melt-processing method employed in this study has been reported recently.¹²⁴ A solution spiro-MeTAD with Li-TFSI and TBP in chlorobenzene was first spin-coated on a TiO₂/D35 film in air. The TiO₂/D35/spiro-OMeTAD film was then heated at 280 °C for 30 seconds in a nitrogen glovebox to let the spiro-OMeTAD melt to infiltrate the mesoporous TiO₂ film. This resulted in an increase in pore-filling fraction from 63 % to 94 %, calculated using SEM images. Also the overlayer thickness of spiro-OMeTAD was reduced to ~ 350 nm, which led to a series resistance of < 20 ohms in the resultant cell as shown in the far forward bias of its JV curve. However, the cell produced an overall efficiency of only 0.33 % and a low V_{oc} of 0.42 V, which is in good agreement with the results of the melt-processed spiro-OMeTAD cell shown in Fig. 4.34 and Table 4.7. The authors also attributed the low V_{oc} to the loss of TBP upon heating, which was supported by a red-shift in the absorption peak of the D35 dye after the melt-infiltration process.

4.2.5 Conclusion

The results in this chapter imply that melt-processing of HTMs to make solid-state DSSCs should be feasible. Indeed, the first solid-state DSSC fabricated by melt-processing of spiro-OMeTAD, together with Li-TFSI and TBP, has been presented here. The cell gives a 1-sun efficiency which, though still only 0.45 %, is ~ 4 times higher than previously reported for melt-processed device. Higher efficiency can be achieved by minimising the overlayer thickness of hole transporting materials left on top of the TiO_2 after the melt-processing procedure. Cell performance can also be improved by utilisation of dyes which show good stability at elevated temperature up to 255 °C when adsorbed on TiO_2 film. Alternatively, melt-processing hole transporting materials which have a melting point < 190 °C can also minimise the detrimental effect on cell performance caused by the heat applied to the TiO_2 /dye electrode. Since the low V_{oc} in our best cell is partly caused by the loss of TBP during melt-processing, replacing TBP by another base with a boiling point > 255 °C will again increase the V_{oc} and thus, the overall efficiency of the cell.

Chapter 5

Preliminary Stability Study on Methylammonium

Lead Halide Perovskite Solar Cells

Abstract

The stability of methylammonium lead triiodide (MAPI) and methylammonium lead iodide chloride (MAPIC) were examined under different humidity, oxygen and light levels. For complete devices with MAPI on mesoporous TiO_2 (mp- TiO_2) scaffold and the polymer P3HT as HTM, it is found that ultra-violet (UV) light causes rapid degradation. Encapsulation significantly enhances the cell stability when tested in air (humidity: ~40 %). Also, heating equivalent cells at 60 °C in the dark for 18 hours does not cause any detrimental effect on cell performance. An encapsulated mp- TiO_2 /MAPI/spiro-OMeTAD solar cell was fabricated. After exposing to 40 sun-equivalent (SE) illumination for 63 hours, the J_{sc} of the cell at 1 SE drops by 7 % only while the V_{oc} decreases by 190 mV.

5.1 Introduction

Most literature in the rapidly expanding area of hybrid perovskite solar cells focuses on the efficiency of devices, with little attention being paid to the critical issue of stability. As a film, methylammonium lead triiodide (MAPI) films was found to show a colour change from brown to yellow when exposed to water.¹²⁵ Reports suggested that water may react with MAPI to form yellow crystals of $(\text{CH}_3\text{NH}_3)_4\text{PbI}_6 \cdot 2\text{H}_2\text{O}$.¹²⁶ On the other hand, methylammonium lead iodide chloride (MAPIC) perovskite was first claimed to be stable to processing in air by Lee *et al.*⁷⁵ Nonetheless, the same research group later reported that MAPIC films are extremely sensitive to water in air until fully crystallised.¹²⁷ MAPIC films have then been generally processed in dry nitrogen filled gloveboxes. Recently, the same research group showed that formamidinium lead triiodide did not show any colour change when stored at 150 °C in air for 60 minutes whereas the colour of MAPI changed from brown to yellow.¹²⁸ However, when being kept in a ~100 % relative humidity atmosphere, the rate of degradation (colour change) of the MAPI films is similar. Study on the stability of complete cells is also limited. Among the stability tests reported in literature, the cells are often stored either in the dark,⁷⁴ encapsulated,⁷⁹ or exposed to a relatively low temperature of 40-45 °C.^{79, 83} Therefore, little is known about the effect of light (including UV light), water and oxygen in air, and heat on complete devices.

In this project, some preliminary stability tests were performed on MAPI and MAPIC films and their solar cells. Six series of perovskite films were prepared. Each series consists of six different perovskite films: flat MAPI (flat layer refers to a compact layer without any mesoporous particles), flat MAPIC, MAPI on mesoporous TiO_2 (mp- TiO_2 /MAPI), mp- TiO_2 /MAPIC, MAPI on mesoporous Al_2O_3 (mp- Al_2O_3 /MAPI) and mp- Al_2O_3 /MAPIC. Each series of films were tested under different humidity levels in air and under light. Photographs of the films were taken after certain time of storage to record to the change in their colour. For complete devices, a series of mp- TiO_2 /MAPI/P3HT solar cells were fabricated. The effect of encapsulation and the cell stability against UV light, heat were examined. For long term stability test, an encapsulated mp- TiO_2 /MAPI/spiro-OMeTAD solar cell was exposed to 40 sun-equivalent (SE) illumination for 63 hours (which delivers over 2500 hours equivalent of 1 sun photo-excitations to the cell). The experimental results will be presented and discussed in this chapter.

5.2 Experimental Methods

Preparation of MAPI and MAPIC Perovskite Films

Glass microscope slides were cut into 1.2 x 1.2 cm² pieces. The glass substrates were cleaned with a glass cleaner, followed by rinsing with deionised (DI) water and IPA. After drying in air for 10 minutes, they were heated on the hotplate (Detlef Gestigkeit Elektrotechnik) at 450 °C for 30 minutes. For mp-TiO₂ films, a diluted paste of TiO₂ nanoparticles from G24i (17 wt% in water) was spin-coated onto the substrates, which was then heated at 450 °C for 30 minutes. For films with mp-Al₂O₃, a diluted alumina paste, prepared by Dr. X. Li in our laboratory as reported previously,¹²⁹ was spin-coated onto the substrates, which was then heated at 400 °C for 30 minutes. The thickness of the TiO₂ and Al₂O₃ films was ~150 nm as measured by the Tencor Alphastep 200 Automatic Step Profiler.

For MAPI films, a 1:1 molar solution of lead iodide and methylammonium iodide in gamma-butyrolactone (1.25 M) was heated and stirred at 60 °C for 1-2 hours until a clear yellow solution was formed. Before use, the mixture was allowed to cool to room temperature and any precipitate was separated from the solution via centrifuging at 8000 revolutions per minute (rpm) for 30 minutes. The supernatant was transferred to another vial where it was diluted by 1/3 with gamma-butyrolactone (GBL). For MAPIC films, a 1:3 molar solution of lead chloride (0.29 M) and methylammonium iodide (0.88 M) in dimethylformamide (DMF) was stirred at room temperature for 1 hour until a clear yellow solution was formed. The solution for MAPI or MAPIC films was spread onto the glass substrate (without mesoporous layer, with mp-TiO₂ or with mp-Al₂O₃) and allowed to sit for 45 seconds and then spin-coated at 1200 rpm for 45 seconds in the glovebox. The substrates with MAPI and MAPIC were then dried at 100 °C for 15 and 45 minutes respectively. The thickness of flat MAPI and MAPIC film on glass without mesoporous layer was also ~150 nm.

Each of the six series of films was stored in a different environment: GB-Dark, GB-Light, Dry-Dark, Dry-Light, Wet-Dark and Wet-Light. The details of each environment were shown in Fig. 5.1. White light-emitting diodes (LEDs) with no ultra-violet (UV) emission were used for illumination. Photographs of films were taken by a Sony DSC-L1 camera as made and after 2 hours, 18 hours, 5 days and 2 weeks of storage. It is noted that the films were taken out of their specific storage environment and left in air (humidity: 40 %, i.e. 6.9 g/m³ at 20 °C) for 5-10 minutes when their photographs were taken. For the Dry-Light, Wet-Dark and Wet-Light series, after storage for 2 weeks, the films were heated at 110 °C for 30 minutes. After that, photographs were taken on them again.

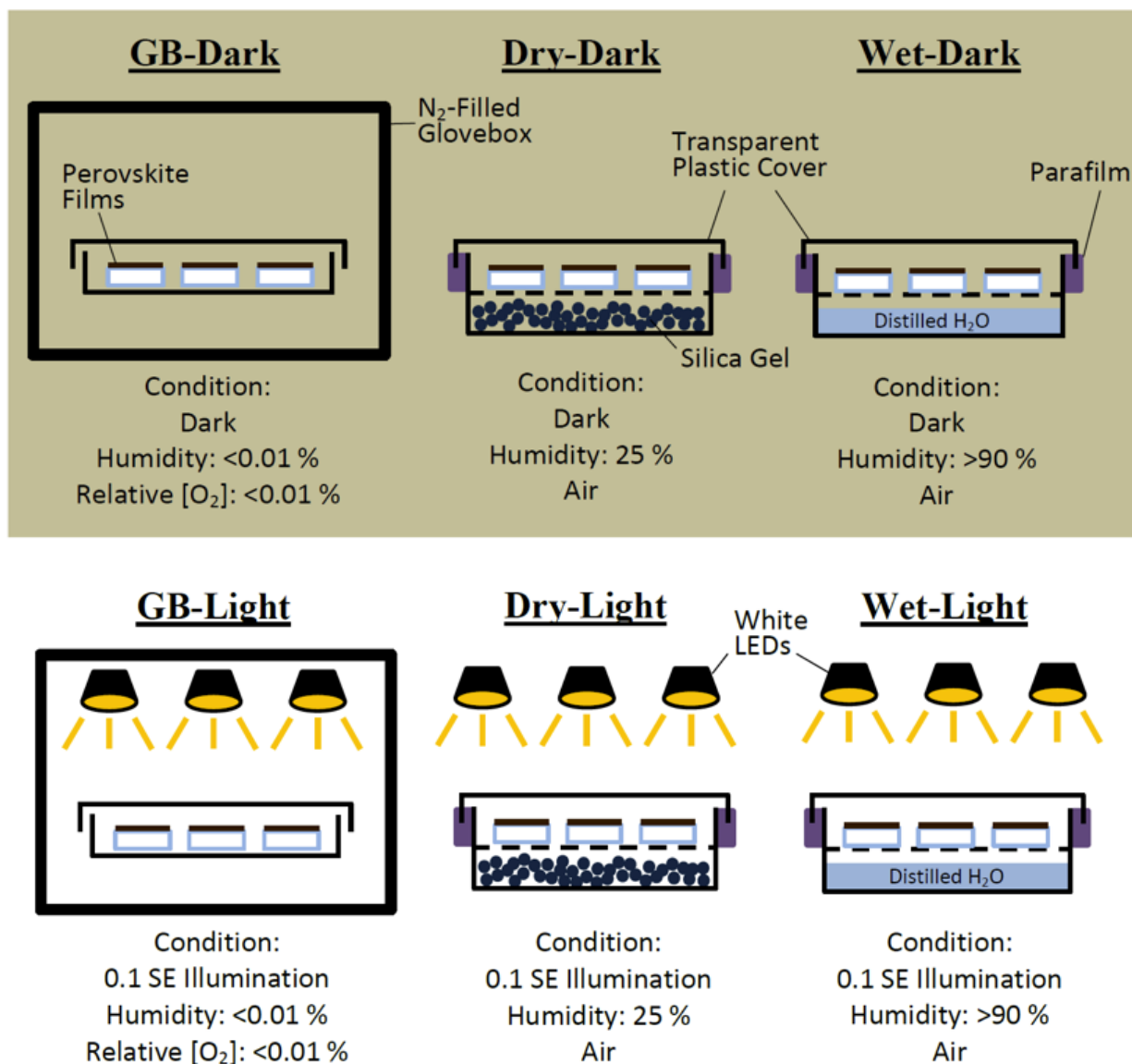


Fig. 5.1 Schematic diagram showing the conditions in which the perovskite films were stored in during the stability test.

MAPI Perovskite Solar Cells

Three types of perovskite solar cells, mp-TiO₂/MAPI/P3HT, mp-TiO₂/MAPI/DPPTTT and mp-TiO₂/MAPI/spiro-OMeTAD, were fabricated as described in Chapter 2. The high light J_{sc} and JV measurements were taken with a Ministat Mark IV potentiostat (0-1 Amp). Illumination was provided by a Luxium plasma lamp (LIFI 4000P 230 Watt), which has a rated output of 4500 lumens. Its output spectrum was shown in Fig. 5.2 and almost all of it is within the visible range. It is noted that the one sun-equivalent (SE) energy of this spectrum will vary depending on the absorption spectrum of the cell under investigation. A 420 nm cutoff filter was used to eliminate UV light when mentioned. Intensity of light incident on solar cells was controlled by varying the distance of the cell from the focal point of the light source. The

distance for one sun-equivalent (SE) illumination was determined for each solar cell by measuring the J_{sc} under simulated AM1.5 irradiation, then varying the distance of cell from Luxim lamp until the same J_{sc} was found. The SE values for other distances were determined from a measured calibration curve. For J_{sc} vs. time experiment, the cell was illuminated at short circuit almost all the time apart from the short periods of time when JV curves were measured. Current density vs. voltage, transient photovoltage and photocurrent, and charge extraction at open and short circuit were measured as described in Chapter 2.

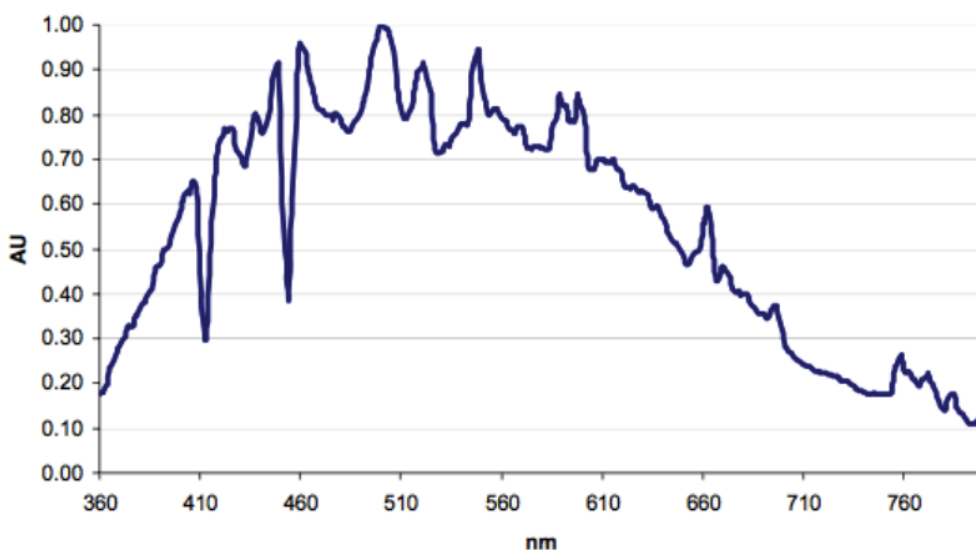


Fig. 5.2 Output spectrum of the Luxim plasma lamp from Luxim Corp.

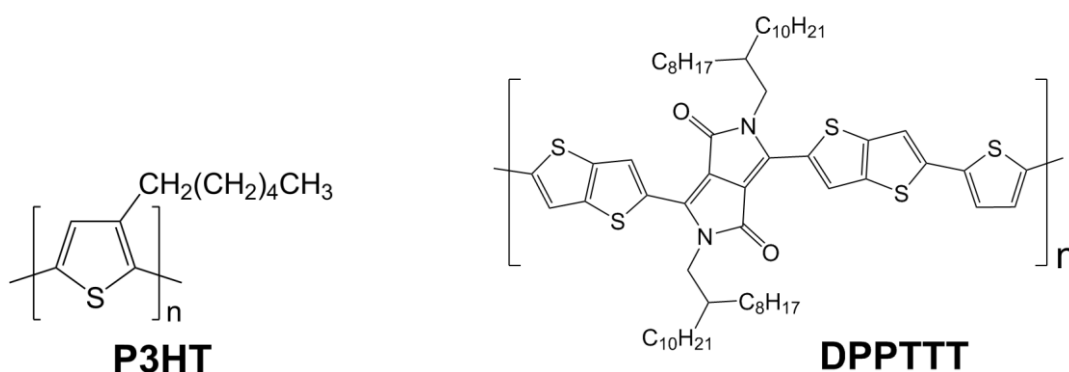


Fig. 5.3 Chemical structures of P3HT and DPPTTT.

5.3 Results

5.3.1 Relative Stability of Perovskite Films against Oxygen and Moisture in Air and Light

Table 5.1 Photos of a series of perovskite films before and after storage for 2 weeks. Film thicknesses (with or without mesoporous layer) are ~150 nm. All films were stored in the dark in a glovebox (humidity: <0.01 %, oxygen level: <0.01 %).


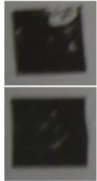



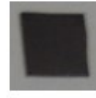

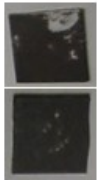




Glovebox, Dark (GB-Dark)						
	Flat MAPI	Flat MAPIC	mp-TiO ₂ /MAPI	mp-TiO ₂ /MAPIC	mp-Al ₂ O ₃ /MAPI	mp-Al ₂ O ₃ /MAPIC
As made						
2 weeks						

Table 5.2 Photos of a series of perovskite films before and after storage for 2 weeks. Film thicknesses (with or without mesoporous layer) are ~150 nm. All films were stored under constant 0.1 sun-equivalent (SE) illumination from white LEDs in a glovebox (humidity: <0.01 %, relative oxygen concentration: <0.01 %).


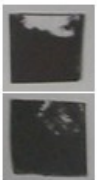

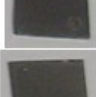



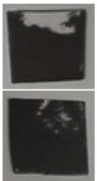






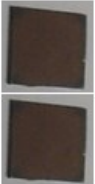



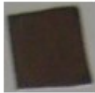
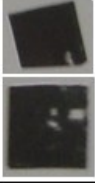
















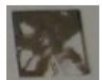







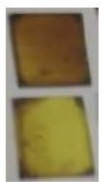





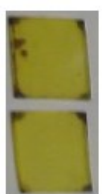









Glovebox, 0.1 SE Illumination (GB-Light)						
	Flat MAPI	Flat MAPIC	mp-TiO ₂ /MAPI	mp-TiO ₂ /MAPIC	mp-Al ₂ O ₃ /MAPI	mp-Al ₂ O ₃ /MAPIC
As made						
2 weeks						

Table 5.3 Photos of a series of perovskite films before and after storage for 2 weeks. Film thicknesses (with or without mesoporous layer) are ~150 nm. All films were stored in the dark in a 'dry' box (humidity: ~25 %, air).

'Dry' Box, Dark (Dry-Dark)						
	Flat MAPI	Flat MAPIC	mp-TiO ₂ / MAPI	mp-TiO ₂ / MAPIC	mp-Al ₂ O ₃ / MAPI	mp-Al ₂ O ₃ / MAPIC
As made						
2 weeks						

As shown in Table 5.1, 5.2 and 5.3, none of the perovskite films shows any observable change in colour after a 2-week storage in the glovebox in the dark (GB-Dark), in the glovebox under 0.1 sun-equivalent (SE) illumination (GB-Light) or in the 'dry' box in the dark (Dry-Dark). The results of GB-Dark and GB-Light show that in the absence of oxygen and water, the application of 0.1-sun illumination from light-emitting diodes (LEDs) does not cause any apparent degradation to the perovskite films during the 2-week testing period. A comparison on the results of GB-Dark and Dry-Dark shows that when stored in the dark, the presence of the relatively small amount of water at 25 % humidity (i.e. 5.8 g/m³ at 25 °C) and atmospheric oxygen does not cause any observable change to the perovskite films during the relatively short testing period.

Table 5.4 Photos of a series of perovskite films before and after storage for different periods of time. Film thicknesses (with or without mesoporous layer) are ~ 150 nm. All films were stored under constant 0.1 sun-equivalent (SE) illumination from white LEDs in a 'dry' box (humidity: $\sim 25\%$, air).

'Dry' Box, 0.1 SE Illumination (Dry-Light)						
	Flat MAPI	Flat MAPIC	mp-TiO ₂ / MAPI	mp-TiO ₂ / MAPIC	mp-Al ₂ O ₃ / MAPI	mp-Al ₂ O ₃ / MAPIC
As made						
2 hours						
18 hours						
5 days						
2 weeks						
2 weeks, 30min @ 110 °C						

In the Dry-Light series (see Table 5.4), after 2 weeks of storage, all the perovskite films show a change of colour from brown to yellow in most or part of the film area. The same change in colour has been reported in literature.^{125-126, 130} The yellow films can possibly be lead iodide which is also yellow in colour. But they do not look similar to the control lead iodide films shown in Table A.1 in Appendix. The appearance of the end-products can possibly be explained by the water of crystallisation of perovskite and the formation of yellow $(\text{CH}_3\text{NH}_3)_4\text{PbI}_6 \cdot 2\text{H}_2\text{O}$ crystals as suggested in literature.^{126, 130b, 131}

When comparing the Dry-Light series with the Dry-Dark series, it is clear that light either is required or simply accelerates the colour change of MAPI and MAPIC perovskite films from brown to yellow in the presence of relatively small amount of water (25 % humidity) and atmospheric oxygen. The latter case is more probable as MAPI has also been found to turn yellow in air over time even when stored in the dark.^{130a} When comparing the GB and Dry series, it is apparent that the yellowing of MAPI and MAPIC requires the presence of water or oxygen or both.

With an aim to remove water from the perovskite film, all the films were heated at 100 °C for 30 minutes. All the films stayed the same, showing the colour change is irreversible which agrees with the observation reported in literature.¹²⁵ When comparing different films within the Dry-Light series, it is found that >90 % of the area of flat MAPI, flat MAPIC, mp-TiO₂/MAPI and mp-Al₂O₃/MAPI films turned yellow after 2 weeks while >60 % of the area of mp-TiO₂/MAPIC and mp-Al₂O₃/MAPIC films remained brown. It could be suggested that MAPIC on a mesoporous layer is less sensitive to the effect of light but no definite conclusion can be drawn from the data available here.

Table 5.5 Photos of a series of perovskite films before and after storage for different periods of time. Film thicknesses (with or without mesoporous layer) are ~ 150 nm. All films were stored in the dark in a 'wet' box (humidity: $>90\%$, air).





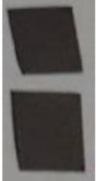



































































'Wet' Box, Dark (Wet-Dark)						
	Flat MAPI	Flat MAPIC	mp-TiO ₂ / MAPI	mp-TiO ₂ / MAPIC	mp-Al ₂ O ₃ / MAPI	mp-Al ₂ O ₃ / MAPIC
As made						
2 hours						
18 hours						
5 days						
2 weeks						
2 weeks, 30min @ 110 °C						

Table 5.6 Photos of a series of perovskite films before and after storage for different periods of time. Film thicknesses (with or without mesoporous layer) are ~150 nm. All films were stored under constant 0.1 sun-equivalent (SE) illumination from white LEDs in a 'wet' box (humidity: >90 %, air).

'Wet' Box, 0.1 SE Illumination (Wet-Light)						
	Flat MAPI	Flat MAPIC	mp-TiO ₂ / MAPI	mp-TiO ₂ / MAPIC	mp-Al ₂ O ₃ / MAPI	mp-Al ₂ O ₃ / MAPIC
As made						
2 hours						
18 hours						
5 days						
2 weeks						
2 weeks, 30min @ 110 °C						

The perovskite films in the Wet-Dark and Wet-Light series (see Table 5.5 and 5.6) show a similar colour change over time. After 18 hours of storage, all the films turn either transparent pale yellow or colourless, which is different to the opaque and intense yellow colour observed in the Dry-Light series. This indicates that the MAPI and MAPIC perovskite films undergo a different mechanism of degradation at a high water level in air. It is found that the transparent

pale yellow or colourless product is similar to the lead iodide control film, which agrees with the postulation that MAPI and MAPIC perovskite degrade entirely to form lead iodide in the presence of sufficient water as the by-products, HI and methylamine, dissolve in water.^{130b} It is also noted that the evolution of perovskite films over time is very similar in the Wet-Dark and Wet-Light series. Therefore, it seems that this degradation mechanism is not significantly or not at all accelerated by light. There is another interesting observation that heating the degraded films in the Wet-Dark series at 110 °C for 30 minutes turned them pale brown/grey. This could be explained by the following hypothesis: a small amount of water saturated with HI and methylamine are left on the surface of the degraded films of lead iodide. Upon heating at 110 °C, water evaporates and lead iodide reacts with the HI and methylamine left behind, resulting in a small amount of MAPI perovskite. However, the same heat treatment on the degraded film in the Wet-Light series does not result in any colour change. Currently, there is no explanation for this experimental observation.

5.3.2 Stability of mp-TiO₂/MAPI Solar Cells

5.3.2.1 Most Efficient mp-TiO₂/MAPI Solar Cells with P3HT, DPPTTT and Spiro-OMeTAD

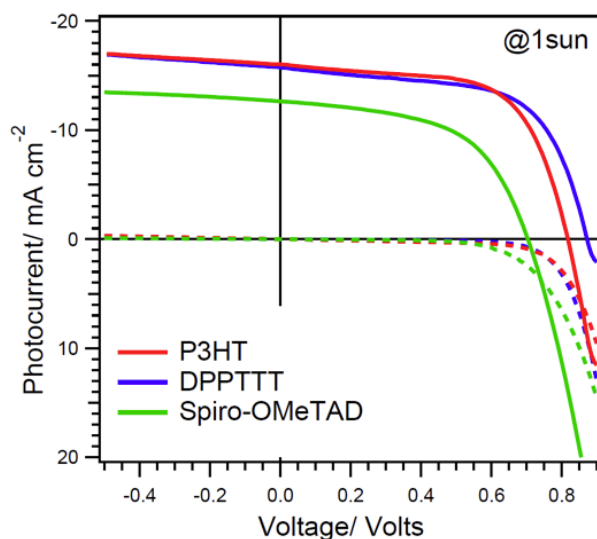


Fig. 5.4 One-sun JV curves of three efficient mp-TiO₂/MAPI solar cells with hole transporting materials (HTMs) as noted in legend.

Table 5.7 One-sun performance of three efficient mp-TiO₂/MAPI solar cells with HTMs as noted.

HTM	$J_{sc}/$ mA cm^{-2}	$V_{oc}/$ V	Fill Factor	Efficiency/ %
P3HT	16.0	0.82	0.63	8.77
DPPTTT	15.7	0.87	0.63	8.61
Spiro-OMeTAD	12.6	0.70	0.56	4.93

Fig. 5.4 and Table 5.7 show the JV results of the best performing mp-TiO₂/MAPI perovskite solar cells with three different hole transporting materials (HTMs). It is noted that the reproducibility of the perovskite cells fabricated for this study is relatively low, when compared to dye-sensitised solar cells. The results of each device shown in Fig. 5.4 and Table 5.7 are the best cells among 15-21 cells of the same type fabricated in 3 different batches. Therefore, it will be noticed that devices of the same type will show some variations in solar cell performance in following parts of the chapter

5.3.2.2 Stability of Encapsulated mp-TiO₂/MAPI/P3HT Solar Cells under Constant Illumination with UV Cutoff Filter vs. without UV Cutoff Filter

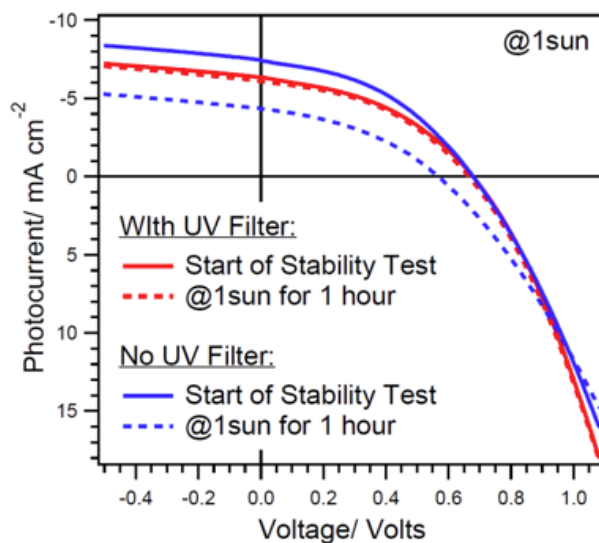


Fig. 5.5 One-sun JV curves of the encapsulated mp-TiO₂/MAPI/P3HT solar cells with and without a 420 nm long pass filter before and after continuous 1 SE illumination from the Luxim lamp for 1 hour.

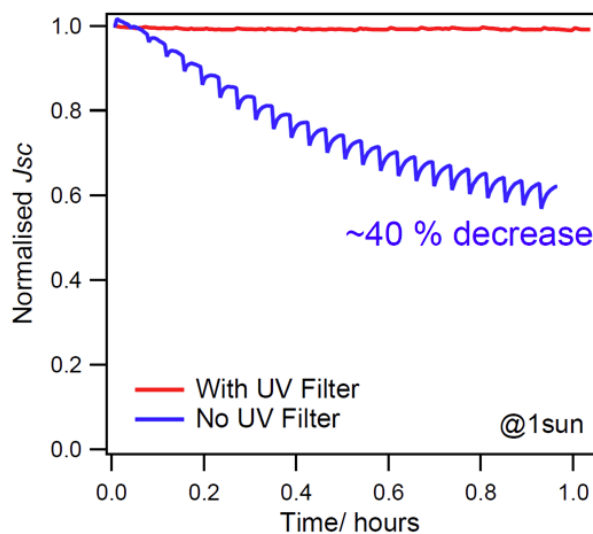


Fig. 5.6 Normalised one-sun J_{sc} of encapsulated mp-TiO₂/MAPI/P3HT solar cells with and without a 420 nm long pass filter as a function of time. The cells were under continuous 1 sun-equivalent (SE) illumination from the Luxim lamp for 1 hour. J_{sc} 's were normalised according to the initial value.

Table 5.8 One-sun performance of the encapsulated mp-TiO₂/MAPI/P3HT solar cell with and without a 420 nm long pass filter before and after continuous 1 SE illumination from the Luxim for 1 hour.

		$J_{sc}/$ mA cm^{-2}	$V_{oc}/$ V	Fill Factor	Efficiency/ %
With UV Filter	Before Stability Test	6.34	0.68	0.41	1.77
	After 1 hour @1sun	6.07	0.67	0.41	1.67
No UV Filter	Before Stability Test	7.41	0.68	0.40	2.02
	After 1 hour @1sun	4.33	0.56	0.36	0.87

After an hour of constant 1 SE illumination, the mp-TiO₂/MAPI/P3HT cell without UV filter shows a 40 % reduction in J_{sc} and a 120 mV decrease in V_{oc} while an identical cell with UV filter shows no degradation in cell performance. It is noted that the cell without UV cutoff filter in Fig. 5.6 shows a trough in J_{sc} periodically. The troughs are the points at which a cyclic JV had just been scanned from J_{sc} to 1.0 V at forward bias, then in an opposition direction to 0.5 V at reverse bias and finally back to J_{sc} . The sudden decline in J_{sc} might be caused by this change in applied voltage. After each sudden decrease, the J_{sc} recovers slowly over time under short circuit, resulting in the troughs in the normalised J_{sc} vs. time curve as shown in Fig. 5.6.

5.3.2.3 Stability of Encapsulated vs. Non-Encapsulated mp-TiO₂/MAPI/P3HT Solar Cells

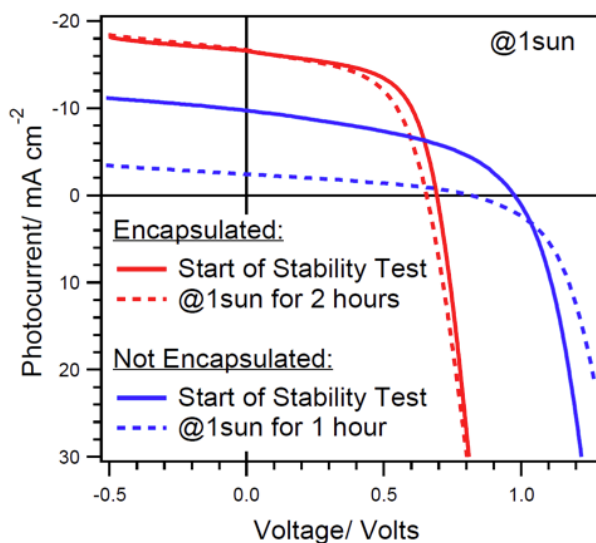


Fig. 5.7 One-sun JV curves of the encapsulated and non-encapsulated mp-TiO₂/MAPI/P3HT solar cells before and after continuous 1 SE illumination from the Luxim lamp for 1-2 hours.

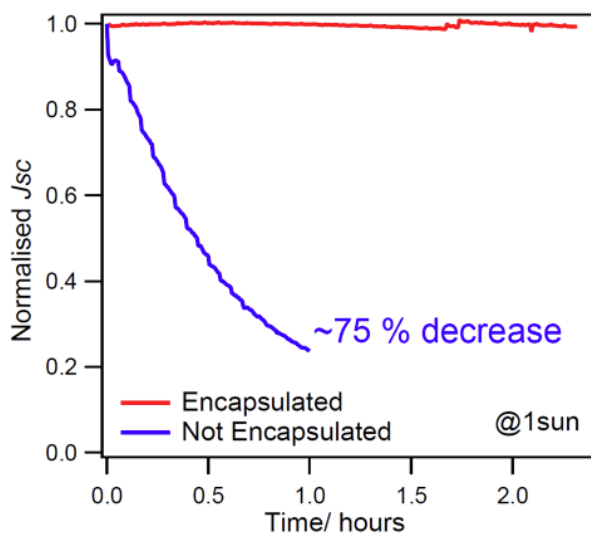


Fig. 5.8 Normalised one-sun J_{sc} of an encapsulated and a non-encapsulated mp-TiO₂/MAPI/P3HT solar cells as a function of time. The cells were under continuous 1 sun-equivalent (SE) illumination from the Luxim lamp with a 420 nm long pass filter for 1-2 hours. Relative humidity was $\sim 40\%$. J_{sc} 's were normalised according to the initial value.

Table 5.9 One-sun performance of the encapsulated and non-encapsulated mp-TiO₂/MAPI/P3HT solar cells before and after continuous 1 SE illumination from the Luxim with a 420 nm long pass filter for 1-2 hours.

		<i>J_{sc}</i> / mA cm ⁻²	<i>V_{oc}</i> / V	Fill Factor	Efficiency/ %
Encapsulated	Before Stability Test	16.7	0.69	0.54	6.22
	After 2 hours @1sun	16.7	0.66	0.52	5.73
Not Encapsulated	Before Stability Test	9.73	0.97	0.44	4.15
	After 1 hour @1sun	2.42	0.82	0.35	0.69

In order to eliminate the effect of UV light, a 420 nm longpass filter was used in both cells in the experiments. The encapsulated mp-TiO₂/MAPI/P3HT cell shows a constant *J_{sc}* over two hours of constant 1 SE illumination while the *J_{sc}* of the non-encapsulated cell decreased by ~75 % after only one hour under the same illumination. It is noted that in the non-encapsulated cell, the illuminated active area turned yellow after the test, which is the same colour change as in mp-TiO₂/MAPI films presented in chapter 5.3.1 when they were kept in a 'dry' box (humidity: 25 %, air) under 0.1 SE illumination over time. Moreover, apart from the reactions of water and oxygen in air with MAPI, the possible evaporation of HI, methylamine and methylammonium iodide should also be considered in the non-encapsulated cell.

It is noted in Fig. 5.7 and Table 5.9 that the *V_{oc}* of the encapsulated cell is ~300 mV lower than that of the non-encapsulated even before the stability test. The reason for the relatively low *V_{oc}* of the encapsulated cell may simply be experimental variation due to the low reproducibility of MAPI and MAPIC perovskite solar cells. It may also be partly due to the possible boil-off of the base 4-tert-butylpyridine (TBP) in the HTM layer during the encapsulation process when heat (>120 °C) was applied to melt the Surlyn gasket on the four sides of the device (See Chapter 2.4 for details). Base is added to spiro-OMeTAD solid-state DSSCs to increase the *V_{oc}*.⁶¹ However, it can be argued that it is unclear if TBP shows the same effect on MAPIC solar cells with P3HT as the HTM.

5.3.2.4. Stability of Encapsulated mp-TiO₂/MAPI/P3HT Solar Cells at 60 °C in the Dark

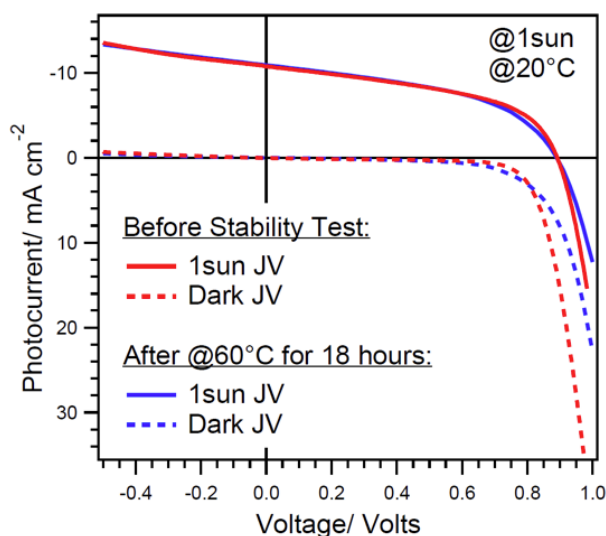


Fig. 5.9 One-sun and dark JV curves of an encapsulated mp-TiO₂/MAPI/P3HT solar cell before and after storage at 60 °C in the dark for 18 hours. JV measurements were taken at 20 °C.

Table 5.10 One-sun performance of the encapsulated mp-TiO₂/MAPI/P3HT solar cell before and after storage at 60 °C in the dark for 18 hours.

	$J_{sc}/$ mA cm^{-2}	$V_{oc}/$ V	Fill Factor	Efficiency/ %
Before Stability Test	10.8	0.89	0.49	4.71
After 18 hours @60°C in dark	10.9	0.89	0.47	4.56

It is found that the application of heat at 60 °C does not cause any detrimental effect on the performance of an encapsulated mp-TiO₂/MAPI/P3HT solar cell. After storing at 60 °C in the dark for 18 hours, the cell showed no significantly change in any of the JV parameters and thus, overall efficiency under one-sun illumination.

5.3.2.5. Most Photo-Stable mp-TiO₂/MAPI Solar Cells with P3HT, DPPTTT and Spiro-OMeTAD

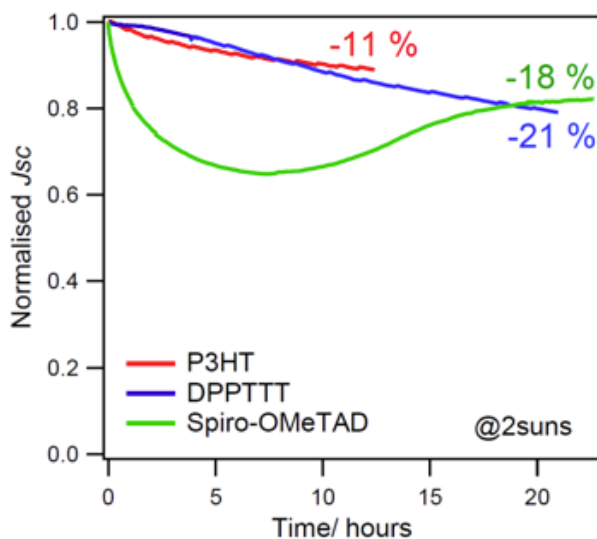


Fig. 5.10 Normalised two-sun J_{sc} of encapsulated TiO₂/MAPI/ solar cells with different HTMs as a function of time. The cells were under continuous 2 sun-equivalent (SE) illumination from the Luxim lamp with a 420 nm long pass filter for 12-23 hours. Temperature ~ 25 °C. J_{sc} 's were normalised according to the initial value.

To accelerate the photo-stability test, the perovskite solar cells were illuminated at 2 SE. Under this condition, the perovskite experiences twice as many photo-excitations than at 1 SE. In order to minimise the effect of water and oxygen in air and UV light from the Luxim lamp during the photo-stability test, the solar cells were encapsulated in the glovebox and a UV cutoff filter was incorporated. It is noted that since the solar cells were placed closer to the lamp, the temperature they experienced during this test was 25 °C, which was slightly higher than that at 1 SE.

As shown in Fig. 5.10, the J_{sc} of the P3HT cells decreases steadily by ~ 11 % after 12 hours at 2 SE while that of DPPTTT cells drops by ~ 18 % after 21 hours. These decreases are mainly due to an increase in series resistance (R_{ser}) of these cells, according to the JV data in Fig. 5.11 and Table 5.11. During the photo-stability test, R_{ser} of P3HT cell increases from 56 to 280 ohms while that of DPPTTT cell rises from 28 to 225 ohms. This also reduces the fill factor and overall efficiency of the two cells significantly (>40 % decrease in overall efficiency in both cells relative to their initial values). In fact, after eliminating the effect of increased R_{ser} and shunt resistance shown in their dark JV curves (Fig. A.30 in Appendix), the photocurrent generated by the P3HT and DPPTTT cells at the end of the photo-stability test are only ~ 5 % and ~ 7 % lower than their initial values respectively.

For spiro-OMeTAD cell, the J_{sc} decreases rapidly by 35 % in the first 7 hours but goes back up afterwards. The increase in J_{sc} seems to slow down slightly after the 18-hour mark but

is kept at a steady rate at about 1.5 % per hour at the end of the 23-hour 2 SE stability test. Unlike P3HT and DPPTTT cells, spiro-OMeTAD cells show no increase in R_{ser} (stays at ~85 ohms) and no degradation in fill factor and V_{oc} . Therefore, the 17 % reduction in overall efficiency at the end of the 23-hour test relative to the initial value is entirely caused by the decreased J_{sc} .

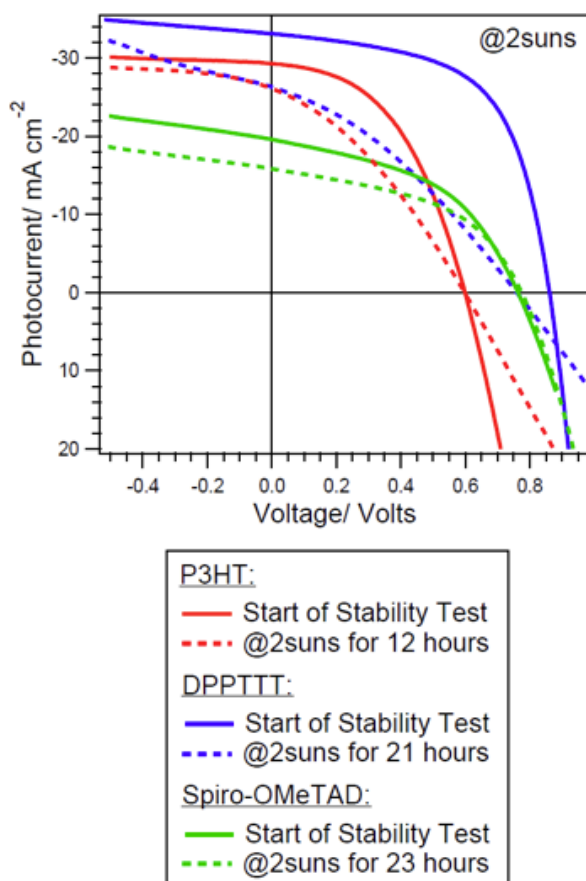


Fig. 5.11 Two-sun JV curves of encapsulated TiO_2 /MAPI solar cells with HTMs before and after the stability test as noted in legend and Fig. 5.10.

Table 5.11 Two-sun performance of encapsulated TiO_2 /MAPI solar cells with HTM as noted before and after the stability test as noted in Fig. 5.10.

HTM		$J_{sc}/$ $mA\ cm^{-2}$	$V_{oc}/$ V	Fill Factor	Efficiency/ %	$R_{ser}/$ Ohms
P3HT	Before Stability Test	29.3	0.60	0.47	4.13	56
	After 12 hours @2suns	26.1	0.60	0.30	2.35	283
DPPTTT	Before Test	33.1	0.86	0.53	7.54	28
	After 21 hours @2suns	26.3	0.76	0.33	3.30	225
Spiro-OMeTAD	Before Test	19.6	0.76	0.46	3.43	85
	After 23 hours @2suns	15.8	0.77	0.47	2.86	83

5.2.3.6 Most Photo-Stable mp-TiO₂/MAPI/Spiro-OMeTAD Solar Cells (Illuminated at 40 SE over 63 Hours)

Photocurrent and Photovoltage over Time, *JV* Measurements

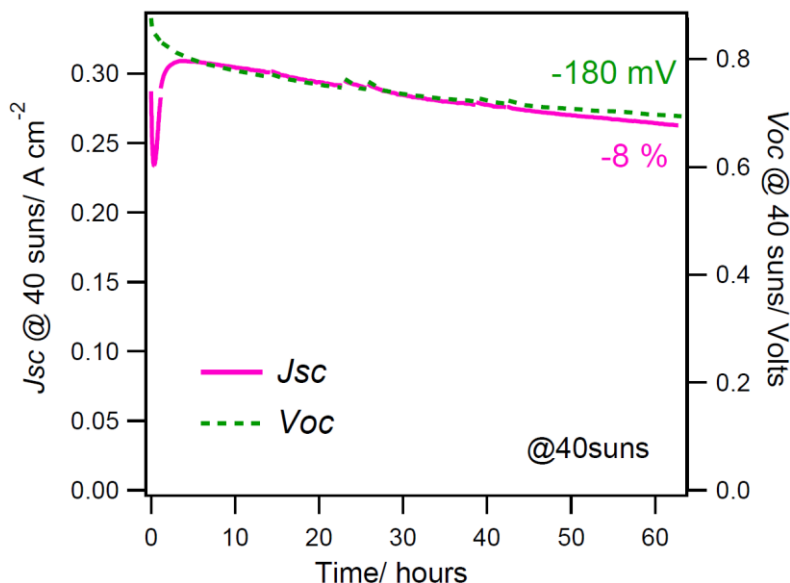


Fig. 5.12 Forty-sun J_{sc} of an encapsulated mp-TiO₂/MAPI/spiro-OMeTAD solar cell as a function of time. The cell was under continuous 40 sun-equivalent (SE) illumination from the Luxim lamp with a 420 nm long pass filter for 63 hours. Gaps correspond to short periods where the cell was at open circuit under illumination. Temperature ~ 50 °C.

Among the three types of cells in this experiment, the mp-TiO₂/MAPI/Spiro-OMeTAD cell shows the highest potential to be photo-stable solar cells under high SE illumination for a long period of time. Therefore, an identical spiro-OMeTAD cell was employed for the next photo-stability test. In order to further accelerate the photo-stability test, a high light intensity of 40 SE was employed. It is noted that the temperature of the cell was ~ 50 °C during the course of the test. Similar to the above experiment, the cell was encapsulated in the glovebox and a UV cutoff filter was used. While the cell was connected at short circuit almost all the time during the photo-stability test, there were short periods of time when *JV* curves were scanned at certain time intervals. Fig. 5.12 shows the short circuit photocurrent density and open circuit voltage during a total of 63 hour of 40 SE continuous exposure. At the start, the J_{sc} decreases rapidly by up to ~ 18 %. Then it goes back up at a slower rate. After reaching a maximum (7 % higher J_{sc} relative to initial value), the J_{sc} decreases slowly. The rate of decay during the final 4 hours was only 0.2 % per hour, which, if linear, would correspond to only 0.005 % per hour at 1 sun.

Interestingly, the V_{oc} also decreases at a high rate in the first hour when the cell is experiencing a rapid drop in J_{sc} (see Fig. 5.12). Then the decrease in V_{oc} slows down. After ~ 2 hours of illumination, the decline in V_{oc} remains slow and relatively steady. As shown in

Fig. 5.13 and Table 5.12, after 63 hours, the loss of J_{sc} at 40 SE is only 8 % relative to initial value while V_{oc} decreases by 180 mV. One-sun JV 's were measured for the same cell before and after the photo-stability test and the results are shown in Fig. 5.14 and Table 5.13. At 1 SE, losses in J_{sc} and V_{oc} are 7 % and 190 mV respectively, similar to the results obtained at 40 SE. After exposure to 40 SE for 63 hours, the same cell was then heated at 60 °C in the dark for 18 hours. This treatment recovers 160 mV in V_{oc} at 1 SE illumination but decreases the J_{sc} by 12 % relative to that before heating.

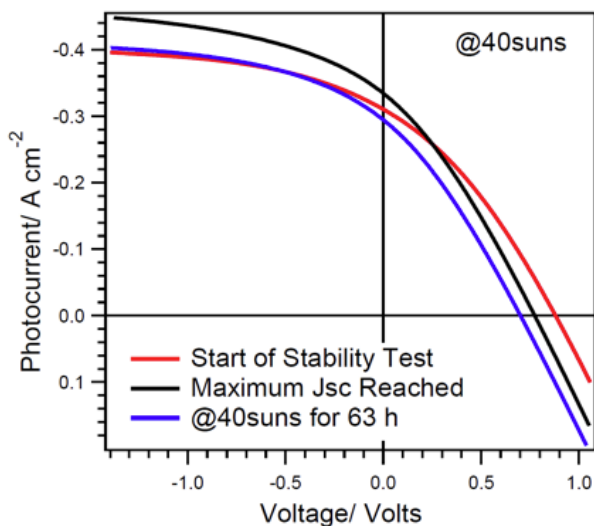


Fig. 5.13 Forty-sun JV curves of the encapsulated mp-TiO₂/MAPI/spiro-OMeTAD solar cell before and after the stability test as noted in Fig. 5.12, and when the J_{sc} was at its maximum. [This figure is reproduced with the permission of the rights holder, WILEY-VCH Verlag GmbH & Co. KGaA, Weinheim.]¹³²

Table 5.12 Forty-sun performance of the encapsulated mp-TiO₂/MAPI/spiro-OMeTAD solar cell before and after the stability test as noted in Fig. 5.12, and when the J_{sc} was at its maximum.

	$J_{sc}/$ mA cm^{-2}	$V_{oc}/$ V	Fill Factor	Efficiency/ %
Start of Stability Test	311	0.88	0.33	2.26
At Maximum J_{sc}	335	0.77	0.31	2.00
After 63 hours @40suns	295	0.70	0.28	1.45

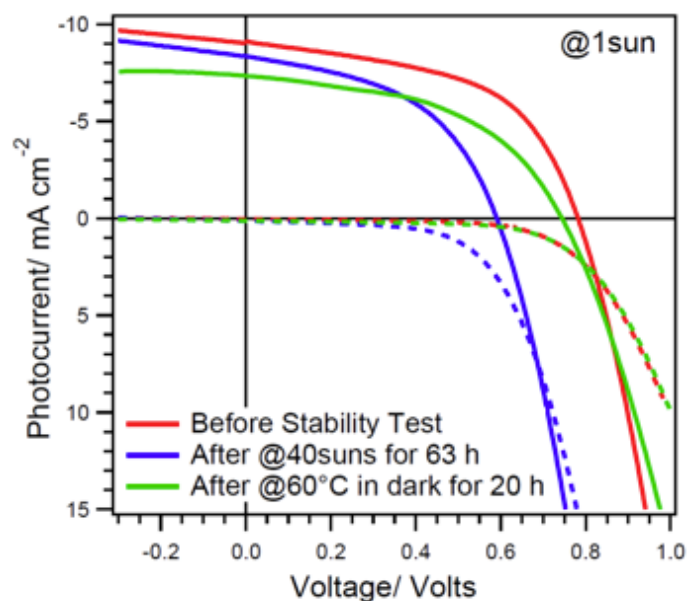


Fig. 5.14 One-sun JV curves of the encapsulated mp-TiO₂/MAPI/spiro-OMeTAD solar cell before and after continuous 40 sun-equivalent (SE) illumination from the Luxim lamp with a 420 nm long pass filter for 63 hours, and the same cell after heating at 60 °C in the dark for 20 hours. [This figure is reproduced with the permission of the rights holder, WILEY-VCH Verlag GmbH & Co. KGaA, Weinheim.]¹³²

Table 5.13 One-sun JV curves of the encapsulated mp-TiO₂/MAPI/spiro-OMeTAD solar cell before and after the stability tests as noted in Fig. 5.14.

	$J_{sc}/$ mA cm^{-2}	$V_{oc}/$ V	Fill Factor	Efficiency/ %
Start of Stability Test	9.04	0.78	0.53	3.74
After 63 hours @40suns	8.36	0.59	0.48	2.37
After 20 hours @60°C in dark	7.34	0.75	0.49	2.70

Transient Photovoltage and Photocurrent, and Charge Extraction Measurements

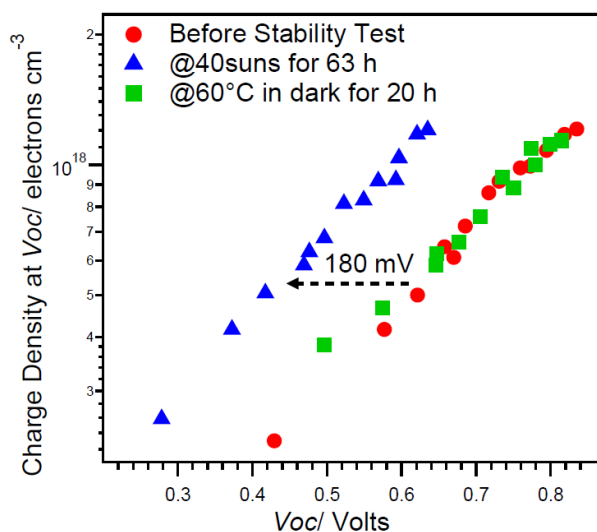


Fig. 5.15 Charge density vs. V_{oc} , of the encapsulated $\text{TiO}_2/\text{MAPI}/\text{spiro-OMeTAD}$ solar cell before and after continuous 40 sun-equivalent (SE) illumination from the Luxim lamp with a 420 nm long pass filter for 63 hours, and the same cell after heating at 60 °C in the dark for 20 hours. [This figure is reproduced with the permission of the rights holder, WILEY-VCH Verlag GmbH & Co. KGaA, Weinheim.]¹³²

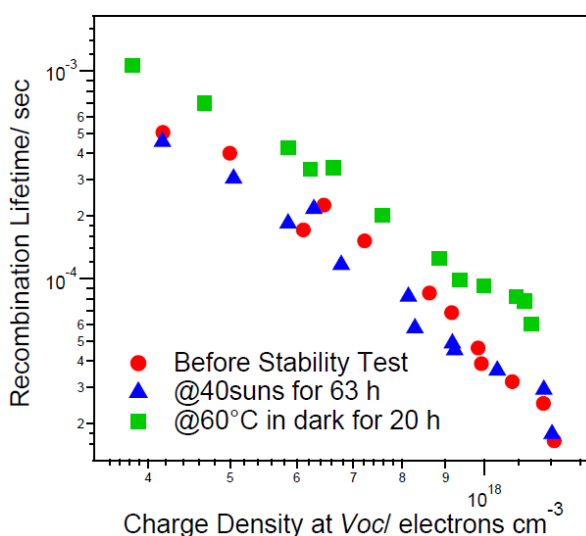


Fig. 5.16 Recombination lifetime vs. charge density, of the encapsulated $\text{TiO}_2/\text{MAPI}/\text{spiro-OMeTAD}$ solar cell before and after the stability tests as noted in Fig. 5.15. [This figure is reproduced with the permission of the rights holder, WILEY-VCH Verlag GmbH & Co. KGaA, Weinheim.]¹³²

It is noted that the charge density presented in Fig. 5.16 and 5.18 might not correspond in the way that we think it does to the quantity of charge in the film under light conditions. The values determined might also have a contribution from some kind of polarization effect. But the charge density data are still presented here for the purpose of comparing recombination and transport rate. After 63 hours of 40 SE illumination, the mp- $\text{TiO}_2/\text{MAPI}/\text{Spiro-OMeTAD}$ cell shows insignificant change in recombination lifetime and a shift in the charge density vs. V_{oc} graph, according to Fig. 5.16 and 5.15 respectively. Since there is no observable change in

charge density at short circuit and transport lifetime as shown in Fig. 5.17 and 5.18, the change in charge density vs. V_{oc} can be interpreted as a left shift of ~ 180 mV. This indicates that the drop in V_{oc} is caused by a decrease in band edge offset at either the mp-TiO₂/MAPI and/or MAPI/spiro-OMeTAD interfaces. It is likely due to a change in ions adsorbed at the interface, which would require the movement of ions presents through the MAPI. These ions are mostly the lithium ions in the spiro-OMeTAD layer. It is also noted that after 63 hours of continuous exposure to 40 SE, heating the same cell at 60 °C in the dark for 20 hours shifts the charge density vs. V_{oc} graph back to the right by ~ 180 mV. This can explain the recovery of V_{oc} after this heat treatment. It could be argued that the 60 % increase in recombination lifetime as shown in Fig. 5.16 might also be partly responsible for the V_{oc} recovery but it could also simply be within random variations.

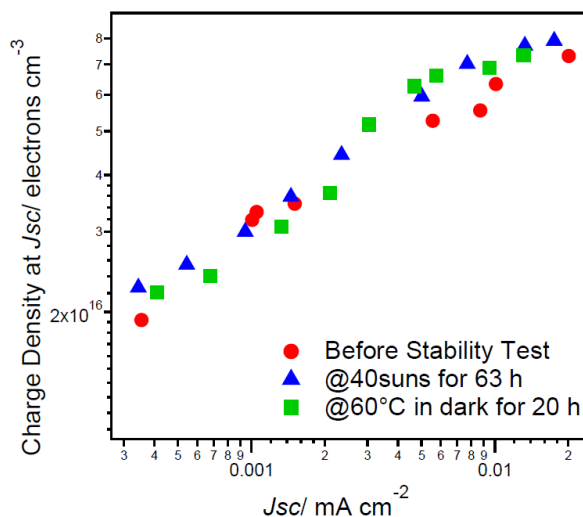


Fig. 5.17 Charge density vs J_{sc} , of the encapsulated TiO₂/MAPI/spiro-OMeTAD solar cell before and after the stability tests as noted in Fig. 5.15. [This figure is reproduced with the permission of the rights holder, WILEY-VCH Verlag GmbH & Co. KGaA, Weinheim.]¹³²

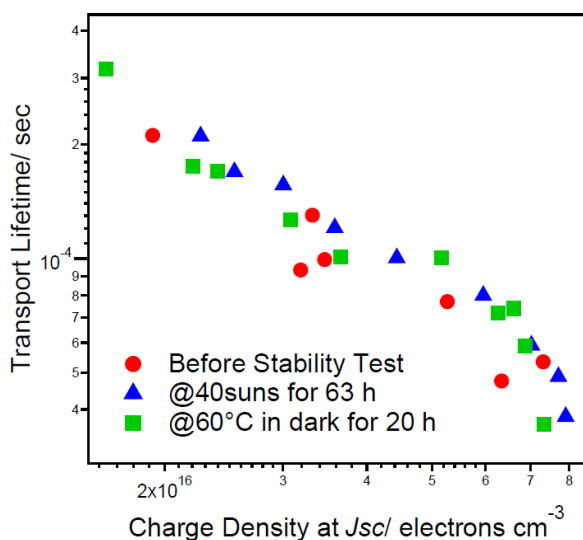


Fig. 5.18 Transport lifetime vs. charge density, of the encapsulated TiO₂/MAPI/spiro-OMeTAD solar cell before and after the stability tests as noted in Fig. 5.15.

5.4 Discussion

From the photos of the MAPI and MAPIC perovskite films evolving under different conditions, it is found that there are at least two mechanisms under which MAPI and MAPIC films degrade, depending on the surrounding environment. At a relatively low humidity of 25 % with atmospheric oxygen, both MAPI and MAPIC films degrade to opaque yellow films. This degradation either requires light or is accelerated by light. In the case where humidity is over 90 %, with atmospheric oxygen, the films turn transparent pale yellow or colourless. Water but not oxygen is always believed to be responsible for the yellowing or discoloration of MAPI and MAPIC perovskite.^{78, 125-127, 130b, 133} Also, a mp-TiO/MAPI solar cell has also been reported to be stable in dry air without encapsulation.¹³⁴ However, according to the results collected in this chapter only, it is not clear whether oxygen plays a part in the colour change observed. To find out that, a similar experiment needs to be conducted where a series of MAPI and MAPIC perovskite films are stored at <0.01 % oxygen and 25 % humidity under light and in the dark and another series at <0.01 % oxygen and >90 % humidity again under light and in the dark.

For complete perovskite solar cells, the reproducibility is found to be relatively low, when compared to dye-sensitised solar cells. For example, in a batch of 9 mp-TiO₂/MAPI/P3HT solar cells made under the same condition on the same day, the overall efficiency can reach as high as 8.77 % but the lowest efficiency is only 3.71 %, with considerable difference in their J_{sc} 's (ranging from 13.7 to 20.3 mA cm⁻²), V_{oc} 's (0.58 to 0.82 V) and fill factors (0.57 to 0.70). Fig. 5.19 shows the variation in JV parameters of all the mp-TiO₂/MAPI solar cells fabricated in 3 batches for this project. In fact, a low reproducibility of performance of both MAPI and MAPIC perovskite solar cells are also found in literature but the reason for that is still not clear.^{75-76, 81a}

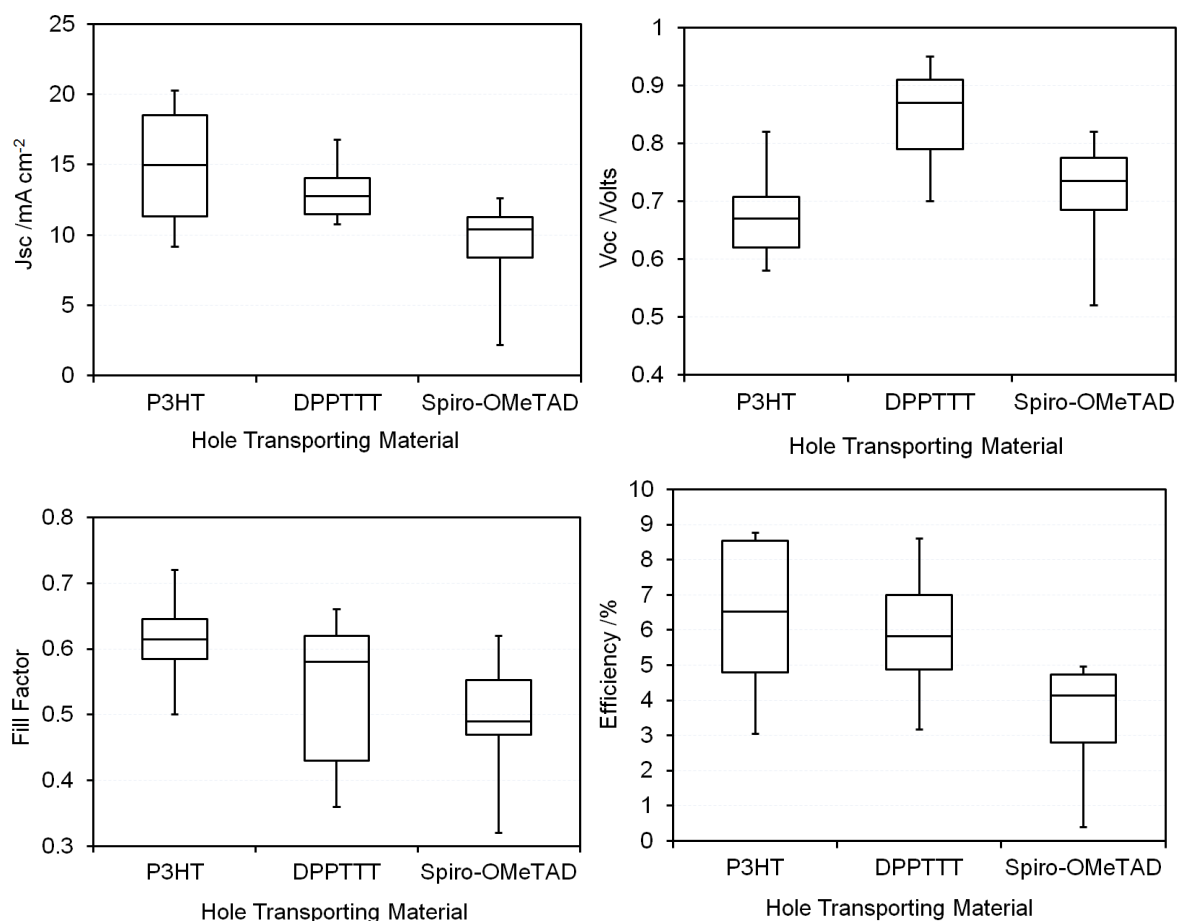


Fig. 5.19 shows the maximum value, 75th percentile, median, 25th percentile and minimum value of the J_{sc} (top left), V_{oc} (top right), fill factor (bottom left), overall conversion efficiency (bottom right) of mp-TiO₂/MAPI with HTMs as indicated in the bottom axes. Number of P3HT cells: 15; DPPTTT cells: 15; spiro-OMeTAD cells: 21.

In this study, it is also demonstrated that encapsulating a mp-TiO₂/MAPI/P3HT cell with Surlyn and coverslip under nitrogen significantly improves its stability when tested in air (humidity: 40 %). However, encapsulation undoubtedly adds cost to production. Moreover, water, oxygen and other gases may still diffuse into and out of the cell over time. A stable cell without encapsulation is always desirable. It has been proposed that replacing the methylammonium ion with an aprotic organic ion such as tetramethylammonium ion may hence the stability of lead halide-type perovskite against water.^{130b} Nevertheless, it is questionable if a perovskite structure can be formed with tetramethylammonium ion due to its relatively big size. It has also been suggested that depositing hydrophobic hole transporting polymers on perovskite can minimise the contact of perovskite with water in air, thus improve the solar cell stability.¹³⁵ However, as shown previously in this chapter, the mp-TiO₂/MAPI cell with P3HT is found to be unstable without encapsulation after only 1 hour at 1 SE. In contrast to this result, it is reported that the mp-TiO₂/MAPI cells with the polymer P3HT and

PDPPDBTE maintain an overall efficiency of 6 and 8 % respectively for 1000 hours in air without encapsulation.^{135a} But these two cells were stored at a relatively low humidity of 20 % and in the dark. In another paper, the polymer PCBTDPP was employed as HTM in a mp-TiO₂/MAPI cell which efficiency is also shown to be stable at 5 % in air for 1000 hours without encapsulation.^{135b} However, similar to the previous paper, this PCBTDPP cell was kept in the dark and the humidity of the storage environment is not reported.

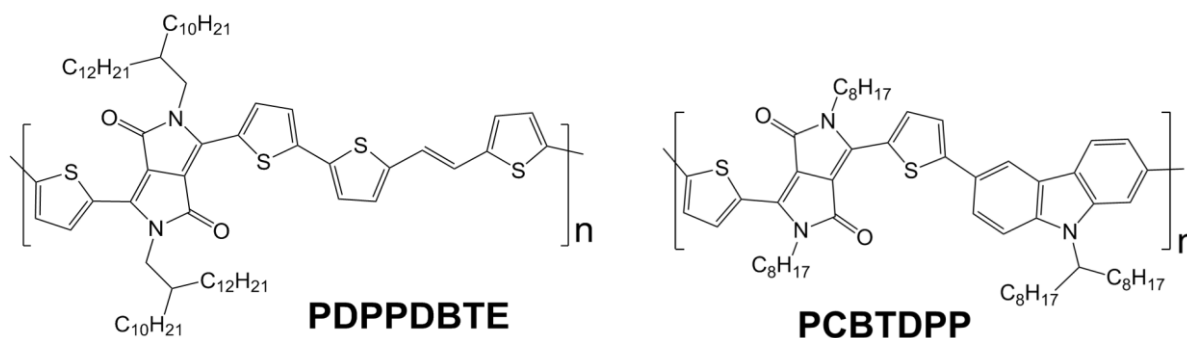


Fig. 5.20 Chemical structures of PDPPDBTE and PCBTDPP.

Introduction of bromide ions to lead-iodide perovskite to form CH₃NH₃Pb(I_{1-x}Br_x)₃ has also been found to improve the stability of the resultant solar cells.⁷⁸ Using a mesoporous TiO₂ scaffold and a polytriarylamine polymer (PTAA) as HTM, Noh *et al.* showed that at a low bromide content ($x < 0.2$), the cell performance degraded significantly when the relative humidity increases from 35 to 55 %. The overall efficiency decreased from ~11 to ~6 % after storage at a relative humidity of 55 % for one day. But when the bromide content was increased above certain level ($x > 0.2$), no degradation in cell performance was observed (overall efficiency maintained at 9-10 %) after storage in the same environment. However, it is not reported whether the cells were kept under light.

As demonstrated in the Results section in this chapter, UV light degrades the performance of mp-TiO₂/MAPI/P3HT solar cell. Similar degradation in J_{sc} and V_{oc} of a mp-TiO₂/MAPIC/spiro-OMeTAD cell solar has been reported in literature.⁸³ The authors proposed a mechanism for UV-induced degradation of mp-TiO₂/perovskite solar cells. Upon absorption of a photon of UV light, the holes generated in TiO₂ react with oxygen radical on at surface oxygen vacancy, desorbing the molecular oxygen. This leaves behind empty, deep surface trap sites and a free electron per site which recombine with the excess of holes in the doped HTM. Upon light absorption, an excited electron in the perovskite is injected into the conduction band of TiO₂ or to the aforementioned deep surface traps. The electrons in these deep traps are immobile and readily recombine with the holes in HTM, thus reducing cell performance. In the same paper, the authors proceeded further by studying cells with Al₂O₃

scaffold and achieved better stability results. They showed that under continuous 0.77-sun illumination at 40 °C without a UV filter, the J_{sc} of a mp- Al_2O_3 /MAPIC/spiro-OMeTAD cell stayed within 12-13 mA cm^{-2} in the first 200 hours. But the V_{oc} decreased from ~ 1.0 V to ~ 0.7 V and fill factor drops from ~ 0.7 to ~ 0.5 , resulting in a decline in overall efficiency from 11 to 5 % over the same period of time. Nevertheless, all the JV parameters remained stable, maintaining the 5 % efficiency over the next 800 hours under the same conditions.

Moreover, it is also shown in this chapter that heating an encapsulated mp- TiO_2 /MAPI/P3HT solar cell at 60 °C in the dark for 18 hours does not degrade the cell performance. To further test the thermal stability of MAPI and MAPIC perovskites, heating the cells at higher temperature (up to 80 °C) for longer period of time will be required. In terms of stability of perovskite solar cells, most attention is currently paid to the effect of water coming from the surroundings. For future study, it will also be interesting to study if any significant quantity of gases such as HI, methylamine and methylammonium come off from the perovskite solar cells when stored at a reasonably high operating temperature of around 80 °C over time.

In this work, an encapsulated mp- TiO_2 /MAPI/spiro-OMeTAD device was exposed to 40 sun-equivalent (SE) constant illumination for 63 hours, which delivers over 2700 hours equivalent of 1 sun photo-excitations. After the stability test, the cell shows a loss of only 7 % in J_{sc} at 1 SE, which indicates that the photocurrent generation is reasonably stable. It is noted that this cell is 100 fold more stable than a similar cells with MAPIC perovskite recently reported.⁸³ However, the reduction of 190 mV in V_{oc} is relatively high. This problem might be addressed replacing spiro-OMeTAD with another hole transporting material where no additives such as Li-TFSI and TBP are required.

5.5 Conclusion

Some preliminary stability tests have been conducted on methylammonium lead triiodide (MAPI) and methylammonium lead iodide chloride (MAPIC) perovskite films and MAPI solar cells. Their films have been shown to degrade via two different mechanisms in air at two different humidity levels (25 and >90 %). Encapsulation and elimination of UV light are required to maintain the performance of mp-TiO₂/MAPI/P3HT cells over time under 1 SE illumination. Moreover, no degradation in cell performance is found in these cells after storage at 60 °C in the dark for 18 hours.

Last but not least, an encapsulated perovskite solar cell with the architecture FTO/compact TiO₂/mp-TiO₂/MAPI/spiro-OMeTAD/Au was fabricated. Its stability under high light was tested. This gives insight into the viability of the technology on practical timescales. However, there are still many critical issues need to be addressed, which includes its stability against UV light, water and possibly oxygen in air, its thermal stability and its toxicity due to the presence of lead. Therefore, in the future, a lot more research on this technology is expected and required before its application in real life.

Chapter 6

Conclusion

Dye-sensitised solar cells (DSSCs) are regarded as a possible alternative to silicon-based photovoltaics because of their potential for low-cost production. The record efficiencies of liquid-state and solid-state DSSCs has reached 12 %²³⁻²⁴ and 7.2 %⁴⁶ respectively. This thesis focuses on the processing of two alternative hole transport media in dye-sensitised solar cells (DSSCs): water-based electrolytes and meltable solid hole transporting materials (HTMs). The performance of the resulting DSSCs has been studied and optimised. In addition, some preliminary stability tests were conducted on methyl ammonium lead halide perovskite films and their solar cells. This thesis provides some guidelines for further development of water-based DSSCs, melt-processing of HTMs in solid-state DSSCs, and perovskite solar cells.

Chapter 3 addresses the wetting and recombination issues of water-based DSSCs. It is shown that it is possible to fabricate efficient DSSCs (up to 4 %) with water as the only solvent. When using triiodide/iodide redox system, significant improvement in overall efficiency above 4 % is not likely. Therefore, alternative electrolyte systems to replace the traditional triiodide/iodide system will be needed.

In solid-state dye-sensitised solar cells, the commonly employed methods to deposit hole transport materials (HTMs), such as spin coating and drop casting, often result in poor pore filling in mesoporous TiO₂ layer. Chapter 4 studies melt-processing of HTMs which has been reported to give a pore filling fraction close to unity.⁶⁹ It is found that the low efficiency of melt-processed DSSCs is mainly due to the heat applied during the melting process which causes a decrease in recombination lifetime. Solid-state DSSCs made with melt-processed spiro-OMeTAD are shown, with efficiency of 0.45 %. Future development of the melt-processing will certainly require the synthesis of thermally stable (up to 255 °C) sensitising dyes.

In literature, power conversion efficiencies above 15 % have been claimed to be achieved by perovskite solar cells. But the stability of these solar cells is still questionable. Stability of MAPI and MAPIC as a film, and TiO₂/MAPI perovskite solar cells are examined in Chapter 5. Although the stability study reported in this thesis is not very extensive, the results show us the obstacles (e.g. the degradation observed when the cells are not encapsulated or exposed to UV light) we need to overcome before applying this technology in real life on a practical timescale.

Further Work

Due to some intrinsic properties of the triiodide/iodide system in water, an alternative redox couple, such as water-soluble $\text{Co}^{(\text{III})/(\text{II})}$ complexes, is required for further development of water-based DSSCs. In addition, the wetting issue of water electrolyte may be addressed by using a dye which consists of many hydrophilic groups on the surface of the molecule and a strong anchor to TiO_2 .

It is found that heating $\text{TiO}_2/\text{Z907}$ and $\text{TiO}_2/\text{D149}$ electrodes at $255\text{ }^\circ\text{C}$ for 1 minute before cell assembly reduces the recombination lifetime of the resultant cells fabricated with triiodide/iodide-based electrolyte. It will be valuable to fabricate similar cells using cobalt electrolytes to see if the same reduction in recombination lifetime will be observed upon the same heat treatment. This may give us some ideas on whether the increase in recombination is generally observed no matter what hole transporting medium is used, possibly due to the presence of certain functional groups in the degraded dye. The information will be useful for the design of new sensitising dyes for the melt-processing technique. To enhance the feasibility of the melt-processing technique in solid-state DSSCs, the development of efficient HTMs with relatively low melting temperature ($<190\text{ }^\circ\text{C}$) and bases with boiling temperature $>255\text{ }^\circ\text{C}$ is also certainly needed.

For perovskite solar cells, more research effort should be made on the intrinsic stability of the perovskite itself in the future. In literature, water has always been considered as the main culprit for the degradation of lead iodide-based perovskite. The effect of oxygen on perovskite should also be studied. It will also be interesting to investigate the possible loss of volatile hydriodic acid, methylamine and methylammonium iodide from methylammonium lead iodide from the perovskite film over time. Moreover, characterisation of the yellow degraded perovskite may possibly give some insight into the development of more stable perovskite solar cells.

References

1. World Population Policies 2013. *United Nations Publication* **2013**.
2. International Energy Outlook 2013. *U.S. Energy Information Administration* **2013**.
3. Lewis, N. S.; Nocera, D. G., Powering the planet: Chemical challenges in solar energy utilization. *Proceedings of the National Academy of Sciences* **2006**, *103* (43), 15729-15735.
4. Research Cell Efficiency Records. *National Renewable Energy Laboratory (NREL), G., Colorado, USA* **2014**.
5. Glunz, S. W.; Preu, R.; Biro, D., Crystalline Silicon Solar Cells – State-of-the-Art and Future Developments. *Comprehensive Renewable Energy* **2012**, *1*, 1-62.
6. O'Regan, B.; Gratzel, M., A low-cost, high-efficiency solar cell based on dye-sensitized colloidal TiO₂ films. *Nature* **1991**, *353*, 737-740.
7. Barnes, P. R. F.; Anderson, A. Y.; Koops, S. E.; Durrant, J. R.; O'Regan, B. C., Electron Injection Efficiency and Diffusion Length in Dye-Sensitized Solar Cells Derived from Incident Photon Conversion Efficiency Measurements. *Journal of Physical Chemistry C* **2008**, *113* (3), 1126-1136.
8. Haque, S. A.; Palomares, E.; Cho, B. M.; Green, A. N. M.; Hirata, N.; Klug, D. R.; Durrant, J. R., Charge Separation versus Recombination in Dye-Sensitized Nanocrystalline Solar Cells: the Minimization of Kinetic Redundancy. *Journal of American Chemical Society* **2005**, *127* (10), 3456-3462.
9. Juozapavicius, M.; Kaucikas, M.; Dimitrov, S. D.; Barnes, P. R. F.; van Thor, J. J.; O'Regan, B. C., Evidence for “Slow” Electron Injection in Commercially Relevant Dye-Sensitized Solar Cells by vis-NIR and IR Pump-Probe Spectroscopy. *Journal of Physical Chemistry C* **2013**, *117* (48), 25317-25324.
10. (a) Cao, F.; Oskam, G.; Meyer, G. J.; Searson, P. C., Electron Transport in Porous Nanocrystalline TiO₂ Photoelectrochemical Cells. *Journal of Physical Chemistry* **1996**, *100* (42), 17021-17027; (b) Peter, L. M.; Ponomarev, E. A.; Franco, G.; Shaw, N. J., Aspects of the photoelectrochemistry of nanocrystalline systems. *Electrochimica Acta* **1999**, *45* (4-5), 549-560.
11. (a) Anderson, A. Y.; Barnes, P. R. F.; Durrant, J. R.; O'Regan, B. C., Quantifying Regeneration in Dye-Sensitized Solar Cells. *Journal of Physical Chemistry C* **2011**, *115* (5), 2439-2447; (b) Martiniani, S.; Anderson, A. Y.; Law, C.; O'Regan, B. C.; Barolo, C., New insight into the regeneration kinetics of organic dye sensitised solar cells. *Chemical Communications* **2012**, *48* (18).
12. Koops, S. E.; O'Regan, B. C.; Barnes, P. R. F.; Durrant, J. R., Parameters Influencing the Efficiency of Electron Injection in Dye-Sensitized Solar Cells. *Journal of American Chemical Society* **2009**, *131* (13), 4808-4818.
13. Richards, C. E.; Anderson, A. Y.; Martiniani, S.; Law, C.; O'Regan, B. C., The Mechanism of Iodine Reduction by TiO₂ Electrons and the Kinetics of Recombination in Dye-Sensitized Solar Cells. *Journal of Physical Chemistry Letters* **2012**, *3* (15), 1980-1984.
14. (a) Li, X.; Reynal, A.; Barnes, P.; Humphry-Baker, R.; Zakeeruddin, S. M.; De Angelis, F.; O'Regan, B. C., Measured binding coefficients for iodine and ruthenium dyes;

- implications for recombination in dye sensitised solar cells. *Physical Chemistry Chemical Physics* **2012**, *14* (44), 15421-15428; (b) O'Regan, B. C.; Walley, K.; Juozapavicius, M.; Anderson, A.; Matar, F.; Ghaddar, T.; Zakeeruddin, S. M.; Klein, C. d.; Durrant, J. R., Structure/Function Relationships in Dyes for Solar Energy Conversion: A Two-Atom Change in Dye Structure and the Mechanism for Its Effect on Cell Voltage. *Journal of American Chemical Society* **2009**, *131* (10), 3541-3548.
15. O'Regan, B.; Moser, J.; Anderson, M.; Graetzel, M., Vectorial electron injection into transparent semiconductor membranes and electric field effects on the dynamics of light-induced charge separation. *Journal of Physical Chemistry* **1990**, *94* (24), 8720-8726.
 16. (a) Chiba, Y.; Islam, A.; Watanabe, Y.; Komiya, R.; Koide, N.; Han, L., Dye-Sensitized Solar Cells with Conversion Efficiency of 11.1%. *Japanese Journal of Applied Physics* **2006**, *45* (7L), L638; (b) Cao, Y.; Bai, Y.; Yu, Q.; Cheng, Y.; Liu, S.; Shi, D.; Gao, F.; Wang, P., Dye-Sensitized Solar Cells with a High Absorptivity Ruthenium Sensitizer Featuring a 2-(Hexylthio)thiophene Conjugated Bipyridine. *Journal of Physical Chemistry C* **2009**, *113* (15), 6290-6297; (c) Yu, Q.; Wang, Y.; Yi, Z.; Zu, N.; Zhang, J.; Zhang, M.; Wang, P., High-Efficiency Dye-Sensitized Solar Cells: The Influence of Lithium Ions on Exciton Dissociation, Charge Recombination, and Surface States. *ACS Nano* **2010**, *4* (10), 6032-6038.
 17. Sauvage, F.; Chhor, S.; Marchioro, A.; Moser, J.; Graetzel, M., Butyronitrile-Based Electrolyte for Dye-Sensitized Solar Cells. *Journal of American Chemical Society* **2011**, *133* (33), 13103-13109.
 18. Yu, Q.; Zhou, D.; Shi, Y.; Si, X.; Wang, Y.; Wang, P., Stable and efficient dye-sensitized solar cells: photophysical and electrical characterizations. *Energy & Environmental Science* **2010**, *3* (11), 1722-1725.
 19. Harikisun, R.; Desilvestro, H., Long-term stability of dye solar cells. *Solar Energy* **2011**, *85* (6), 1179-1188.
 20. Flasque, M.; Van Nhien, A. N.; Swiatowska, J.; Seyeux, A.; Davoisne, C.; Sauvage, F., Interface Stability of a TiO₂/3-Methoxypropionitrile-Based Electrolyte: First Evidence for Solid Electrolyte Interphase Formation and Implications. *ChemPhysChem* **2014**, *15* (6), 1126-1137.
 21. Sapp, S. A.; Elliott, C. M.; Contado, C.; Caramori, S.; Bignozzi, C. A., Substituted Polypyridine Complexes of Cobalt(II/III) as Efficient Electron-Transfer Mediators in Dye-Sensitized Solar Cells. *Journal of American Chemical Society* **2002**, *124* (37), 11215-11222.
 22. Nusbaumer, H.; Moser, J.; Zakeeruddin, S. M.; Nazeeruddin, M. K.; Grätzel, M., Co^{II}(dbbip)₂²⁺ Complex Rivals Tri-iodide/Iodide Redox Mediator in Dye-Sensitized Photovoltaic Cells. *Journal of Physical Chemistry B* **2001**, *105* (43), 10461-10464.
 23. Yella, A.; Lee, H.; Tsao, H. N.; Yi, C.; Chandiran, A. K.; Nazeeruddin, M. K.; Diao, E. W.; Yeh, C.; Zakeeruddin, S. M.; Grätzel, M., Porphyrin-Sensitized Solar Cells with Cobalt (II/III)-Based Redox Electrolyte Exceed 12 Percent Efficiency. *Science* **2011**, *334* (6056), 629-634.
 24. Green, M. A.; Emery, K.; Hishikawa, Y.; Warta, W.; Dunlop, E. D., Solar cell efficiency tables (version 43). *Progress in Photovoltaics: Research and Applications* **2014**, *22* (1), 1-9.

25. Jiang, R.; Anderson, A.; Barnes, P. R. F.; Xiaoe, L.; Law, C.; O'Regan, B. C., 2000 hours photostability testing of dye sensitised solar cells using a cobalt bipyridine electrolyte. *Journal of Materials Chemistry A* **2014**, *2* (13), 4751-4757.
26. Yun, J.; Lee, S.; Jeong, Y.; Lee, H.; Kwon, J.; Lee, G., Reduction of Defects in SiO_x Vapor Permeation Barriers on Polymer Substrates by Introducing a Sputtered Interlayer. *Japanese Journal of Applied Physics* **2009**, *48* (5R), 055503.
27. Liska, P.; Vlachopoulos, N.; Nazeeruddin, M. K.; Comte, P.; Graetzel, M., cis-Diaquabis(2,2'-bipyridyl-4,4'-dicarboxylate)ruthenium(II) sensitizes wide band gap oxide semiconductors very efficiently over a broad spectral range in the visible. *Journal of American Chemical Society* **1988**, *110* (11), 3686-3687.
28. Nazeeruddin, M. K.; Liska, P.; Moser, J.; Vlachopoulos, N.; Grätzel, M., Conversion of Light into Electricity with Trinuclear Ruthenium Complexes Adsorbed on Textured TiO₂ Films. *Helvetica Chimica Acta* **1990**, *73* (6), 1788-1803.
29. Liu, Y.; Hagfeldt, A.; Xiao, X.; Lindquist, S. E., Investigation of influence of redox species on the interfacial energetics of a dye-sensitized nanoporous TiO₂ solar cell. *Solar Energy Materials and Solar Cells* **1998**, *55* (3), 267-281.
30. Jung, Y.; Yoo, B.; Lim, M. K.; Lee, S. Y.; Kim, K., Effect of Triton X-100 in water-added electrolytes on the performance of dye-sensitized solar cells. *Electrochimica Acta* **2009**, *54* (26), 6286-6291.
31. Risbridger, T. A. G.; Castro, F. A.; Cameron, P. J., Two-Dimensional Photocurrent and Transmission Mapping of Aqueous Dye-Sensitized Solar Cells. *Journal of Physical Chemistry C* **2012**, *116* (42), 22253-22260.
32. Chen, C.; Yang, X.; Cheng, M.; Zhang, F.; Sun, L., Degradation of Cyanoacrylic Acid-Based Organic Sensitizers in Dye-Sensitized Solar Cells. *ChemSusChem* **2013**, *6* (7), 1270-1275.
33. Sumita, M.; Sodeyama, K.; Han, L.; Tateyama, Y., Water Contamination Effect on Liquid Acetonitrile/TiO₂ Anatase (101) Interface for Durable Dye-Sensitized Solar Cell. *Journal of Physical Chemistry C* **2011**, *115* (40), 19849-19855.
34. Hahlin, M.; Johansson, E. M. J.; Schölin, R.; Siegbahn, H.; Rensmo, H. K., Influence of Water on the Electronic and Molecular Surface Structures of Ru-Dyes at Nanostructured TiO₂. *Journal of Physical Chemistry C* **2011**, *115* (24), 11996-12004.
35. (a) Macht, B.; Turrión, M.; Barkschat, A.; Salvador, P.; Ellmer, K.; Tributsch, H., Patterns of efficiency and degradation in dye sensitization solar cells measured with imaging techniques. *Solar Energy Materials and Solar Cells* **2002**, *73* (2), 163-173; (b) Tributsch, H., Dye sensitization solar cells: a critical assessment of the learning curve. *Coordination Chemistry Reviews* **2004**, *248* (13-14), 1511-1530.
36. Mastroianni, S.; Lembo, A.; Brown, T. M.; Reale, A.; Di Carlo, A., Inside Cover: Electrochemistry in Reverse Biased Dye Solar Cells and Dye/Electrolyte Degradation Mechanisms. *ChemPhysChem* **2012**, *13* (12), 2806-2806.
37. Mastroianni, S.; Asghar, I.; Miettunen, K.; Halme, J.; Lanuti, A.; Brown, T. M.; Lund, P., Effect of electrolyte bleaching on the stability and performance of dye solar cells. *Physical Chemistry Chemical Physics* **2014**, *16* (13), 6092-6100.
38. Asghar, M. I.; Miettunen, K.; Mastroianni, S.; Halme, J.; Vahlman, H.; Lund, P., In situ image processing method to investigate performance and stability of dye solar cells. *Solar Energy* **2012**, *86* (1), 331-338.

39. Zhu, K.; Jang, S.; Frank, A. J., Effects of water intrusion on the charge-carrier dynamics, performance, and stability of dye-sensitized solar cells. *Energy & Environmental Science* **2012**, *5* (11), 9492-9495.
40. Kong, E.; Lim, J.; Chang, Y.; Yoon, Y.; Park, T.; Jang, H. M., Aerosol OT/Water System Coupled with Triiodide/Iodide (I_3^-/I^-) Redox Electrolytes for Highly Efficient Dye-Sensitized Solar Cells. *Advanced Energy Materials* **2013**, *3* (10), 1344-1350.
41. Su, Y. H.; Lai, W. H.; Teoh, L. G.; Hon, M. H.; Huang, J. L., Layer-by-layer Au nanoparticles as a Schottky barrier in a water-based dye-sensitized solar cell. *Applied Physics A* **2007**, *88* (1), 173-178.
42. Lai, W. H.; Su, Y. H.; Teoh, L. G.; Hon, M. H., Commercial and natural dyes as photosensitizers for a water-based dye-sensitized solar cell loaded with gold nanoparticles. *Journal of Photochemistry and Photobiology A: Chemistry* **2008**, *195* (2-3), 307-313.
43. Saito, H.; Uegusa, S.; Murakami, T. N.; Kawashima, N.; Miyasaka, T., Fabrication and efficiency enhancement of water-based dye-sensitized solar cells by interfacial activation of TiO₂ mesopores. *Electrochemistry* **2004**, *72* (5), 310-316.
44. Kaneko, M.; Nomura, T.; Sasaki, C., Photoinduced Charge Separation in an Aqueous Phase Using Nanoporous TiO₂ Film and a Quasi-Solid Made of Natural Products. *Macromolecular Rapid Communications* **2003**, *24* (7), 444-446.
45. Law, C.; Pathirana, S. C.; Li, X.; Anderson, A. Y.; Barnes, P. R. F.; Listorti, A.; Ghaddar, T. H.; O'Regan, B. C., Water-Based Electrolytes for Dye-Sensitized Solar Cells. *Advanced Materials* **2010**, *22* (40), 4505-4509.
46. Burschka, J.; Dualeh, A.; Kessler, F.; Baranoff, E.; Cevey-Ha, N.; Yi, C.; Nazeeruddin, M. K.; Grätzel, M., Tris(2-(1H-pyrazol-1-yl)pyridine)cobalt(III) as p-Type Dopant for Organic Semiconductors and Its Application in Highly Efficient Solid-State Dye-Sensitized Solar Cells. *Journal of American Chemical Society* **2011**, *133* (45), 18042-18045.
47. (a) Tennakone, K.; Kumara, G. R. R. A.; Kumarasinghe, A. R.; Wijayantha, K. G. U.; Sirimanne, P. M., A dye-sensitized nano-porous solid-state photovoltaic cell. *Semiconductor Science and Technology* **1995**, *10* (12), 1689; (b) Tennakone, K.; Kumara, G. R. R. A.; Kottegoda, I. R. M.; Wijayantha, K. G. U., The photostability of dye-sensitized solid state photovoltaic cells: factors determining the stability of the pigment in a nanoporous n-TiO₂/cyanidin/p-CuI cell. *Semiconductor Science and Technology* **1997**, *12* (1), 128; (c) Tennakone, K.; Kumara, G. R. R. A.; Kottegoda, I. R. M.; Wijayantha, K. G. U.; Perera, V. P. S., A solid-state photovoltaic cell sensitized with a ruthenium bipyridyl complex. *Journal of Physics D: Applied Physics* **1998**, *31* (12), 1492; (d) Kumara, G. R. A.; Konno, A.; Shiratsuchi, K.; Tsukahara, J.; Tennakone, K., Dye-Sensitized Solid-State Solar Cells: Use of Crystal Growth Inhibitors for Deposition of the Hole Collector. *Chemistry of Materials* **2002**, *14* (3), 954-955; (e) Meng, Q. B.; Takahashi, K.; Zhang, X. T.; Sutanto, I.; Rao, T. N.; Sato, O.; Fujishima, A.; Watanabe, H.; Nakamori, T.; Urugami, M., Fabrication of an Efficient Solid-State Dye-Sensitized Solar Cell. *Langmuir* **2003**, *19* (9), 3572-3574.
48. Perera, V. P. S.; Tennakone, K., Recombination processes in dye-sensitized solid-state solar cells with CuI as the hole collector. *Solar Energy Materials and Solar Cells* **2003**, *79* (2), 249-255.

49. O'Regan, B.; Schwartz, D. T.; Zakeeruddin, S. M.; Grätzel, M., Electrodeposited Nanocomposite n-p Heterojunctions for Solid-State Dye-Sensitized Photovoltaics. *Advanced Materials* **2000**, *12* (17), 1263-1267.
50. O'Regan, B.; Lenzmann, F.; Muis, R.; Wienke, J., A Solid-State Dye-Sensitized Solar Cell Fabricated with Pressure-Treated P25-TiO₂ and CuSCN: Analysis of Pore Filling and IV Characteristics. *Chemistry of Materials* **2002**, *14* (12), 5023-5029.
51. Premalal, E. V. A.; Kumara, G. R. R. A.; Rajapakse, R. M. G.; Shimomura, M.; Murakami, K.; Konno, A., Tuning chemistry of CuSCN to enhance the performance of TiO₂/N719/CuSCN all-solid-state dye-sensitized solar cell. *Chemical Communications* **2010**, *46* (19), 3360-3362.
52. Senadeera, G. K. R.; Jayaweera, P. V. V.; Perera, V. P. S.; Tennakone, K., Solid-state dye-sensitized photocell based on pentacene as a hole collector. *Solar Energy Materials and Solar Cells* **2002**, *73* (1), 103-108.
53. Kroeze, J. E.; Hirata, N.; Schmidt-Mende, L.; Orizu, C.; Ogier, S. D.; Carr, K.; Grätzel, M.; Durrant, J. R., Parameters Influencing Charge Separation in Solid-State Dye-Sensitized Solar Cells Using Novel Hole Conductors. *Advanced Functional Materials* **2006**, *16* (14), 1832-1838.
54. Kim, H.; Wamser, C. C., Photoelectropolymerization of aniline in a dye-sensitized solar cell. *Photochemical & Photobiological Sciences* **2006**, *5* (10), 955-960.
55. Raoul, C.; Yibing, C.; George, S., Solid-state Ru-dye solar cells using polypyrrole as a hole conductor. *Journal of Physics D: Applied Physics* **2004**, *37* (1), 13.
56. Jian, L.; Takahiro, O.; Yasuko, H.; Takeshi, S.; Kenichiro, W.; Michio, M., Solid-State Dye-Sensitized Solar Cells Using Poly[2-methoxy-5-(2-ethylhexyloxy)-1,4-phenylenevinylene] as a Hole-Transporting Material. *Japanese Journal of Applied Physics* **2006**, *45* (11R), 8728.
57. (a) Senadeera, R.; Fukuri, N.; Saito, Y.; Kitamura, T.; Wada, Y.; Yanagida, S., Volatile solvent-free solid-state polymer-sensitized TiO₂ solar cells with poly(3,4-ethylenedioxythiophene) as a hole-transporting medium. *Chemical Communications* **2005**, (17), 2259-2261; (b) Xia, J.; Masaki, N.; Lira-Cantu, M.; Kim, Y.; Jiang, K.; Yanagida, S., Influence of Doped Anions on Poly(3,4-ethylenedioxythiophene) as Hole Conductors for Iodine-Free Solid-State Dye-Sensitized Solar Cells. *Journal of American Chemical Society* **2008**, *130* (4), 1258-1263.
58. (a) Zafer, C.; Karapire, C.; Serdar Sariciftci, N.; Icli, S., Characterization of N, N'-bis-2-(1-hydroxy-4-methylpentyl)-3, 4, 9, 10-perylene bis (dicarboximide) sensitized nanocrystalline TiO₂ solar cells with polythiophene hole conductors. *Solar Energy Materials and Solar Cells* **2005**, *88* (1), 11-21; (b) Takahashi, K.; Nakanishi, T.; Yamaguchi, T.; Nakamura, J.; Murata, K., Performance Enhancement by Blending Merocyanine Photosensitizer in TiO₂ Polythiophen Solid-state Solar Cells. *Chemistry Letters* **2005**, *34* (5), 714-715; (c) Zhu, R.; Jiang, C.; Liu, B.; Ramakrishna, S., Highly Efficient Nanoporous TiO₂-Polythiophene Hybrid Solar Cells Based on Interfacial Modification Using a Metal-Free Organic Dye. *Advanced Materials* **2009**, *21* (9), 994-1000; (d) Jiang, K.; Manseki, K.; Yu, Y.; Masaki, N.; Suzuki, K.; Song, Y.; Yanagida, S., Photovoltaics Based on Hybridization of Effective Dye-Sensitized Titanium Oxide and Hole-Conductive Polymer P3HT. *Advanced Functional Materials* **2009**, *19* (15), 2481-2485; (e) Mor, G. K.; Kim, S.; Paulose, M.; Varghese, O. K.; Shankar, K.; Basham,

- J.; Grimes, C. A., Visible to Near-Infrared Light Harvesting in TiO₂ Nanotube Array–P3HT Based Heterojunction Solar Cells. *Nano Letters* **2009**, *9* (12), 4250-4257.
59. Chang, J. A.; Rhee, J. H.; Im, S. H.; Lee, Y. H.; Kim, H.; Seok, S. I.; Nazeeruddin, M. K.; Grätzel, M., High-Performance Nanostructured Inorganic–Organic Heterojunction Solar Cells. *Nano Letters* **2010**, *10* (7), 2609-2612.
 60. Bach, U.; Lupo, D.; Comte, P.; Moser, J. E.; Weissortel, F.; Salbeck, J.; Spreitzer, H.; Grätzel, M., Solid-state dye-sensitized mesoporous TiO₂ solar cells with high photon-to-electron conversion efficiencies. *Nature* **1998**, *395* (6702), 583-585.
 61. Krüger, J.; Plass, R.; Cevey, L.; Piccirelli, M.; Grätzel, M.; Bach, U., High efficiency solid-state photovoltaic device due to inhibition of interface charge recombination. *Applied Physics Letters* **2001**, *79* (13), 2085-2087.
 62. Kwon, Y. S.; Lim, J.; Song, I.; Song, I. Y.; Shin, W. S.; Moon, S.; Park, T., Chemical compatibility between a hole conductor and organic dye enhances the photovoltaic performance of solid-state dye-sensitized solar cells. *Journal of Materials Chemistry* **2012**, *22* (17), 8641-8648.
 63. Melas-Kyriazi, J.; Ding, I. K.; Marchioro, A.; Punzi, A.; Hardin, B. E.; Burkhard, G. F.; Tétreault, N.; Grätzel, M.; Moser, J.; McGehee, M. D., The Effect of Hole Transport Material Pore Filling on Photovoltaic Performance in Solid-State Dye-Sensitized Solar Cells. *Advanced Energy Materials* **2011**, *1* (3), 407-414.
 64. Margulis, G. Y.; Hardin, B. E.; Ding, I. K.; Hoke, E. T.; McGehee, M. D., Parasitic Absorption and Internal Quantum Efficiency Measurements of Solid-State Dye Sensitized Solar Cells. *Advanced Energy Materials* **2013**, *3* (7), 959-966.
 65. Snaith, H. J.; Humphry-Baker, R.; Chen, P.; Cesaie, I.; Zakeeruddin, S., M.; Grätzel, M., Charge collection and pore filling in solid-state dye-sensitized solar cells. *Nanotechnology* **2008**, *19* (42), 424003.
 66. (a) Schmidt-Mende, L.; Grätzel, M., TiO₂ pore-filling and its effect on the efficiency of solid-state dye-sensitized solar cells. *Thin Solid Films* **2006**, *500* (1–2), 296-301; (b) Ding, I. K.; Tétreault, N.; Brillet, J.; Hardin, B. E.; Smith, E. H.; Rosenthal, S. J.; Sauvage, F.; Grätzel, M.; McGehee, M. D., Pore-Filling of Spiro-OMeTAD in Solid-State Dye Sensitized Solar Cells: Quantification, Mechanism, and Consequences for Device Performance. *Advanced Functional Materials* **2009**, *19* (15), 2431-2436.
 67. Han, H.; Bach, U.; Cheng, Y.; Caruso, R. A., Increased nanopore filling: Effect on monolithic all-solid-state dye-sensitized solar cells. *Applied Physics Letters* **2007**, *90* (21), 213510.
 68. Ding, I. K.; Melas-Kyriazi, J.; Cevey-Ha, N.; Chittibabu, K. G.; Zakeeruddin, S. M.; Grätzel, M.; McGehee, M. D., Deposition of hole-transport materials in solid-state dye-sensitized solar cells by doctor-blading. *Organic Electronics* **2010**, *11* (7), 1217-1222.
 69. (a) Fredin, K.; Johansson, E. M. J.; Blom, T.; Hedlund, M.; Plogmaker, S.; Siegbahn, H.; Leifer, K.; Rensmo, H., Using a molten organic conducting material to infiltrate a nanoporous semiconductor film and its use in solid-state dye-sensitized solar cells. *Synthetic Metals* **2009**, *159* (1–2), 166-170; (b) Juozapavicius, M.; O'Regan, B. C.; Anderson, A. Y.; Grazulevicius, J. V.; Mimaite, V., Efficient dye regeneration in solid-state dye-sensitized solar cells fabricated with melt processed hole conductors. *Organic Electronics* **2012**, *13* (1), 23-30.

70. Leijtens, T.; Ding, I. K.; Giovenzana, T.; Bloking, J. T.; McGehee, M. D.; Sellinger, A., Hole Transport Materials with Low Glass Transition Temperatures and High Solubility for Application in Solid-State Dye-Sensitized Solar Cells. *ACS Nano* **2012**, *6* (2), 1455-1462.
71. (a) Ishihara, T., Optical properties of PbI₂-based perovskite structures. *Journal of Luminescence* **1994**, *60–61* (0), 269-274; (b) Kitazawa, N.; Watanabe, Y.; Nakamura, Y., Optical properties of CH₃NH₃PbX₃ (X = halogen) and their mixed-halide crystals. *Journal of Materials Science* **2002**, *37* (17), 3585-3587; (c) Calabrese, J.; Jones, N. L.; Harlow, R. L.; Herron, N.; Thorn, D. L.; Wang, Y., Preparation and characterization of layered lead halide compounds. *Journal of American Chemical Society* **1991**, *113* (6), 2328-2330; (d) Papavassiliou, G. C.; Koutselas, I. B., Structural, optical and related properties of some natural three- and lower-dimensional semiconductor systems. *Synthetic Metals* **1995**, *71* (1–3), 1713-1714; (e) Hirasawa, M.; Ishihara, T.; Goto, T., Exciton Features in 0-, 2-, and 3-Dimensional Networks of [PbI₆]⁴⁻ Octahedra. *Journal of Physical Society of Japan* **1994**, *63* (10), 3870-3879; (f) Tanaka, K.; Takahashi, T.; Ban, T.; Kondo, T.; Uchida, K.; Miura, N., Comparative study on the excitons in lead-halide-based perovskite-type crystals CH₃NH₃PbBr₃ CH₃NH₃PbI₃. *Solid State Communications* **2003**, *127* (9–10), 619-623; (g) Umebayashi, T.; Asai, K.; Kondo, T.; Nakao, A., Electronic structures of lead iodide based low-dimensional crystals. *Physical Review B* **2003**, *67* (15), 155405; (h) Knop, O.; Wasylshen, R. E.; White, M. A.; Cameron, T. S.; Oort, M. J. M. V., Alkylammonium lead halides. Part 2. CH₃NH₃PbX₃ (X = Cl, Br, I) perovskites: cuboctahedral halide cages with isotropic cation reorientation. *Canadian Journal of Chemistry* **1990**, *68* (3), 412-422.
72. Kojima, A.; Teshima, K.; Shirai, Y.; Miyasaka, T., Organometal Halide Perovskites as Visible-Light Sensitizers for Photovoltaic Cells. *Journal of American Chemical Society* **2009**, *131* (17), 6050-6051.
73. Im, J.; Lee, C.; Lee, J.; Park, S.; Park, N., 6.5% efficient perovskite quantum-dot-sensitized solar cell. *Nanoscale* **2011**, *3* (10), 4088-4093.
74. Kim, H.; Lee, C.; Im, J.; Lee, K.; Moehl, T.; Marchioro, A.; Moon, S.; Humphry-Baker, R.; Yum, J.; Moser, J. E.; Gratzel, M.; Park, N., Lead Iodide Perovskite Sensitized All-Solid-State Submicron Thin Film Mesoscopic Solar Cell with Efficiency Exceeding 9%. *Scientific Reports* **2012**, *2*.
75. Lee, M. M.; Teuscher, J.; Miyasaka, T.; Murakami, T. N.; Snaith, H. J., Efficient Hybrid Solar Cells Based on Meso-Superstructured Organometal Halide Perovskites. *Science* **2012**, *338* (6107), 643-647.
76. Heo, J. H.; Im, S. H.; Noh, J. H.; Mandal, T. N.; Lim, C.; Chang, J. A.; Lee, Y. H.; Kim, H.; Sarkar, A.; Nazeeruddin, K.; Gratzel, M.; Seok, S. I., Efficient inorganic-organic hybrid heterojunction solar cells containing perovskite compound and polymeric hole conductors. *Nature Photonics* **2013**, *7* (6), 486-491.
77. Zhang, W.; Smith, J.; Hamilton, R.; Heeney, M.; Kirkpatrick, J.; Song, K.; Watkins, S. E.; Anthopoulos, T.; McCulloch, I., Systematic Improvement in Charge Carrier Mobility of Air Stable Triarylamine Copolymers. *Journal of American Chemical Society* **2009**, *131* (31), 10814-10815.
78. Noh, J. H.; Im, S. H.; Heo, J. H.; Mandal, T. N.; Seok, S. I., Chemical Management for Colorful, Efficient, and Stable Inorganic–Organic Hybrid Nanostructured Solar Cells. *Nano Letters* **2013**, *13* (4), 1764-1769.

79. Burschka, J.; Pellet, N.; Moon, S.; Humphry-Baker, R.; Gao, P.; Nazeeruddin, M. K.; Grätzel, M., Sequential deposition as a route to high-performance perovskite-sensitized solar cells. *Nature* **2013**, *499* (7458), 316-319.
80. Stranks, S. D.; Eperon, G. E.; Grancini, G.; Menelaou, C.; Alcocer, M. J. P.; Leijtens, T.; Herz, L. M.; Petrozza, A.; Snaith, H. J., Electron-Hole Diffusion Lengths Exceeding 1 Micrometer in an Organometal Trihalide Perovskite Absorber. *Science* **2013**, *342* (6156), 341-344.
81. (a) Ball, J. M.; Lee, M. M.; Hey, A.; Snaith, H. J., Low-temperature processed meso-superstructured to thin-film perovskite solar cells. *Energy & Environmental Science* **2013**, *6* (6), 1739-1743; (b) Wojciechowski, K.; Saliba, M.; Leijtens, T.; Abate, A.; Snaith, H. J., Sub-150 °C processed meso-superstructured perovskite solar cells with enhanced efficiency. *Energy & Environmental Science* **2014**, *7* (3), 1142-1147.
82. Snaith, H. J.; Abate, A.; Ball, J. M.; Eperon, G. E.; Leijtens, T.; Noel, N. K.; Stranks, S. D.; Wang, J. T.; Wojciechowski, K.; Zhang, W., Anomalous Hysteresis in Perovskite Solar Cells. *Journal of Physical Chemistry Letters* **2014**, *5* (9), 1511-1515.
83. Leijtens, T.; Eperon, G. E.; Pathak, S.; Abate, A.; Lee, M. M.; Snaith, H. J., Overcoming ultraviolet light instability of sensitized TiO₂ with meso-superstructured organometal trihalide perovskite solar cells. *Nature Communications* **2013**, *4*.
84. Liu, M.; Johnston, M. B.; Snaith, H. J., Efficient planar heterojunction perovskite solar cells by vapour deposition. *Nature* **2013**, *501* (7467), 395-398.
85. (a) Anderson, M. A.; Gieselmann, M. J.; Xu, Q., Titania and alumina ceramic membranes. *Journal of Membrane Science* **1988**, *39* (3), 243-258; (b) Liu, Y.; Hagfeldt, A.; Xiao, X.; Lindquist, S., Investigation of influence of redox species on the interfacial energetics of a dye-sensitized nanoporous TiO₂ solar cell. *Solar Energy Materials and Solar Cells* **1998**, *55* (3), 267-281.
86. Bronstein, H.; Chen, Z.; Ashraf, R. S.; Zhang, W.; Du, J.; Durrant, J. R.; Shakya Tuladhar, P.; Song, K.; Watkins, S. E.; Geerts, Y.; Wienk, M. M.; Janssen, R. A. J.; Anthopoulos, T.; Sirringhaus, H.; Heeney, M.; McCulloch, I., Thieno[3,2-b]thiophene–Diketopyrrolopyrrole-Containing Polymers for High-Performance Organic Field-Effect Transistors and Organic Photovoltaic Devices. *Journal of American Chemical Society* **2011**, *133* (10), 3272-3275.
87. Matar, F.; Ghaddar, T. H.; Walley, K.; DosSantos, T.; Durrant, J. R.; O'Regan, B., A new ruthenium polypyridyl dye, TG6, whose performance in dye-sensitized solar cells is surprisingly close to that of N719, the 'dye to beat' for 17 years. *Journal of Materials Chemistry* **2008**, *18* (36), 4246-4253.
88. Topoglidis, E.; Astuti, Y.; Duriaux, F.; Grätzel, M.; Durrant, J. R., Direct Electrochemistry and Nitric Oxide Interaction of Heme Proteins Adsorbed on Nanocrystalline Tin Oxide Electrodes. *Langmuir* **2003**, *19* (17), 6894-6900.
89. (a) Sommeling, P. M.; O'Regan, B. C.; Haswell, R. R.; Smit, H. J. P.; Bakker, N. J.; Smits, J. J. T.; Kroon, J. M.; van Roosmalen, J. A. M., Influence of a TiCl₄ Post-Treatment on Nanocrystalline TiO₂ Films in Dye-Sensitized Solar Cells. *Journal of Physical Chemistry B* **2006**, *110* (39), 19191-19197; (b) O'Regan, B. C.; Durrant, J. R.; Sommeling, P. M.; Bakker, N. J., Influence of the TiCl₄ Treatment on Nanocrystalline TiO₂ Films in Dye-Sensitized Solar Cells. 2. Charge Density, Band Edge Shifts, and Quantification of Recombination Losses at Short Circuit. *Journal of Physical Chemistry C* **2007**, *111* (37), 14001-14010.

90. Xu, W. W.; Kershaw, R.; Dwight, K.; Wold, A., Preparation and characterization of TiO₂ films by a novel spray pyrolysis method. *Materials Research Bulletin* **1990**, *25* (11), 1385-1392.
91. (a) O'Regan, B. C.; Lenzmann, F., Charge Transport and Recombination in a Nanoscale Interpenetrating Network of n-Type and p-Type Semiconductors: Transient Photocurrent and Photovoltage Studies of TiO₂/Dye/CuSCN Photovoltaic Cells. *Journal of Physical Chemistry B* **2004**, *108* (14), 4342-4350; (b) O'Regan, B.; Xiaoe, L.; Ghaddar, T., Dye adsorption, desorption, and distribution in mesoporous TiO₂ films, and its effects on recombination losses in dye sensitized solar cells. *Energy & Environmental Science* **2012**, *5* (5), 7203-7215.
92. Jeanbourquin, X. A.; Li, X.; Law, C.; Barnes, P. R. F.; Humphry-Baker, R.; Lund, P.; Asghar, M. I.; O'Regan, B. C., Rediscovering a Key Interface in Dye-Sensitized Solar Cells: Guanidinium and Iodine Competition for Binding Sites at the Dye/Electrolyte Surface. *Journal of American Chemical Society* **2014**, *136* (20), 7286-7294.
93. Law, C.; Moudam, O.; Villarroja-Lidon, S.; O'Regan, B., Managing wetting behavior and collection efficiency in photoelectrochemical devices based on water electrolytes; improvement in efficiency of water/iodide dye sensitised cells to 4%. *Journal of Materials Chemistry* **2012**, *22* (44), 23387-23394.
94. (a) Katzin, L. I.; Gebert, E., The Iodide-Iodine-Triiodide Equilibrium and Ion Activity Coefficient Ratios I. *Journal of American Chemical Society* **1955**, *77* (22), 5814-5819; (b) Datta, J.; Bhattacharya, A.; Kundu, K. K., Relative Standard Electrode Potentials of I₃⁻/I⁻, I₂/I₃⁻, and I₂/I⁻ Redox Couples and the Related Formation Constants of I₃⁻ in Some Pure and Mixed Dipolar Aprotic Solvents. *Bulletin of Chemical Society of Japan* **1988**, *61* (5), 1735-1742; (c) Boschloo, G.; Gibson, E. A.; Hagfeldt, A., Photomodulated Voltammetry of Iodide/Triiodide Redox Electrolytes and Its Relevance to Dye-Sensitized Solar Cells. *Journal of Physical Chemistry Letters* **2011**, *2* (24), 3016-3020.
95. van Brakel, J.; Heertjes, P. M., Analysis of diffusion in macroporous media in terms of a porosity, a tortuosity and a constrictivity factor. *International Journal of Heat and Mass Transfer* **1974**, *17* (9), 1093-1103.
96. (a) Kron, G.; Rau, U.; Dürr, M.; Miteva, T.; Nelles, G.; Yasuda, A.; Werner, J. H., Diffusion Limitations to I₃⁻/I⁻ Electrolyte Transport Through Nanoporous TiO₂ Networks. *Electrochemical and Solid-State Letters* **2003**, *6* (6), E11-E14; (b) Barnes, P. R. F.; Anderson, A. Y.; Durrant, J. R.; O'Regan, B. C., Simulation and measurement of complete dye sensitised solar cells: including the influence of trapping, electrolyte, oxidised dyes and light intensity on steady state and transient device behaviour. *Physical Chemistry Chemical Physics* **2011**, *13* (13), 5798-5816.
97. Wang, M.; Moon, S.; Zhou, D.; Le Formal, F.; Cevy-Ha, N.; Humphry-Baker, R.; Grätzel, C.; Wang, P.; Zakeeruddin, S. M.; Grätzel, M., Enhanced-Light-Harvesting Amphiphilic Ruthenium Dye for Efficient Solid-State Dye-Sensitized Solar Cells. *Advanced Functional Materials* **2010**, *20* (11), 1821-1826.
98. von Hippel, P. H.; Wong, K., Neutral Salts: The Generality of Their Effects on the Stability of Macromolecular Conformations. *Science* **1964**, *145* (3632), 577-580.
99. Zhang, H.; Qiu, L.; Xu, D.; Zhang, W.; Yan, F., Performance enhancement for water based dye-sensitized solar cells via addition of ionic surfactants. *Journal of Materials Chemistry A* **2014**, *2* (7), 2221-2226.

100. Xiang, W.; Huang, F.; Cheng, Y.; Bach, U.; Spiccia, L., Aqueous dye-sensitized solar cell electrolytes based on the cobalt(ii)/(iii) tris(bipyridine) redox couple. *Energy & Environmental Science* **2013**, *6* (1), 121-127.
101. (a) Tian, H.; Gabrielsson, E.; Lohse, P. W.; Vlachopoulos, N.; Kloo, L.; Hagfeldt, A.; Sun, L., Development of an organic redox couple and organic dyes for aqueous dye-sensitized solar cells. *Energy & Environmental Science* **2012**, *5* (12), 9752-9755; (b) Daeneke, T.; Uemura, Y.; Duffy, N. W.; Mozer, A. J.; Koutura, N.; Bach, U.; Spiccia, L., Aqueous Dye-Sensitized Solar Cell Electrolytes Based on the Ferricyanide–Ferrocyanide Redox Couple. *Advanced Materials* **2012**, *24* (9), 1222-1225.
102. Son, H.; Prasittichai, C.; Mondloch, J. E.; Luo, L.; Wu, J.; Kim, D. W.; Farha, O. K.; Hupp, J. T., Dye Stabilization and Enhanced Photoelectrode Wettability in Water-Based Dye-Sensitized Solar Cells through Post-assembly Atomic Layer Deposition of TiO₂. *Journal of American Chemical Society* **2013**, *135* (31), 11529-11532.
103. Choi, H.; Jeong, B.; Do, K.; Ju, M. J.; Song, K.; Ko, J., Aqueous electrolyte based dye-sensitized solar cells using organic sensitizers. *New Journal of Chemistry* **2013**, *37* (2), 329-336.
104. (a) Palomares, E.; Clifford, J. N.; Haque, S. A.; Lutz, T.; Durrant, J. R., Control of Charge Recombination Dynamics in Dye Sensitized Solar Cells by the Use of Conformally Deposited Metal Oxide Blocking Layers. *Journal of American Chemical Society* **2002**, *125* (2), 475-482; (b) O'Regan, B. C.; Scully, S.; Mayer, A. C.; Palomares, E.; Durrant, J., The Effect of Al₂O₃ Barrier Layers in TiO₂/Dye/CuSCN Photovoltaic Cells Explored by Recombination and DOS Characterization Using Transient Photovoltage Measurements. *Journal of Physical Chemistry B* **2005**, *109* (10), 4616-4623; (c) Fabregat-Santiago, F.; Garcia-Cañadas, J.; Palomares, E.; Clifford, J. N.; Haque, S. A.; Durrant, J. R.; Garcia-Belmonte, G.; Bisquert, J., The origin of slow electron recombination processes in dye-sensitized solar cells with alumina barrier coatings. *Journal of Applied Physics* **2004**, *96* (11), 6903-6907.
105. Guo, J.; She, C.; Lian, T., Effect of Insulating Oxide Overlayers on Electron Injection Dynamics in Dye-Sensitized Nanocrystalline Thin Films. *Journal of Physical Chemistry C* **2007**, *111* (25), 8979-8987.
106. Juris, A.; Balzani, V.; Barigelletti, F.; Campagna, S.; Belser, P.; von Zelewsky, A., Ru(II) polypyridine complexes: photophysics, photochemistry, electrochemistry, and chemiluminescence. *Coordination Chemistry Reviews* **1988**, *84* (0), 85-277.
107. (a) Wang, Y.; Hang, K.; Anderson, N. A.; Lian, T., Comparison of Electron Transfer Dynamics in Molecule-to-Nanoparticle and Intramolecular Charge Transfer Complexes. *Journal of Physical Chemistry B* **2003**, *107* (35), 9434-9440; (b) Moser, J.; Puntchihewa, S.; Infelta, P. P.; Graetzel, M., Surface complexation of colloidal semiconductors strongly enhances interfacial electron-transfer rates. *Langmuir* **1991**, *7* (12), 3012-3018; (c) Rodriguez, R.; Blesa, M. A.; Regazzoni, A. E., Surface Complexation at the TiO₂(anatase)/Aqueous Solution Interface: Chemisorption of Catechol. *Journal of Colloid and Interface Science* **1996**, *177* (1), 122-131; (d) Liu, Y.; Dadap, J. I.; Zimdars, D.; Eisenthal, K. B., Study of Interfacial Charge-Transfer Complex on TiO₂ Particles in Aqueous Suspension by Second-Harmonic Generation. *Journal of Physical Chemistry B* **1999**, *103* (13), 2480-2486.
108. (a) Zhang, X.; Liu, H.; Taguchi, T.; Meng, Q.; Sato, O.; Fujishima, A., Slow interfacial charge recombination in solid-state dye-sensitized solar cell using Al₂O₃-coated nanoporous TiO₂ films. *Solar Energy Materials and Solar Cells* **2004**, *81* (2), 197-203;

- (b) Zhang, X.; Sutanto, I.; Taguchi, T.; Tokuhiko, K.; Meng, Q.; Rao, T. N.; Fujishima, A.; Watanabe, H.; Nakamori, T.; Uragami, M., Al₂O₃-coated nanoporous TiO₂ electrode for solid-state dye-sensitized solar cell. *Solar Energy Materials and Solar Cells* **2003**, *80* (3), 315-326; (c) Alarcón, H.; Boschloo, G.; Mendoza, P.; Solis, J. L.; Hagfeldt, A., Dye-Sensitized Solar Cells Based on Nanocrystalline TiO₂ Films Surface Treated with Al³⁺ Ions: Photovoltage and Electron Transport Studies. *Journal of Physical Chemistry B* **2005**, *109* (39), 18483-18490.
109. (a) Antila, L. J.; Heikkilä, M. J.; Mäkinen, V.; Humalamäki, N.; Laitinen, M.; Linko, V.; Jalkanen, P.; Toppari, J.; Aumanen, V.; Kemell, M.; Myllyperkiö, P.; Honkala, K.; Häkkinen, H.; Leskelä, M.; Korppi-Tommola, J. E. I., ALD Grown Aluminum Oxide Submonolayers in Dye-Sensitized Solar Cells: The Effect on Interfacial Electron Transfer and Performance. *Journal of Physical Chemistry C* **2011**, *115* (33), 16720-16729; (b) Lin, C.; Tsai, F.; Lee, M.; Lee, C.; Tien, T.; Wang, L.; Tsai, S., Enhanced performance of dye-sensitized solar cells by an Al₂O₃ charge-recombination barrier formed by low-temperature atomic layer deposition. *Journal of Materials Chemistry* **2009**, *19* (19), 2999-3003.
110. Son, H.; Wang, X.; Prasittichai, C.; Jeong, N. C.; Aaltonen, T.; Gordon, R. G.; Hupp, J. T., Glass-Encapsulated Light Harvesters: More Efficient Dye-Sensitized Solar Cells by Deposition of Self-Aligned, Conformal, and Self-Limited Silica Layers. *Journal of American Chemical Society* **2012**, *134* (23), 9537-9540.
111. (a) Boschloo, G.; Hagfeldt, A., Characteristics of the Iodide/Triiodide Redox Mediator in Dye-Sensitized Solar Cells. *Accounts of Chemical Research* **2009**, *42* (11), 1819-1826; (b) Rowley, J. G.; Farnum, B. H.; Ardo, S.; Meyer, G. J., Iodide Chemistry in Dye-Sensitized Solar Cells: Making and Breaking I-I Bonds for Solar Energy Conversion. *Journal of Physical Chemistry Letters* **2010**, *1* (20), 3132-3140.
112. Fredin, K.; Johansson, E. M. J.; Hahlin, M.; Schölin, R.; Plogmaker, S.; Gabrielsson, E.; Sun, L.; Rensmo, H., Solid state dye-sensitized solar cells prepared by infiltrating a molten hole conductor into a mesoporous film at a temperature below 150 °C. *Synthetic Metals* **2011**, *161* (21-22), 2280-2283.
113. (a) Greijer Agrell, H.; Lindgren, J.; Hagfeldt, A., Degradation mechanisms in a dye-sensitized solar cell studied by UV-VIS and IR spectroscopy. *Solar Energy* **2003**, *75* (2), 169-180; (b) Amirnasr, M.; Nazeeruddin, M. K.; Grätzel, M., Thermal stability of cis-dithiocyanato(2,2'-bipyridyl)4,4'-dicarboxylate ruthenium(II) photosensitizer in the free form and on nanocrystalline TiO₂ films. *Thermochimica Acta* **2000**, *348* (1-2), 105-114; (c) Nazeeruddin, M. K.; Amirnasr, M.; Comte, P.; Mackay, J. R.; McQuillan, A. J.; Houriet, R.; Grätzel, M., Adsorption Studies of Counterions Carried by the Sensitizer cis-Dithiocyanato(2,2'-bipyridyl-4,4'-dicarboxylate) Ruthenium(II) on Nanocrystalline TiO₂ Films. *Langmuir* **2000**, *16* (22), 8525-8528.
114. (a) Toivola, M.; Peltokorpi, L.; Halme, J.; Lund, P., Regenerative effects by temperature variations in dye-sensitized solar cells. *Solar Energy Materials and Solar Cells* **2007**, *91* (18), 1733-1742; (b) Sommeling, P. M.; Späth, M.; Smit, H. J. P.; Bakker, N. J.; Kroon, J. M., Long-term stability testing of dye-sensitized solar cells. *Journal of Photochemistry and Photobiology A: Chemistry* **2004**, *164* (1-3), 137-144; (c) Sastrawan, R.; Beier, J.; Belledin, U.; Hemming, S.; Hinsch, A.; Kern, R.; Vetter, C.; Petrat, F. M.; Prodi-Schwab, A.; Lechner, P.; Hoffmann, W., New interdigital design for large area dye solar modules using a lead-free glass frit sealing. *Progress in Photovoltaics: Research and Applications* **2006**, *14* (8), 697-709; (d) Hinsch, A.; Kroon, J. M.; Kern, R.; Uhlendorf, I.; Holzbock, J.; Meyer, A.; Ferber, J., Long-term stability of dye-sensitised solar cells.

- Progress in Photovoltaics: Research and Applications* **2001**, *9* (6), 425-438; (e) Tuyet Nguyen, P.; Rand Andersen, A.; Morten Skou, E.; Lund, T., Dye stability and performances of dye-sensitized solar cells with different nitrogen additives at elevated temperatures—Can sterically hindered pyridines prevent dye degradation? *Solar Energy Materials and Solar Cells* **2010**, *94* (10), 1582-1590; (f) Lee, H.; Bae, S.; Jo, Y.; Kim, K.; Jun, Y.; Han, C., A high temperature stable electrolyte system for dye-sensitized solar cells. *Electrochimica Acta* **2010**, *55* (24), 7159-7165; (g) Noda, S.; Nagano, K.; Inoue, E.; Egi, T.; Nakashima, T.; Imawaka, N.; Kanayama, M.; Iwata, S.; Toshima, K.; Nakada, K.; Yoshino, K., Development of large size dye-sensitized solar cell modules with high temperature durability. *Synthetic Metals* **2009**, *159* (21–22), 2355-2357; (h) Li, Q.; Zhao, J.; Sun, B.; Lin, B.; Qiu, L.; Zhang, Y.; Chen, X.; Lu, J.; Yan, F., High-Temperature Solid-State Dye-Sensitized Solar Cells Based on Organic Ionic Plastic Crystal Electrolytes. *Advanced Materials* **2012**, *24* (7), 945-950; (i) Hirose, F.; Shikaku, M.; Kimura, Y.; Niwano, M., IR Study on N719 Dye Adsorption with High Temperature Dye Solution for Highly Efficient Dye-Sensitized Solar Cells. *Journal of Electrochemical Society* **2010**, *157* (11), B1578-B1581.
115. Park, Y.; Mee Jung, Y.; Sarker, S.; Lee, J.; Lee, Y.; Lee, K.; Jin Oh, J.; Joo, S., Temperature-dependent infrared spectrum of $(\text{Bu}_4\text{N})_2[\text{Ru}(\text{dcbpyH})_2(\text{NCS})_2]$ on nanocrystalline TiO_2 surfaces. *Solar Energy Materials and Solar Cells* **2010**, *94* (5), 857-864.
 116. Fredin, K.; Anderson, K. F.; Duffy, N. W.; Wilson, G. J.; Fell, C. J.; Hagberg, D. P.; Sun, L.; Bach, U.; Lindquist, S., Effect on Cell Efficiency following Thermal Degradation of Dye-Sensitized Mesoporous Electrodes Using N719 and D5 Sensitizers. *Journal of Physical Chemistry C* **2009**, *113* (43), 18902-18906.
 117. Barnes, P. R. F.; Liu, L.; Li, X.; Anderson, A. Y.; Kisserwan, H.; Ghaddar, T. H.; Durrant, J. R.; O'Regan, B. C., Re-evaluation of Recombination Losses in Dye-Sensitized Cells: The Failure of Dynamic Relaxation Methods to Correctly Predict Diffusion Length in Nanoporous Photoelectrodes. *Nano Letters* **2009**, *9* (10), 3532-3538.
 118. O'Regan, B. C.; López-Duarte, I.; Martínez-Díaz, M. V.; Forneli, A.; Albero, J.; Morandeira, A.; Palomares, E.; Torres, T.; Durrant, J. R., Catalysis of Recombination and Its Limitation on Open Circuit Voltage for Dye Sensitized Photovoltaic Cells Using Phthalocyanine Dyes. *Journal of American Chemical Society* **2008**, *130* (10), 2906-2907.
 119. Law, C.; Spence, R.; O'Regan, B., Brief air heating of TiO_2 /dye films, to 120-250 °C; the effect on resulting liquid junction dye sensitised solar cells (DSSCs) and melt-processed solid-state DSSCs. *Journal of Materials Chemistry A* **2013**, *1* (45), 14154-14161.
 120. Thompson, J.; Blyth, R. I. R.; Mazzeo, M.; Anni, M.; Gigli, G.; Cingolani, R., White light emission from blends of blue-emitting organic molecules: A general route to the white organic light-emitting diode? *Applied Physics Letters* **2001**, *79* (5), 560-562.
 121. Schölin, R.; Karlsson, M. H.; Eriksson, S. K.; Siegbahn, H.; Johansson, E. M. J.; Rensmo, H., Energy Level Shifts in Spiro-OMeTAD Molecular Thin Films When Adding Li-TFSI. *Journal of Physical Chemistry C* **2012**, *116* (50), 26300-26305.
 122. Abate, A.; Leijtens, T.; Pathak, S.; Teuscher, J.; Avolio, R.; Errico, M. E.; Kirkpatrick, J.; Ball, J. M.; Docampo, P.; McPherson, I.; Snaith, H. J., Lithium salts as "redox active" p-type dopants for organic semiconductors and their impact in solid-state dye-sensitized solar cells. *Physical Chemistry Chemical Physics* **2013**, *15* (7), 2572-2579.

123. Howie, W. H.; Harris, J. E.; Jennings, J. R.; Peter, L. M., Solid-state dye-sensitized solar cells based on spiro-MeOTAD. *Solar Energy Materials and Solar Cells* **2007**, *91* (5), 424-426.
124. Bailie, C. D.; Unger, E. L.; Zakeeruddin, S. M.; Gratzel, M.; McGehee, M. D., Melt-infiltration of spiro-OMeTAD and thermal instability of solid-state dye-sensitized solar cells. *Physical Chemistry Chemical Physics* **2014**, *16* (10), 4864-4870.
125. Zhao, Y.; Zhu, K., Optical bleaching of perovskite (CH₃NH₃)PbI₃ through room-temperature phase transformation induced by ammonia. *Chemical Communications* **2014**, *50* (13), 1605-1607.
126. Baikie, T.; Fang, Y.; Kadro, J. M.; Schreyer, M.; Wei, F.; Mhaisalkar, S. G.; Graetzel, M.; White, T. J., Synthesis and crystal chemistry of the hybrid perovskite (CH₃NH₃)PbI₃ for solid-state sensitised solar cell applications. *Journal of Materials Chemistry A* **2013**, *1* (18), 5628-5641.
127. Eperon, G. E.; Burlakov, V. M.; Docampo, P.; Goriely, A.; Snaith, H. J., Morphological Control for High Performance, Solution-Processed Planar Heterojunction Perovskite Solar Cells. *Advanced Functional Materials* **2014**, *24* (1), 151-157.
128. Eperon, G. E.; Stranks, S. D.; Menelaou, C.; Johnston, M. B.; Herz, L. M.; Snaith, H. J., Formamidinium lead trihalide: a broadly tunable perovskite for efficient planar heterojunction solar cells. *Energy & Environmental Science* **2014**, *7* (3), 982-988.
129. Gimeno, N.; Li, X.; Durrant, J. R.; Vilar, R., Cyanide Sensing with Organic Dyes: Studies in Solution and on Nanostructured Al₂O₃ Surfaces. *Chemistry – A European Journal* **2008**, *14* (10), 3006-3012.
130. (a) Zhao, Y.; Zhu, K., Charge Transport and Recombination in Perovskite (CH₃NH₃)PbI₃ Sensitized TiO₂ Solar Cells. *Journal of Physical Chemistry Letters* **2013**, *4* (17), 2880-2884; (b) Frost, J. M.; Butler, K. T.; Brivio, F.; Hendon, C. H.; van Schilfgaarde, M.; Walsh, A., Atomistic Origins of High-Performance in Hybrid Halide Perovskite Solar Cells. *Nano Letters* **2014**, *14* (5), 2584-2590.
131. Vincent, B. R.; Robertson, K. N.; Cameron, T. S.; Knop, O., Alkylammonium lead halides. Part 1. Isolated PbI₆⁴⁻ ions in (CH₃NH₃)₄PbI₆•2H₂O. *Canadian Journal of Chemistry* **1987**, *65* (5), 1042-1046.
132. Law, C.; Miseikis, L.; Dimitrov, S.; Shakya-Tuladhar, P.; Li, X.; Barnes, P. R. F.; Durrant, J.; and O'Regan B. C., Performance and Stability of Lead Perovskite/TiO₂, Polymer/PCBM, and Dye Sensitized Solar Cells at Light Intensities up to 70 Suns, *Advanced Materials* **2014**, DOI: 10.1002/adma.201402612 (Only online version was available at the time of submitting thesis)
133. Niu, G.; Li, W.; Meng, F.; Wang, L.; Dong, H.; Qiu, Y., Study on the stability of CH₃NH₃PbI₃ films and the effect of post-modification by aluminum oxide in all-solid-state hybrid solar cells. *Journal of Materials Chemistry A* **2014**, *2* (3), 705-710.
134. Ku, Z.; Rong, Y.; Xu, M.; Liu, T.; Han, H., Full Printable Processed Mesoscopic CH₃NH₃PbI₃/TiO₂ Heterojunction Solar Cells with Carbon Counter Electrode. *Scientific Reports* **2013**, *3*.
135. (a) Kwon, Y. S.; Lim, J.; Yun, H.; Kim, Y.; Park, T., A diketopyrrolopyrrole-containing hole transporting conjugated polymer for use in efficient stable organic-inorganic hybrid solar cells based on a perovskite. *Energy & Environmental Science* **2014**, *7* (4), 1454-1460; (b) Cai, B.; Xing, Y.; Yang, Z.; Zhang, W.; Qiu, J., High performance hybrid solar

cells sensitized by organolead halide perovskites. *Energy & Environmental Science* **2013**, 6 (5), 1480-1485.

Appendix

Recombination lifetimes of water-based vs. MPN- and ACN-based DSSCs

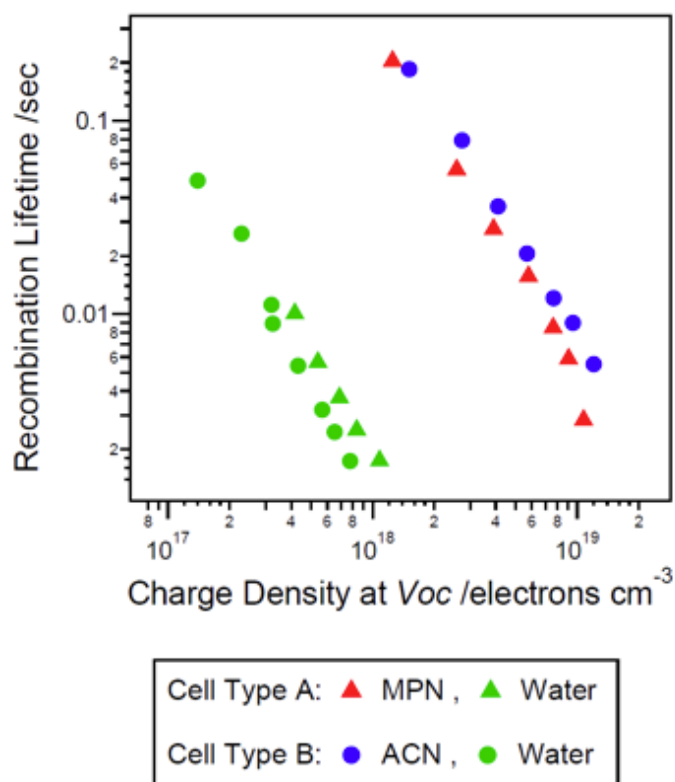


Fig. A.1 Recombination lifetime vs. charge density of D149 DSSCs with different solvents in electrolyte. (**Cell Type A:** TiO₂ film: G24i paste, 8.4 μm; Dye: D149 1:4 cheno; Electrolytes: 1 M GuI and 20 mM iodine in solvent as noted in legend. **Cell Type B:** TiO₂ film: G24i paste, 4.1 μm; Dye: D149 1:4 cheno; Electrolytes: 2 M NaI, 20 mM iodine and 0.5 M GuSCN in solvent as noted in legend.)

Water-based Z907 DSSCs with Varying Iodine Concentrations

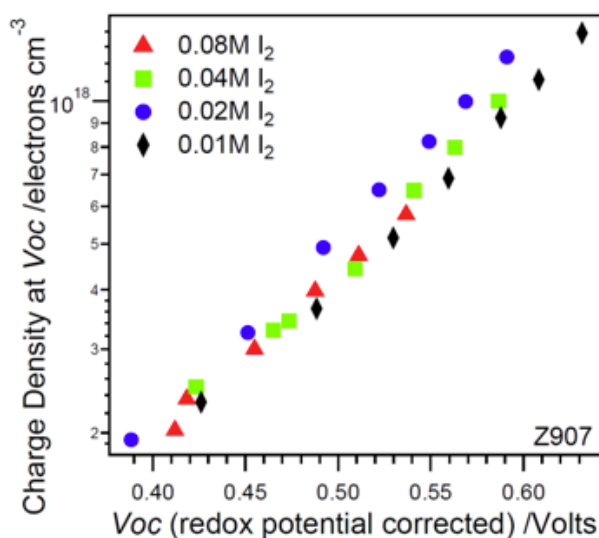


Fig. A.2 Charge density vs. redox potential corrected V_{oc} of water-based Z907 DSSCs with varying added iodine concentration. (TiO₂ film: G24i paste, 8.9 μm ; Dye: Z907 1:100 cheno; Electrolytes: Water with 2M NaI, 0.5 M GuSCN, ~saturated cheno, and iodine as noted in legend.) In order to eliminate the effect of change in redox potential, the V_{oc} 's are corrected according to the Nernst equation (9).

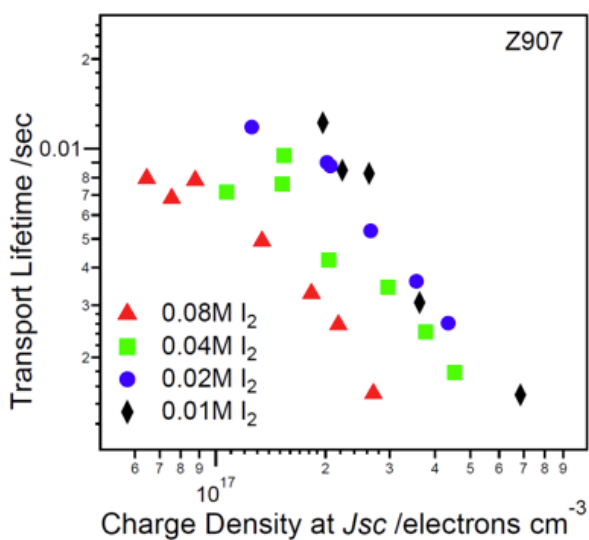


Fig. A.3 Transport lifetime vs. charge density of water-based Z907 DSSCs with varying added iodine concentration. Conditions as in Fig. A.2.

Water-based D149 DSSCs with Varying Iodine Concentrations

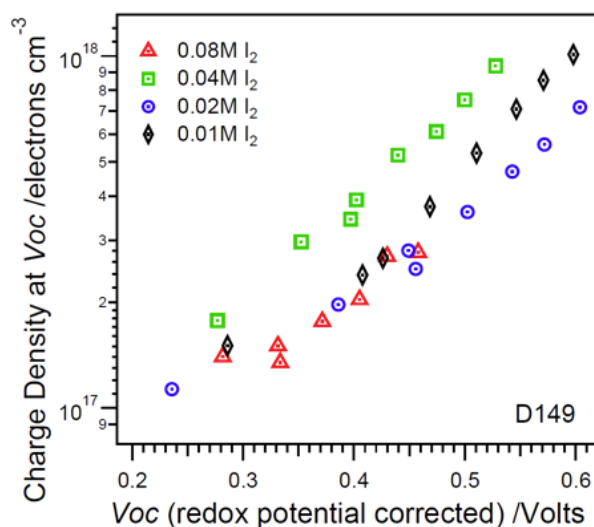


Fig. A.4 Charge density vs. redox potential corrected V_{oc} of water-based D149 DSSCs with varying added iodine concentration (TiO₂ film: DyeSol, 6.7 μm ; dye: D149 1:4 cheno; Electrolytes: Water with 2 M NaI, 0.1 M GuSCN, ~saturated cheno, and iodine as noted in the legend.) In order to eliminate the effect of change in redox potential, the V_{oc} 's are corrected according to the Nernst equation (9).

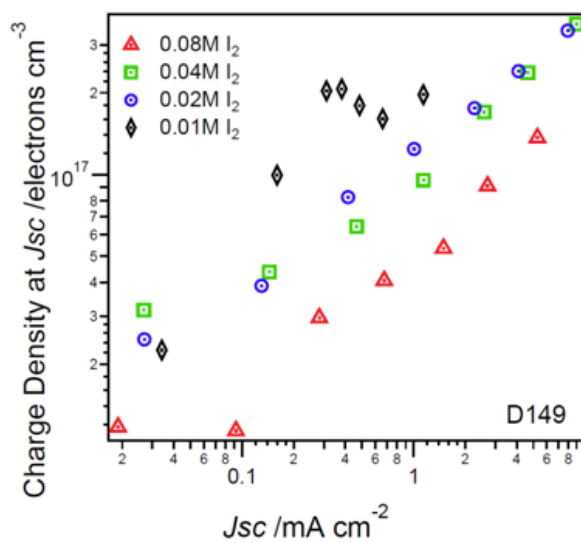


Fig. A.5 Charge density vs. J_{sc} of water-based D149 DSSCs with varying added iodine concentration. Conditions as in Fig. A.4.

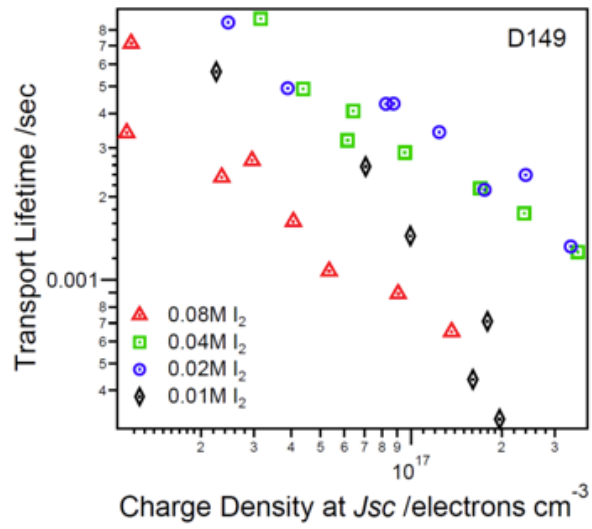


Fig. A.6 Transport lifetime vs. charge density of water-based D149 DSSCs with varying added iodine concentration. Conditions as in Fig. A.4.

Water-based Z907 DSSCs with Varying Iodide Concentrations

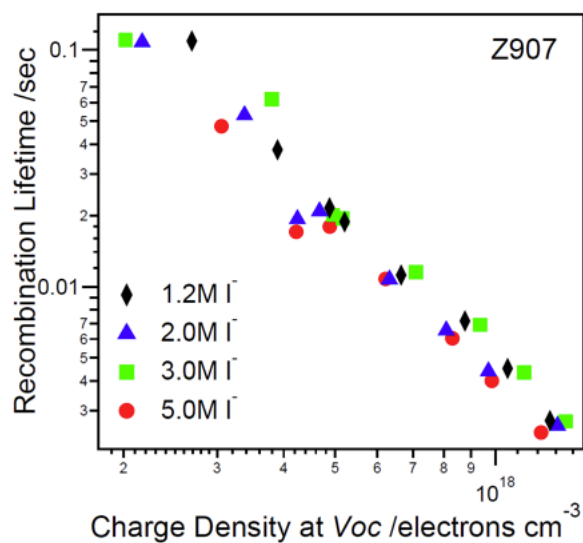


Fig. A.7 Recombination lifetime vs. charge density of water-based Z907 DSSCs with varying iodide concentration. (TiO₂ film: G24i paste, 8.1 μm ; Dye: Z907 1:100 cheno; Electrolytes: Water with 20 mM iodine, 0.5 M GuSCN, ~saturated cheno, and sodium iodide as noted in legend.)

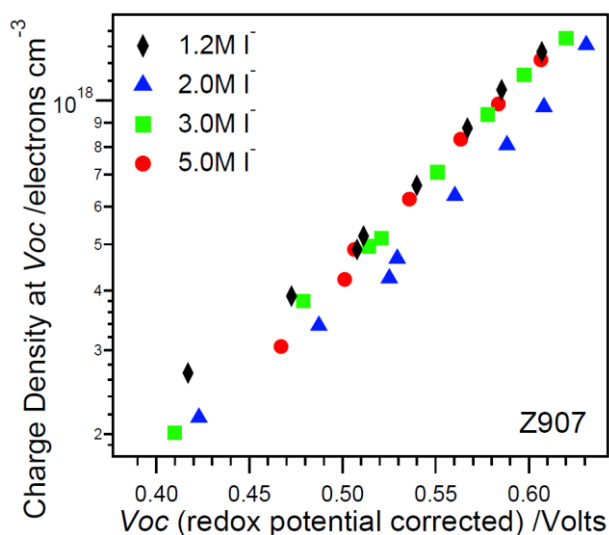


Fig. A.8 Charge density vs. redox potential corrected V_{oc} of water-based Z907 DSSCs with varying iodide concentration. Conditions as in Fig. A.7. In order to eliminate the effect of change in redox potential, the V_{oc} 's are corrected according to the Nernst equation (9).

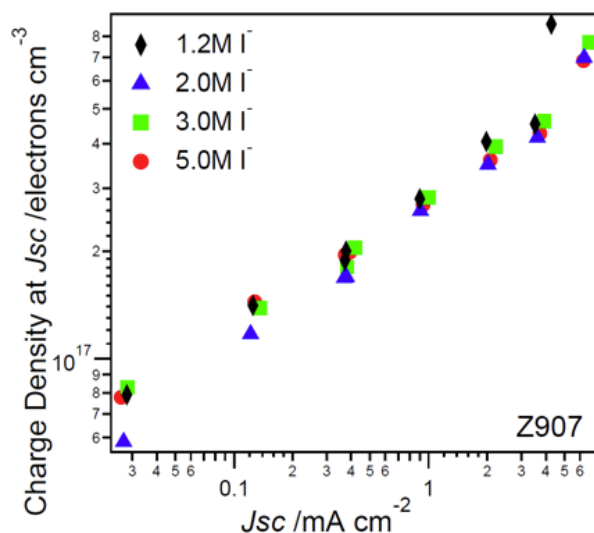


Fig. A.9 Charge density vs. J_{sc} of water-based Z907 DSSCs with varying iodide concentration. Conditions as in Fig. A.7.

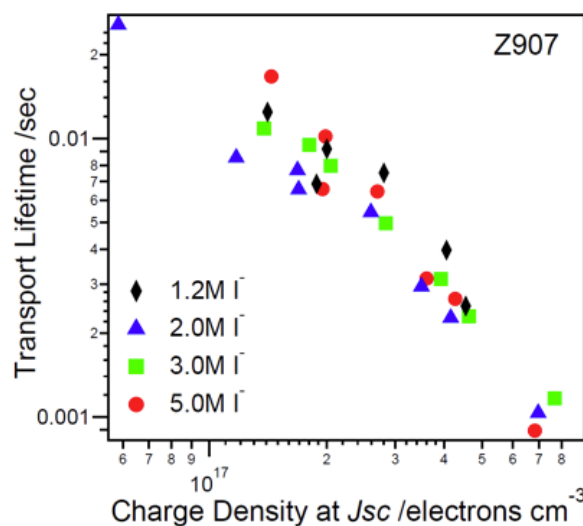


Fig. A.10 Transport lifetime vs. charge density of water-based Z907 DSSCs with varying iodide concentration. Conditions as in Fig. A.7.

Water-based D149 DSSCs with Varying Iodide Concentrations

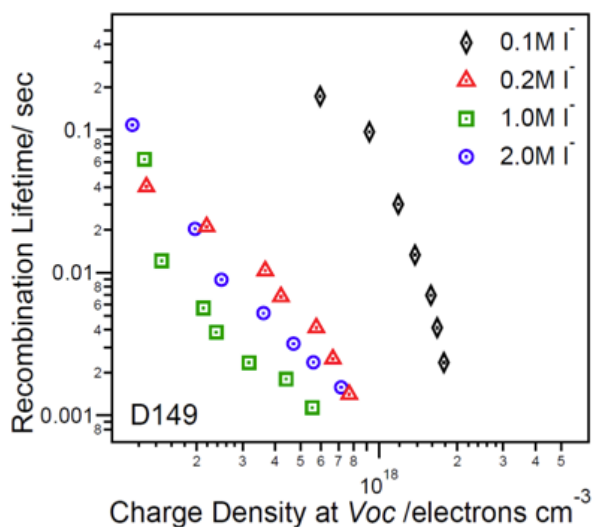


Fig. A.11 Recombination lifetime vs. charge density of water-based D149 DSSCs with varying iodide concentration. (TiO₂ film: DyeSol, 6.8 μm; Dye: D149 1:4 cheno; Electrolytes: Water with 0.02 M iodine, 0.1 M GuSCN, ~saturated cheno, with iodide as noted in the legend.)

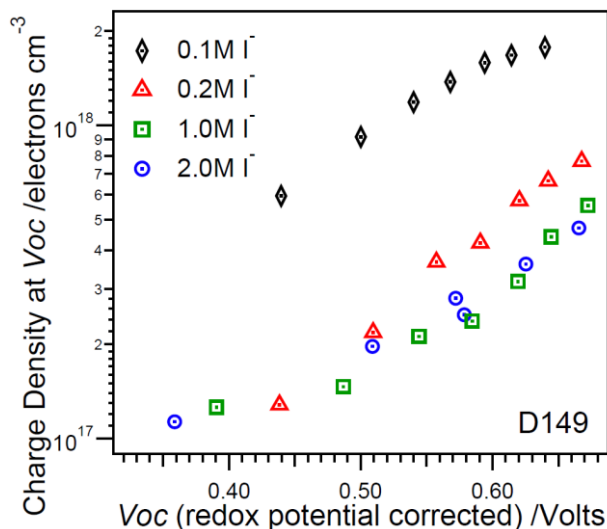


Fig. A.12 Charge density vs. redox potential corrected V_{oc} of water-based D149 DSSCs with varying iodide concentration. Conditions as in Fig. A.11. In order to eliminate the effect of change in redox potential, the V_{oc} 's are corrected according to the Nernst equation (9).

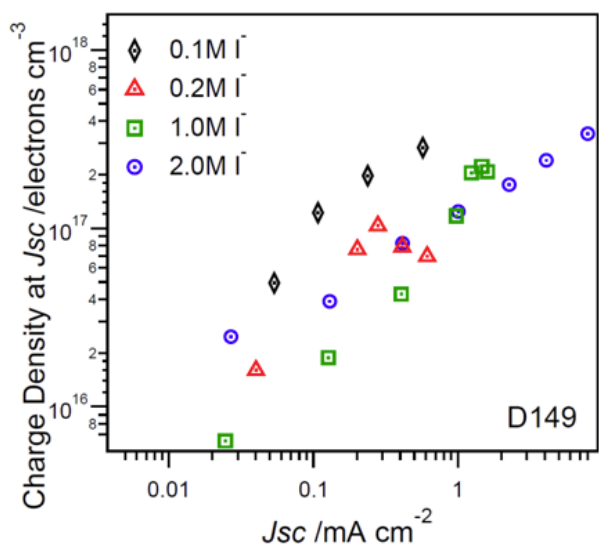


Fig. A.13 Charge density vs. J_{sc} of water-based D149 DSSCs with varying iodide concentration. Conditions as in Fig. A.11.

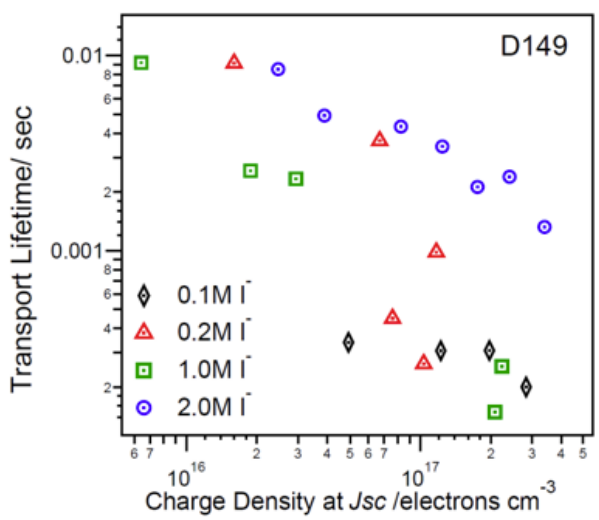


Fig. A.14 Transport lifetime vs. charge density of water-based D149 DSSCs with varying iodide concentration. Conditions as in Fig. A.11.

Water-based D149 DSSCs with Varying Guanidinium Iodide and Iodine Concentrations

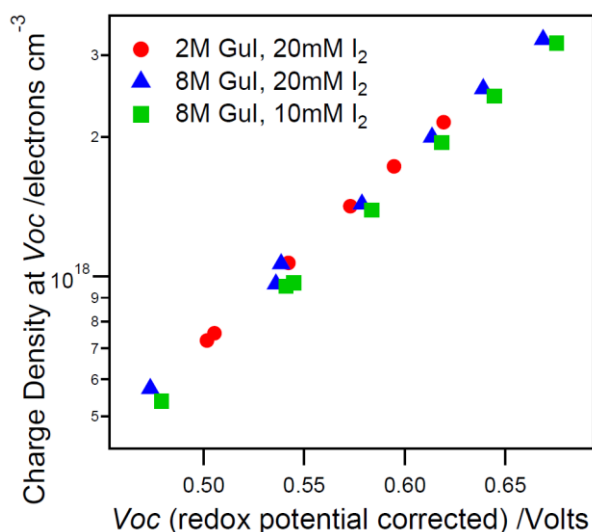


Fig. A.15 Charge density vs. redox potential corrected V_{oc} of water-based D149 DSSCs with varying guanidinium iodide and iodine concentrations. (TiO₂ film: G24i Paste, 4.6 μm ; Dye: D149 1:4 cheno; Electrolytes: Water with 0.5 M GuSCN, ~saturated cheno, with guanidinium iodide and iodine as noted in the legend) In order to eliminate the effect of change in redox potential, the V_{oc} 's are corrected according to the Nernst equation (9).

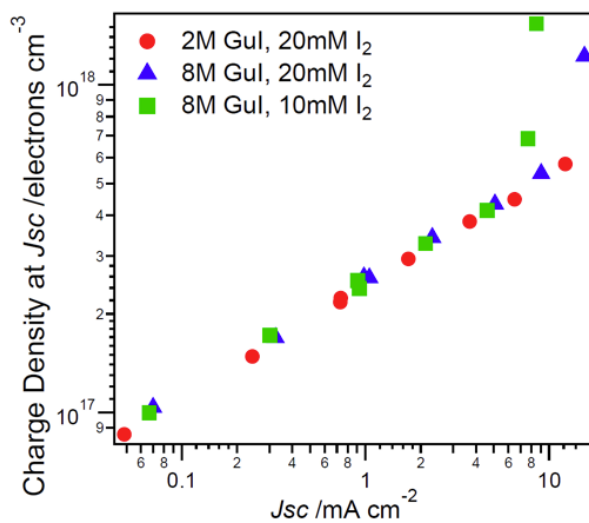


Fig. A.16 Charge density vs. J_{sc} of water-based D149 DSSCs with varying guanidinium iodide and iodine concentrations. Conditions as in Fig. A.15.

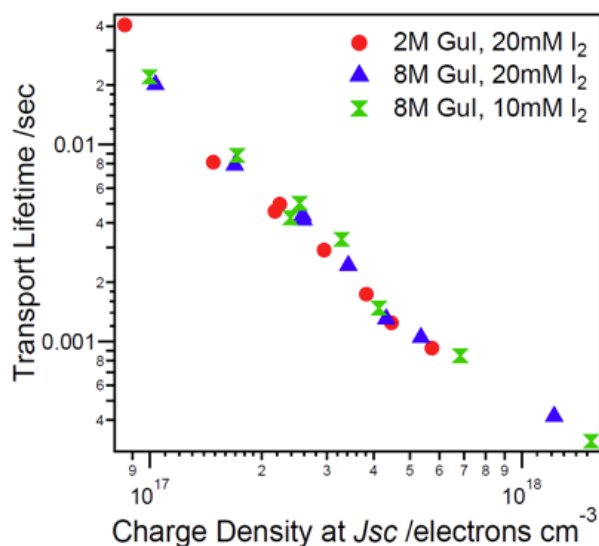


Fig. A.17 Transport lifetime vs. charge density of water-based D149 DSSCs with varying guanidinium iodide and iodine concentrations. Conditions as in Fig. A.15.

Effect of Heat and Toluene Treatment on $\text{TiO}_2/\text{Z907}$ Films

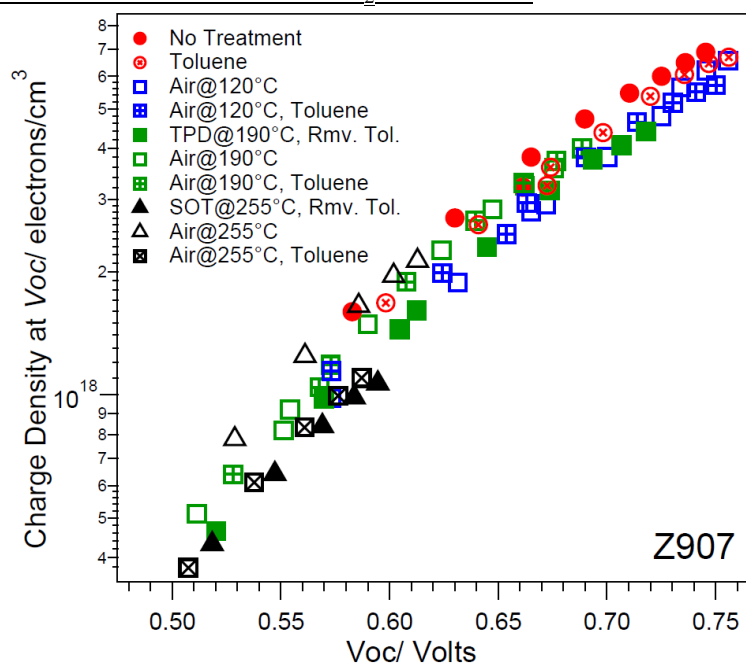


Fig. A.18 Charge density vs. V_{oc} of liquid-state DSSCs fabricated with Z907-sensitized TiO_2 electrodes (DyeSol, 7 μm) having undergone different treatments as noted in legend. Electrolyte was 0.8 M PMII, 50 mM iodine, 50 mM GuSCN, 0.28 M TBP and 25 mM LiI in MPN. (Rmv. Tol. indicates HTM Removed by Toluene) [This figure is reproduced with the permission of the rights holder, The Royal Society of Chemistry.]¹¹⁹

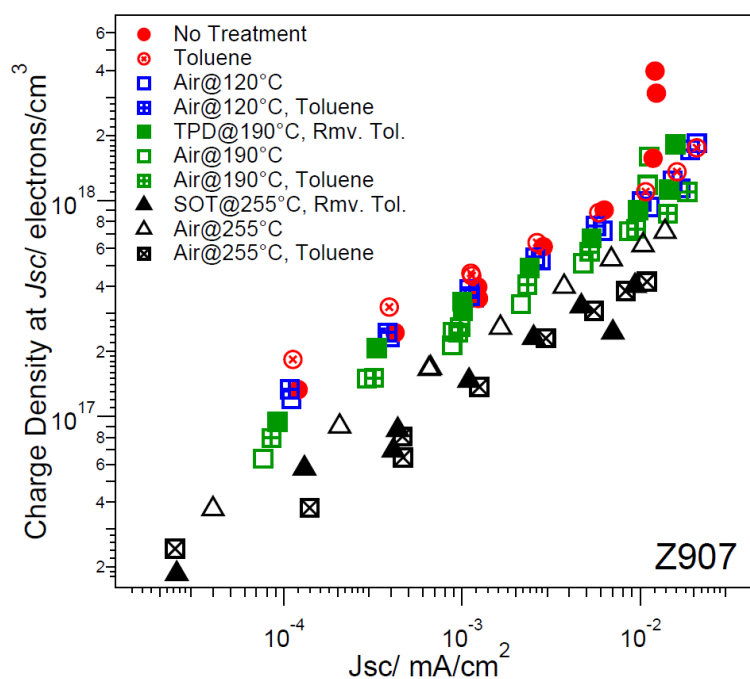


Fig. A.19 Charge density vs. J_{sc} of liquid-state DSSCs fabricated with Z907-sensitised TiO_2 electrodes (DyeSol, 7 μm) having undergone different treatments as noted in legend. Conditions as in Fig. A.18. (Rmv. Tol. indicates HTM Removed by Toluene) [This figure is reproduced with the permission of the rights holder, The Royal Society of Chemistry.]¹¹⁹

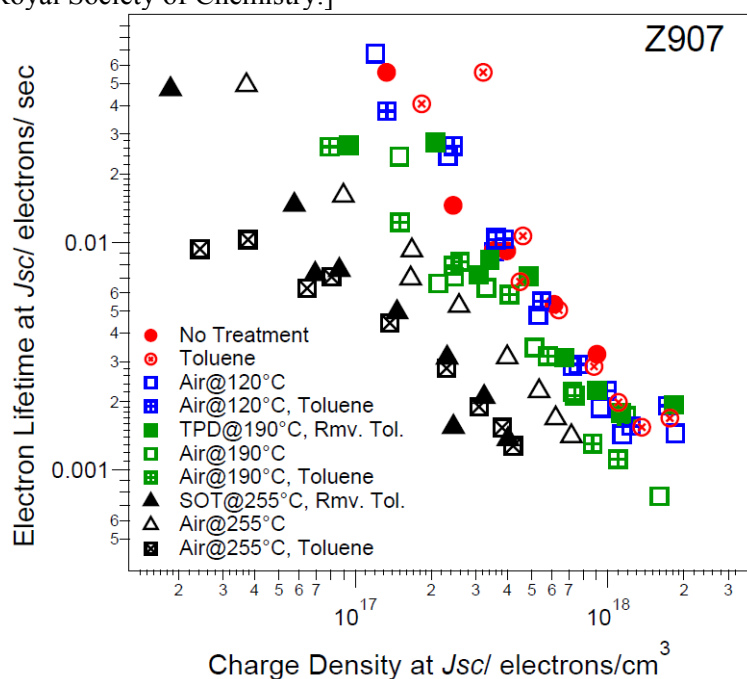


Fig. A.20 Electron lifetime at J_{sc} vs. charge density of liquid-state DSSCs fabricated with Z907-sensitised TiO_2 electrodes (DyeSol, 7 μm) having undergone different treatments as noted in legend. Conditions as in Fig. A.18. (Rmv. Tol. indicates HTM Removed by Toluene)

Effect of Different Treatments on TiO₂/D149 Films

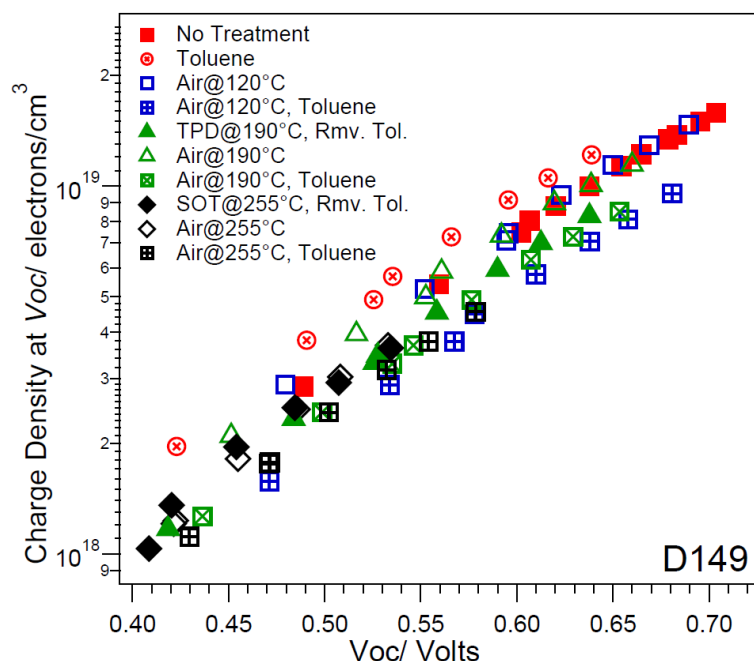


Fig. A.21 Charge density vs. V_{oc} of liquid-state DSSCs fabricated with D149-sensitized TiO₂ electrodes (DyeSol, 7 μ m) having undergone different treatments as noted in legend. Electrolyte: 0.8 M NaI, 40 mM iodine and 0.2 M GuSCN in MPN. (Rmv. Tol. indicates HTM Removed by Toluene) [This figure is reproduced with the permission of the rights holder, The Royal Society of Chemistry.]¹¹⁹

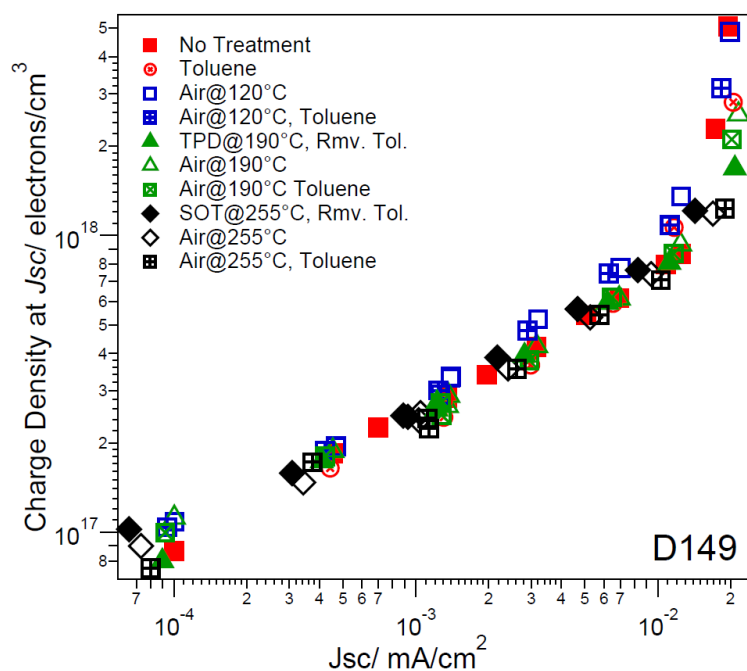


Fig. A.22 Charge density vs. J_{sc} of liquid-state DSSCs fabricated with D149-sensitized TiO₂ electrodes (DyeSol, 7 μ m) having undergone different treatments as noted in legend. Conditions as in Fig. A.21 (Rmv. Tol. indicates HTM Removed by Toluene) [This figure is reproduced with the permission of the rights holder, The Royal Society of Chemistry.]¹¹⁹

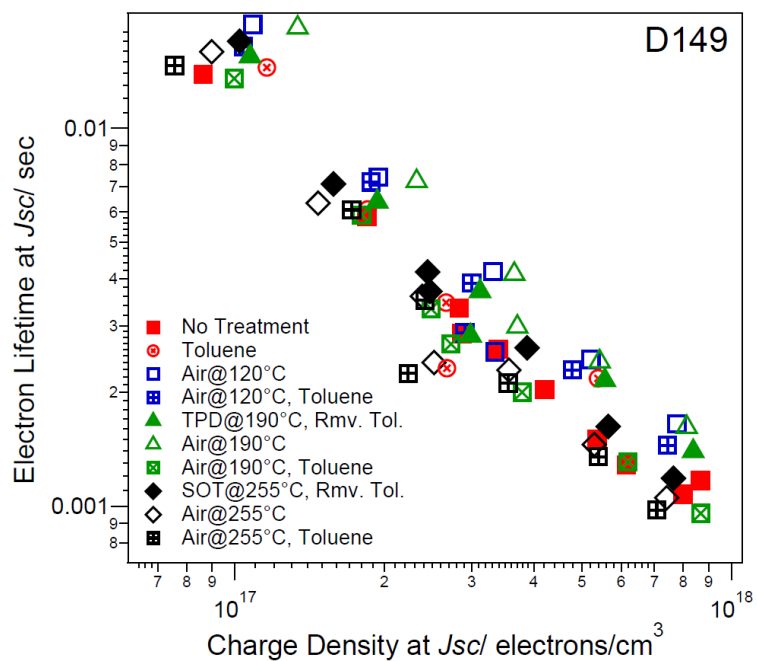


Fig. A.23 Electron lifetime at J_{sc} vs. charge density of liquid-state DSSCs fabricated with D149-sensitised TiO_2 electrodes (DyeSol, 7 μm) having undergone different treatments as noted in legend. Conditions as in Fig. A.21. (Rmv. Tol. indicates HTM Removed by Toluene)

Effect of Heat Treatment on 1.3 μm thick TiO_2 /Z907 Films

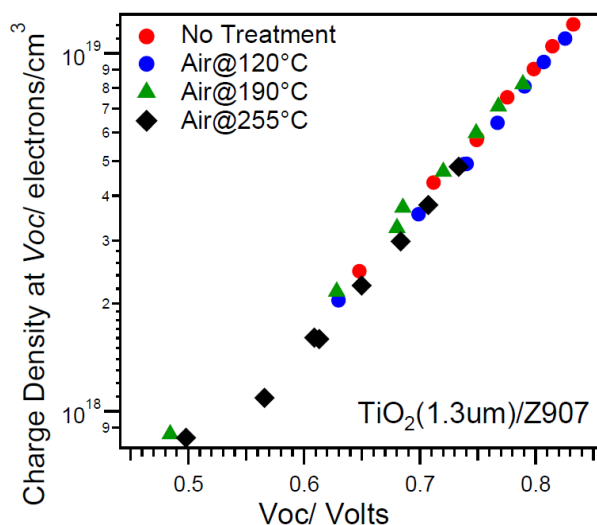


Fig. A.24 Charge density vs. V_{oc} of liquid-state DSSCs fabricated with Z907-sensitised TiO_2 electrodes (transparent, 1.3 μm) heated at different temperatures for 1 minute. Electrolyte: 0.8 M PMII, 50 mM iodine, 50 mM GuSCN, 0.3 M benzimidazole in MPN. [This figure is reproduced with the permission of the rights holder, The Royal Society of Chemistry.]¹¹⁹

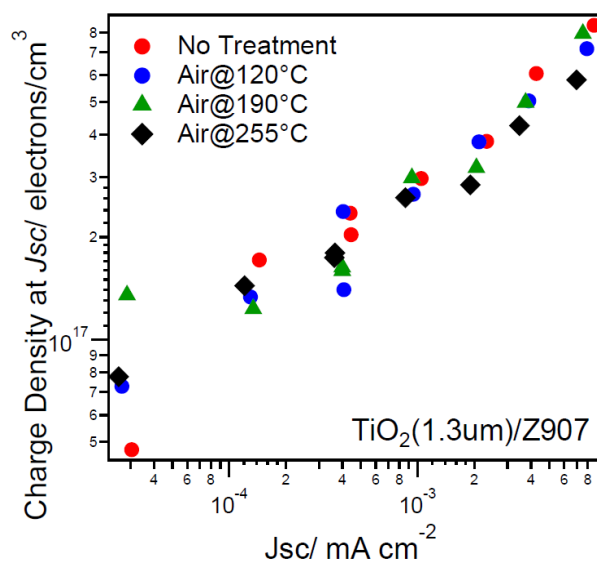


Fig. A.25 Charge density vs. J_{sc} of liquid-state DSSCs fabricated with Z907-sensitised TiO_2 electrodes (transparent, 1.3 μm) heated at different temperatures for 1 minute. Conditions as in Fig. A.24.

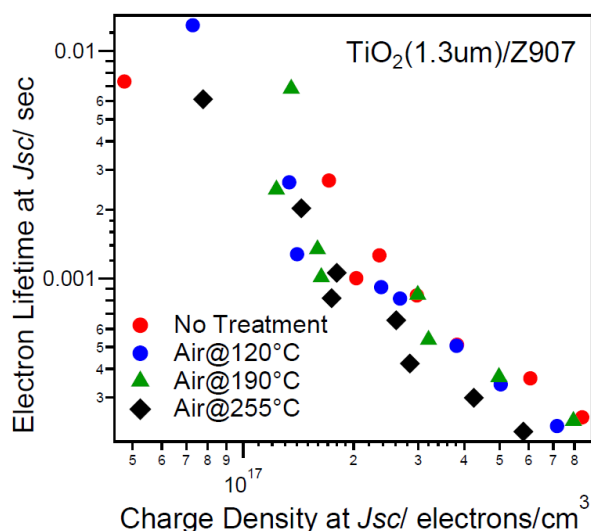


Fig. A.26 Electron lifetime at J_{sc} vs. charge density of liquid-state DSSCs fabricated with Z907-sensitised TiO_2 electrodes (transparent, 1.3 μm) heated at different temperatures for 1 minute. Conditions as in Fig. A.24.

Effect of Heat Treatment on 2 μm thick TiO_2 /D149 Films

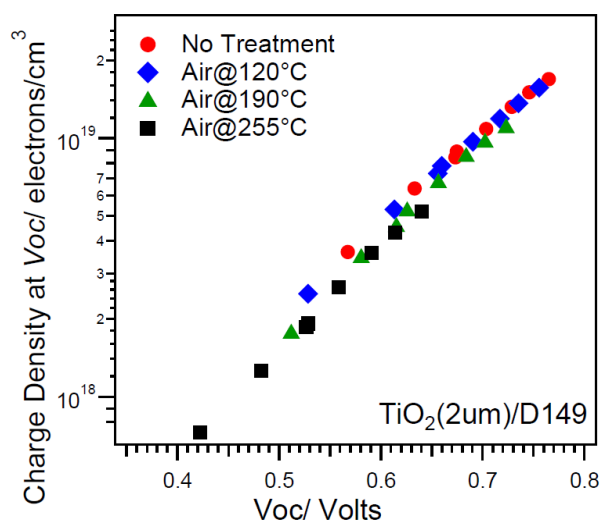


Fig. A.27 Charge density vs. V_{oc} of liquid-state DSSCs fabricated with D149-sensitised TiO_2 electrodes (transparent, 2 μm) heated at different temperatures for 1 minute. Electrolyte: 0.8 M NaI, 40 mM iodine and 0.2 M GuSCN in MPN. [This figure is reproduced with the permission of the rights holder, The Royal Society of Chemistry.]¹¹⁹

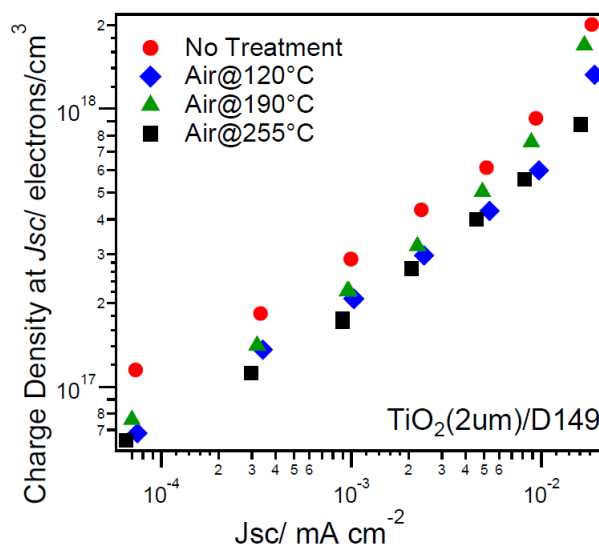


Fig. A.28 Charge density vs. J_{sc} of liquid-state DSSCs fabricated with D149-sensitised TiO₂ electrodes (transparent, 2 μm) heated at different temperatures for 1 minute. Conditions as in Fig. A.27.

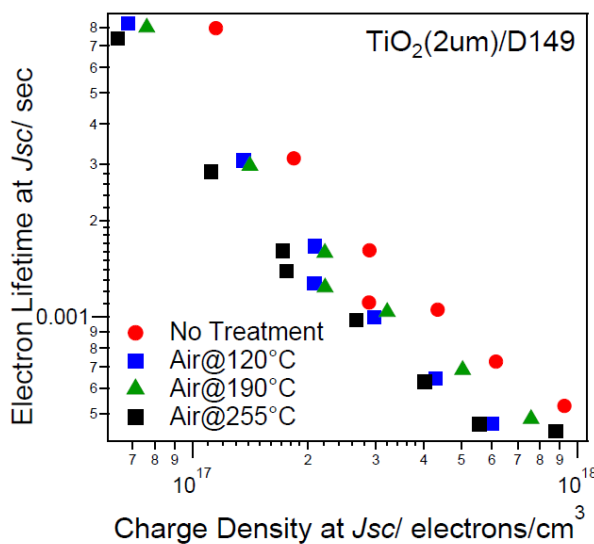


Fig. A.29 Electron lifetime at J_{sc} vs. charge density of liquid-state DSSCs fabricated with D149-sensitised TiO₂ electrodes (transparent, 2 μm) heated at different temperatures for 1 minute. Conditions as in Fig. A.27.

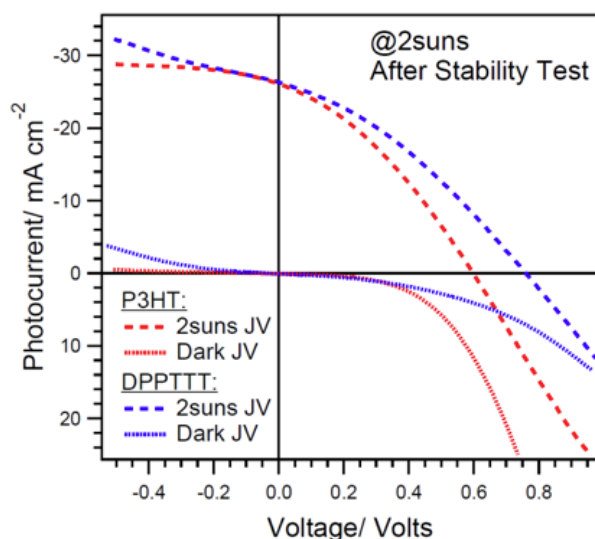
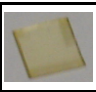
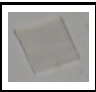
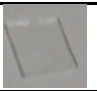
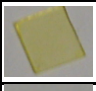
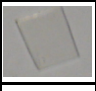

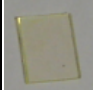
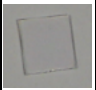



Fig. A.30 Two-sun and dark JV curves of encapsulated TiO_2/MAPI solar cells with HTMs after the stability test of continuous illumination (P3HT: @2 suns for 12 hours; DPPTTT: @2 suns for 21 hours).

Table A.1 shows the photos of lead iodide, lead chloride and methylammonium iodide ($\text{NH}_3\text{CH}_3\text{I}$ or MAI) on a glass plate with or without mesoporous titania (mp-TiO_2) layer or mesoporous alumina ($\text{mp-Al}_2\text{O}_3$) layer. Film thicknesses (with or without mesoporous layer) are ~ 150 nm.

Control Films					
PbI_2		PbCl_2		$\text{NH}_3\text{CH}_3\text{I}$	
$\text{mp-TiO}_2/\text{PbI}_2$		$\text{mp-TiO}_2/\text{PbCl}_2$		$\text{mp-TiO}_2/\text{NH}_3\text{CH}_3\text{I}$	
$\text{mp-Al}_2\text{O}_3/\text{PbI}_2$		$\text{mp-Al}_2\text{O}_3/\text{PbCl}_2$		$\text{mp-Al}_2\text{O}_3/\text{NH}_3\text{CH}_3\text{I}$	

Summary of Permission for Third Party Copyright Works

Page Number	Type of work: text, figure, map, etc.	Source work	Copyright holder & year	Work out of copyright	Permission to re-use	Permission requested	Permission refused	Orphan work
Page 63, 64	Fig. 3.1, 3.2	Advanced Materials 2010, 22 (40), 4505-4509	© 2010 WILEY-VCH Verlag GmbH & Co. KGaA, Weinheim		✓			
Page 66, 67, 69, 82-85, 88 ,98	Fig. 3.4, 3.5, 3.7, 3.15, 3.16, 3.18, 3.19, 3.23, 3.34 Table 3.1, 3.2, 3.4, 3.8	Journal of Materials Chemistry 2012, 22 (44), 23387-23394	© The Royal Society of Chemistry 2012	✓				
Page 123 133- 137, 195-197, 199, 200	Fig. 4.17, 4.28, 4.29, 4.30, 4.31, 4.32, 4.33, 4.34, A.18, A.19, A.21, A.22, A.24, A.27 Table 4.6, 4.7	Journal of Materials Chemistry A 2013, 1, 14154-14161	© The Royal Society of Chemistry 2013	✓				
Page 162-165	Fig. 5.13, 5.14, 5.15, 5.16 ,5.17	Advanced Materials 2014, DOI: 10.1002/adma.201402612	© 2014 WILEY-VCH Verlag GmbH & Co. KGaA, Weinheim		✓			